UNIVERSIDAD COMPLUTENSE DE MADRID
Facultad de Ciencias Biológicas

Departamento de Bioquimica y
Biologia Molecular

FUNCTIONALIZED BIOMATERIALS FOR TISSUE ENGINEERING

BIOMATERIALES FUNCIONALIZADOS PARA INGENIERÍA DE TEJIDOS

Tesis Doctoral
Ana María Santos Coquillat

Dirigida por Endzhe Matykina y Alberto Gallardo Ruiz

Madrid, 2018

UNIVERSIDAD COMPLUTENSE DE MADRID

FACULTAD DE CIENCIAS BIOLÓGICAS

DEPARTAMENTO DE BIOQUÍMICA Y BIOLOGÍA MOLECULAR

TESIS DOCTORAL

Functionalized biomaterials for tissue engineering

Biomateriales funcionalizados para ingeniería de tejidos

MEMORIA PARA OPTAR AL GRADO DE DOCTORA PRESENTADA POR

Ana María Santos Coquillat

DIRECTORES:

Endzhe Matykina

Alberto Gallardo Ruiz

Madrid
Ed. electrónica 2019

“What we know is a drop, what we don't know is an ocean.”

Isaac Newton

En memoria de José Luis López Lacomba

Quien nos enseñó a vivir intensamente

Agradecimientos

En primer lugar, me gustaría agradecer a mis directores de tesis por su ayuda y apoyo durante este tiempo. Endzhe, gracias por las interminables horas de reuniones, tu determinación y por todo lo que me has enseñado. Alberto, gracias por tus consejos y por estar ahí en los momentos duros. Por último, a Kike, gracias por ayudarme durante todos estos años y guiarme en este camino.

A José Luis y Vivi por acogerme en su grupo y enseñarme a amar la investigación. A toda la gente que ha compartido conmigo esta etapa en el IEB (Chus, Giulia, Irene, Miguel, Isa, David, Maria K, Lauri, Ana, Marian, Susana, Javi, Rodri…) y me la han hecho infinitamente más amena. A toda la gente del grupo de Caracterización de Materiales (Yanira, Marina, Rafa, María…), en especial a Raúl y a Marta por sus muchos consejos y enseñanzas. A todo el grupo de FUPOL por ayudarme y apoyarme, especialmente a Juan, Carlos, Helmut, Felipe, Elma y Anselmo.

A mis compañeras y compañeros de la carrera; Carolina, Manu, Maria, Kathe, Anna, Rober, Dani, Xabel… y del Máster; Juan, María G, Rober, María T, Esther sin los que no habría llegado hasta aquí. A todo el profesorado que me ha marcado, enseñado y, en definitiva, guiado durante el camino.

A mi madre y a mi padre por apoyarme siempre, enseñarme la importancia de formarme y que la mejor herencia es el conocimiento.

A mis hermanas, Ari e Irene, por estar ahí siempre, a las cuales admiro inmensamente por su capacidad artística y su visión de la vida. A toda mi familia y amistades por animarme en esta etapa.

A Rubén por tener siempre una sonrisa, por su ánimo constante y su comprensión.

Table of contents

FUNCTIONALIZED BIOMATERIALS FOR TISSUE ENGINEERING

Tissue engineering has introduced a new paradigm in medical care: the properties of modern biomaterials have to address multiple functions related to the needs of specific age groups of the patients and different diseases. The literature review carried out in the Introduction of the Thesis approaches the specificities of bone regeneration mechanisms and discloses how these have been addressed in the past by several generations of biomaterials. Both the traditional and newly developed materials for permanent and temporary implant applications are reviewed. Surface modification is revealed as the main strategy employed for functionalization of biomaterials. The most important surface modification techniques that lead to simultaneous modification of the composition and topography of the surface of the core materials are discussed. Advances in hybridization of biomaterials via combination of surface treated core materials with polymeric top-coat systems and cell sheet engineering are reviewed.

The objective of this Thesis is to validate a hybrid approach for tissue regeneration in which biomaterials for permanent and temporary implant applications can be multifunctionalized by means of surface modification and used in combination with cell therapy.

Chapter I evaluates bioactivity of electrochemical surface treatments based on *anodizing* of commercially pure Ti, Ti6Al4V and pure Zr for permanent dental and orthopaedic applications. The effects of coating surface topography and composition modified by *in situ* incorporation of various chemical elements (such as Ca, P, Mg, Zn, Si or F) are evaluated with respect to bone homeostasis related cells (such as osteoblasts and osteoclasts). The incorporation of fluoride as an antibacterial element in the coating surface reveals a reduction in bacteria colonization and a bactericidal effect. Possibility of tailoring bone homeostasis and loading capacity and release rate of model protein (albumin) via *in situ* modification of surface composition and topographic features is shown. The binding/release mechanism of the protein depending on the surface composition is underpinned. Using an *in vivo* porcine model study a superior bone-to-implant contact is demonstrated for commercially pure Ti screws with a surface modified with Ca,P-based ceramic coatings compared with non-treated implants.

In Chapter 2 Mg0.8Ca alloy was investigated as a biodegradable material for bone regeneration and cardiovascular temporary applications, using *plasma electrolytic oxidation* ceramic coatings with a dual functionality: (i) control of the degradation rate and (ii) targeted bioactivity via incorporation of chemical elements (Si, Ca, P, F). By direct cell seeding studies a surface composition containing Si, Ca and P was pinpointed as a universally adequate for endothelial, premyoblastic and osteoblasts, i.e. potentially suitable for both orthopaedic and cardiovascular

applications. Extracts obtained by immersion of surface-modified Mg0.8Ca alloy were evaluated in terms of biocompatibility, osteoblasts and osteoclasts differentiation studies and their co-culture; Si-Ca-P based surface treatment supported all of these processes. A proof of concept of a hybrid metal/ceramic/polymeric biomaterial is demonstrated using functionalization of ceramic coating on Mg alloy by polymeric coating (polycaprolactone) with porous structure obtained by *Breath Figures* approach. Hierarchical growth of premyoblastic cells over the obtained hybrid structure is demonstrated.

In Chapter 3 *polystyrene platforms* are selectively functionalized using Breath Figures technique with antibacterial motifs (DMAEMA, PAA) located inside the pores of the polymer. It is shown that modulation of pore diameter to 3-5 μm enables bacteria to reach inside the pores and be selectively killed by contact with DMAEMAQ or PAA groups, whereas mammalian cells stay adhered to the surface maintaining normal adhesion and proliferation.

In Chapter 4 *vinyl-lactam based hydrogels* are investigated as new hydrogel biomaterials with a capacity for simultaneous modification of surface charge and topography for potential application in cell therapy as possible cell harvesting supports and further transplants. Biovalidation of the ionic VCL (Vinylcaprolactam) hydrogels is carried out using endothelial cells. Sulfobetain zwitterionic-VCL hydrogel is shown to be the most promising with respect to endothelial cells compared with other ionic VCL hydrogels (positive, negative, zwitterionic and pseudo-zwitterionic) and a VP (Vinylpyrrolidone)-based hydrogel. The neutral hydrogel is evaluated with three different cell types (endothelial, macrophagic and preosteoblastic) cultured on free VCL-based thermosensitive hydrogels and transplanted into a TCP platform. The surface charged (positive, negative and pseudo-zwitterionic) VP hydrogels supported on polycarbonate are also discriminated with respect to endothelial cell growth and transplant potential. The topographic characteristics (large, intermediate and small periodicity of the surface wrinkles) of negatively charged polycarbonate supported VP hydrogels modulating the endothelial, preosteoblastic and macrophagic cell transplant success are determined, confirming the importance of intermediate and small wrinkle conditions for promotion of endothelial and macrophagic cell lines.

As a result, each Chapter constituted biovalidation screening stages during the process of design and selection of different elements of a potential hybrid biomaterial, that would comprise metallic, ceramic, polymeric materials and cell components. The findings disclosed the effects of three key steps of multifunctionalization of biomaterials for permanent or temporary implant application on different tissue regeneration processes, underpinning the roles of surface topography and chemistry of metallic, ceramic and polymeric biomaterials in various processes, such as cell adhesion, proliferation, differentiation, and antibacterial activity.

BIOMATERIALES FUNCIONALIZADOS PARA INGENIERÍA DE TEJIDOS

La ingeniería de tejidos ha establecido un nuevo paradigma en la medicina: las propiedades de los biomateriales modernos han de cumplir diversas funciones relacionadas con las necesidades de la sociedad, las cuales varían según los grupos de edad específicos y las distintas enfermedades de los pacientes. La revisión bibliográfica realizada en la Introducción de esta Tesis Doctoral aborda los mecanismos de regeneración ósea y revela las estrategias que han sido empleadas en el pasado por varias generaciones de biomateriales. Además, se analizan tanto los materiales tradicionales como los recientemente desarrollados para su aplicación como implantes permanentes y temporales. La modificación de la superficie de estos implantes se ha confirmado como la principal estrategia aplicada para la funcionalización de biomateriales. Por ello, se discuten las técnicas más importantes que conducen a la modificación simultánea de la composición y la topografía de la superficie de los materiales base. Asimismo, se revisan los avances en la generación de biomateriales híbridos a través de la combinación de materiales tratados superficialmente con la adición de capas poliméricas y se relacionan con la ingeniería de monocapas celulares.

El objetivo de esta Tesis es validar un enfoque híbrido para la regeneración de tejidos en el que los biomateriales se puedan multifuncionalizar mediante la modificación de su superficie y se utilicen en combinación con la terapia celular para su aplicación como implantes permanentes y temporales.

En el Capítulo I se analizó la bioactividad de los tratamientos de superficie electroquímicos basados en anodizado de Ti comercialmente puro, Ti6Al4V y Zr puro para aplicaciones permanentes en el ámbito de la odontología y la ortopedia. Los efectos de la topografía de la superficie del recubrimiento y de la composición modificada mediante la incorporación *in situ* de diversos elementos químicos (como Ca, P, Mg, Zn, Si o F) se evaluaron con respecto a las células responsables de la homeostasis ósea (como los osteoblastos y los osteoclastos). La incorporación de fluoruro como elemento antibacteriano en la superficie del recubrimiento reveló una reducción en la colonización bacteriana y un efecto bactericida adicional. Se mostró la posibilidad de modular los procesos de homeostasis ósea, la capacidad de carga y la tasa de liberación de la proteína modelo (albúmina) a través de la modificación *in situ* de la composición de la superficie y de las características topográficas. El mecanismo de unión/liberación de la proteína se describió como dependiente de la composición de la superficie. Mediante un estudio *in vivo* en modelo porcino, se analizó el contacto hueso-implante utilizando implantes de Ti comercialmente puros con una superficie modificada con recubrimientos cerámicos basados en Ca y P, mostrando una mejora en comparación con los implantes no tratados.

En el Capítulo 2, se estudió la aleación Mg0.8Ca como un material biodegradable para su uso en regeneración ósea y aplicaciones cardiovasculares temporales, utilizando recubrimientos cerámicos de oxidación electrolítica por plasma con una doble funcionalidad: (i) control de la tasa de degradación y (ii) bioactividad dirigida mediante la incorporación de especies químicas (Si, Ca, P, F). Mediante estudios de siembra directa de células en su superficie, el recubrimiento que contenía Si, Ca y P se identificó como adecuado para células endoteliales, premioblásticas y osteoblásticas, es decir, potencialmente útil para aplicaciones ortopédicas y cardiovasculares. Los extractos obtenidos por inmersión de la aleación Mg0.8Ca modificada en la superficie se evaluaron en términos de biocompatibilidad, estudios de diferenciación de osteoblastos, osteoclastos y cocultivo de los mismos; nuevamente el tratamiento de superficie basado en Si-Ca-P se mostró más favorable en todos estos procesos. Finalmente, se realizó una prueba de concepto con un biomaterial híbrido que constaba de una base de metal (Mg0.8Ca) con un recubrimiento cerámico y la adición de un material polimérico (PCL) con estructura porosa obtenida mediante el método *Breath Figures*. Se demostró el crecimiento jerárquico de células premioblásticas sobre la estructura híbrida obtenida.

En el Capítulo 3, se funcionalizaron selectivamente plataformas de poliestireno mediante la técnica de *Breath Figures* con motivos antibacterianos (DMAEMA, PAA) ubicados dentro de los poros del polímero. Se mostró que la modulación del diámetro de poro a 3-5 µm permite que las bacterias alcancen el interior de los poros y mueran de forma selectiva por contacto con los grupos DMAEMAQ o PAA, mientras que las células de mamífero (endoteliales) permanecen adheridas a la superficie del material manteniendo niveles normales de adhesión y proliferación.

En el Capítulo 4, los hidrogeles basados en vinil-lactamas se analizaron como nuevos biomateriales con capacidad para la modificación simultánea de la carga superficial y la topografía, proponiendo su posible aplicación en terapia celular como soportes para crecimiento celular y trasplante. La biovalidación de los hidrogeles iónicos basados en VCL (vinilcaprolactama) se llevó a cabo con células endoteliales. El hidrogel VCL que presenta zwitteriones sulfobetaínicos se muestra como el más prometedor con respecto a las células endoteliales en comparación con otros hidrogeles iónicos VCL (positivo, negativo, zwitterionico y pseudo-zwitterionico) y el control basado en VP (vinilpirrolidona). El hidrogel neutro se evaluó utilizando tres tipos de células diferentes (endotelial, macrofágica y preosteoblástica) cultivadas en hidrogeles termosensibles libres basados en VCL, las cuales se trasplantaron a una nueva placa de cultivo. Por otro lado, mediante el análisis de los hidrogeles de VP cargados en superficie (positivo, negativo y pseudo-zwitteriónico) soportados en policarbonato también se observaron diferencias con respecto al crecimiento de células endoteliales y al potencial de trasplante, siendo la carga negativa la más favorable. Se determinó que las características topográficas (periodicidad grande, intermedia y pequeña de las arrugas superficiales) de los hidrogeles de VP cargados

negativamente formados sobre soportes de policarbonato pueden modular el comportamiento de las células endoteliales, preosteoblásticas y macrofágicas. Más concretamente, las células endoteliales y macrofágicas se vieron favorecidas por lo las arrugas intermedias y pequeñas en términos de crecimiento y trasplante.

Como resultado, cada Capítulo ha constituido una etapa de selección empleando la biovalidación de los materiales, con objeto de diseñar y seleccionar los diferentes elementos de un potencial biomaterial híbrido. Este biomaterial híbrido incluiría materiales metálicos, cerámicos, poliméricos y componentes celulares. Los resultados de esta Tesis han puesto de manifiesto tres pasos clave en el proceso de la multifuncionalización de biomateriales para la aplicación de implantes permanentes o temporales en diferentes procesos de regeneración de tejidos, siendo la topografía de superficie y química de biomateriales metálicos, cerámicos y poliméricos determinante para diferentes procesos como la adhesión celular, la proliferación, diferenciación y actividad antibacteriana.

List of figures

List of tables

Disclosure

This doctoral Thesis includes material from papers by the author [1-7]. Chapter 1 uses material from references [1, 2, 5, 6] and Section 1.1.2. is based on submitted material. On the other hand, Chapter 2 is based on unpublished material. Chapter 3 is based on references [3, 7]. Chapter 4 is based on [4] and submitted material. Some material from each of these papers has also been incorporated into methodology section.

Most part of the non-biological characterization of the materials of Chapter 1 was done by other co-authors (Marta Mohedano, Rafael Gonzalez Tenorio, Beatriz Mingo) and is gratefully acknowledged. Chapter 3 material synthesis and characterization results were performed by Nelson Vargas with Juan Rodríguez Hernández. Chapter 4 materials; VCL hydrogels were prepared by María Eugenía Pérez Ojeda. VP PC supports were prepared by Noelia Luján. This data is included in this doctoral Thesis for the sake of understanding of the relationship of the material characteristics with the biological evaluation results.

DRX studies were carried out by Centro de Asistencia a la Investigación Difracción de Rayos X from UCM. ICP-OES liberation measurements were performed by Centro de Asistencia a la Investigación de Técnicas Geológicas from UCM. All Confocal Raman studies were performed by Adolfo Del Campo from Instituto de Cerámica y Vidrio – CSIC.

In vivo surgery was possible thanks to the help of Ramón Martínez Corría and histological treatment of the implants by Laura García de Frutos. We thank Noricum Implants S.L for kindly providing material for this study.

Anodization of Zirconium samples was carried out by Andrea Gómez Sánchez from Instituto de Investigaciones en Ciencia y Tecnología de Materiales CONICET.

Mg0.8Ca alloy was kindly provided by Helmholtz-Zentrum Geesthacht.

Antibacterial evaluation of Chapter 3 was done by Aitziber Cortajarena and Ane Dorronsoro from CIC biomaGUNE.

List of Publications

- E. Martínez Campos, **A. Santos-Coquillat**, B. Mingo, R. Arrabal, M. Mohedano, A. Pardo, V. Ramos, J.L. López Lacomba, E. Matykina, Albumin loaded PEO coatings on Ti - Potential as drug eluting systems, Surface and Coatings Technology, 283 (2015) 44-51. **DOI: 10.1016/j.surfcoat.2015.10.045**
- E. Martínez-Campos, T. Elzein, A. Bejjani, M.J. García-Granda, **A. Santos-Coquillat**, V. Ramos, A. Muñoz-Bonilla, J. Rodríguez-Hernández, Toward Cell Selective Surfaces: Cell Adhesion and Proliferation on Breath Figures with Antifouling Surface Chemistry, ACS Applied Materials & Interfaces, 8 (2016) 6344-6353. **DOI: 10.1021/acsami.5b12832**
- M.R. Katunar, A. Gomez Sanchez, **A. Santos Coquillat**, A. Civantos, E. Martinez Campos, J. Ballarre, T. Vico, M. Baca, V. Ramos, S. Cere, *In vitro* and *in vivo* characterization of anodised zirconium as a potential material for biomedical applications, Materials Science and Engineering C, 75 (2017) 957-968. **DOI: 10.1016/j.msec.2017.02.139**
- N. Vargas-Alfredo, **A. Santos-Coquillat**, E. Martínez-Campos, A. Dorronsoro, A.L. Cortajarena, A. Del Campo, J. Rodríguez-Hernández, Highly Efficient Antibacterial Surfaces Based on Bacterial/Cell Size Selective Microporous Supports, ACS Applied Materials and Interfaces, 9 (2017) 44270-44280. **DOI: 10.1021/acsami.7b11337**
- E. Martínez-Campos, **A. Santos-Coquillat**, M.E. Pérez-Ojeda, A. Civantos, C. Elvira, H. Reinecke, C. García, V. Ramos, J. Rodríguez-Hernández, A. Gallardo, Thermosensitive hydrogel platforms with modulated ionic load for optimal cell sheet harvesting, European Polymer Journal, 103 (2018) 400-409. **DOI: 10.1016/j.eurpolymj.2018.04.021**
- **A. Santos-Coquillat**, R. Gonzalez Tenorio, M. Mohedano, E. Martinez-Campos, R. Arrabal, E. Matykina, Tailoring of antibacterial and osteogenic properties of Ti6Al4V by plasma electrolytic oxidation, Applied Surface Science, 454 (2018) 157-172. **DOI: 10.1016/j.apsusc.2018.04.267**
- **A. Santos-Coquillat**, E. Martínez-Campos, M. Mohedano, R. Martínez-Corriá, V. Ramos, R. Arrabal, E. Matykina, *In vitro* and *in vivo* evaluation of PEO-modified titanium for bone implant applications, Surface and Coatings Technology, 347 (2018) 358-368. **DOI: 10.1016/j.surfcoat.2018.04.051**
- N. Vargas-Alfredo, E. Martínez-Campos, **A. Santos-Coquillat**, A. Dorronsoro, A.L. Cortajarena, A. del Campo, J. Rodríguez-Hernández, Fabrication of biocompatible and efficient antimicrobial porous polymer surfaces by the Breath Figures approach, Journal of Colloid and Interface Science, 513 (2018) 820-830. **DOI: 10.1016/j.jcis.2017.11.050**

Patent

Recubrimientos tipo hidrogel en base vinil-lactamas. **Number: ES 2678773 A1 Date: 17/08/2018 Application Number: P 201730039 Date:16/01/2017.**

List of abbreviations

α-MEM alpha modified Eagle medium

AC Alternating current

ALP Alkaline phosphatase

AMS Iron-based absorbable metal stents

BF Breath figures

BGs Bioactive glasses

BIC Bone-to-implant contact

BMP-2 Bone morphogenetic protein 2

BRONJ Bisphosphonate-related osteonecrosis of the jaw

BSA Bovine serum albumin

BSE Backscattered scanning electron

CVD Cardiovascular disease

DC Discontinuous current

DCD Discrete crystalline deposition

DE Doubled-etched

DMEM Dulbecco's modified Eagle medium

DMF Dimethylformamide

ECM Extracellular matrix

EGF Epithelial growth factor

FA Fluorapatite

FBS Foetal bovine serum

FGF Fibroblast growth factor

GFP Green fluorescent protein

HA Hydroxyapatite

HSC Hematopoietic stem cells

IEL Internal elastic lamina

iPSC-MP Human induced pluripotent stem cell-derived mesenchymal progenitor

ISR In-stent restenosis

LBL Layer-by-layer

LCST Lower critical solution temperature

MALPB Maleic anhydride-g-liquid polybutadiene

M-CSF Macrophage-colony stimulating factor

MSC Mesenchymal stem cells

PAA Poly(acrylic acid)

PC Polycarbonate

PCL Poly(ε-caprolactone)

PDGF Human platelet-derived growth factor

PDMAEMA Polystyrene-b-poly(dimethylaminoethyl methacrylate)

PE Polyetilene

PEGMA Poly(ethylene glycol) methyl ether methacrylate

PEO Plasma electrolytic oxidation

PET/PU Polyethylene terephthalate /Polyurethane

PFA Paraformaldehyde

PGA Poly(glycolic acid)

PHB Poly(3-hydroxybutyrate)

PLA Poly(lactic acid)

PLGA Poly(lactic-co-glycolic acid)

PLLA Poly-L-Lactic acid

PMMA Polymethylmethacrylate

pNIPAm Poly(N-isopropylacrylamide)

PSS Poly styrene sulfonate

PP Polypropylene

PS Polystyrene

PRP Platelet-rich plasma

RANKL Receptor activator of nuclear factor-k ligand

RMS Root mean square

SEM Scanning electron microscope

SLA Sandblasted large-grit acid-etched

SSIs Surgical site infections

TCP Tissue culture plastic

TE Tissue Engineering

TGF-β Transforming growth factor beta

THF Tetrahydrofurane

Ti CP Commercially pure titanium

TPS Titanium plasma sprayed

TRAP Tartrate-resistant acid phosphatase

VEGF Vascular endothelial growth factor

VCL Vinylcaprolactam

VP Vinylpyrrolidone

VPTT Volume phase transition temperature

UTS Ultimate tensile strength

1. State of the art: Literature review

1.1. Regenerative medicine and Tissue Engineering

As it was firstly defined by Langer and Vacanti in 1993, Tissue Engineering (TE) is ‘‘an interdisciplinary field of research that applies the principles of engineering and the life sciences towards the development of biological substitutes that restore, maintain, or improve tissue function’’[8]. This field is based on the knowledge of the formation of the tissues and their regeneration, and ambitions to promote new functional tissues, rather than just to implant new spare parts in comparison to the classical biomaterial vision [9]. However, basic principles of TE have been applied since ancient times, as many examples can be found of skin or dental grafting in the historical record. Nowadays TE combines tightly cell biology, materials science, reactor engineering, and clinical research in order to achieve this new approach. Since its origin, it is believed that TE could induce a new revolution in the healthcare system by repairing or replacing disease or damaged tissues [8-14]. It has been projected that TE market will grow remarkable in the following years; in 2016 it was valued at approximately five billion dollars [15]. In the future, artificially developed tissues or organs substitutes could be fabricated on demand.

TE can be useful in numerous fields, as bone, cartilage, skin, heart, vascular or liver regeneration. For instance, two million bone grafts worldwide per year are being used as bone substitutes and bone grafting has emerged as the second most frequent tissue transplantation worldwide, being blood transfusion the first [16]. Bone engineering seems to be expanding as bone related diseases are increasing proportionally as the median age of the population and reconstructions after severe injuries (accidents or tumorigenic resections) are needed. Likewise, investigations in the TE area in the past decade include advances in materials engineering, cells engineering and tissue architecture as a consequence of the development of advanced techniques e.g. 3D printing, iPSCs… (Figure 1.1). In a near future replacement or repaired tissues have to be indistinguishable from normal, healthy tissues in structure and function [17].

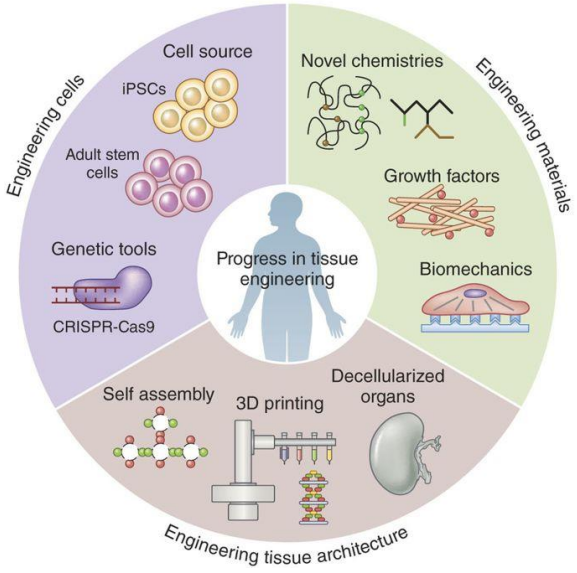

Figure 1.1. Tissue engineering development in the past decade [18].

In order to reach the maximum potential of this discipline three pillars; cells, materials and signals (Figure 1.2), have to be combined and promote advances in all areas. Cell culture methods and renewable cell sources, together with a deeper understanding of cell biology mechanisms, permits a wide range of biological tools to achieve tissue regeneration. Furthermore, as already exposed different cell sources are available such as differentiated cells, progenitors, adult stem cells or iPSCs. Also the transdifferentiation or phenotype switching, gene editing (CRISPR-cas9) could be an alternative approach for cellular replacement. Since the establishment of cell lines at the end of the twentieth century *in vitro* studies have evolve widely and they are need to validate in the first stages a candidate biomaterial. Many different cell models are available such as macrophagic RAW 264.7, preosteoblastic MC3T3, premyoblastic C2C12-GFP and endothelial C166-GFP murine cell lines that are going to be used in this doctoral Thesis. In addition, vascularization, mitigation of host responses and controlled drug delivery of signalling molecules are gaining importance in the field [18, 19].

Nevertheless, still new materials design is crucial to obtain an improved biocompatibility, responsiveness (smart materials), specificity and other critical properties (antibacterial or antifouling platforms o drug delivery systems) [9]. Different attempts have been made to create scaffolds that can emulate the three-dimensional environment (different surface chemistries, architectures or degradation rates). These scaffolds have to be able to foster and direct cellular process (attachment, migration, proliferation, and differentiation, among others) [9] in order to imitate the physiological state.

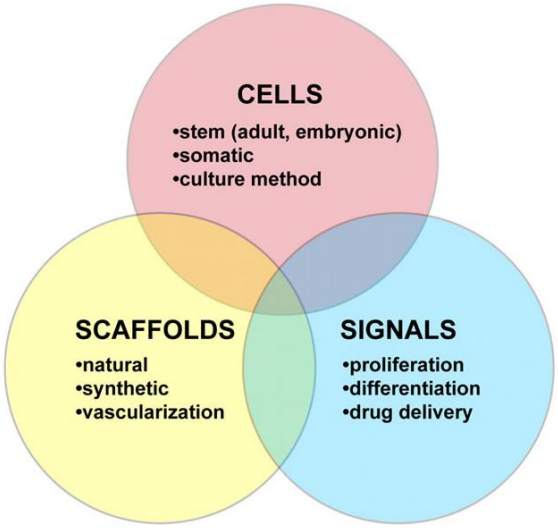

Figure 1.2. Three pillars of tissue engineering [19].

Biomaterials have revolutionised modern medicine being main components of dental implants, orthopaedic implants, sutures, and numerous medical devices [9]. Originally, biomaterials were defined only as synthetic materials. Later, natural origin (viable or non-viable) materials were also added, and the definition now includes any substance, other than active pharmaceuticals, that may come in contact with the biological systems of humans or animals [20]. Biomaterials can be classified in different groups: synthetic (metals, polymers, ceramics, composites), nature-derived (e.g. plant-derived, tissue-derived) and semi-synthetic or hybrid. One of the firsts strategies was the use of polymers with mammalian cells and nowadays we are able to make skin for burns or skin ulcers patients, and various other polymer/cell combinations are being explored such as corneas, cartilage, bone and liver [21].

The naturally derived materials category includes polymers such as silk and chitosan or purified ECM-based molecules including collagen, elastin, and glycosaminoglycans. Biomaterials scientific field is known to have strong bounds with health market, and many of these strategies are translated into commercial products. For instance, alginate (PhytaCare™) and chitosan (HemCon™) are being used as wound dressings and silk (Ethicon) as suture material. On the other hand, other biomaterials on the market that include growth factors to control cell activity and promote tissue healing. It can be highlighted the use of INFUSE® Bone Graft (Medtronic) an absorbable collagen sponge carrier with bone morphogenetic protein 2 (BMP-2) applied in degenerative disc disease, or REGRANEX® (Healthpoint Biotherapeutics) an hydrogel with recombinant human platelet-derived growth factor (PDGF) to treat diabetic ulcers in lower limbs [22].

A biocompatible and implantable biomaterial should be well integrated in the tissue without any harmful effects, avoiding an immune response following the formation of fibrotic tissue or its

encapsulation. Moreover, the biocompatibility of a biomaterial is assessed by the evaluation of their ability to induce cell or tissue death (cytotoxicity), cancer formation (carcinogenicity), to genetic damage (mutagenicity), immune responses (pyrogenicity and allergenicity) or blood clotting (thrombogenicity) [23]. In order to commercialised a biomaterial ISO standards (such as ISO 10993, among others) should be evaluated for their applicability to the clinical application [24]. Nowadays, one of key fields where tissue engineering application has promoted a remarkable impact is in bone regeneration therapies, both in academic research and market outcomes.

1.1.1. Bone regeneration

In the human body, the skeleton plays essential roles in mobility, locomotion, calcium homeostasis, haematopoiesis and protection. Tissue engineering has been proposed as a strategy for the treatment of irreversible tissue defects related to bone tissue [19].

Bone tissue presents a hierarchical structure and can be classified as cortical or compact bone constituent of about 80 % of the skeleton, and trabecular bone, also known as cancellous or spongy bone (~20% skeleton). Cortical bone is considered as nearly solid presenting ∼3–5% spaces for osteocytes, canaliculi, blood vessels, and erosion cavities, among others (Figure 1.3) [25-29]. Osteons (~100 μm diameter), are cylindrical structures formed by osteocytes, are in charge of forming the compact bone. Moreover, there is an inner channel (the haversian canal) that comprises blood vessels surrounded by small cavities called lacunae that contain each an osteocyte. The lacunae and the haversian canals are connected by a net of small channels (canaliculi), these permit cell–cell interactions and exchange of nutrients and metabolites is promoted [30]. Oppositely, trabecular bone presents a porous network arranged in a sponge-like form, with a honeycomb of branching bars, plates and rods of various sizes called trabeculae.

This porous network is filled with bone marrow, a tissue composed of blood vessels, nerves, and several cell types, from which trabecular osteocytes receive nutrients. The porosity varies between 50-90% resulting in an inferior modulus and ultimate compressive strength (about 20 times less) in comparison with compact bone [25-29]. The honeycomb-like network of trabeculae forming cancellous bone also has a lamellar organization, but internal canals and blood vessels are missing.

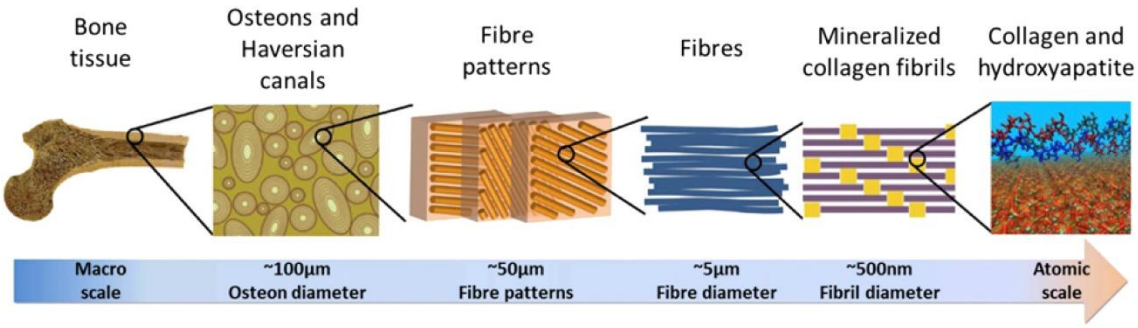

Figure 1.3. Hierarchical structure of bone ranging from the macroscale skeleton to nanoscale [31].

Moreover, bone tissue that acts as organism support presents a bone matrix composed of an organic and an inorganic phase. The inorganic crystalline mineral part is mainly formed by hydroxyapatite (65–70%) and on the hand, the organic part is composed of mainly type-I collagen, as well as type-III and type-IV collagen; other non-collagenous structures include glycoproteins, proteoglycans, sialoproteins constituents of the remaining 25–30% of the total matrix. The function of HA crystals is to provide strength and toughness and collagen provides flexibility [31, 32], Figure 1.3 presents the scale of the components of bone.

Bone is constituted by different cell populations with several origins. It is mainly formed by osteoblasts derived from Mesenchymal Stem Cells (MSC), osteocytes (which differentiate from osteoblasts) and osteoclasts derived from pluripotent Hematopoietic Stem Cells (HSC). As already described, osteocytes are embedded in the bone matrix and are the most abundant cells in the bone tissue. Bone remodelling is a precise process highly regulated by the balance between bone formation (osteoblasts) and bone resorption (osteoclasts) throughout life, including fractures and other conditions (Figure 1.4). The formation, preservation and resorption of this remarkable tissue depends on interaction of these cell types. In these processes all have well-defined tasks being essential for the maintenance of a healthy bone tissue [33, 34].

Bone remodelling presents therefore two opposite phenotypes on the bone cell population. On the one hand, the osteogenic phenotype, which secretes bone matrix at the bone resorption location, and on the other hand the osteoclastogenic phenotype, which supports the osteoclastogenesis in the old or damaged bone area. The latter phenotype stimulates the macrophagic population derived of HSC by the expression of the receptor activator of nuclear factor-k ligand (RANKL), which is essential for osteoclast formation and function. Macrophage-colony stimulating factor (M-CSF) is also a critical factor for the generation of osteoclasts, both *in vivo* and *in vitro.* These cytokines are in charge of osteoclast survival and are inductors of the differentiation, even in the absence of osteoblastic cells. As the differentiation proceeds, macrophages differentiate into pre-osteoclasts and the merging process begins originating large multinucleated osteoclasts with increased substrate resorption ability [35, 36].

To initiate the bone resorption mechanism, the multinucleated cells first adhere to the substrate and their cytoskeleton reorganizes, they assume polarized morphology, form ruffled borders and form a sealing zone with an actin ring that closes the bone matrix in roughly circular areas. The sealing zone prevents the escape of acids and protons that are being generated as a consequence of the resorption process. There is also a secretion of enzymes that are able to digest collagen fibbers and other bone matrix proteins, such as cathepsin K (actively participates in the bone resorption) and tartrate-resistant acid phosphatase (TRAP, whose secretion is normally related with the resorptive behaviour)[36].

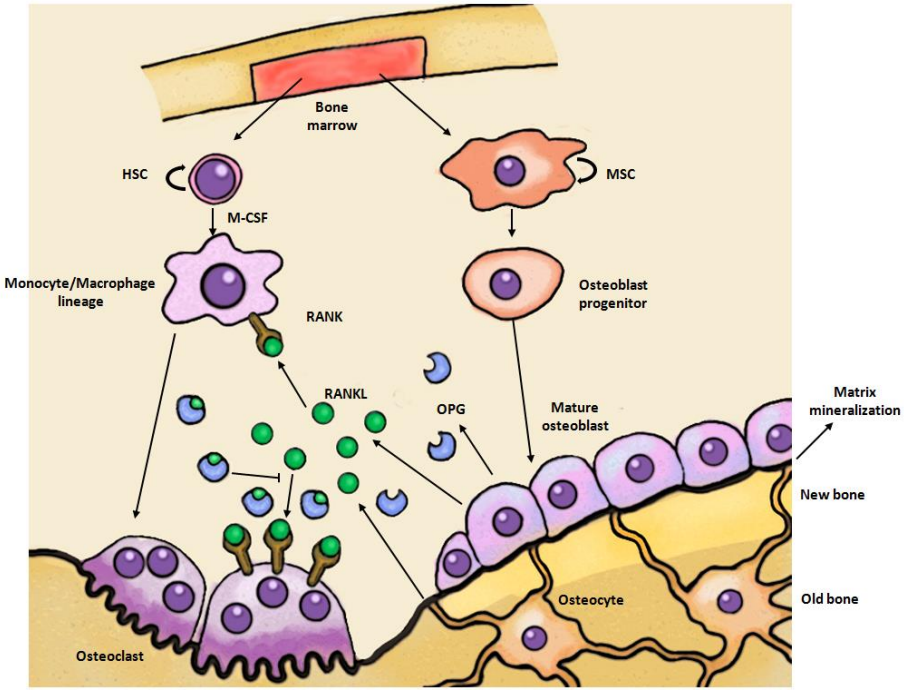

Figure 1.4. Bone homeostasis. The primary populations responsible of bone remodelling came from the bone marrow stem cells (HSC and MSC) and is achieved by osteoclasts and osteoblasts, which communicate closely with each other through different signals.

Bone tissue undergoes constant remodelling in order to ensure the maintenance of its structural integrity. During endochondral bone development, bone-forming osteoblasts colonize regions of cartilage tissue that will be replaced by bone. However, in adulthood, bone remodelling and repair involve osteogenic cells as they reach the sites that need to be rebuilt in order to promote a healthy tissue. If this mechanism fails, the consequences range from breaks not healing effectively to major problems such as osteoporosis. It has been well established that remodelling process involves close communications between osteoblasts (bone forming cells) and osteoclasts (bone resorbing cells). These cells work together in a tightly regulated cycle (Figure 1.4) [29, 32, 35]. After the old bone area is resorbed, osteoclasts will die by apoptosis. Subsequently, differentiated osteoblasts with osteogenic phenotype secrete bone matrix and it becomes mineralized (Figure

1.4) so the resorbed area of bone is found refilled with new bone [35, 36]. Finally, after osteoblasts deposit new matrix, three possible scenarios can be found: i) osteoblasts can transform into osteocytes and, therefore, stay embedded in the recently formed mineralized tissue, ii) die by apoptosis such as osteoclasts, or iii) transform into bone lining cells, which are dormant osteoblasts with a flat morphology present in inactive (non-remodelling) bone surfaces [37].

On the other hand, when fractures take place a lost in the skeletal integrity is produced and the bone vascular network is disturbed in the concrete location. These two phenomena produce a compromised nutrient and oxygen flow and distress the marrow structure. After this, tissue regeneration process starts resulting in three key phases: the inflammation (reactive) phase, the reparative phase, and the remodelling phase [38]. The latter is similar to the previous described bone remodelling in undamaged bones, in bone healing the process involves a combination of callus (bony and cartilaginous material that establish a linking bridge through a bone fracture during the reparative phase) resorption by osteoclasts and bone deposition by osteoblasts and can take months to years to obtain a fully repaired bone [38]. Effective therapies for bone engineering need to initiate the migration and recruitment of osteoprogenitor cells so biologically active signalling molecules (growth factors, drugs and gene deliveries) can be used for this matter. This process is followed by cell proliferation and differentiation that allows matrix formation along with the bone remodelling of the bone.

Design of a biomaterial for bone regeneration requires a balance of an osteoinductive cellular microenvironment, diffusion of soluble factors, flexibility, and mechanical loading appropriate for the anatomical site. The gold standard for many years of bone replacement was the autologous bone graft (bone originated from the patient's own body), it was a source of compatible osteogenic cells and presented the osteoinductive factors required for bone healing and regeneration. However, many inconveniences appeared as it is a limited source and may involve tissue morbidity. On the other hand, allografts (bone originated from other organism) present a significant risk of infection and to induce immunogenic mechanisms of rejection. As a possible solution, different kind of biomaterials have been analysed to avoid the use of autologous or allogenic bone grafts. Synthetics materials such as ceramics and metals have been widely investigated. Nevertheless, as it will be more extensively reviewed later, metals provide immediate mechanical support at the implantation site but in general display poor integration with the tissue, and an infection or fatigue loading can induce their failure. Ceramics in contrast present very low tensile strength and are fragile, therefore not recommended to be used in locations of significant torsion, bending, or shear stress [26]. For all these reasons, there is no an optimal biomaterial useful for every lesion, and many features need to be considered in order to choose the best therapeutic option.

Phenomena such as cell adhesion or proliferation on the implant surface, or the degree of bone matrix secretion can be crucial to determine implantation success. In order to study these relationships, different terms are used in the implantology field. Osteoinduction is a process of osteogenesis induction where undifferentiated and pluripotent cells develop into the bone-forming cell lineage. This phenomenon is usually observed in bone healing process, such as a fracture. Osteoconduction is a term used in combination with implants and it is defined as the ability to support the attachment of osteoblast and osteoprogenitor cells, and allow the migration and ingrowth of these cells within the three-dimensional architecture of the implant. For instance, some implant materials that present low biocompatibility (copper, silver and bone cement) displays reduced or no osteoconduction potential. Osseointegration is the stable anchorage of an implant achieved by direct bone-to-implant contact without the formation of fibrous tissue. Both osteoconduction and osseointegration mechanism are determined by biological factors and by their response to an implanted foreign material. The osteoconductive response is important in first stages of implantation, however successful osseointegration is a key characteristic to ensure bone anchorage over a long period and therefore the final implantation performance [39].

When suggesting new biomaterials different characteristics have to be considered such as porosity, surface chemistry (charge or wettability properties) or roughness parameters. Interconnection of the pores affects the rate of migration, nutrient/waste diffusion, and the ability of the cells to interact with each other [40]. Moreover, angiogenesis and vasculogenesis are critical processes for most tissues and organs. In order to promote homeostasis and functionality an effective oxygen transfer, delivery of nutrients, and transport and clearance of metabolic waste have to be promoted and if not the failed vascularization fallouts in necrosis [41]. There, this feature should also be taken into account when designing a biomaterial.

In this doctoral Thesis, a wide approach is applied in order to analyse cell behaviour over different types of biomaterial's surfaces under the tissue engineering basic principles. Focusing on bone regeneration, the most important types of implants will be reviewed, attending to their historical and actual applications, their functionalization possibilities and finally their cytocompatibility and other important biological implications.

1.2 Biomaterials for orthopaedics and dentistry

As described above, biomaterials design requires the selection of several features that determines final implantation success, especially in bone clinical applications. Biomaterials development during the last century has brought up different categories: first generation (known as bioinert materials), second generation (bioactive or biodegradable materials) and third generation

(materials designed to promote responses at a molecular level combining different properties) [42, 43].

The first applications of biomaterials were in permanent implants mainly for orthopaedics and dentistry. Bone fractures, total joint replacement, low back pain, osteoporosis, scoliosis and loss of dental pieces have to be amended by using permanent, temporary or biodegradable devices. These devices are meant to substitute or repair bone, cartilage or ligaments and tendons. The cited generations appeared as a consequence of the requirements and properties of the materials involved. First or the second generation biomaterials are still widely studied and successfully applied every day in many applications. On the other hand, third-generation biomaterials are going to be applied in new treatments and applications and would not substitute plainly the materials from the generations preceding [42].

Table 1.1. Three generations of biomaterials adapted from [23].

Generation	Bioactivity	Clinical goals	Examples
First	Biologically inert	No harm to tissues	Co-alloys; Stainless Steels: Ti Alumina; Zirconia Polyurethane; Polymethylmethacrylate
Second	Bioactive or biodegradable	Tissue-bonding	Surface modified Ti alloys Hydroxyapatite Calcium phosphate Surface bioactive glasses
Third	Biodegradable	Tissue regeneration	Magnesium alloys Degradable Bioglass® Degradable polymers (PLA, PCL, *etc.*)

First generation biomaterials

As described in Table 1.1, first generation materials for bone tissue include metals, ceramics and polymers. From the first type, stainless steel and cobalt–chrome-based alloys were initially introduced at the beginning of the twentieth century. Later on, titanium (Ti) and Ti alloys were introduced by the 1940s. First-generation ceramic biomaterials most frequently used are alumina, zirconia and several porous ceramics. Polymer biomaterials of the first generation are silicone rubber, PE (polyetilene), acrylic resins, polyurethanes, polypropylene (PP) and polymethylmethacrylate (PMMA).

Second generation biomaterials

Second generation materials promote bioactivity in bone repair and fixation applications based on induction of mineralization and binding between the bone tissue and the implant. Ceramic-based biomaterials (bioactive glasses (BGs), ceramics, glass–ceramics and composites) from this

group have been used in orthopaedic and dental applications. Several of them are also based on Si that promotes osteogenesis. When this element is incorporated into apatites, more bone tissue is formed. This can be explained by the Si–OH groups on the material surface that cause the nucleation and formation of more apatite layers and therefore, material–bone bonding is enhanced [42].

On the other hand, the metallic materials used in orthopaedics and dentistry are not bioactive. In order to obtain bioactive metals two strategies can be implemented: coating the surface of the implant with a bioactive ceramic (HA and BGs) or surface chemically modification of the surface by deposition of a bioactive ceramic *in vivo*. This approach has been widely studied in Ti alloys together with other surface modification methods.

Third generation biomaterials

The third-generation biomaterials are supposed to stimulate specific cellular responses at the molecular level [43]. Therefore, bioactivity and biodegradability concepts are combined together obtaining bioabsorbable materials with bioactive properties. Design of new porous structures on 3D aiming to foster cells and induce proliferation or functionalize surfaces with peptide motifs mimicking the ECM components seeking specific cell responses are being investigated. Moreover, drug or growth factors delivery or control of cell behaviour through mechanotransduction are also of interest [42].

In the recent years, a new generation of biomaterials is being proposed, **the fourth generation**, consisting on biomimetic and smart materials [44]. Next, a comprehensive review of most important permanent implants for orthopaedic and dental use from three generations analysed will be presented.

1.3. Permanent Implants

Biomaterials of the first or second generation cannot stop being used as biomaterials, all three generations have an important part to play. For those applications in which permanent implants are indispensable traditional metallic implants such as Ti alloys still can be improved in many ways. Nowadays, different approaches in order to improve the bioactive properties and the post-implantation success rate are being investigated.

Commercially pure Ti (Ti CP) and its alloys are widely applied in medical area. The applications include dental implants and parts for orthodontic surgery, joint replacement parts for hip, knee, shoulder, spine, elbow and wrist, bone fixation materials like nails, screws, nuts and plates and others like housing device for the pacemakers and artificial heart valves, surgical instruments and components in high-speed blood centrifuges [45].

1.3.1 Ti Alloys

Ti CP grade 4 (ASTM F67) and Ti6Al4V (ASTM F136) are the most common Ti-based alloys investigated in dentistry and orthopaedics because of their outstanding corrosion resistance, inertness to body environment, passivation capacity, biocompatibility and osseointegration. Ti CP presents a single-phase alpha microstructure and has been described as a gold standard in dentistry. Ti CP is available in four grades (Table 1.2) where the oxygen content varies between 18 wt.% and 0.40 wt.% and Fe content between 0.20 wt.% and 0.50 wt.%. Ti CP grade 4 contains the highest amount of oxygen, up to 0.40 wt.%, and its concentration differences make a substantial effect on the physical and mechanical properties (highest tensile and yield strengths) [45-47].

Table 1.2. Impurity limits for commercial pure titanium (wt. %) adapted from [23].

Materials	**N**	**C**	**H**	**Fe**	**O**
ASTM grade 1	0.03	0.08	0.015	0.20	0.18
ASTM grade 2	0.03	0.08	0.015	0.30	0.25
ASTM grade 3	0.05	0.08	0.015	0.30	0.35
ASTM grade 4	0.05	0.08	0.015	0.50	0.40

However, for load-bearing applications, such as total hip and total knee replacements, Ti CP yield strength is not sufficiently high [48]. For the improvement of this property alloying has become an excellent approach. Yet, some concerns related to the toxicity of various alloying elements do exist [49].

Based on their microstructure after processing, titanium alloys are categorized into four classes: α alloys, near-α alloys, α–β alloys, and β alloys. Ti6Al4V presents a biphasic alpha–beta microstructure, Al and V alloying elements stabilize this microstructure and in consequence the mechanical properties are improved (with twice as high yield and strength values than Ti CP) [47].

When selecting alloying elements for the development of a biomedical Ti alloy preferably non-toxic ones have to be selected. There are no metals that are entirely inert or non-toxic, therefore when designing a metallic implant those considered as trace elements in the organism or within the limits of toxicity should be chosen. The ranking of pure metal cytotoxicity from most potent to least potent follows this tendency: Cu > Al > Ag > V > Mn > Cr > Zr > Nb > Mo > Ti CP. Taking into account these considerations, recently alloys containing Ti, Nb, Ta and Zr have been developed. Alloys such as Ti–29Nb–13Ta–4.6Zr, Ti–35Nb–7Zr–5Ta and many others have been investigated [45].

Zr is employed as an alloying element because of its high resistance to corrosion. Zr is refractory and presents high affinity for oxygen like Ti. Therefore, a protective oxide layer forms spontaneously on its surface when exposed to an oxygen-containing environment. This formed layer is self-healing and protects the base metal from chemical attack at temperatures up to 300 °C [23]. The metal by itself has also been considered for orthopaedic applications showing promising characteristics *in vivo* [50, 51]. However, very little information is known about cell behaviour on pure Zr and in consequence is going to be investigated in this Thesis.

For the sake of clarity, dental and orthopaedic specific requirements are going to be depicted on the following sections.

1.3.2 Dental implants

In dentistry and dental surgery, different metallic biomaterials have been used, including dental restoration, endodontic implantations and orthodontics applications. Cobalt alloys and Ti CP grade 4 are currently being used to replace tooth roots, stainless steels and NiTi alloys are applied as corrective archwires, and HgAgSn amalgam was used as a restorative material [23]. Particularly, dental root implants from Ti CP or titanium alloy have an extensive and successful history of clinical application of more than forty years [52]. Furthermore, these kinds of implants have promoted progress in dental, oral and maxillofacial surgery, being able to restore tooth loss and provide a replacement of lost orofacial structures as a result of trauma, neoplasia and congenital defects with excellent performance in terms of safety and long-term stability [46, 52, 53]. The endosseous implant is the most common type consisting of a discrete, single implant unit (screw- or cylinder-shaped being the usual forms) placed in a drilled space within dentoalveolar or basal bone [53]. Dental implants are likewise applied to support craniofacial reconstructions and for orthodontic appliances [46].

Ti presents high biocompatibility, high strength, stiffness and relatively low density. More notably, Ti implants are able to osseointegrate with bone tissue [54]. In 1964, Brånemark disclosed the osseointegration phenomenon for Ti implants, describing that an implant is osseointegrated when newly formed bone tissue is in intimate contact with the implant surface with no interposition of fibrous/connective tissue [46, 53]. This characteristic considerably increases the long-term performance of the implants, diminishing loosening and failure risks. With this finding the exploration of dental and surgical applications of Ti alloys started [42].

The high biocompatibility of Ti is due to its reduced rate of ion release. This release is non-toxic and in consequence it does not promote an immune reaction. This is the result of the formation of an adhesive titanium dioxide (TiO_2) layer at the surface which provides exceptional chemical inertness. Passivation is a process that occurs when pure titanium or its alloys are exposed to air

producing a ~2–7 nm thick TiO_2 layer formed in a few seconds. This thin layer makes titanium-based materials highly resistant to corrosion and was described to permanently fuse with the bone [25, 42, 54]. Later on, with the studies of Albrektsson *et al.* the role of surface characteristics gained significance as they were the first to relate the possible effect of the implant surface on the biological response [55, 56].

Nevertheless, this mentioned interaction between the Ti implant surface and the tissue does not implicate a chemical bond with bone. As a result of the non-chemical bonding with bone a slow fixation of Ti dental implants and the possible gradual loosening after an extended time can occur [53]. It is highly important to comprehend the interactions between the host bones and the titanium implant. Many *in vitro* and *in vivo* studies have also revealed that this kind of interactions relay essentially on the surface of implant features [49]. More specifically, the successful osseointegration of a dental implant material depends on how the cells react to the material, mainly including a good cell adhesion to the surface. The initial interactions between the host cells and the implant include cell attachment, adhesion, and spreading. These processes determine the ability of the cells to stay and proliferate on the implant's surface, and in consequence bone tissue formation around the implant area [52]. Therefore, the surface of the implants has been widely studied as it is considered a critical factor to the final outcome of the titanium-based implants. Surface characteristics such as roughness and topography are important variables that determine cell response [52]. For all this reasons, numerous investigations have been performed to promote a faster and better osseointegration.

Surface modifications of dental implants

Nowadays there are more than 1300 implant systems with different shape, dimensions, bulk and surface material, thread design, implant-abutment connection, surface topography, surface chemistry, wettability and surface modification [57]. The surface topography of dental implants is crucial for adhesion and differentiation of osteoblasts during the initial phase of osseointegration as well as in long-term bone remodelling. Many different surface modifications by different subtracting and additive methods have been evaluated and applied on marketed implants (Table 1.3) in order to improve the osseointegration process and provide these implants with bone-bonding ability. Examples of subtractive processes include: machined, electropolishing, mechanical polishing, sand-blasting, acid-etching, electrochemical anodic oxidation. Examples of additive processes: HA and other Calcium phosphate coatings, Ti plasma sprayed (TPS) surfaces and ion deposition [56, 58].

For a very long time Brånemark Standard Implants were considered the gold standard for implant surfaces. This type of implants were machined with a turning process, however imperfections along these machined surfaces enable osteogenic cells to attach and to deposit bone, thus

generating a bone-to-implant interface [58, 59]. Other methods were designed to obtain microrough titanium surfaces (e.g. by sandblasting and/or acid-etching) or apply HA coatings to give their surfaces bioactive properties. Yet, most part of the current methods present some disadvantages. As an example, surface roughening methods can lead to increased soft-tissue growth onto the bone-implant interface with a negative effect on the contact between the implant area and the bone. HA coating layer has a tendency to disintegrate under specific conditions, causing fissures on the surface of the implant. Moreover, when deposited by plasma-spray, an accurate control of the chemical composition, crystallographic structure and crystallinity of the coating is not achieved. The resulting HA layer turns up to be mechanically and chemically unstable [52].

Table 1.3. Surface treatments on commercial dental implants.

Treatment	Methodology/Composition	Product/Company
Mechanical	Machined Ti	Brånemark Standard Implants (**Nobel Biocare**) Restore Machined Implants (**Lifecore Dental**)
Surface Plasma Spray (TPS)	Welding Ti powder in Ar atmosphere. Plasma spraying of Ti alloy powder onto implant substrate.	IMZ TPS (**Densply Friadent**) Bonefit (**Straumann Institute**) Restore TPS (**Lifecore Dental**) Steri-Oss TPS (**Nobel Biocare**)
Hydroxyapatite (HA)	Electrophoretic deposition, sol-gel processing, hot isostatic pressing, flame spraying, plasma spraying and laser pulse deposition.	IMZ HA (**Densply Friadent**) Restore HA (**Lifecore Dental**) Steri-Oss HA (**Nobel Biocare**)
Sandblasting	Propelling a stream of grainy alumina, titania or hydroxiapatite onto the surface.	Al_2O_3-Standard, Hex (**Osteoplant**) TiO_2-TiOblast (**Astra Tech**) HA- Renova, Prima (**Lifecore Dental**)
Double-etched (DE)	Mixtures of acids ($HCl+H_2SO_4$, $HF+HNO_3$)	Osseotite (**Zimmer Biomet**) Steri-Oss Etched (**Nobel Biocare**)
Anodised surfaces (PEO)	Electrochemical anodic oxidation at high voltage.	TiUnite- Replace, Perfect, Direct (**Nobel Biocare**) BioSpark surface- Genesis (**Keystone Dental**)
Discrete Crystalline Deposition (DCD)	Calcium phosphate (CaP) particules are deposited on a double acid-etched surface by sol-gel process.	Nanotite/T3 **(Zimmer Biomet)**
Sandblasted large-grit acid-etched (SLA)	Two-step procedure: sandblasting with ceramic particles/ etching in mixtures of acids.	Al_2O_3/($HCl+H_2SO_4$) - e.g. SLA-Standard Implants, (**Straumann Institute**) SPI, DFI and ATIE (**Alpha Bio**) TiO_2/($HF+ HNO_3$)-OsseoSpeed (**Astra Tech**) Ossean (**Intra-Lock**)

The usual topographic parameters to describe the surface roughness are the 2-dimensional R_a (profile roughness average) and the 3-dimensional S_a (area roughness average). The majority of dental implants on the market have a R_a of 1-2 µm; this range provides an optimal degree of roughness to promote osseointegration [60]. While a growing number of surface modifications

with rough surfaces are proposed and compared with 'machined' surfaces, still there is no clarity about whether one surface modification is better than another [58].

Other strategies to diminish osseointegration time are focused on modification of the surface chemistry that influences surface charge and wettability. Proteins are absorbed before cells are able to adhere to the surface after a biomaterial is implanted. As soon as the proteins attached to the surface the cell-implant interactions are favoured. Some cell types, including osteoblasts and fibroblasts, have a preferential union to the absorbed proteins rather than to the implanted material. The orientation of the adsorbed molecules after implantation can change as a result of the surface energy of the biomaterial and after posterior cell adhesion [54]. Moreover, surface wettability is highly dependent on surface energy, an increased wettability improves the implant surface and physiologic environment interaction [52]. This chemical property can be measured by water contact angle which ranges from 0º on very hydrophilic surfaces to greater than 90º on hydrophobic surfaces. Highly hydrophilic surfaces are supposed more desirable than the hydrophobic in terms of their interactions with biological fluids, cells and tissues. Titanium implant surfaces present contact angle measurements between 0° (hydrophilic) to 140° (hydrophobic) [61, 62].

Primary implant failure due to deficient osseointegration occurs in 1-2% of patients within the first few months. Secondary implant failure appears in about 5% of the patients several years after successful osseointegration and usually caused by peri-implantitis [63]. Therefore, a major issue to be addressed when designing a dental implant is to avoid this kind of infections. Peri-implantitis has been defined as an inflammatory reaction associated with loss of supporting bone around an osseointegrated implant in function. The TiO_2 oxide layer formed on the surface of implants promotes a union with the superficial gingivae limiting the contact with oral microorganisms. When dental implants develop an infection, the microorganisms involved are generally the same as in periodontal disease (Gram-negative anaerobes and spirochaetes). In the same manner as with orthopaedic implants, after an infection dental implants are hard to treat and often have to be removed [53].

Hence, researchers are still looking for new surface treatment methods with added functionality that can avoid the above shortcomings. The clinical goals of biomaterial research are: (i) optimization of implant stability by interacting with cascades of osseointegration, (ii) the improvement of peri-implants soft tissue integration and the reduction of peri-implantitis by impairing bacterial adhesion to the implant surface [64].

1.3.3. Orthopaedic implants

Two types of joints can be considered in the skeletal system: the mobile joints between long bones (e.g. hip, knee, ankle, shoulder, and elbow) and the more static joints (e.g. skull, wrist, and tooth). In the particular case of orthopaedic implants for load bearing applications, different desirable characteristics must be accomplished in order to replace bone: excellent biocompatibility, superior corrosion resistance in body environment, high strength and low modulus, high fatigue and wear resistance, high ductility and no cytotoxicity [45].

For every specific application the selection of the material in use depend on the mechanical properties (Young's modulus, ultimate tensile strength (UTS) and toughness). For example, the material response to repeated cyclic loads or strains depends on their fatigue strength and this parameter will determine the long-term success of the implant subjected to cyclic loading. Fatigue strength refers to the maximal amplitude of cyclic stress that can be applied to a material without causing fatigue failure [23]. A wide range of metallic materials have been used in this area, these include: 316L stainless steel, Co-based alloys, Ti and Ti-based alloys. In Table 1.4, commercial implants available for hip replacements are presented.

Table 1.4. Major orthopaedic implant manufacturers and examples of materials for hip replacements, adapted from [23] .

Company	Products	Materials
Zimmer Biomet	Zimmer® ML Taper Hip Prosthesis with Kinectiv® Technology	Metal-on-UHMWPE wrought Co-based alloy
	Metasul® Metal-on-Metal articulation	Forged Co-based alloy
	Echo™ Hip System	Forged cobalt–chrome alloy
	Taperloc® Complete Hip Stem	Titanium alloy Ti6Al4V
	Avenir® Hip System	Titanium alloy Ti6Al4V
Depuy (Johnson and Johnson) (JNJ)	AML® Total Hip System	CoCrMo alloy
	Austin Moore Hemi-Arthroplasty	CoCrMo alloy
	Prodigy® Total Hip System	CoCrMo alloy
Stryker Corp.	Accolade TMZF	TMZF alloy
	Accolade C Femoral Component	Forged cobalt–chrome alloy
Smith & Nephew (SNN)	SMF Short Modular Femoral Hip	Cobalt–chrome alloy
Wright Medical	Perfecta® RS Stem	Titanium alloy
	Perfecta® Plasma Spray Stems	Titanium alloy
Exactech	AcuMatch® L-Series (Cemented Stems)	Forged cobalt–chrome alloy
	AcuMatch® L-Series (Press-Fit Stems)	Forged titanium alloy

Although many materials are being commercialized, still failure after long-term use is not uncommon. A higher modulus than that of the bone, low wear and corrosion resistance and lack of biocompatibility are the main reasons of this failure [45]. As a result of low wear and corrosion resistance of the implants in the body fluid, non compatible metal ions are released from the implants into the organism. Implant loosening and wear debris are also a consequence of the low wear resistance, causing different reactions in the tissue of the implant area. The released ions can cause allergic and toxic reactions [23]. Despite the enormous number of metals and alloys that can be produced in metallurgical industry, only a few have resulted biocompatible and capable of long-term success as an implant material. Thus development of implants with high corrosion and wear resistance is major issue for the longevity of the material in the human system [47].

For example, stainless steel has the higher corrosion rate than other orthopaedically suitable alloys, i.e. such as Ti6Al4V, and its use is recommended for temporary implants, such as bone reconstruction plates and screws. The main reason is that stainless steels alloying elements usually produce chronic allergy and toxic reactions in the host body evident after long post-implantation period [47]. Also, even though Ti and Co-Cr present negligible corrosion in the body, metal ions can diffuse through the oxide layer and become accumulated in the tissue [65]. Some elements with toxic effects (Ni, Cr and Co) are released from stainless steel and Co-Cr alloys due to the ion liberation into the body environment. Moreover, stainless steel and Co-Cr alloys present a greater elastic modulus than bone, this results in bone resorption and loosening of implant after some years of implantation due to an inadequate stress transfer to bone [45].

Surface modifications for orthopaedic implants

It has been established that clinical success of surgical implants depends on two main processes: initial fixation in the first few months and maintenance of the fixation over the long term. As it has been described in the dental implants Section 1.3.2, the success or failure of the osseointegration process in permanent implants is determined by the surface characteristics (surface chemistry, roughness and topography) [66]. Hence, an appropriate surface is critical for the implant to integrate properly within the adjacent bone. More specifically, with surface engineering a better performance of Ti-based orthopaedic devices of multiple times over its natural ability can be achieved. Same surface modification techniques that are used for dental implants are also applicable for orthopaedic implants and prosthesis (plasma spray, physical or chemical vapour deposition, ion implantation, electrochemical oxidation, acidic or alkali etching, sol–gel, heat-treatment, and surface machining or grinding) [25]. For example, Avenir® Hip System Cementless Stem (Figure 1.5) from Zimmer Biomet consists on forged Ti6Al4V with sandblasted finish with a double layered coating plasma spray of commercially pure titanium

(50μm) and a hydroxyapatite coating (110μm). Taperloc® Complete Hip System is treated with porous plasma spray.

Figure 1.5. Avenir® Hip System and Taperloc® Complete Hip System (treated with porous plasma spray) by Zimmer Biomet.

Adhesion of the coating or surface treatment with the substrate and wear resistance are more important for orthopaedic implants that may be subject to friction than in case of dental implants. Therefore, there are still less surface treatment options available for orthopaedic commercial implants.

Infections around the area of implantation of the biomaterial are an important complication of modern orthopaedic surgery and involves patient's pain and functional losses. The infection on implanted devices goes as follows; first a colonisation of microorganisms on the implant surface and lastly the development of a biofilm [49]. This kind of infections are named as orthopaedic surgical site infections (SSIs). It has been estimated that up to 2.5% of primary hip and knee arthroplasties and up to 20% of revision arthroplasties are complicated by infections, *Staphylococcus aureus* being the main cause. A deep infection can promote an implant removal, increased morbidity and even mortality [67].

This issue has become an enormous concern and a challenge for Health Care Systems. Diverse substances and technological approaches have been investigated to be implemented as antibacterial features. In order to obtain a new surgical implant with these properties some considerations have to be made: the implant has to maintain its biocompatibility, the anti-infective efficiency has to be proved, fixation properties cannot be compromised, durability of the anti-infective effect and the mechanical characteristics of the antibacterial coating have to be preserved.

Antibacterial surface technologies can employ metals (Ag, Zn, Cu, Zr etc.), non-metal elements (e.g., Se), organic substances (antibiotics, anti-infective peptides, chitosan, other substances), and their combinations [67]. Silver (Ag) is the most used antibacterial element biomedical applications. Dissolved Ag cations interfere with bacterial cell membrane permeability and

cellular metabolism. However, it has been found that Ag ion accumulation can be harmful for the organism. Cu and Zn are trace metals involved in multiple enzymatic and cellular processes. These metals also have potent antibacterial effects on a wide spectrum of bacterial species. Metallic biomaterials that incorporated with calcium, phosphorous, magnesium and fluoride ions also show promising results in promoting osseointegration. These ions, when incorporated into metallic implants surfaces also promote deposition of natural apatite through an ion exchange reaction [68].

New "smart coatings" are designed to be sensitive and responsive to diverse stimuli. All coatings must be biocompatible and not promote significant immune or foreign-body response, be osteoconductive, i.e. promote adhesion, proliferation and growth on the surface of the implant obtaining a bone-implant bonding and lastly, be osteoinductive, i.e. induce the differentiation of the adjacent stem into osteogenic cells. These kind of coatings should also present diverse functionalities such as anticorrosive, homeostatic, antibacterial, antifungal, among others.

Advanced electrochemical techniques are a promising emerging strategy that enable modification of surface composition and topography in one step and provide a foundation of a smart coating that can absorb and release the drugs. Usually smart coatings are obtained in a multi-step procedure, however, advanced anodizing can provide the incorporation of inorganic elements into the coating and the desired added functionalities in just one process. This approach will be discussed in the next section.

Electrochemical treatments based on anodizing

Anodizing consists in an electrochemical process that enables growth of the natural oxide layer present in the metallic surface. The metal is immersed into the electrolyte and an external current is applied by power supply where the material is anode and an auxiliary electrode is cathode.

The thickness of the formed oxide by anodizing can reach a hundred of micrometres or just a few nanometres, this outcome depends on the variables applied (voltage, treatment time, current density, the pH and the dissolving capacity of the electrolyte). Surface topography, pore conformation, crystalline structure and the chemistry of the oxides can be modulated adapting these variables [69, 70]. In Figure 1.6, two different structures formed by anodizing are presented a) TiO_2 nanotubes formed in fluoride-containing electrolytes and b) a 200 nm barrier film formed in alkaline electrolyte.

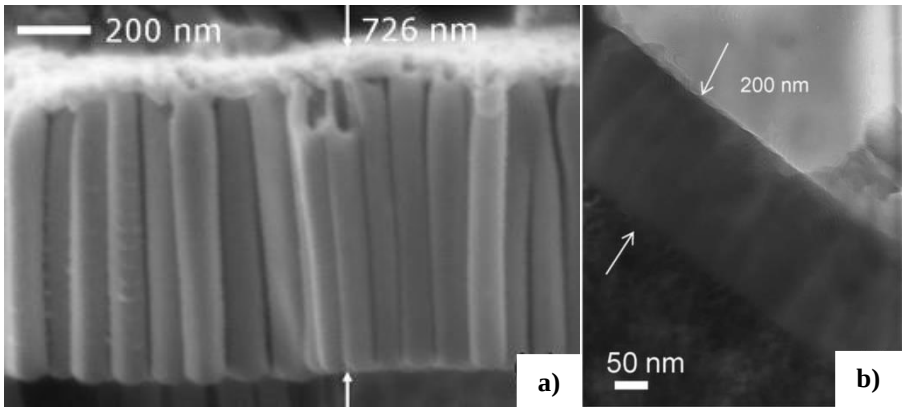

Figure 1.6. Cross-sectioned anodized titanium. a) Scanning electron micrographs of TiO_2 nanotubes b) transmission electron micrograph of Ti dioxide (TiO_2) surface. Adapted from [71, 72].

The PEO (plasma electrolytic oxidation) process is an advanced high voltage anodizing technique that can be performed on different metallic substrates; for biomedical applications mainly Ti and Mg have been studied. Similarly to anodizing, the substrate of interest is immersed into the electrolyte (usually alkaline) and polarized anodically. The treatment can be applied in either current input or voltage input mode with the necessary power provided by either DC or AC power supplies. During PEO the formation of a resistive anodic barrier layer is promoted on the substrate and for dielectric breakdown of the anodic oxide film to take place a high voltage needs to be applied. This dielectric breakdown induces the formation of microdischarges, characterized by optical and acoustic emission [73, 74].

In contrast to anodizing, PEO coating formation occurs mainly at the sites of plasma microdischarges which are changing in nature, number, intensity, and life time (from a few μs to a few ms) during treatment mostly as a consequence of the increasing thickness of the layer. In Figure 1.7, the conventional anodizing process takes place from 0 V to 120 V and a change in the colour can be distinguished along the course; when the voltage surpasses that of the gas breakdown the sparks start to appear (130V) and become more intense and visible with the voltage increment. The temperature of the plasma can reach up to 10000 K and the species of the electrolyte are drawn inside the microdischarge channel, where pressure can reach several tens of atmospheres and electrochemical, plasma-chemical and thermally assisted processes, such as oxidation and melting, take place [73-76]. Such conditions promote formation of new phases consisting of both the electrolyte and substrate species.

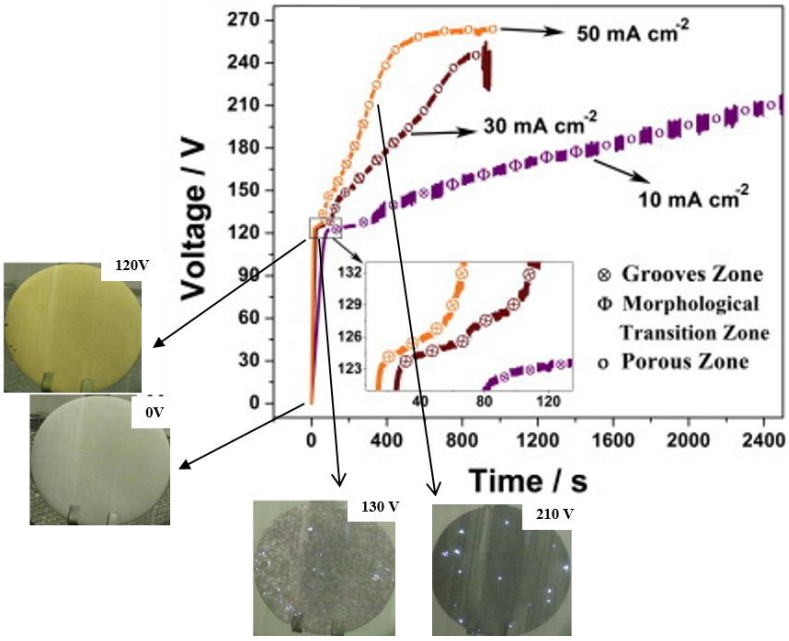

Figure 1.7. Typical voltage-time dependencies and visual appearance of titanium sample during transition from anodizing to plasma electrolytic oxidation. Adapted from [77].

Therefore, PEO is considered a particularly appropriate surface modification method for biomedical implants and surgical devices applications. The ceramic coating composition can be tailored by introducing bioactive elements (Ca, P, Zn, Mg, Ag, Sr, Mn, Si, Zr) into the electrolyte and promoting the formation of compounds (e.g. hydroxyapatite, fluorapatite, tricalcium phosphate) [78]. Furthermore, the microstructure (e.g. anatase-to-rutile ratio [79, 80]), porosity, and topography can also be tailored [81]. PEO coatings have been shown to enhance osteoblast cell proliferation and adhesion [82], promote the development of extracellular matrix [83] and formation of hydroxyapatite *in vitro* [84]. On the other hand, i*n vivo* studies have shown that PEO-modified dental implants accelerate the osseointegration and improve bone-to-implant contact [85]. Regarding the clinical performance of the commercial PEO-modified implants (e.g. TiUnite, NobelBiocare, Figure 1.8) there is evidence of success in immediate loading procedures [58, 86-88].

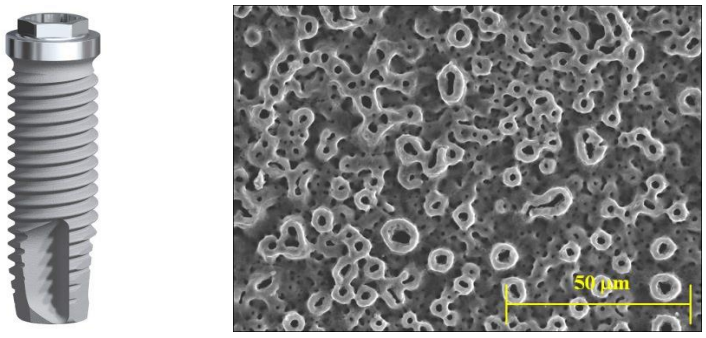

Figure 1.8. Brånemark System Mk III TiUnite with machined collar on the left. Secondary electron microscopy of NobelBiocare dental implant (TiUnite surface) on the right [89].

This surface modification has the potential to fulfil all the desired characteristics of smart implant systems described before. To date, many studies have been carried out such as the ones by Sul *et al*. [85, 90-94] studying the influence of surface chemistry and topography in relation to oxidation processes applying PEO and using different acids and alkaline as electrolytes. Electrolytes containing P, Si, Ca and Mg changed the chemical composition and the topography of the coatings. In general, oxidized implants have revealed stronger bone anchorage than the past gold standard machined implants, in animal experiments and human clinical studies. Roughness parameters have been widely evaluated and it has been established that moderate roughness is ideal as a consequence of its perfect fit to connective tissue/bone cells [58]. Antibacterial properties of PEO treated Ti have been tested, where Ag was incorporated into the coatings [95, 96] or Zn [97] and Cu [98]. *Caracterización, Corrosión y Degradación de Materiales de Interés Tecnológico* group from the Universidad Complutense de Madrid already studied formation of PEO coatings with overstoichiometric ratio of Ca/P. Showing an enrichment of Ca and P in the formed outer layer of the coating and the formation of HA after the exposure into a SBF medium for 1 week (Figure 1.9). Moreover, these coatings were also evaluated in terms of cell proliferation [79].

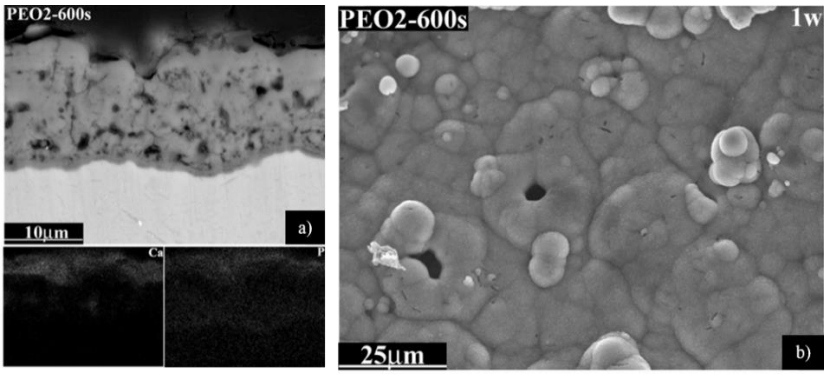

Figure 1.9. Backscattered electron images of the coatings cross sections of PEO2-600 s and respective X-ray elemental maps for Ca and P. b) PEO2-600 s coating after 1 week of immersion in SBF adapted from [81].

However, there are no systematic studies that evaluate the optimal ratio of Ca/P, how many different species can be incorporated into the ceramic coating and how these species are liberated from the implant, the possible drug loading of the oxidized implants depending of the topographical features (porosity or composition). Likewise, there practically are no previous *in vitro* studies of PEO-treated systems evaluating not only osteoblasts behaviour but also other participants in bone homeostasis e.g. osteoclasts.

1.4. Biodegradable implants

As it was described in the previous Section metals are more suitable for load-bearing applications in comparison with ceramics or polymeric materials because of their high mechanical strength and fracture toughness. However, for temporary implants applications, (third generation materials) biodegradable formulations are excellent candidates. Such implants commonly have been developed from polymers such as PGA (poly(glycolic acid)), PLA (poly(lactic acid)), PLGA (poly(lactic-co-glycolic acid)) or PET/PU (polyethylene terephthalate)/polyurethane) [99, 100]. Although, their mechanical properties are worse when applied in prosthesis or implants that are subjected to loads in comparison to some metallic materials [101]. Furthermore, polymer degradation occurs by hydrolysis resulting in acidity, which again might induce phenomena like foreign body reactions and, with the creation of an acidic pH environment, may enhance osteoclastogenesis to the detriment of osteoblastogenesis [102, 103]. Biodegradable ceramics have also been evaluated due to their porous structure and biodegradation rate. Bone formation at the surface of the ceramic can be favoured due to interconnection of pores as their presence are important for material's osteoconductive characteristic. However, biodegradable ceramics have some disadvantages, mainly fragility and poor tensile strength, for being used for this application [100]. Biodegradable metallic implants have been mainly based on magnesium (Mg), zinc (Zn) and iron (Fe). There are less studies of Zn and Fe since the accumulation of unfavourable degradation products after implantation can be prejudicial [100].

Taking into account bone natural characteristics, the use of biomaterials in this field implies hardness, tenacity, friction resistance, osseointegration of the implant, strong cellular adhesion or immune response modulation. However, this kind of materials present limitations due to the possible release of toxic metallic ions and/or particles via corrosion mechanisms or wear processes that can induce inflammatory cascades, reducing biocompatibility and resulting in possible tissue loss. Moreover, the elastic moduli of most of the existing metallic biomaterials (except Mg) are not very similar to the one of natural bone tissue (Table 1.5), resulting in stress shielding effects which reduce the stimulation of new bone growth and remodelling processes that can destabilize the implant. Not always there is a requirement for a permanent implant; in the case of plates, screws and pins used to secure serious fractures those have to be removed by a second surgical procedure after the tissue has healed satisfactorily. Therefore, by avoiding a secondary procedure we can reduce the cost to the health care system, diminish the infection risk and possible morbidity to the patient [104]. Mg based materials are the most favourable for bone applications as it presents the most similar mechanical properties and non-harmful degradation products.

Table 1.5. Mechanical properties of different materials designed for bone implant applications adapted from [104].

Properties	Natural bone	Mg	Ti alloy	Co–Cr alloy	Stainless steel	Synthetic HA
Density (g/cm^3)	1.8–2.1	1.74–2.0	4.4–4.5	8.3–9.2	7.9–8.1	3.1
Elastic modulus (Gpa)	3–20	41–45	110–117	230	189–205	73–117
Compressive yield strength (Mpa)	130–180	65–100	758–1117	450–1000	170–310	600
Fracture toughness (MPam$^{1/2}$)	3–6	15–40	55–115	N/A	50–200	0.7

Besides bone regeneration and reconstruction, cardiovascular stents application requires also the development of biodegradable biomaterials [105]. Stents are expendable after 12-24 months as their function is accomplished and there is an increased risk of restenosis (narrowing of a blood vessel, leading to restricted blood flow) if not removed surgically, when a stent is used and restenosis occurs, this is called in-stent restenosis or ISR [106]. For this cardiovascular application, the first treatment applied is the mechanical widening of the narrowed or obstructed arteries by inflating a balloon followed by placement of a stent (angioplasty) (Figure 1.10). In case of non-degradable stents, this procedure can trigger restenosis, a signalling cascade that leads to vessel remodelling; a decreased cellularisation and an increased extracellular matrix accumulation can occur. This negative process of remodelling can be reduced with the incorporation of a biodegradable stent, nevertheless the incidence of restenosis is still significant (25%). Other possible complications of a non-degradable stent are: physical irritation, long-term endothelial/vascularisation dysfunction, chronic inflammatory reactions, thrombosis, abolition of the vasomotor component at the implantation site, and impaired adjacent vessel segment behaviour [103]. As with bone reconstruction applications, the idea of avoiding a second surgery is still an important consideration.

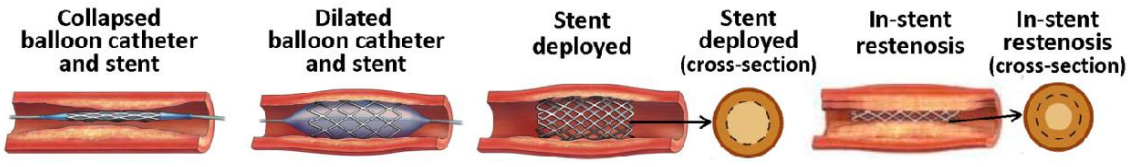

Figure 1.10. Procedure of angioplasty and stent incorporation leading to restenosis [107].

The first biodegradable implants for cardiovascular applications were polymers [108] and metals (iron 316L SS, Armco® Fe and Mg). Due to their mentioned superior mechanical properties compared to polymers, all the metallic stents were developed faster. Even though iron is an essential element in the metabolism, its excess can be toxic and deficiency can cause different pathologies. The toxicity of the possible implanted stents would not be reached considering the small quantities involved (~40mg). Iron-based absorbable metal stents (AMS) present low corrosion rate, not a desirable characteristic for stent application, where a quicker degradation rate is preferred. These mentioned facts indicate that magnesium-based AMS are more advantageous [103].

As already described, Mg seems to be the ideal material for both applications. Moreover, this material also presents the following main positive characteristics; i) density and elastic modulus similar to biological tissues [109]. ii) Capacity of degradation in physiological fluids. iii) Mg is the second most abundant, intracellular, divalent cation which participates in processes such as of calcium absorption, as a enzymatic cofactor, cicatrisation o neurotransmitters generation [110]. iv) Mg is essential to metabolism, and it excess is generally excreted by the urinary tract very quickly. v) Mg and its corrosion products exhibit high biocompatibility and low thrombogenicity. vi) Bone contains approximately 67% of the body's magnesium, 30% of this being exchangeable due to its presence on the surface of bone, thus providing a dynamic store for the maintenance of magnesium homeostasis [103].

Biodegradability of Mg alloys is based in its low reduction potential (-2.37 V) and the existence of galvanic pairs due to the presence of secondary phases in the alloy microstructures. When in contact with biologic fluids, a superficial magnesium oxide (MgO) and magnesium hydroxide ($Mg(OH)_2$) layer are formed. This formed layer in contrast to the titanium oxide layer does not significantly protect the substrate, as it develops cracks. Other degradation products include bioactive compounds such as amorphous calcium phosphate or magnesium calcium apatite ($((Ca1-xMgx)_{10}(PO_4)_6OH_2$) that can precipitate on the surface of magnesium-based metals incubated in physiological electrolyte. A similar degradation mechanism has been detected in the corrosion layer of magnesium-based metals that have been implanted *in vivo* [104]. In the corrosion process of magnesium there is an anodic reaction in which Mg^{2+} ions are released and a catodic reaction with a molecular hydrogen liberation [111].

$$Mg(s) \rightarrow Mg^{+}(aq) + 2e^{-}$$

$$2H_2O(aq) + 2e \rightarrow Mg(OH)_2(s) + H_2(g)$$

$$Mg + 2H_2O \rightarrow Mg_2OH + H_2$$

Although a high degradation speed can be useful for fast resorption of the implant, it has consequences for its functionality as the biomaterial mass is diminished and the structural integrity can be lost [101]. On the other hand, H_2 gas liberation can present a risk for the organism when bubbles are accumulated in the tissues [112]. The daily limited uptake of H_2 is 0.01 mL/cm^2, making a controlled regulation of the liberation necessary [113].

1.4.1. Mg alloys

One strategy to improve the mechanical properties and control the degradation rate is the development of Mg alloys as it has been evidenced with AZ31, AM50 or AZ91D. Nevertheless, many of the elements used in this alloys are toxic, the Al present in all three alloys is related with neuropathologies including Alzheimer's disease [114]. The selection of alloying elements is subject to their biocompatibility in order to obtain biomedical grade alloys. The elements investigated with respect to their biocompatibility include rare earth elements (such as yttrium and gadolinium), zirconium, manganese, zinc, calcium, lithium, and strontium, among others. Biocompatibility of rare earths is still in question, although the toxicity of any element is dependent on its final concentration [103]. For example, Ca promotes bone regeneration and its absorption is increased in combination with Mg [110]. In blood serum Ca is present at a 0.919-0.993 mg/L concentration, thus, Ca liberation from the implant could be positive as it can participate in homeostasis signalling processes. Besides Ca, Zn is also highly biocompatible and both improve the mechanical properties (ductility and age hardening). Both Ca and Zn in concentrations below 1 wt. % are relatively inert in terms of corrosion, but above this concentration the intermetallic particles form galvanic pairs with Mg matrix [115].

In the past years, Mg–Y, Mg–Zr, WE43, WE 54, Mg–Zn, Mg–Zn–Mn, Mg–Bi–Ca and Mg–Zn–Ca, Mg–Zn–Ca–Pd alloys have been evaluated for their suitability. More recently, Mg alloys such as Mg–Nd–Zn–Zr, Mg–Gd–Zn–Zr, MgNd2, Mg–Dy, ZEK100, Mg–Sr, Mg–Zn–Sr and Mg–3Sc–3Y have become of interest [109].

As a result, from the past years' research in the field, commercial implants based on Mg alloys are already available for some specific applications. The first magnesium implant for application in humans, a compression screw MAGNEZIX® CS (Syntellix AG, Hanover, Germany) was approved in 2013 [102]. This screw is based on the Mg alloy MgYREZr (magnesium-yttrium-rare earth-zirconium alloy) that has been proved to be biocompatible, presents osteoconductive properties, a good tissue reactivity with no inflammation and no allergic reactions. Projected as a substitute for titanium screws for fixation during corrective surgery in patients with a mild hallux valgus (i.e. deformity characterised by lateral deviation of the big toe) [103]. Three clinical studies have been performed on this innovation, reporting about MAGNEZIX® CS fixations of Chevron

osteotomies. Other possible applications of this implant include intra- and extraarticular fractures, non-unions, bone fusions, bunionectomies and osteotomies [102].

On the other hand, for cardiovascular applications a bare metal stent (BMS, 93% Mg and 7% rare-earth metals) from BIOTRONIK (Berlin, Germany) has been investigated for two specific medical conditions: in a human clinical trial for coronary arteries (Clinical Performance and Angiographic Results of Coronary Stenting with Absorbable Metal Stents or PROGRESS-AMS) and in infrapopliteal artery of patient with critical limb ischaemia. BIOTRONIK AMS was then improved by the addition of a tantalum radiopaque end-markers and replacing Paclitaxel with Sirolimus (DREAMS 2 AMS), a drug that inhibits the proliferation of lymphocytes and smooth-muscle cells in order to avoid restenosis of a treated vessel [116].

Other product in this field for other application is Velox CD (Transluminal Technologies LLC, Syracuse, USA), applied for wound closure of arteriotomies. The implant is based on a magnesium alloy (containing magnesium, aluminium, and iron) proven biocompatible and fully bioabsorbable [103]. The implant's intraluminal portion dissolves within 24 hours, while the remainder is completely resorbed within two weeks.

Lastly, a scaffold for osteochondral regeneration (large and severe osteochondral lesions) has also been evaluated. MaioRegen (Fin-Ceramica Faenza S.p.A., Faenza, Italy) is a multi-layered scaffold based on Type I equine collagen and Mg-HA, with the aim to mimic the osteocartilage tissue [103]. Furthermore, other commercial Mg alloys (e.g. Mg-Zn-RE) have been clinically validated for biomedical use [117].

As we have reviewed with previous metallic biomaterials, several surface modifications have been also evaluated to improve Mg-based implant behaviour.

Surface modifications of Mg alloys

The principal limitations of the use of un-treated Mg alloys implants are: fast corrosion, excessive hydrogen gas generation, gas pockets accumulation near the implant, local pH value of body fluid increase [109]. Local alkalization can affect negatively the pH dependent physiological reaction balances around the Mg implant, leading to an alkaline poisoning effect if the pH value exceeds 7.8 *in vivo*. Therefore, further improvements in Mg corrosion rate control are needed. This task can be approached in different ways: use of high purity Mg [118] alloying and/or developing a surface treatment or coating. These strategies can also be combined. Coatings and surface treatments strategies can be used not only to increase corrosion resistance but also to add other characteristics related to the biocompatibility and biological activity of magnesium-based implants [104]. However, to the author's best knowledge there are not Mg-based commercial implants with surface modifications based on chemical or electrochemical methods.

Many different surface modification methods have been evaluated on Mg:

Table 1.6. Surface modification methods evaluated on Mg adapted from [109].

	Treatment
Chemical methods	Acid etching
	Alkaline passivation
	Immersion in alkaline solution followed by heat-treatment
	Conversion coatings
	Formation of layered double hydroxides
	Self-assembled monolayers
	Sol–gel coatings
	Polymeric coatings
Physical methods	Sputtering
	Ion implantation
	Thermal spraying
	Electron beam treatments
	Laser surface processing
	Physical vapour deposition
Electrochemical methods	Anodic oxidation
	Microarc or plasma electrolytic oxidation
	Electrophoretic deposition

Among them, it is well-known that PEO is an electrochemical treatment that outstands for its capacity of controlling the magnesium corrosion rate [119]. As a result of PEO, ceramic-like thick and stable coatings can be formed on Mg alloys, with different coating features (composition, microstructure, porosity, and roughness) modulated by the electrical parameters of the process and the composition of the electrolyte in order to obtain the desirable functions. One of the most interesting functionalization is the possible improvement of the bioactivity.

The surface of ceramic-like PEO coatings present pores and cracks as a consequence of the plasma microdischarges and thermal effects. Excessive porosity can induce a faster degradation of Mg implant due to easy access of corrosive species of physiological medium through the coating towards the substrate. Infiltration of polymers into the pores and cracks to seal the PEO coating has been proposed as one the methods of improving the corrosion resistance [109]. For example, PEO coatings formed on AZ31 Mg alloy were coated with maleic anhydride-g-liquid

polybutadiene (MALPB), a polymeric compound with low-molecular weight (number-average molecular weight: 1020) and low viscosity. Lu *et al.* [120] and Guo *et al*. [121] used poly-l-Lactic acid (PLLA) over PEO coatings formed on WE42 Mg alloys. Liu *et al.* [122] used a layer-by-layer (LBL) self-assembly technique of chitosan and poly (styrene sulfonate) (PSS) polyelectrolyte multilayers on PEO coated WE43 Mg alloy. This method consisted in the adsorption of polyanions and polycations through electrostatic interactions between them.

Also, on a PEO-coated Mg–Zn–Ca alloy propolis and polylactic acid were deposited by sol–gel method to seal the pores [123]. Another similar approach was based on a multilayered coating consisting of a first layer of an electroless nickel or a PLLA coating, a second layer with a drug loaded organic polymer coating and a top layer with a drug free organic polymer coating over a PEO coated Mg alloy [124, 125].

A post-treatment strategy using biodegradable polymers could be an excellent approach to solve the disadvantages of the PEO coating. Their possible use as a coating of the core material (e.g. magnesium alloys) could implement several desired characteristics. Furthermore, this top layer could also be modified topographically to improve its bioactivity or even be used as drug reservoir.

Polymeric layer surface modification: Breath figures strategy

Topographic changes on the surface of a material of interest such as the presence of pores is usually a required characteristic. Moreover, extension and distribution of the pores can determine if cells would adhere, proliferate and migrate on the material. The formation of a porous surface can be obtained by Breath Figures (BF) methodology; it is based on the evaporation of a polymeric solution under moist atmosphere. When the solvent evaporates the temperature of the solvent surface decreases and therefore it favours water vapour condensation obtaining ordered water droplets arrays at the solution−air interface (Figure 1.11). If the surface is not wetted by the vapour, moisture condenses on the cold surface forming water droplets that grow during the evaporation giving rise to distinct water droplet arrangements on the surface [40, 126].

Different biodegradable polymers that include PLLA, poly(ε-caprolactone) (PCL), PLGA, poly(3-hydroxybutyrate) (PHB) are being used for the preparation of BF films due to their potential applications in biomedical applications [127]. This kind of polymers could be used as a coating for the previously proposed strategies (e.g. cardiovascular stents or bone reconstruction plates) aiming to avoid a second surgery procedure and improve the properties of the implant.

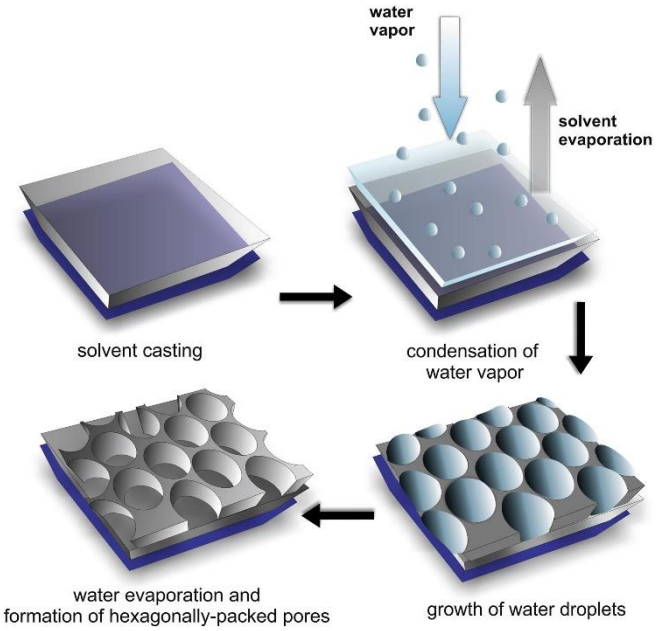

Figure 1.11. Breath figure mechanism [40].

This phenomenon was first described by François *et al.* that observed the formation of films with monodisperse pore size after evaporating star-shaped polystyrene or polystyrene-polyparaphenylene block copolymer solutions in carbon disulfide under a flow of moist air [128]. Diverse features were described to influence the final porosity organization including humid conditions, type of solvent, polymer architecture and polymer molecular mass. BF is a commonly observed phenomenon in daily life. One example is the fog that appears on a window when we breathe on it. This is also the origin of the name "breath figure"[127].

Usually, a droplet of a polymer solution is located on a solid support and cast adjusting the relative humidity of the chamber (< 50% being required). The use of this technique has increased significantly and it can be explained by the following facts; i) self-removal of the template favours a reduction on the production time and costs, ii) a wide range of materials can be used from polymers to hybrid nanocomposites [126].

Among all the possible applications, in the tissue engineering field can be used as platforms for cell culture with the aim to module cell behaviour. Their tailored surface porosity can be of great interest to study cell-biomaterial interaction mechanisms and even favouring cell adhesion processes. Moreover, the formed pores could be used as containers of molecules or proteins of interest, served as protection sites for bioadhesive molecules, applied as drug delivery systems or as a 3D microenvironment (Figure 1.12). In our context, many of the proposed improvements of cell behaviour could be of great used for the Mg based implants.

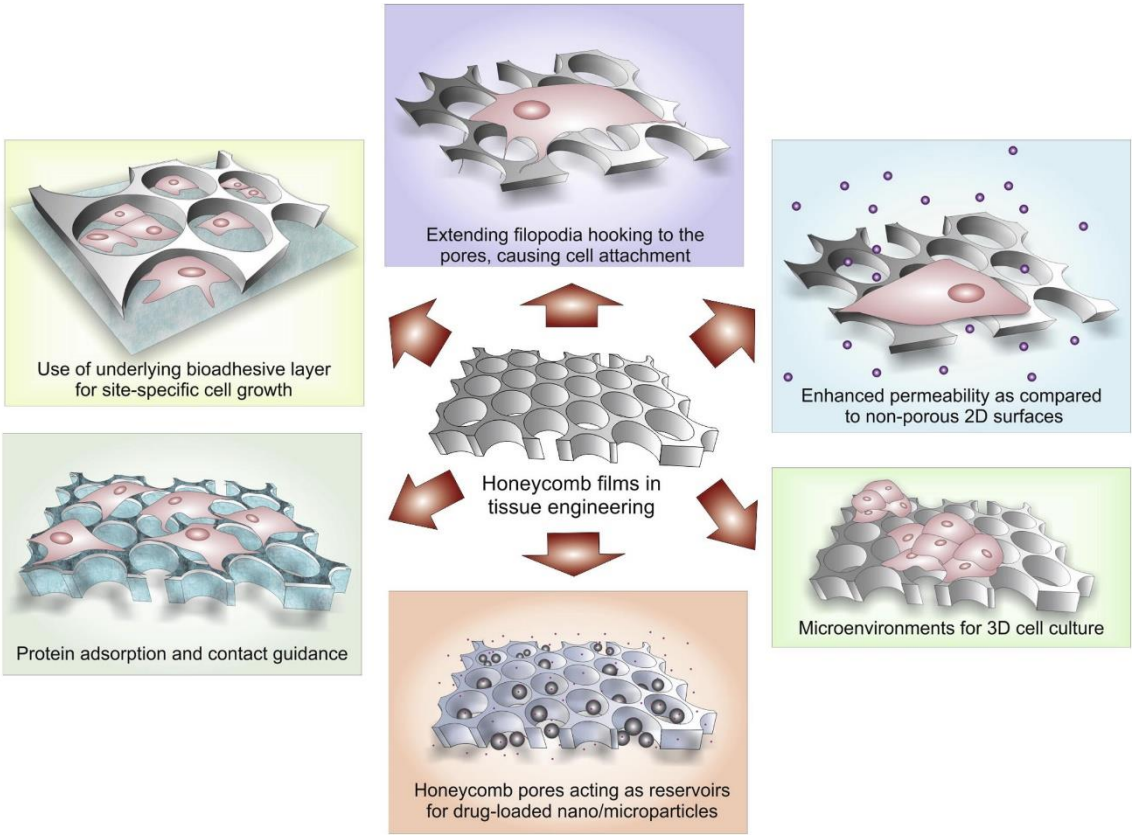

Figure 1.12. Proposed strategies of breath figures applications in tissue engineering [40].

A key feature is the interconnected porosity of BF films enabling them with high loading capacity. This includes low solubility drugs that can be embedded into hydrophobic polymer matrices or even encapsulated into the porous films. For instance, PU based honeycomb membranes with the active compounds/assay reagents dispensed on the pores where able to dispense relevant concentrations of this compounds with minimum systemic toxicity [129].

As has already been described biomedical coatings design needs to fulfil diverse characteristics, the inhibition of bacterial contamination is one of them and BF surface modification can be an interesting strategy added to the incorporation of bioactive elements into the PEO coating. For instance, PMMA and PU honeycomb films have been proposed as coatings for biomedical devices [130]. Also, antibacterial agents' deposition can be of great interests to avoid bacterial infections. Other strategies investigated by J. Rodriguez-Hernández FUPOL group from ICTP-CSIC include the co-polymerization and selective modification of the pore inner part by mixture of a PS-*b*-PAA diblock copolymer and a homopolymer (PS) for recognition and selective bacterial adhesion (Figure 1.13) [131]. A similar functionalization was performed inside the pores of PS films with Poly(ethylene glycol) methyl ether methacrylate (PEGMA) or 2,3,4,5,6-pentafluorostyrene PEGMA groups that selectively allowed cell growth and proliferation whereas the antifouling properties were maintained [132]. Selective surface chemical modification

remains an extremely interesting strategy that has not been widely explored with this technique and PS based platforms constitute an ideal model for its study.

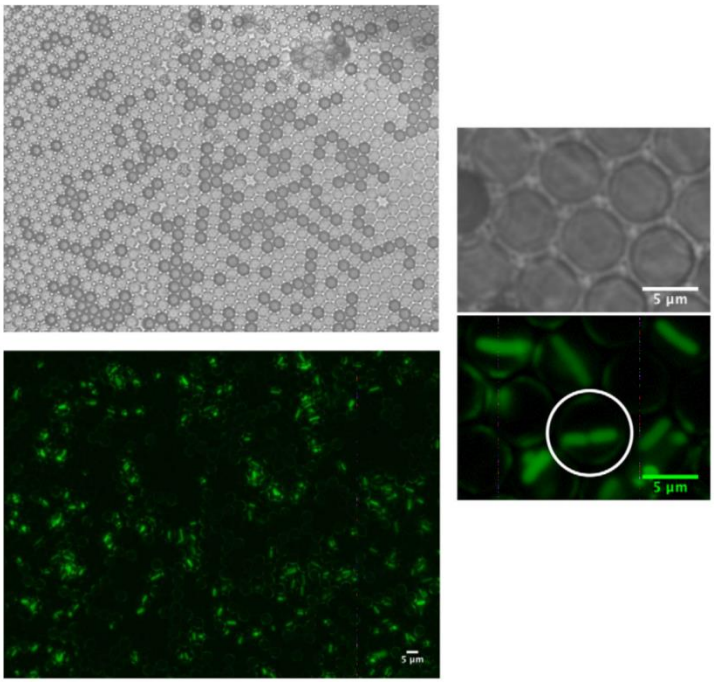

Figure 1.13. Interaction of the surface with fluorescent *E. coli*. Top panels: Optical microscope images of the polymer surfaces in which a rather regular pattern of pores can be observed. Bottom panels: Fluorescent image of the surfaces with the immobilized bacteria [131].

New biodegradable implants can be proposed based on Mg alloys and surface modifications as PEO can reduce the degradation mechanisms and add new functionalities. In addition, PEO coating composition can be modulated in agreement with the specific needs of the applications. However, detailed information on interaction of PEO-coated biomedical Mg alloys with the host biological media and different tissue regeneration processes is still scarce. In a following step, the interaction of PEO structures with polymeric hierarchical top-coats and their potential for intelligent coating systems needs to be addressed. These top-coats can be further functionalized in terms of topography and chemical composition by BF approach.

1.5. Cell sheet engineering

Tissue engineering pivots mainly in three components: biomaterials/scaffolds, cells and signals. Since the beginning of TE, biomaterial design and surface modifications improvements have been of great relevance for the final outcome of an implant. However, in the past years many efforts have been made to upgrade its performance by using cellular components. The already engineered materials can incorporate patient's own cells (autologous transplant) or from a compatible donor (allogenic transplant). Many attempts using single cell suspension injections have been evaluated or for instance, the use of PRP (Platelet-Rich Plasma) for bone grafts, tooth extractions,

periodontal surgery or implant surgery is widely applied every day in clinical practice. PRP is applied in a gel formulation, based on a mix of PRP (derived from the centrifugation of autologous whole blood) with thrombin and calcium chloride. In bisphosphonate-related osteonecrosis of the jaw (BRONJ) pathology it has been suggested to enhance wound healing and bone maturation [133]. More complex therapies have also been explored, based on the combination of mesenchymal stem cells, fibrin and PRP within the dental implant on dogs [134]. Other clinical approaches proposed include cell reprogramming of human induced pluripotent stem cell-derived mesenchymal progenitor (iPSC-MP) cells, which can be isolated from a small biopsy, into bone-forming cells, cultured on the surface of Ti implants for two weeks and decellularized after this time [135].

However a change of paradigm was proposed as it is believed that tissue reconstruction could be based on cell sheets and no single cells [136]. Cell sheet technology was developed by Okano's Laboratory aiming to avoid the use of biodegradable scaffolds with single cells incorporation as these technologies have obvious limitations in the reconstruction of a tissue. When applied to clinical therapies a faster patient recovery can be obtained since autologous or compatible cells can be cultured and applied directly on the injured part/area. The use of additional materials, for instance carrier substrates or scaffolds, can bring complications associated with traditional TE approaches such as host inflammatory responses to polymeric-based materials [137, 138]. Therefore, with the use of cell sheets these complications can be avoided. Other strategy could be the application of this technology on permanent implants such as dental implants as a tool to improve an implant success rate by favouring the osseointegration process is a promising strategy can be promoted, obtaining also immune system reaction reduction. Predifferentiated cells with a proper extracellular matrix expression or co-culture of different cell types could be transplanted into the implant. This new proposed strategy is going to be explored in this Thesis.

The first noninvasive cell sheet harvest and transplantation applications were performed using temperature-responsive culture surfaces based on pNIPAm (poly(N-isopropylacrylamide)). Consequently, cell sheet technology has been mainly based on thermoresponsive culture material that allows adhesion and proliferation of cell cultures and is based on a temperature trigger for cell and cell sheet detachment on demand [139].

Cell sheet engineering has been evaluated already for different applications: multilayer human keratinocytes for skin regeneration purposes [140], renal epithelial cell sheets [141], reepithelialization of the corneal surfaces [142], urothelial cell sheets for bladders *in vitro [143]* and *in vivo* [144], periodontal ligament cell sheets applied *in vivo* [145]. Furthermore, cell sheet transplantation had an outstanding performance in comparison to cell injection for cardiac tissue repair proposes [146].

Bone cell sheet engineering has been less developed than other tissues, only a few studies had been performed. Pirraco *et al.* first attempted to a monolayer transplant of bone cells (rat bone marrow stromal cell) with thermoresponsive PNIPAM based culture dishes and then improve it using vascularized cell sheets obtained by the coculture with endothelial cells [147, 148]. On the other hand another scenario is found with cartilage tissue, layered chondrocyte sheets prepared in the same temperature-responsive culture dish and applied *in vitro* [149] and *in vivo* in a porcine model [150] with actual application in patients.

A company (CellSeed) has already developed a series of cultureware products based in poly-isopropylacrylamide-PNIPAm (UpCell's, RepCell®, HydroCellTM). Moreover, it is also developing therapeutic applications such as esophageal epithelium cell sheets and regeneration of cartilage tissue using cell sheets among others (Table 1.7). E.g. a new treatment using cell sheets prepared from the patient's oral mucosa is under a clinical trial in Japan in order to obtain a product license [151] after the results obtained by Okano's group research [152, 153].

Table 1.7. Cell sheet engineering ongoing applications adapted from [154].

Application	Clinical stage	Ref
Corneal epithelial reconstruction	Clinically approved Used for patients	[142]
Treatment for heart failure	Clinically approved Used for patients	[146]
Esophagus regeneration	This therapy is currently being performed in patients after esophageal endoscopic submucosal dissection	[152, 153]
Periodontal regeneration	Performed in patients	[145]
Cartilage regeneration	Performed in patients	[149, 150]
Sealing of lung air leaks	Clinical investigation in patients	[155]
Regeneration of middle ear cavity mucosa	Performed in patients	[156]
Pancreatic cell sheet	No clinical practice Studies currently underway	[157]
Hepatocyte sheet	No clinical practice Studies currently underway	[158]
Prevention of intrauterine adhesions	No clinical practice Studies currently underway	[159]
MSC sheet for wound healing in diabetes	No clinical practice Studies currently underway	[160]

However, there are still improvements (topographic features, new materials as supports…) to make in terms of materials design for their use in cell sheet engineering. For this matter, FUPOL group from ICTP-CSIC developed hydrogels (polymer networks able to uptake water) based on Vinylpyrrolidone (VP) prepared by free radical polymerization reaction via UV curing to be used as a cell sheet platform [161, 162]. The application of these hydrogels was as a cell culture platform and posterior transplant without the requirement of any chemical agents. Cells transplant is performed by mechanical detachment of cell cultures after the seeded cells are allowed to grow over the surfaces and become confluent. Moreover, other strategies are being explored including the preparation of wrinkled and hydrophylized polycarbonate (PC) surfaces by the procedure indicated in Figure 1.14 [163]. Surface chemistry and surface topography can be modulated in this manner (Figure 1.14).

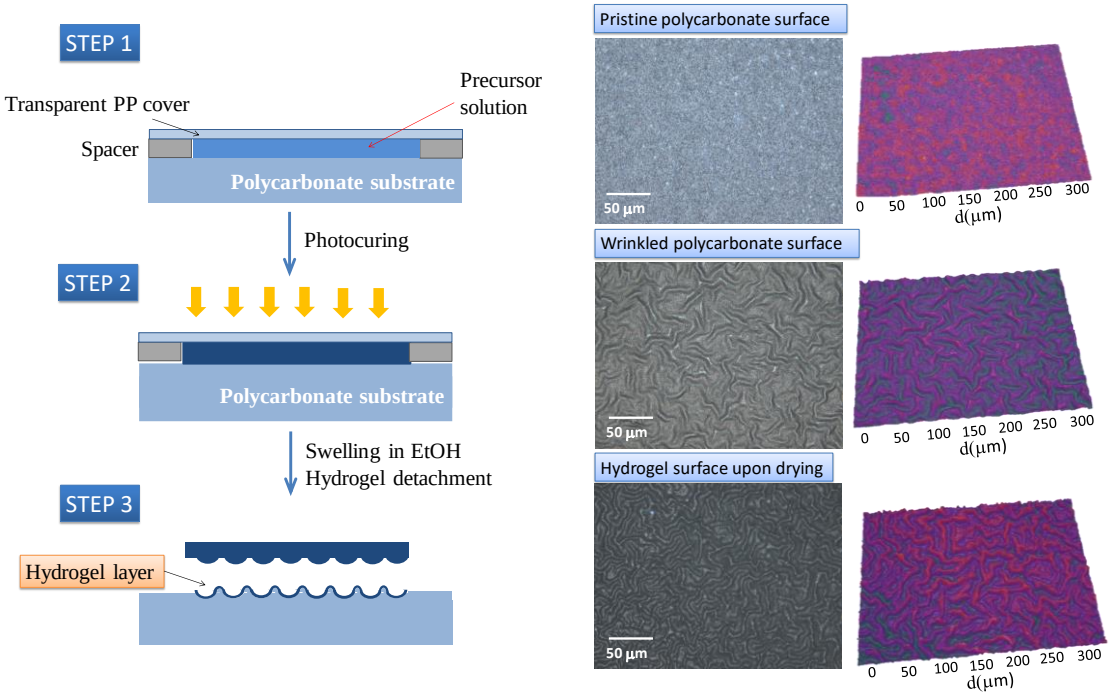

Figure 1.14. Left: strategy for the preparation of wrinkled hydrogel surfaces involving 3 steps. Step 1: setup with an empty chamber in which the photosensitive mixture is incorporated. Step 2: upon a certain time in contact with the PC the mixture is irradiated using UV light. Step 3: cover removal and swelling. Upon swelling the hydrogel detaches leaving a thin hydrogel layer on top of the PC surface [163].

These hydrogels are structurally VP-based. pVP is known as a water-soluble, nontoxic, biocompatible, chemically inert, temperature-resistant, pH-stable, non-ionic and colourless nature polymer widely used in industry [164]. The first commercial applications were as a complex formed with cross-linked pVP and polyphenols for the clarification of beverages or complexed with iodine with linear pVP as an effective disinfectant of very low toxicity (Betadine®). Other applications in the pharmaceutical field as binding or film forming agents for tablets, and as solubilizing agents for injections [165].

Nowadays, the combination of its physical and chemical properties (biocompatibility, non-toxicity, chemical stability, good solubility in water and many organic solvents, affinity to complex both hydrophobic and hydrophilic substances) validate pVP as a biomaterial in diverse medical and nonmedical applications (pharmaceutical industry and medicine, optical and electrical applications, membranes, adhesives, environmental applications, among others). One of the first uses in biomedical application was as blood plasma expander, also has a common use in drug manufacture (tablets, granules, pelettes, soft gelatine capsules, gels, hydrogels, films and coatings, membranes and mats of nanofibers, powders, syrups, oral or injectable solutions), as a coating for medical devices or applied in contact lenses [164]. These characteristics makes this polymer of great interest to be used as cell growth platform.

When this strategy was set up, this group attempted to prepare new hydrogels based on pVCL (Poly(N-vinylcaprolactam)). VCL and VP are molecularly close (structurally and electronically) (Figure 1.15). This polymer presents thermosensitiviness, similar to the above mentioned pNIPAm. At 37 ºC the hydrogel it is in a 'hydrophobic state' and it permits cell adhesion and proliferation on its surface, but upon a decrease of the temperature, the hydrogel swells increasing the size (Figure 1.16 B) and allowing cell or cell monolayer detachment. This technology also allows a transplant without the requirement of any chemical agents and maintains the unions between cells. ECM (Extracellular cell matrix) can stay untouched, integrins, focal adhesions, hemidesmosomes and other unions are not destroyed in the process. This process is similar to the observed pNIPAm substrates as the detachment of the culture starts when the ambient temperature is lowered below the LCST (Lower critical solution temperature) of the material and therefore the cells take-off from the material [166].

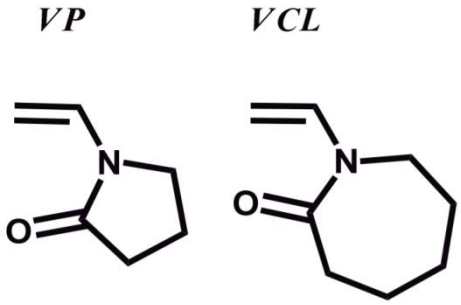

Figure 1.15. VP and VCL structures.

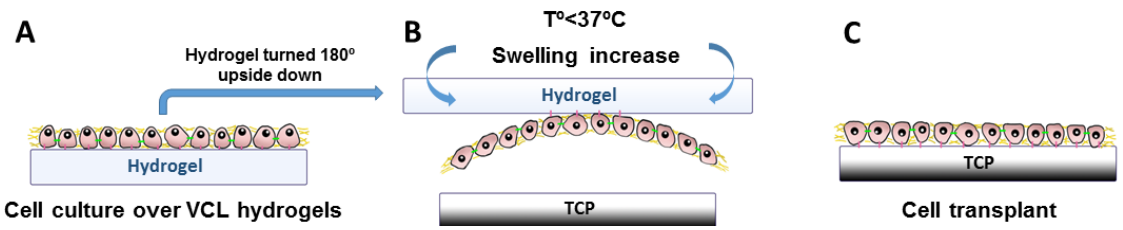

Figure 1.16. Scheme of transplant mechanism under temperature stimuli.

The developed technology promoted a Patent in 2017 (P201730039) and later on the establishment of a new company based on this knowledge, **ReleasyCell S.L**. This technology aims to compete with the traditional cell culture strategies and with the already developed platforms based on smart hydrogels.

pVCL, which is the type of polymer that constitute the mentioned thermosensitive hydrogel, has been an excellent candidate for biomedical and environmental applications as it is biocompatible [167], a fact that has not been thoroughly demonstrated for PNIPAm. VCL was proven biocompatible with the first study on cytotoxicity of pVCL and pVCL grafted with Poly(ethylene oxide) published in 2005 [167, 168].

Other characteristics of pVCL are that it is soluble in polar and non-polar solvents (water (below 31 °C), alcohols, DMF, DMSO, tetrahydrofurane (THF), p-dioxane, chloroform, and dichloromethane), it has film formation properties, presents good complexing properties with organic molecules, and can inhibit crystal growth. pVCL is proposed for several applications including the following; Biomedical applications: Entrapment of enzymes and cells, drug delivery, tissue engineering [169, 170], Bio-analytical applications: sensors, Temperature responsive liquid chromatography, Membrane chromatography, Liquid–liquid extraction, Displacement chromatography, Affinity chromatography and Nanotechnology/catalytic applications [168].

Related to the tissue engineering applications above mentioned, both pNIPAm-based systems and VCL-hydrogels are being proposed as supports for cell transplants. However, the strategies for the obtainment of the exposed cell transplant platforms are different, as pNIPAm-based systems are usually surface grafts or coatings of macromolecular chain sizes (<5-10 nm), VCL-hydrogels, on the other hand are prepared as hydrated networks that can reach thicknesses of several hundred microns. This latter strategy, allows the stimulation of cell culture through the loading and controlled release of the VCL support with active compounds as there are significant differences in their dimensions compared with the classic approach of pNIPAm-based systems and, furthermore, this strategy is encouraged by its hydrated character. Moreover, VCL-hydrogels are flexible systems, and direct transplant to the target surface can be done without using intermediate devices, in contrast for the pNIPAm based surfaces is required.

Hydrogels Functionalization

In order to improve the cell growth and transplant success rate different modifications can be made into the proposed hydrogels. Hydrogels are extremely flexible in terms of functionalization as many properties can be adapted o modulated. These features can be tailored to improve their biological behaviour. On the one hand, polymer's topography can be modified in order to mimic

biological microenvironment. On the other hand, surface charge and/or chemical or biological groups can also affect cell activity.

It has been established that different topographies affect cell adhesion and subsequently proliferation, or other processes such as cell differentiation. Topographic modifications, including lines, pores, wrinkles or grooves can promote cell activity. The majority of the studies of surface topography related with cell adhesion have been focused on surface roughness as a surface characteristic. Even though surface roughness directly affects in both *in vitro* and *in vivo* cellular morphology, proliferation, and differentiation [171] surface pattern size as well as the shape of the motifs can affect the cell adhesion process too [172].

The interaction between different topographical surface patterns and cellular activities has been widely described [173], several types of pattern models in a range of sizes (microscale, nanoscale, and hierarchical structures consisting of both) and shapes (pillar, hole, groove, grate, grid, and island) were evaluated. More specifically, De Bartolo *et al.* [174] described the neuronal behaviour, considered large cells, in polymeric surfaces with a variable roughness from the nanoscale (6.26 nm) to microscale (200 nm). On the contrary with smaller cells the situation can differ, Chung *et al.* [175] described an enhanced cell adhesion and growth of human vein endothelial cells on surfaces with nano to submicrometer scale roughness (10–102 nm). Related to differentiation processes from mesenchymal cells, Abagnale *et al.* [176] proved that surface topography promoted adipogenic and osteogenic lineages.

Another key characteristic that can also regulate cell activity is the surface charge. From a wide point of view, the role of total negative or positive charge in cell activity has been deeply discussed [177]. However, cell response mainly depends on the specific cell line studied and the particular experimental conditions, and it's difficult to assume a rule to describe a general cell behavior. Moreover, mixed situations such as the presence of zwitterionic or pseudo-zwitterionic groups can also affect eukaryotic and also prokaryotic cell behaviour.

In addition, hydrogels can present surface modifications with different groups in order to give them characteristics such as protein recognition sites/cues (e.g. RGD, laminin, vitronectin), growth factors (PDGF, VEGF), polymer brushes or incorporation of groups with antibacterial effect. More specifically polymers can be modified to trigger more complex mechanisms as cell differentiation processes (mineralization, vascularization…). Both physicochemical and topographic surface characteristics of scaffolds are vital parameters in controlling and affecting cellular adhesion and proliferation.

In the particular case of VP and VCL hydrogels these surface modifications can be modulated by the methacrylate union obtained charged groups or topographically by the use of different support

materials as molds. In the previous described studies [161, 162], VP was polymerized with different ionic methacylates (M): anionic (M-SO_3^-), cationic (MN^+), zwitterionic sulfobetain (M-N^+-SO_3^-), zwitterionic phosphoryl choline (M-PO_3^--N^+), or pseudo-zwitterionic (stoichiometric amounts of M-SO_3^- and M-N^+). The VCL-based hydrogels can also incorporate the adequate methacrylate into the polymerization solution and photocured by the same process as VP hydrogels.

Final summary

Once accomplished literature review of proposed biomaterials and their main applications in tissue engineering, a Summary Table is presented in order to clarify the focus of this Doctoral Thesis (Table 1.8). Challenges related to these biomaterials, proposed strategies and clinical applications are shown.

Table 1.8. Proposed biomaterials in the literature review.

	Material	Challenges	Proposed strategies	Application
PERMANENT	Ti Ti6Al4V	Osseoinductive Antibacterial Bone homeostasis cell types (osteoclasts)	*In situ* functionalization with inorganic species	Dental implants Orthopaedic
	Zr	Cell behaviour Possible use as alternative to conventional implantable material	Anodizing	Orthopaedic cementless implants
TEMPORARY	Mg PCL/PS	Degradation control Functionalization of the surface with different top layers	*In situ* functionalization with inorganic species 3D polymeric top layer Prototype of selective functionalization	Bone regeneration (screws, plates, pins, osteosynthesis) Stents
CELL THERAPY	VCL VP	Cell harvesting platform Surface functionalization Antibacterial	Surface chemistry and topographic modifications for polymeric platforms	Cell sheet engineering for tissue regeneration

2. Objectives

The proposed research programme of this Thesis is based on the following hypothesis: it is possible to generate a combined therapeutic approach for tissue regeneration that comprises multifunctional biomaterials for permanent and biodegradable implant applications that can be used in combination with cell therapy. This mixed strategy would combine the benefits of metallic, ceramic and/or polymeric biomaterials and cellular components (single cells or monolayers). The functionalities such materials would address include: (i) bone regeneration capacity joined with added functionality such as antibacterial effect in case of permanent biomaterials, (ii) controlled degradation rate and mechanical integrity combined with improved biological response through bioactive hierarchy of the surface.

In order to create such hybrid biomaterial several approaches to surface functionalization are envisaged: (i) *in situ* electrochemical modification of topography and composition of metallic biomaterials for permanent implants (Ti, Zr) and biodegradable implants (Mg) with bioactive species through the formation of bio-ceramic coatings, (ii) post-functionalization of the modified surface by loading it with active agents that can be local dispensed after implantation; (iii) deposition of 3D polymeric hierarchical structures (PCL) on the top of the surface-modified metallic materials; (iv) selective functionalization of polymeric structures targeting specific responses of cells and bacteria; (v) hydrogel functionalization to improve cell transplant applications.

This Thesis aims at generation of a proof of concept of each of the aforementioned tasks on each key material individually, as well as on combinations of metal+ceramic and metal-ceramic-polymeric materials. The proof of concept will be validated for the selected materials through *in vitro* cell and molecular biology techniques and *in vivo* surgeries, when appropriate.

The specific objectives of the research programme that constitute the multifunctionalization steps are as follows:

(i) *In situ* electrochemical modification

- Evaluate the effect of bioactive species (Ca, P, Si, Zn, Mg, F) in the surface-modified titanium and magnesium and their short-term and mid-term liberation on cells participating in various tissue regeneration processes including differentiation processes and bone homeostasis.
- Evaluate bioactivity of Zr as possible implantable load-bearing material and the effects of anodizing on Zr surface on cell behaviour, including differentiation mechanisms.

- Evaluate the antibacterial effect of surface functionalization of selected materials with active species.
- Evaluate the effect of degradation process of surface-modified biodegradable Mg alloy as a result of its interaction with biological medium on proliferation and differentiation of different types of cells involved in orthopaedic and cardiovascular implant applications, using in vitro studies in extracts.

(ii) Surface loading with active agents

- Determine the loading/unloading capacity of the selected materials modified with bioactive species as a function of surface topography and composition, using a model protein.

(iii) Deposition of polymeric hierarchical structures

- Interaction of ceramic coating structures with polymeric hierarchical top-coats and their potential for intelligent coating systems using premyoblastic cells.

(iv) Selective functionalization of polymeric structures

- Assess the possible functionalization of PS by breath figures methodology in order to obtain selective surfaces against bacteria. Incorporation of antibacterial groups such as DMAEMAQ and PAA.

(v) Hydrogel functionalization to improve cell transplant applications

- Biovalidate VCL and VP based hydrogels for future cell sheet engineering applications
- Determine the cell growth and transplant potential of the charge free hydrogel (VCL) of different cell types.
- Evaluate the influence of surface chemistry of functionalized hydrogels in cell growth and transplant.
- Determine the effect of surface chemistry and topography of supported VP hydrogels in cell behaviour and transplant.

3. Methodologies

3.1. Materials

3.1.1. Titanium alloys

Commercially pure (CP) Grade I titanium foil (0.2 Fe, 0.18 O, 0.03 N, 0.015 H, and 0.18 C (max wt.%)) specimens with the dimensions 30 × 30 × 0.5 mm. Ti6Al4V specimens (Grade V, max wt.%: 0.25 Fe, 0.02 O, 0.05 N, 0.015 H, 0.08C, 3.5–4.5 V, 5.5–6.76 Al, bal. Ti) with the dimensions 30 × 30 × 0.5 mm. All materials were degreased in isopropanol and rinsed in distilled water. Following the specimens were pickled in a mixture of 12 mL HF (40 wt. %), 40 mL HNO_3 (70 wt. %) and 48 mL H_2O for ~ 40 s at room temperature and neutralized in a 10 H_2O:1 $CaCO_3$ suspension, rinsed in distilled water and dried. Lacquer 45 resin (McDermid plc.) was applied in order to delimit a working area of 3 or 6 cm^2. For *in vivo* studies commercial Grade IV dental implants without surface treatment (4 mm diameter, 15 mm length; Lot. Nº12004; Noricum SL) were used.

3.1.2. Zirconium alloys

Commercially pure zirconium (99.5% Roberto Cordes S.A., Argentina) plane samples of 1 cm^2 were supplied by CONICET. All samples were mechanically polished with 600 grit emery paper, degreased with ethanol and rinsed with deionized water.

3.1.3. Magnesium alloys

Mg 0.8 wt. % Ca alloy (mass fraction: 0.61% Ca, 0.003% Fe, 0.0021% Cu, 0.0009% Ni, 0.023% Si %, 0.02% Al, 0.006% Zn, 0.05% Mn, 0.000039% Be and Mg balance) were kindly supplied by Helmholtz-Zentrum Geesthacht. All the samples were ground successively with SiC papers to P1200 grit size and cleaned with deionized water and isopropanol before the PEO treatment.

3.1.4. Polymeric material

The monomers, t-butyl acrylate (tBA) (Sigma-Aldrich, 98%), dimethylaminoethyl methacrylate (DMAEMA, AR) and high-molecular-weight polystyrene (PS) (Sigma, Aldrich, 99%) was used as a polymeric matrix. Polymers used on Chapter 3 were synthesized by ICTP CSIC FUPOL group. Polycaprolactone was kindly supplied by FUPOL group.

Potassium sulfopropylmethacrylate *(M-SO_3^-)*, [2-(Methacryloyloxy)ethyl] trimethylammonium chloride solution (*M-N^+*), [2-(methacryloyloxy)ethyl]dimethyl-(3-sulfopropyl) ammonium hydroxide (*M-N+-SO_3^-*), 2-Methacryloyloxyethyl phosphorylcholine (*M-PO_3^--N^+*),

vinylpyrrolidone (*VP*), vinylcaprolactam (*VCL*), ethylene glycol dimethacrylate (*C1*), 1-hydroxyl cyclohexyl phenyl ketone (*HCPK*) and azobisisobutyronitrile (*AIBN*) were purchased from Sigma (Sigma-Aldrich, St. Louis, MO). The polycarbonate (PC) employed throughout this study was provided by Orbi-Tech in the form of a 3 mm filament.

Hydrogels were synthesized one-step by a conventional radical polymerization using Milli-Q water or mixtures water/ethanol as solvents as described on [4]. The photopolymerization was carried out for 40 minutes under UV radiation (λ=365 nm) in a UVP ultraviolet lamp (model CL-1000L, 230V). VP hydrogels on PC supports were prepared as described on [163].

3.1.5. Cell lines

C2C12-GFP. This is a mouse pre-myoblast cell line (ATCC® CRL 1772™). Green Fluorescent Protein (GFP) was expressed due to previous lentivirus infection of this cell line allowing to be evaluated through an opaque material. Routine passaging of the cell line was performed with Dulbecco's Modified Eagle Medium (DMEM) (D6429, Sigma-Aldrich, St. Louis, MO), supplemented with 10% foetal bovine serum (FBS, Hyclone®, Thermo Scientific) plus antibiotics (100 U/mL penicillin and 100 µg/mL streptomycin sulphate; Sigma-Aldrich, St. Louis, MO). Cells were incubated at 37 °C with 5% CO_2 and the medium was refreshed every 2 or 3 days. This cell line can be evaluated by fluorescence microscopy (FITC filter λex/λem = 490/525 nm).

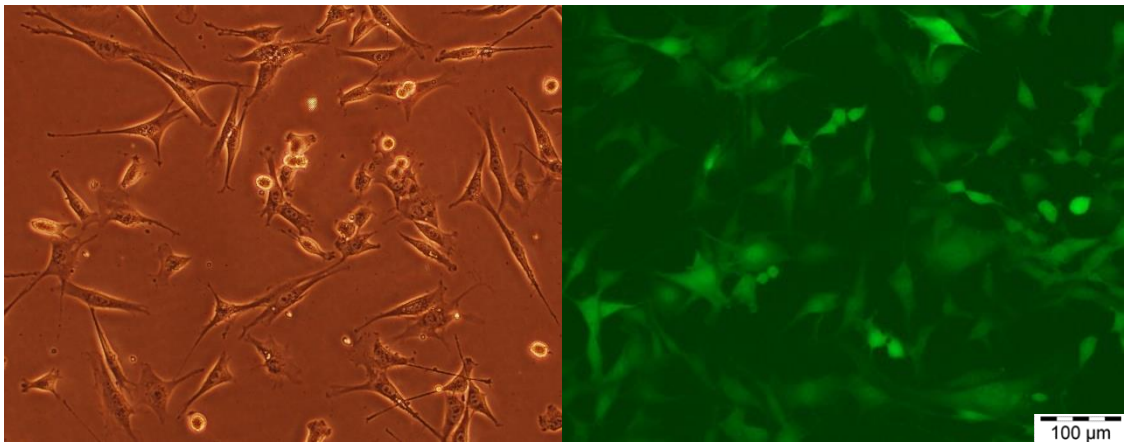

Figure 2.1. Premyoblastic cells growing over TCP, left micrograph bright field and right fluorescence.

C166-GFP. This cell line is a mouse endothelial model (ATTC® CRL-2583™). Routine passaging of the cell line was performed with Dulbecco's Modified Eagle Medium (DMEM) (D6429, Sigma-Aldrich, St. Louis, MO), supplemented with 10% foetal bovine serum (FBS, Hyclone®, Thermo Scientific) plus antibiotics (100 U/mL penicillin and 100 µg/mL streptomycin sulphate; Sigma-Aldrich, St. Louis, MO). Cells were incubated at 37 °C with 5% CO_2 and the medium was refreshed every 2 or 3 days. This cell line requires the addition G-418 antibiotic at a

final concentration of 0.2 mg/mL for the maintenance of the fluorescence. This cell line was evaluated by fluorescence microscopy (FITC filter λex/λem = 490/525 nm).

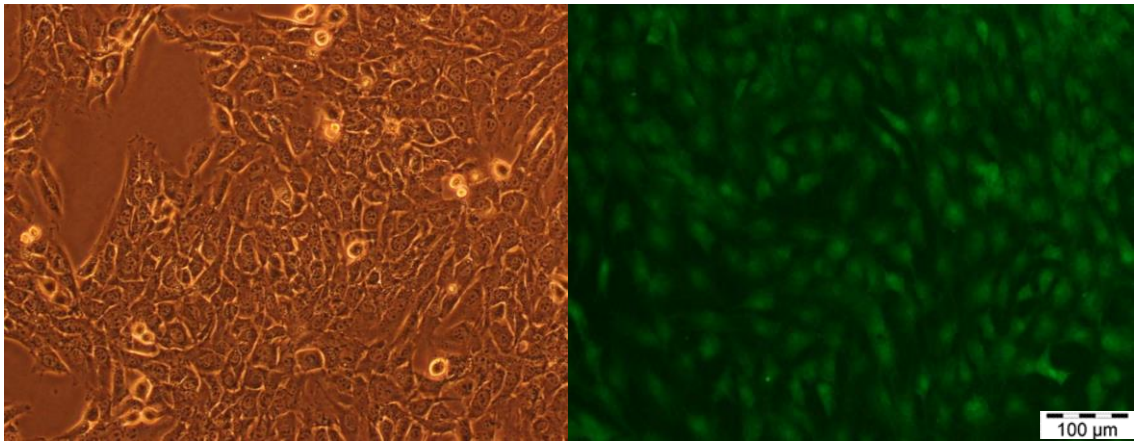

Figure 2.2. Endothelial cells growing over TCP, left micrograph bright field and right fluorescence.

MC3T3-E1. This is a mouse preosteoblastic cell line (ATCC® CRL-2593™). Cells were maintained in complete Alpha Modified Eagle medium (α-MEM A10490, Gibco, UK) without ascorbic acid supplemented with 10% foetal bovine serum (FBS, Hyclone®, Thermo Scientific) plus antibiotics (100 U/mL penicillin and 100 µg/mL streptomycin sulphate, Sigma-Aldrich, St. Louis, MO) incubated at 37 °C with 5% CO_2. For cell differentiation, cells were cultured in completed maintenance medium with 50 µg/mL of ascorbic acid, 10 nM dexamethasone and 10 mM β-glycerol phosphate, complete differentiation medium was changed every 3 or 4 days.

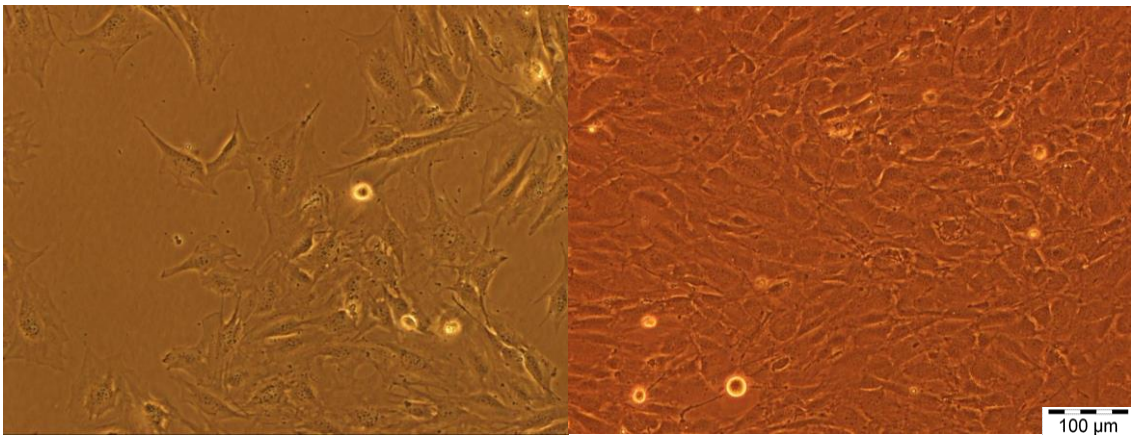

Figure 2.3. Premyoblastic cells growing over TCP, left micrograph low confluence and right high confluence.

RAW 264.7. This cell line is a mouse macrophagic model (ATCC® TIB-71™) used as an immune system and osteoclast differentiation model [178]. Two populations can be distinguished: adherent and non-adherent. This macrophagic cell line can also be modulated towards M1 (pro-inflammatory) or M2 (anti-inflammatory) phenotypes. Unlike primary osteoclast precursors, there is no requirement for the addition of macrophage colony stimulating factor (M-CSF). RAW

cells were maintained in an undifferentiated state by culture in completed D-MEM (D6429, Sigma-Aldrich, St. Louis, MO) and the medium was changed every 3 days. For differentiation, cells were plated at 1.5-2 × 10^4 per cm^2 in completed medium (α-MEM, A10490, Gibco, UK) supplemented with 50 ng/mL of recombinant RANKL (PeproTech Inc. Rocky Hill, NJ) during 5 days, incubated at 37 °C with 5% CO_2.

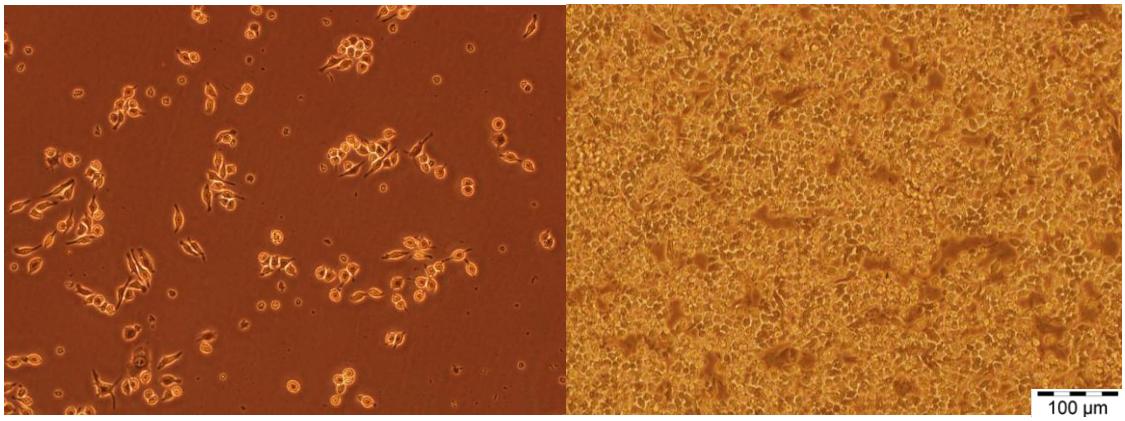

Figure 2.4. Macrophagic cells growing over TCP, left micrograph low confluence and right high confluence.

3.2. Surface modification

3.2.1. Anodizing

Three surface conditions were compared: *as received* pure zirconium (Zr0, control), zirconium anodized at a constant potential of 30 V (Zr 30 V) and at 60 V (Zr 60 V) during 60 min in 1 mol L^{-1} H_3PO_4.

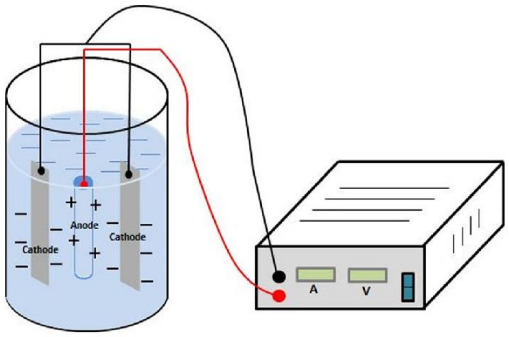

Figure 2.5 Anodizing step scheme where the anode is the Zr sample and cathode is a stain steel counterelectrode [179].

3.2.2. PEO

PEO treatment was carried out using a 2 kW regulated AC power supply (EAC-S2000, ET Systems electronic). A 50 Hz frequency square waveform voltage signal with 50% duty cycle

(Figure 2.6 b) was applied with a positive-to-negative pulse ratio dependent on the sample (Table 2.1), limiting the root mean square (rms) current density value to 300 or 400 mA/cm^2. The treatment was performed in a 1 L or 2 L double-walled cell with re-circulating cooling system that maintained the temperature of the electrolyte at 20 °C. The cathode was made of AISI 316 stainless steel and for Ti grade I and Ti6Al4V samples a plate with dimensions of 7.5×15 cm was used. For 3D PEO treatment in Ti Grade IV screws and Mg0.8Ca samples a circular mesh AISI 316 stainless steel cathode was utilised. Electrical contact with the specimens was provided through an isolated copper screw connection. The rms voltage and current responses were controlled electronically, with a sampling time of 0.1 s, employing a Keithley KUSB-3116 data acquisition card (16 bit, 500 Ks/s) and Labview program (National Instruments). Instantaneous voltage and current values were monitored using a 2-channel Tektronix TDS 2012B oscilloscope at 100 MHz sampling rate.

Table 2.1. PEO conditions.

Material/alloy	Time (s)	Positive pulse/ Negative pulse voltage (V)	Root mean square current density (mA/cm^2)
Ti grade I and IV (Section 1.1.1.)	90/600	+490/-60	400
Ti grade I (Section 1.1.2.)	300	+490/-30	300
Ti6Al4V	90-600	+490/-30	300
Mg0.8Ca	300	+430/-50	138

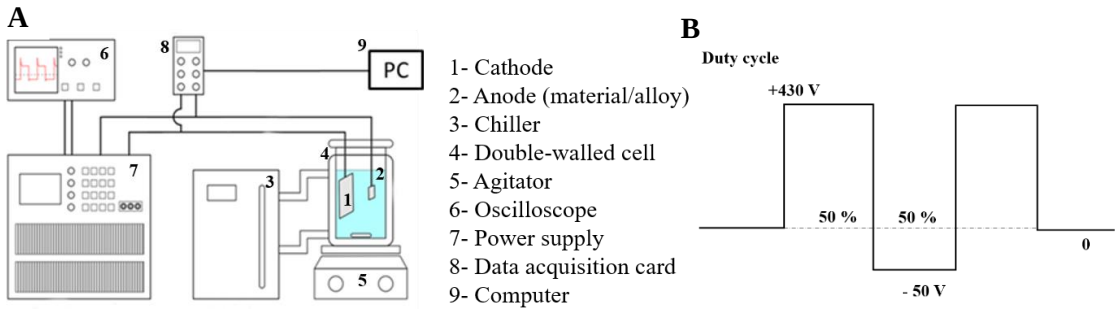

Figure 2.6. PEO setup scheme (A); an example of square voltage waveform design (B).

Section 1.1.1 coatings were formed in 0.125 M calcium acetate and 0.025 M sodium dihydrogen phosphate electrolyte. The electrolytes were suspensions with pH 7.0. Ti grade I (Section 1.1.2) and Ti6Al4V (Section 1.2.2) electrolytes are summarized on Table 2.2. Lastly, electrolytes used on Mg0.8Ca alloy are included in Table 2.3.

Table 2.2. Composition and characteristics of true solutions electrolytes for Ti grade I (Section 1.1.2) and Ti6Al4V (Section 1.2.2).

Electrolyte components	***Ti-1PEO***	***Ti-2PEO***	***Ti-3PEO***	***Ti-4PEO PEO Si/F-Electrolyte***	***PEO-Electrolyte***
	g/L	g/L	g/L	g/L	g/L
CaLact*·$5H_2O$	15.4	15.4	15.4	15.4	15.4
$NaH_2PO_4·2H_2O$	3.9	3.9	3.9	3.9	3.9
$Na_2EDTA·2H_2O$	20.5	20.5	20.5	20.5	20.5
NaOH	4.43	-	6	6	-
ZnO	-	2.0	-	3	2.0
$Na_2SiO_3·5H_2O$	-	3.0	-	2	3.0
$MgSO_4$	-	3.0	11.3	12.3	-
NaF	-	-	16.2	18.9	-
pH	7.60	4.22	4.51	12.28	11.3
σ, *mS/cm*	14.73	16.21	10.63	18.87	16.2

*CaLact: $Ca(CH_3CHOHCOO)_2·5H_2O$

Table 2.3. Chemical composition, pH and conductivity of suspension PEO electrolytes used for Mg alloy.

Electrolyte components	***PEO-B***	***PEO-4F***	***PEO-8F***	***PEO-9Si***
	g/L	g/L	g/L	g/L
KOH	1	1	1	1
$Na_3PO_4·12H_2O$	10	10	10	10
CaO	2.9	2.9	2.9	2.9
NaF	-	4	8	-
$Na_2SiO_3·5H_2O$	-	-	-	9
pH	12.7	12.4	12.5	12.9
σ, *mS/cm*	13.9	23.5	30.2	22.7

3.2.3. Breath figures

This technique allows us to prepared porous surfaces with modulated size and disposition. Our evaluated polymers (PCL and PS) were dissolved in chloroform and exposed to a humid flow. Water starts to condense on the surface and then evaporates leaving a pore where it was. Figure 2.7 summarises the mechanism.

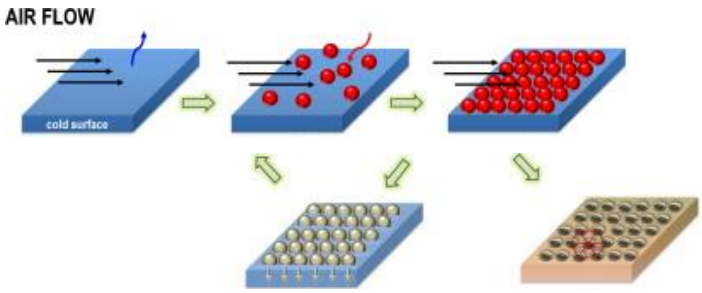

Figure 2.7. Model of pattern formation by the breath figures approach adapted from [126].

- Polycaprolactone was used at a final concentration of 20 mg/mL.
- Blends with variable amounts of high-molecular-weight polystyrene matrix (between 100 and 80 wt. %) and block copolymer (0 and 20 wt. %) were prepared, maintaining the polymer (30 mg/mL). The block copolymers employed were PS $_{42}$-*b*-PDMAEMA$_{16}$ and a quaternized PS$_{42}$-*b*-PDMAEMAQ$_{16}$.
- A high molecular weight polystyrene (80 wt. %) was blended with a 20 wt. % of the different block copolymers and dissolvent in chloroform to reach a polymer concentration of 30 mg/mL. The block copolymers employed were PS$_{42}$-*b*-PAA$_{47}$, PS$_{42}$-*b*-PAA$_{25}$ or PS$_{23}$-*b*-PAA$_{12}$ and the functionalized homologues PS$_{42}$-*b*-PAA$_{47}$/NISIN, PS$_{42}$-*b*-PAA$_{25}$/NISIN or PS$_{23}$-*b*-PAA$_{12}$/NISIN.

The final microporous films were prepared by casting using glass wafers as supports for the last two conditions and for the firsts it was prepared over the Mg-PEO samples. The experimental conditions were room temperature and a constant humidity in the closed chamber (controlled using saturated salt solutions). The most interesting samples were obtained using saturated vapour humidities (>99% relative humidity (RH)). As a control for Chapter 3 experiments, a micropatterned polystyrene (PS) surface was fabricated using chloroform as solvent. This solution was casted under a saturated vapour atmosphere.

3.2.4. Surface functionalization of PS with Nisin

The modification was realized by addition of a freshly solution in water of EDC 1 mg/mL and the same volume of solution in water N-Hydroxysuccinimide (NHS) 5 mg/mL. The surfaces were incubated for 5 min and a 1 mg/mL Nisin solution (same volume as EDC and NHS) in water was added under slight stirring. The reaction was allowed to proceed during one night at room temperature in order to complete the reaction and finally the porous surface was extensively washed with Millipore water to remove unreacted Nisin.

3.2.5. Protein loading of PEO-treated implants

50 µL of BSA solution, which contained 75 µg/µL × 50 µL = 3750 µg of BSA, was placed on the surface of each specimen, using three replicas for each coating and Ti CP control; the drop uniformly covered the surface without spilling over the specimen edges. After 6 h at room temperature the remaining excess of the drop (4±1 µL) was removed by a micropipette and the specimens were left to dry at room temperature for 24 h. Samples were placed individually in a 24 well plate (Corning Costar) and 600 µl of PBS 1X pH 7.4 (Gibco) were added to each well. To simulate *in vitro* conditions, the plates were maintained in a humidified incubator at 37ºC with 5% CO_2. Samples of 20 µL PBS were collected at different times (1h, 2h, 3h, 4h, 24h and 48h) and the volume was not replaced. BSA delivery was measured by Bradford Microassay (BioRad). 10 µL of the collected samples were placed in a 96 well plate (Corning Costar) and 60 µL of Bradford reagent and 230 µL of distilled water were added, mixed, and incubated at room temperature for 15 min. Colorimetric measurements of each well were done at 590 nm in a microplate-reader (Synergy HT, Brotek). Assays were performed on each sample type in triplicate and blank readouts were subtracted from the measured absorbance. All measurements are expressed as mean ± standard deviation (SD).

3.3. Surface characterization

3.3.1. Morphology, microstructure and composition

Scanning electron microscopy (SEM) provides a highly magnified image of the surface of the material, virtually identical to a "true" visualisation. Three principle types of images, corresponding to their physical basis, can be produced in the SEM: secondary electron images, determined by the topography, backscattered electron images, determined by the atomic mass of the elements and elemental X-ray maps that enable semi-quantitative analysis of the elemental composition. Energy-Dispersive X-Ray Spectroscopy (EDS) systems can detect X rays from all the elements in the periodic table with atomic number (Z) higher than 4 (beryllium).

JEOL JSM6400 scanning electron microscope (SEM) equipped with Oxford Link energy dispersive X-ray (EDS) microanalysis spectrometer was employed to examine the plan views and cross-sections of the coatings. Cross-sections were prepared by grinding through successive grades of silicon carbide paper, with final polishing to a 1 µm diamond finish (Ti) or colloidal silica solution mixed with hydrogen peroxide in 4:1 (Mg). For PS substrates a Philips XL30 microscope with an acceleration voltage of 25 kV was used.

Raman spectra and images were recorded in a Confocal Raman Microscopy integrated with atomic force microscopy (AFM) on a CRM-Alpha 300 RA microscope (WITec, Ulm, Germany)

equipped with Nd:YAG dye laser (maximum as described in [3, 7]. This laser-based technique of high resolution provides information about structure and chemical composition.

3.3.2. Crystalline structure

X-ray diffraction (XRD) is a non-destructive technique based on diffraction phenomena with an incident beam of X-rays on a crystalline solid sample. that provides information about the crystalline structure of the materials and therefore, allows the identification of the phase composition of the material.

XRD was used for phase identification using a Philips X'Pert diffractometer (CuKα = 0.154056 nm) at a scanning speed of 0.01º per second for a scan range of 2Θ from 5 to 90º and evaluated using PANalytical's X'PertHighScore software (ICDD PDF4+).

3.3.3. Topography

Initial surface analysis was performed using an Infinite Focus SL instrument (Alicona Gmbh, Graz, Austria). 2D and 3D simulations were obtained and surface data was analyzed with IF-Measure Suite software to extract topographic information (R_a and S_a). Topographic images and area roughness parameter S_a (arithmetic average of the absolute profile deviations) were obtained using an Nikon ADE Phase SHIST MicroXAM100 optical profilometer and analyzed with SPIP (3.3.9.0 version) software. Roughness parameters (R_a and R_z) were obtained using a Surtronic 25 roughness tester (Taylor Hobson) and Talyprofile software. The presented values are an average of 2 measurements performed over a length of 2.8 mm. A focus-variation optical 3D profilometer (InfiniteFocus SL, ALICONA) was used to evaluate R_a, S_a, S_v and S_{10z} roughness parameters. Cross sectional profiles and 3D images of the wrinkled surfaces (Chapter 4) were characterized by using a Zeta-20 True Color 3D Optical Profiler from Zeta Instruments.

3.3.4. Coating thickness

A Fischer ISOSCOPE FMP10 portable eddy current meter was used to measure the coatings thickness with an average of ten measurements, and later on validated with cross-sectional SEM images. Coating thicknesses (cited as an average of 10 measurements) were measured by the eddy current method, using a Fischer ISOSCOPE FMP10 portable instrument.

3.3.5. Porosity

The pore population density and pore size of the coatings have been estimated using ImageJ software. The porosity percentage, pore population density and pore size of the coatings have been estimated using ImageJ software, using minimum 3 images per coating. Image analysis of the coating surface was carried out using three SEM micrographs taken at arbitrarily locations.

3.3.6. Wettability

Wettability of the materials was measured using FTA1000 Drop Shape Analysis System (First Ten Angstroms) and the accompanying FT32 software. Sessile drops were recorded in a trigger mode, within 25 s from the moment the drop touched the surface. Contact angles were measured over 50 frames taken at 0.5 s intervals with an average of three measurements for each surface treatment; the variability of the measurements was within ± 10%.

3.3.7. Microhardness

Vickers microhardness was measured on coating cross-sections using AKASHI MVK-E3 and applying the following equation, using a load of 10 g or 25 g, as required, applied during 15 s, and citing an average of 10 measurements.

$$HV = \frac{2F\sin\frac{136^{o}}{2}}{d^{2}} \qquad HV = 1.854\frac{F}{d^{2}} \text{ approximately}$$

3.4. Swelling of hydrogels

In vitro swelling experiments were performed gravimetrically as a function of temperature (5–70 °C) in distilled water as described in [4].

The volume phase transition temperature, VPTT, was defined as the midpoint temperature at which the hydrogel showed an increase of 50 % in swelling from the baseline value, the baseline being above the transition temperature. VPTT is the valid parameter to describe LCST-type thermosensitivity in networks.

3.5. Ion release analysis

3.5.1. ICP-OES

Immersion tests were performed at (37±0.5) ºC using specimens with a total exposed area of 4 cm^2 placed in tightly sealed containers with 25 mL of 0.9% NaCl solution. Ca, P, Mg, Si, Ti, Zn, Al and V ions release, as required for specific materials, was analysed after 60, 28 or 5 days of immersion. Prior to measurement, the immersion solutions were acidified with 200 μL of nitric acid (65 wt. %) in order to dissolve the titanium hydroxide precipitated as a result of hydrolysis of Ti^{4+} in neutral pH. The samples were analysed by inductively coupled plasma optical emission spectroscopy (ICP-OES) using a Perkin-Elmer 3300 DV instrument, operating at RF power of 1.3 kW, with a plasma flow of 1 L min^{-1}, sample flow rate of 0.8 mL min^{-1} and argon (plasma maintaining carrier gas) flow of 0.8 L min^{-1}. The blank solution (0.9 % NaCl) was included into the batch measurements as a reference. The results are cited as an average of three replica measurements.

3.5.2. Fluoride ion selective electrode

F^- release was measured daily during the first 2 weeks and after 30 days of immersion of in 45 mL of 0.9% NaCl solution (total exposed area of 4 cm^2) for Ti6Al4V samples. For Mg0.8Ca samples in 20 mL of 0.9% NaCl solution (total exposed area of 3.7 cm^2) measurements at 24 and 120 h were performed. Two specimens for each type of material were used for reproducibility. A fluoride ion-selective electrode (ISE, Crison) consisting of a lanthanum fluoride monocrystal membrane doped with europium was used. The membrane potential difference generated in the selective electrode, based on the concentration of F^- in the solution, was measured using a pH meter (GLP22, Crison). The instrument calibration was performed using F^- standards (50 ppb, 100 ppb, 500 ppb, 1 ppm and 2.5 ppm) prepared from a fluoride standard of 100 mg/mL. In order to unify the ionic strength and pH of the solutions for correct determination of fluoride concentration, 3 mL of F^- containing aliquots were mixed with 6 mL of a total ionic strength adjustment buffer (TISAB) (57 mL/L acetic acid, 58 g/L sodium chloride, 4 g/L 1,2diaminocyclohexane-N,N,N',N'-tetraacetic acid in distilled water with pH 5.0-5.5 adjusted with 6 M sodium hydroxide).

3.6. pH measurements

The pH measurements of the cell culture were carried out using a Crison 5028 microelectrode and a Crison pH Basic 20 instrument.

3.7. Biological evaluation

In order to evaluate the obtained materials direct seeding studies were performed with all of them. All the materials were previously sterilized and all the experimental conditions for each Section are compiled in Table 2.4.

Table 2.4. Direct assays conditions for all the evaluated biomaterials.

	Section 1.1.1	Section 1.1.2	Section 1.2.1	Section 1.2.2
Material	**Ti grade I**	**Ti grade I**	**Zr**	**Ti6Al4V**
Cell line	MC3T3 RAW 264.7	MC3T3 RAW 264.7	C166-GFP C2C12-GFP MC3T3 RAW 264.7	MC3T3
Cell density (cells/cm^2)	3×10^4 2×10^4	2×10^4 1.5×10^4	1×10^4 1×10^4 1×10^4 2×10^4	2×10^4
Culture time (h)	168/336 120	168 120	48 96 120 120	168
Sterilization	Autoclave, UV	Autoclave, UV	Autoclave, UV	Autoclave, UV

	Section 2.1	Section 2.2	Section 3.1	Section 4.1	Section 4.2
Material	**Mg0.8Ca**	**Mg0.8Ca+ PCL**	**PS**	**VCL**	**VP**
Cell line	C166-GFP C2C12-GFP MC3T3 RAW 264.7	C2C12-GFP	C166-GFP	C166-GFP MC3T3 RAW 264.7	C166-GFP MC3T3 RAW 264.7
Cell density (cells/cm^2)	3×10^4 3×10^4 3×10^4 2×10^4	3×10^4	1.5×10^4	1.5×10^4 1.5×10^4 1.5×10^4	1.5×10^4 3×10^4 2×10^4
Culture time (h)	96	96	96	96 72	72 96
Sterilization	Ethanol, UV	Ethanol, UV	Ethanol, UV	Ethanol, UV	Ethanol, UV

For studies presented in Chapter 2 complete medium was changed every day to avoid alkalization in all the experiments.

All the cells evaluated growing over the materials by SEM were fixed and dehydrated with several ethanol gradients of increased concentrations and dried in a chamber with silica gel. For the evaluation of the biodegradable Mg alloy, extracts were obtained as follows: Mg0.8Ca alloy and PEO coated samples were maintained in complete DMEM (FBS and P/S) during 5 days with an immersion ratio [180, 181] of 1.25 mL per cm^2 and simulated *in vitro* conditions (37ºC, 95%

relative humidity and 5% CO_2). The extract media obtained in this manner were used for the following *in vitro* studies. As described in Table 2.5 different ratios (1:2 and 1:10) were used for cytocompatibility studies with C2C12-GFP and C166-GFP. For differentiation studies a 1:4 extraction medium; αMEM or DMEM ratio was selected based on previous bibliography [182] with these two differentiation murine models.

For extract studies MC3T3 cells cultured for 7 days in 1:4 extract, changed to differentiation medium and left incubating for another 7 days. Differentiation medium consisted in completed maintenance medium with 50 µg/mL ascorbic acid, 10 nM dexamethasone and 10 mM β-glycerolphosphate. Complete differentiation medium was changed every 2 or 3 days. RAW 264.7 cells supplemented with 50 ng/mL of recombinant RANKL (Receptor Activator of NFκb Ligand, PeproTech) and at day 3 extract medium with RANKL was changed with completed differentiation fresh medium (complete DMEM with RANKL).

In co-culture studies, MC3T3 cells were plated and allow to grow for 24 hours in complete α-MEM medium. After this time, RAW 264.7 cells were seeded over the preosteoblasts in 1:4 extract medium. RANKL was added when the macrophages where plated and refreshed when the extract medium was changed at day 3. The cells were co-cultured for 5 days (D1 starting after RAW 264.7 seeding).

Table 2.5. Extracts studies experimental conditions from Chapter 2 section 2.1.

Cell line	Cell density (cells/cm^2)	Culture time (h)	Extract dilution
C166-GFP	1.5×10^4	120	1:2/1:10
C2C12-GFP	1.5×10^4	120	1:2/1:10
MC3T3	1.5×10^4	168/336	1:4
RAW 264.7	1.5×10^4	120	1:4
Coculture: MC3T3/RAW 264.7	1×10^4/1.5×10^4	120	1:4

Hydrogels preparation for cell culture

All hydrogels (VCL and VP-based) were sterilized with a 70 % ethanol solution rinsing six times during 10 minutes each. Then, they were washed six times with PBS, exposed to UV radiation for 30 minutes for each side of the hydrogel and washed twice with DMEM or α-MEM.

For thermosentitive hydrogels the temperature of culture conditions (37 °C) was simulated using a hot plate with a constant temperature for the material cutting process obtaining 2 cm^2 samples fitting the 24 well plates (Corning Costar). After cutting them, samples were left overnight incubated at 37 °C and 5 % of CO_2 with DMEM 10 % Fetal Bovine Serum (FBS) and 1 % of antibiotics (100 U/mL penicillin and 100 µg/mL streptomycin sulfate).

3.7.1. Cytoskeleton and nuclei staining

In order to visualize the cultured cells over the materials a cytoskeleton and nuclei staining is performed and we can obtain a fluorescence image of the cells. This technique requires the fixation of the cells to obtain a static image of the display of culture over the substrate.
Cells on the material were fixed with 4% paraformaldehyde (PFA) solution for 15 min. After PFA was removed, cells were rinsed with PBS twice and permeabilized with 0.1% (v/v) Triton X-100, washed with PBS and stained with Texas Red®-X phalloidin (Life Technologies), a high-affinity F-actin probe conjugated to red fluorochrome, for 20 min at room temperature and in darkness, followed by Hoechst staining (Invitrogen, Molecular Probes ®) for nuclei visualization. Finally, fluorescent-labelled cells were observed using an inverted fluorescence microscope (Olympus IX51) with a TRICT filter (λex/λem=550/600 nm) for actin and DAPI filter for Hoechst (λex/λem = 380/455 nm) using CellD analysis software (Olympus).

3.7.2. Metabolic activity: Alamar Blue

Metabolic activity over surfaces was measured using Alamar Blue assay (Biosource); a non-toxic technique that quantitatively measures the reducing power of the cell culture (mitochondrial activity), providing an estimation of cytocompatiblity and viability. It is based on resazurin dye an oxidation-reduction indicator that changes its colour when enters the cell membrane. Each well received a 10% of the culture volume of Alamar Blue dye, and samples were incubated for 90 min. The fluorescence (λex/λem 535/590 nm) of each well was measured using a plate-reader (Synergy HT). Surfaces were analysed on each sample type in triplicate.

3.7.3. Alkaline phosphatase assay

Early osteogenic ability was evaluated by measuring the activity of ALP (alkaline phosphatase), which is a biochemical marker for osteoblastic activity. ALP is an osteoblast marker localized in the membrane and expressed highly in the secretory face. ALP is one of the initial functional genes expressed when the bone matrix calcification starts.
The MC3T3-E1 cells were cultured changing the differentiation medium every 2 or 3 days. After the removal of the culture medium, plate wells were washed with PBS. Afterwards, 250 µL/well of lysis buffer (50 mM Tris pH 6.8, 0.1% Triton X-100, 2 mM $MgCl_2$) was added. Three temperature cycles of 30 min were performed from -80°C to 37°C. After centrifugation at 13,000 rpm for 5 min, 25 µL of upper phase was assayed for ALP activity in 96-well plates, using p-nitrophenyl phosphate (Sigma-Aldrich) in 2-amino-2-methyl-1-propanol buffer as a substrate in a total volume of 150 µL. After 60 min at 37°C, the reaction was stopped with 50 µL of 1 M NaOH and the absorbance was measured at 405 nm on Microplate Reader (Synergy HT). The protein content was determined using the Bradford Assay (Bio Rad), employing bovine serum

albumin as a standard. Each cited value was obtained by averaging the results of three samples. The assay was performed in triplicate for each material and the absorbance results were normalized to a p-nitrophenol standard curve and then relativized to total protein content (Bradford assay).

3.7.4. Collagen secretion (Sirius Red Staining)

Collagen type I is considered a differentiation marker during osteoblastogenesis. It is required for posterior mineralization of the organic matrix.
Collagen I secretion of the MC3T3-E1 cells was evaluated by Sirius Red staining. Sirius red is an acidic hydrophilic staining that colours collagen fibbers in red, the sulfonic acid groups bind with the basic/cationic groups of collagen fibbers. After culturing cells were fixed with 4% paraformaldehyde (PFA) solution for 15 min, washed with PBS twice and incubated with Picro Sirius Red Stain Kit (abcam) for 30 min. Samples were washed twice with acetic acid and pictures were taken at 50× with an optical microscope (Olympus BX51). Finally, Sirius Red stained samples were dissolved in 0.2 M NaOH/methanol (1:1) and the absorbance was measured at a wavelength of 540 nm on Microplate Reader (Synergy HT).

3.7.5. Mineralization (Alizarin Red)

Calcium forms an Alizarin Red S-calcium complex in a chelation process, and the end product is a bright red stain. Alizarin red is a commonly used stain to identify calcium containing osteocyte in differentiated culture. microcrystalline or noncrystalline calcium phosphate salts.

Calcium deposits in the cells were confirmed by staining with Alizarin Red-S (AR-S, Sigma). After culture time point, cells were fixed with 4% paraformaldehyde (PFA) solution for 15 min, washed twice with deionized water and incubated with 40 mM AR-S at pH 4.1 for 30 min at room temperature. Then, after washing 3 times with deionized water to remove free Ca ions, the stained cultures were photographed with an inverted optical microscope (Olympus IX51).

3.7.6. Tartrate-resistant acid phosphatase

One of the most important osteoclastic marker is tartrate resistant acid phosphatase (TRAP), an enzyme that it is expressed during osteoclastogenesis and it is capable of bone resorption. This enzyme was studied by three methodologies:

1. TRAP staining was performed using a commercial kit by the manufacture instructions (Sigma-Aldrich). Cells were incubated in a solution of Naphthol AS-BI phosphoric acid and Fast Garnet GBC.

2. To measure TRAP activity on Ti, the cells were harvested and incubated in 250 µL 0.1% Triton X-100 for 40 min. 80 µL of cell lysate was incubated in 80 µL of phosphatase substrate solution (20 mM p-nitrophenyl phosphate and 80 mM tartaric acid in 0.09 M citrate buffer, Sigma-Aldrich, St. Louis, MO) at RT for 40 min. After incubation the reaction was stopped with 40 µL of 1 M NaOH. Absorbance at 405 nm was measured using a microplate reader (Synergy HT, Brotek). This assay was performed on each sample type in triplicate.
3. TRAP was also studied using immunocytochemistry. For TRAP staining rabbit anti-TRAP (1/200; Santa Cruz Biotechnology) and anti-rabbit (1/200; Millipore) antibodies were used. The staining protocol was performed as standard procedures (PFA 4% fixation; Blocking Solution: 5% Normal Donkey Serum; 0.3% Triton X-100 in 1x PBS). The visualization of the fluorescent-labelled cells was performed in an inverted fluorescence microscope (Olympus IX51) with a TRICT filter (λex/λem=547/572 nm) using CellD analysis software (Olympus).

3.7.7. Biofilm formation

Staphylococcus aureus were grown in a TSB medium for 18 hours at 37ºC and agitation (120 g). Bacterial culture was centrifuged at 3,000 rpm for 5 min and resuspended in MilliQ water. Absorbance was measured up to O.D=0.16 (640 nm) corresponding to 10^8 cfu/mL, using MilliQ water as reference pattern. Concentration was adjusted to 1×10^5 cfu/mL adding 50 µL of the 10^8 cfu/mL suspension to 50 mL of TSB medium. Sterilized samples were incubated with 1 mL of the bacteria suspension in 24-well plate for 24 hours to allow biofilm formation. Materials were washed twice using PBS to avoid unspecific bacterial adhesion and remove planktonic bacteria and then fixated with PFA 4% for 15 minutes. In order to evaluate the biofilm formation and viability, a LIVE/DEAD™ BacLight™ (ThermoFisher Scientific) was used. Staining was performed for 15 min in dark conditions at room temperature, following by rinsing twice with PBS. Samples were photographed using a fluorescence microscope (Olympus IX51). For the image analysis three areas of each material were taken randomly at 200× magnification and the micrographs were analysed with ImageJ software. For live/dead merging, pictures were taken at 100× magnification.

3.7.8. In vivo surgical procedure

A domestic pig (age 12 months) was used for the evaluation of PEO-coated Ti. The animal was premedicated with intramuscular injections of 10 mg/kg ketamine and 0.5 mg/kg midazolam. After premedication, the animal was taken to the operating room, and general anaesthesia was obtained by intravenous injection of 3 mg/kg propofol and by 1-2 sprays of xylocaine 10%. The pig was placed in a supine position and then prepared and draped under aseptic conditions. Anaesthesia during the procedure was inhalatory (isoflurane 1.3-2% and sevoflurane 2.3%) and

continue infusion of FLK solution (NaCl 0.9% and 0.15 mg/mL Fentanile+ 5% lidocaine 10 mL + 50 mg/mL ketamine 2 mL) by bolus of 3 mL/kg + 3 mL/kg/hour. The maxilla was exposed via a linear skin incision, the periosteum was incised, and the periosteal flaps were raised. Dental implants were inserted into the inferior maxilla of the pigs mandible. The implant sites were prepared using a standard gentle surgical technique with sharp drills, as recommended by the manufacturer. All drilling procedures were carried out under profuse sterile saline irrigation. Dental implants were placed through the inferior maxilla reaching the medullar channel. After implantation, closure screws were used to leave the implants submerged, and the wounds were closed in layers with resorbable sutures (Vicryl, Brussels, Belgium). This animal study was approved by the Ethical Review Committee of *Instituto de Investigación Sanitaria del Hospital Clínico San Carlos* (Complutense University of Madrid).

Postoperative care. The animal received analgesic (meloxicam 0.2 mg/kg intravenous and buprenorphine 0.2 mg/kg subcutaneous every 24 hours) and antibiotics (amoxicillin clavulanic acid 17 mg/kg) intramuscularly before surgery and in the postoperative days during 7 days every 24 hours.

3.7.9. Histological analysis

The animal was euthanized after 8 weeks with 1 g/10 kg sodium thiopental by intravenous injection. The maxilla sections with the implants inside were harvested, and the soft tissues were stripped off. The implant sections were then carefully sectioned so each specimen consisted of an implant with the surrounding 5 mm of bone. The specimens were fixed in 10% buffered formalin, dehydrated in increasing concentrations of ethanol, from 70% to 99.5% in 15 days, and embedded in methylmethacrylate (Technovit 7200 VLC, Haerus Kulzer GmbH, Wehrheiam, Germany). Then, samples were treated using an electric diamond saw and grinding system. All specimens were cut parallel to the axis of the implant.

A total of 2 slices for implant type were then stained with Levai Laczko. Digital images of the histologic sections were taken using an optic microscope (20×; Olympus BX51), covering all implant surfaces. These images have been used for bone-to-implant contact (BIC) evaluation, and analysed using Adobe Photoshop CS6. Region of interest (ROI) included from the second to the fifth spire of the screw thread, and was measured using a grid of 300 μm square for both sides of each implant.

3.7.10. NaF cytotoxicity

C166-GFP, C2C12-GFP and MC3T3 cell lines were incubated for 24 hours with known concentrations of NaF. Cells were seeded with a density of 1.5×10^4 cells/cm^2 at a 24 well plate. Different concentrations of NaF (mM): 0.5, 1, 1.75, 2.5, 5 and 7.5 were evaluated.
Metabolic activity was measured in NaF treated at 24 h. Alamar Blue assay was performed as previously described, with this technique an estimation of cytocompatiblity and viability can be obtained. Each condition was analysed in triplicate.

3.7.11. Methodology for thermal cell sheet detachment

Cell cultured hydrogels were turned upside down and located in new TCP wells. After that, cold medium was added to each well in order to reach T≤27 °C. A temperature probe (SC1, Biocote, UK) was used to monitor this process and new TCP wells were maintained in a cold environment with a soft orbital agitation during this process. After 45 min, hydrogels were removed and TCP wells were reincubated at 37 °C with CO_2.

3.7.12. Statistical analysis

Statistical analysis of TRAPq, % of BIC values, total bacteria surface coverage and dead bacteria over surfaces (%) (mean ± SD) and extracts cytocompatibility was performed using an unpaired Student's t-test with Graph Pad Prism 4 software. Significant differences stand for: * ($p\leq0.05$), ** ($p\leq0.01$), *** ($p\leq0.001$).

4. Results and discussion

Chapter 1: Evaluation of electrochemical treatments of metals for permanent implants applications

1.1. Dental applications

1.1.1. Biological evaluation of surface-modified titanium

As considered in the literature review (Section 1.3), PEO treatment is a promising technique that has been already applied in commercial implants for dentistry. Many studies are being performed in order to upgrade the functionality of PEO coatings formed on Ti CP. Still, main topics such as the interaction between osteoblasts and osteoclasts or even the role of osteoclasts on the longevity of the implants is underestimated. In order to promote an increased osseointegration and implantation success rate, the surface modification of the implant must present proper characteristics at cellular and molecular levels, taking into account that topography and surface chemistry of a biomaterial regulate cell processes, including bone homeostasis. An osteoblastic (MC3T3 murine cell line) and osteoclastic (RAW 264.7 murine cell line) cell model are going to be evaluated in terms of attachment, differentiation and activity over PEO-modified Ti surfaces with overstoichiometric Ca/P ratio of ~2.0 and ~4.0. Additionally, a model protein, bovine serum albumin (BSA), is going to be studied in order to map out the loading/unloading capacity of PEO coated Ti for potential applications in drug-loaded dental implants. BSA is a common protein present in animal serum (60% of its composition) and is often used as a model protein to study loading efficiency of biomimetic Ca-P coatings on titanium substrates. In addition, BSA can also serve as a carrier to deliver drugs, antibiotics and growth factors [183-185]. Finally, a preliminary surgical approach has been studied in a pig model in order to test the biocompatibility and osseointegration of these PEO-modified surfaces.

Coatings characterization

Two PEO coatings were formed over Ti CP Grade I and Grade IV for 90 s (PEO-90s) or 600 s (PEO-600s) of treatment time with a Ca and P based suspension electrolyte. The morphology and composition of PEO coatings was reproducible on both types of Ti. Figure 3.1 A-B reveals the typical porous surface morphology of the coatings. PEO-90s presents a more homogenous surface with a Surface roughness (S_a) and pore population density are 1.05 μm and 36×10^3 pores/mm^2 (Table 3.1). On the other hand, PEO-600s presented higher values with 1.88 μm and 10×10^3 pores/mm^2, respectively. PEO-90s coating was ~5 μm thick and the thickness significantly increased up to ~15 μm when the PEO time was increased to 600 s (Table 3.1). Both coatings are crystalline as depicted from XRD analysis and present a mixture of anatase and rutile (Figure 3.1

C). From the anatase-to-rutile ratio, determined semiquantitatively, it can be observed that the fraction of rutile increases from 23% to 85% with treatment time.

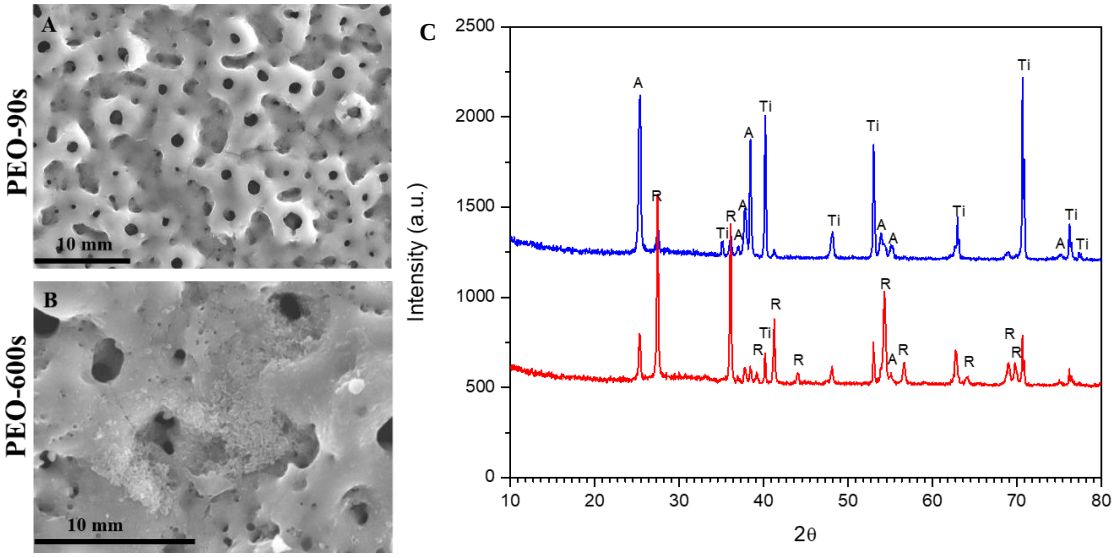

Figure 3.1. Secondary electron micrographs of PEO-coated Ti CP (A-B)**.** X-ray diffraction patterns of PEO-modified Ti CP (C).

Table 3.1. Coatings characterization.

Parameter	Ti CP	PEO-90s	PEO-600s
Thickness, μm		5	15
Roughness, S_a, nm	420 ±50	1050 ±50	1880 ±30
Pore popul. density, pores/mm^2		36100	10000

The surface composition (Table 3.2) analysis obtained by EDS confirms further increase in the Ca/P ratio from 2.0 to 4.0 in the thin superficial layer of the coatings.

Table 3.2. Elemental composition of the coatings, at.%.

Coating	O	P	Ca	Ti	Ca/P
PEO-90s	59.9	2.3	4.6	33.2	2.0
PEO-600s	66.1	1.5	6.0	26.4	4.0

The cross sections of the PEO coatings formed on Noricum dental implants are presented in Figure 3.2. The examination of the backscattered scanning electron micrographs at higher magnification (Figure 3.2 A, C, D, F) revealed that both coatings comprised an outer porous layer and sub-micrometric inner dense barrier layer adjacent to the substrate.

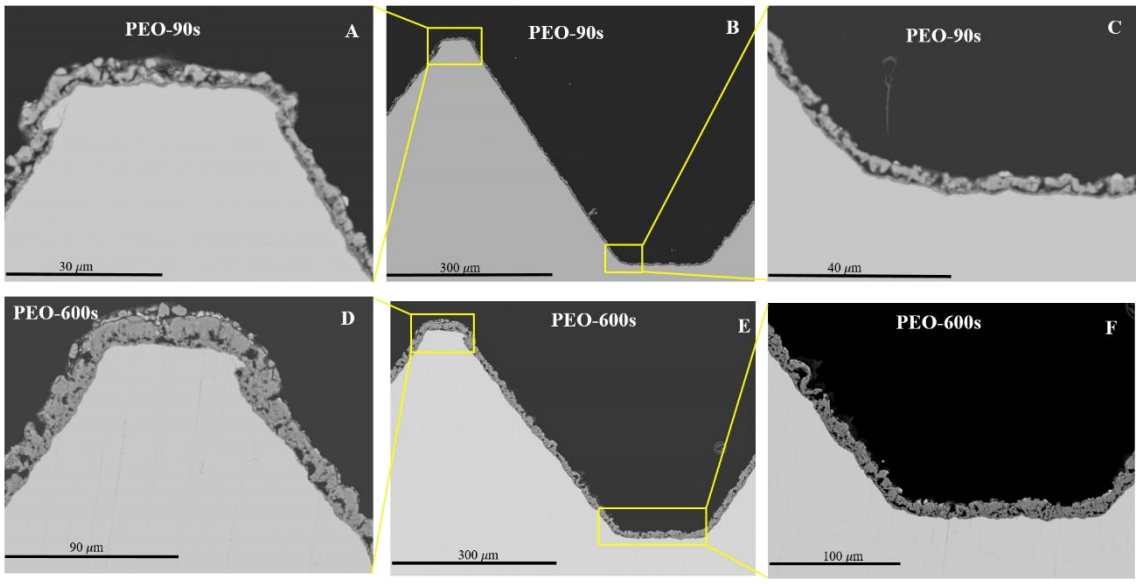

Figure 3.2. Cross-sectional backscattered electron micrographs of PEO-coated implant threads at different magnifications: A-C) PEO-90s; D-F) PEO-600s.

In Figure 3.3 the final macroscopic appearance of the PEO-treated implant (B) and the original Noricum dental implant is presented (A). The ceramic coating was formed all over the 3D structure.

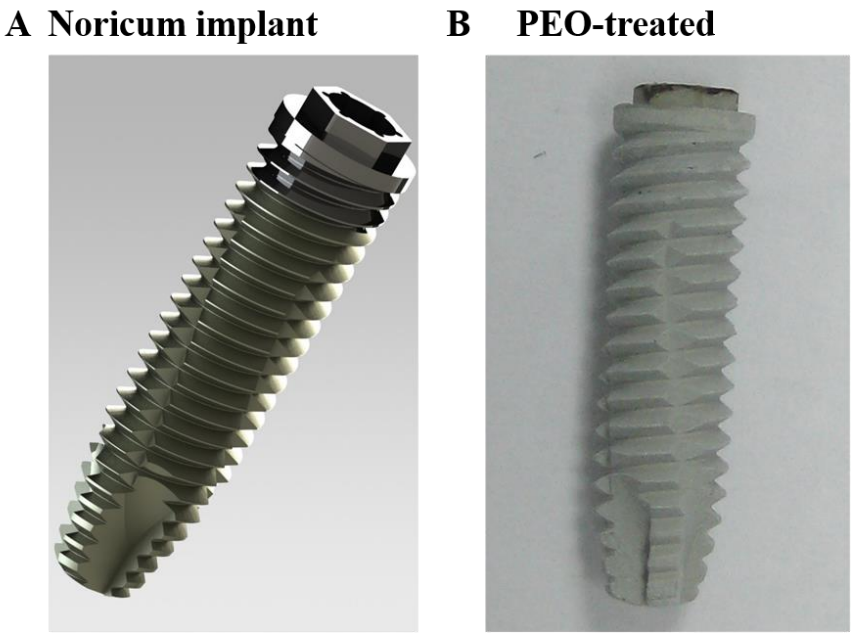

Figure 3.3. Noricum implant as received (A) and PEO-treated implant (B).

Osteoblast differentiation over the materials surface

The preosteoblastic MC3T3 cells were cultured at a cell density of 3×10^4 cells/cm^2 with differentiation medium during 7 days over the materials to evaluate osteoblastic proliferation and early bone matrix formation on culture prepared Ti plates. Actin and Hoechst staining's were performed on cells growing over Ti CP, PEO-90s and PEO-600s to evaluate the growth and monolayer distribution in these conditions (Figure 3.4 A). A dense cell monolayer was formed in all the conditions with a homogenous nuclei disposal, showing no significant differences between different samples. In order to evaluate early osteoblastic differentiation and bone matrix formation an ALP (alkaline phosphatase) activity assay was performed after 7 days of culture. The ALP activity levels similar were to Ti control for both PEO coatings (PEO-90s and PEO-600s), with slightly higher values found in PEO-90s surface.

SEM micrographs (Figure 3.4 A) present MC3T3-E1 cell culture state after maintenance in osteogenic media over the titanium surfaces for 14 days. The osteoblastic cells presented a finest colonization of both PEO porous surfaces (90 s and 600 s). Many of the pores were covered with the cell monolayer and it appears to be growing on different levels due to the appreciable coating roughness (Figure 3.1 A, B). This may have affected the actin/Hoechst staining visualization (Figure 3.4 A) where some areas are empty in the image corresponding to deeper levels of material surface. PEO coatings could support osteoblastic adhesion and proliferation on all the topographic features of the surface which is in concordance with other studies [83, 186].

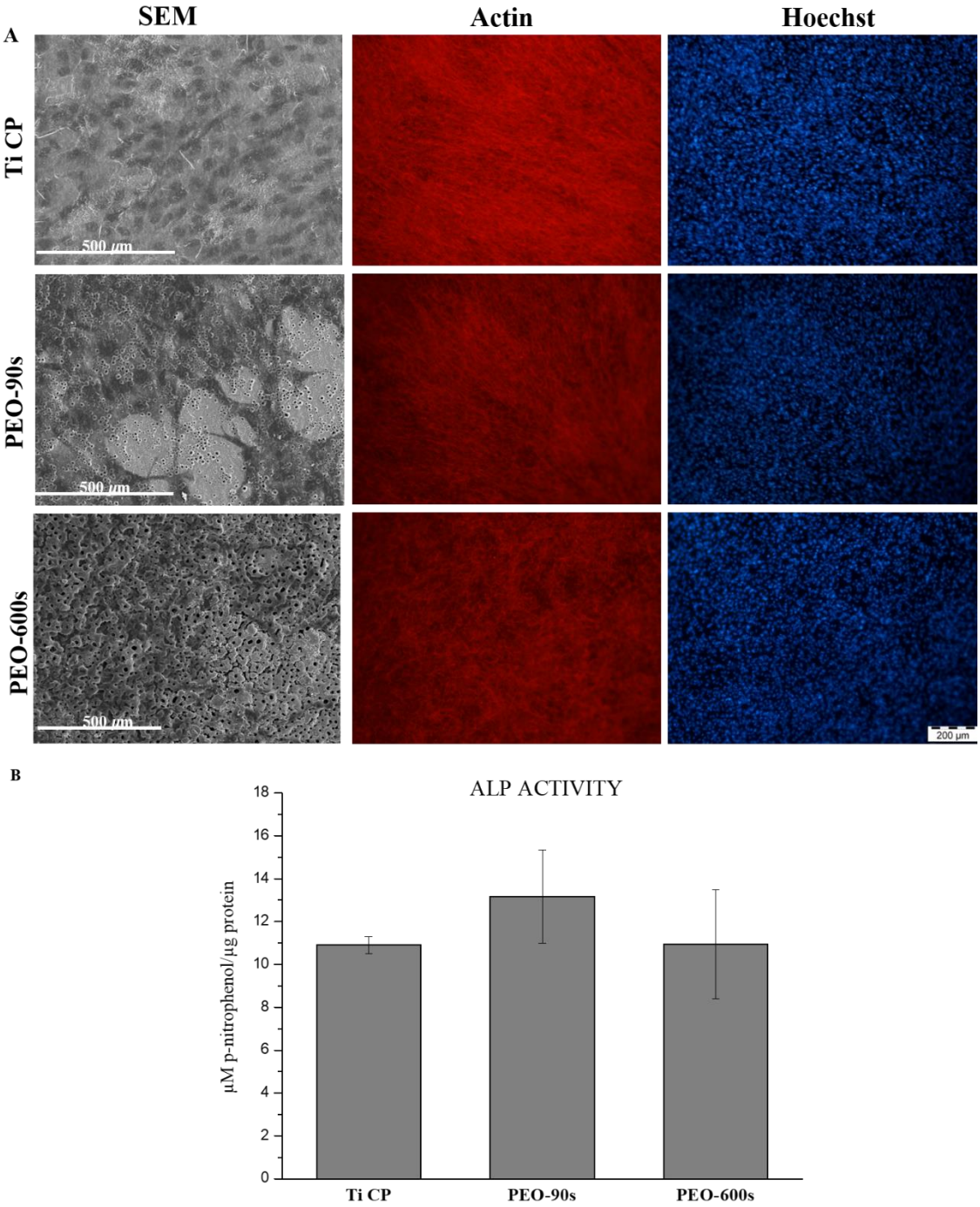

Figure 3.4. A. Secondary electron micrographs images of MC3T3-E1 cells cultured on different samples (Ti CP, PEO-90s and PEO-600s) after 14 days of culture and fluorescence images for actin (red) stained with Red Texas-phalloidin and the nucleus (blue) with Hoechst after 7 days of growth. B. ALP activity of MC3T3-E1 cells on different Ti surfaces at 7 days of culture. Data were normalized with total protein content.

Osteoclast differentiation over the materials surface

The murine macrophage cell line RAW 264.7 was used as a model to induce *in vitro* osteoclastogenesis over coated and non-coated titanium surfaces. To analyse undifferentiated

precursors proliferation, macrophages were cultured over the control and the PEO modifications for 5 days without adding RANKL at a cell density of 2×10^4. Cells grew all over the materials, with more extended morphology (SEM images) over Ti CP because of its low roughness (S_a=420±50 nm). No macrophagic polarization to M1 phenotype (pro-inflammatory phenotype) was detected after 5 days of culture, indicating no immune system response to the materials (Figure 3.5).

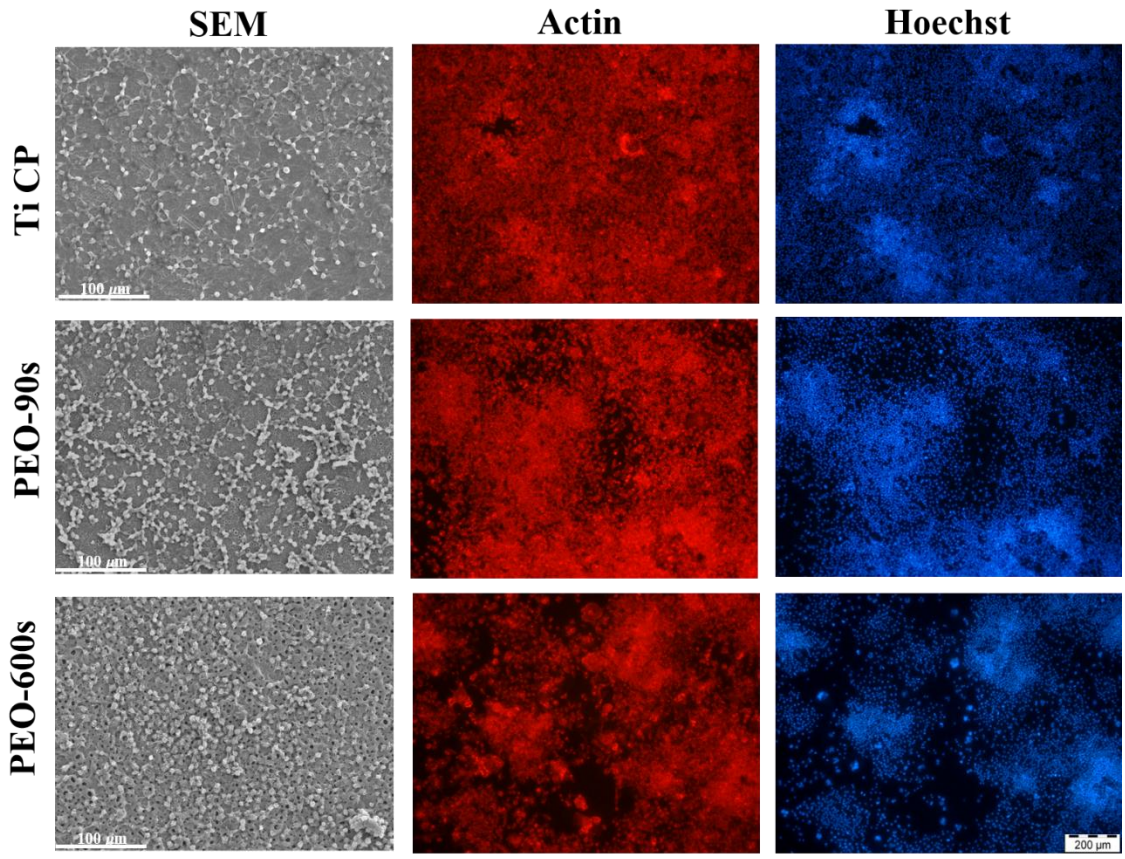

Figure 3.5. Secondary electron micrographs (left) of RAW 264.7 cells growing over the materials after 5 days of culture. At the centre and the right, fluorescence images of RAW 264.7 cells cultured on the different samples after 5 days of incubation are shown. Actin (red) was stained with Red Texas-phalloidin and the nucleus (blue) was stained with Hoechst.

The formation of osteoclast under these conditions were evaluated using RAW 264.7 cell line cultured with recombinant RANKL. In order to evaluate the osteoclastogenesis process after 5 days of culture (when differentiation is completed in this cell model) an immunocytochemistry of TRAP on each sample was performed. This acid phosphatase constitutes one of the most important osteoclastic markers. Therefore, in Figure 3.6 multinucleated osteoclasts were detected over all the surfaces with different number of nuclei corresponding to blue staining (Hoechst) in merged pictures (Figure 3.6 C). It is worth reminding that macrophagic precursors need to previously fuse with each other to form a preosteoclast. Results on Ti CP were similar to the widely describe control plastic (TCP) in presence of RANKL, as large osteoclasts with several

microns of cytoskeleton were formed. As for PEO-based samples osteoclasts were more rounded and almost the whole cell was positive for TRAP staining, showing that PEO treated surfaces allowed migration and fusion of osteoclastic precursors. On the PEO-600s a higher number of osteoclasts per area (Figure 3.6 A) were detected. Furthermore, TRAP quantification results disclosed that Ti CP and PEO-600s presented similar activity (Figure 3.6 B), while in PEO-90s osteoclastic activity was diminished with statistically significant values ($p \leq 0.05$) compared to Ti CP.

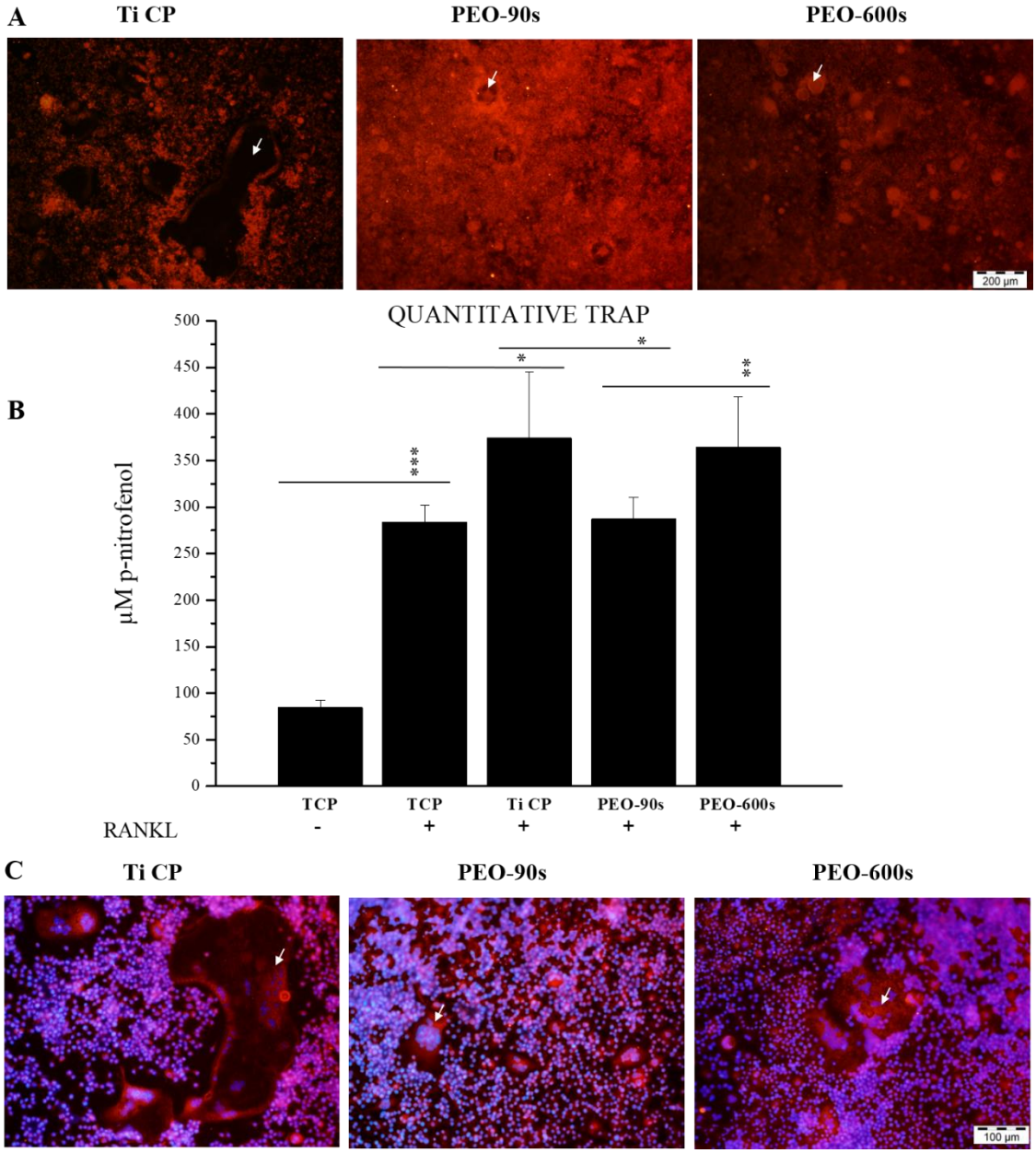

Figure 3.6. A. Tartrate-resistant acid phosphatase (TRAP) immunocytochemistry of RAW 264.7 cells after 5 days of differentiation in presence of RANKL. B. TRAP activity test in control samples (TCP and Ti CP) and in the modified Ti surface (PEO-90s and PEO-600s) at day 5. C. Merged images of TRAP immunocytochemistry (red) and Hoechst staining (blue) showed multinucleated osteoclasts in all the samples. Arrowhead: osteoclast. Significant differences stand for: * ($p \leq 0.05$), ** ($p \leq 0.01$), *** ($p \leq 0.001$).

Drug loading model

Albumin was loaded into the PEO coatings and Ti CP as a protein model in order to evaluated their potential as drug carriers. Representative SEM plan view images of PEO-coated titanium and Ti CP control with and without BSA are shown in Figure 3.7. The micrographs reveal the presence of a thick albumin film, formed on the surface of all the loaded materials.

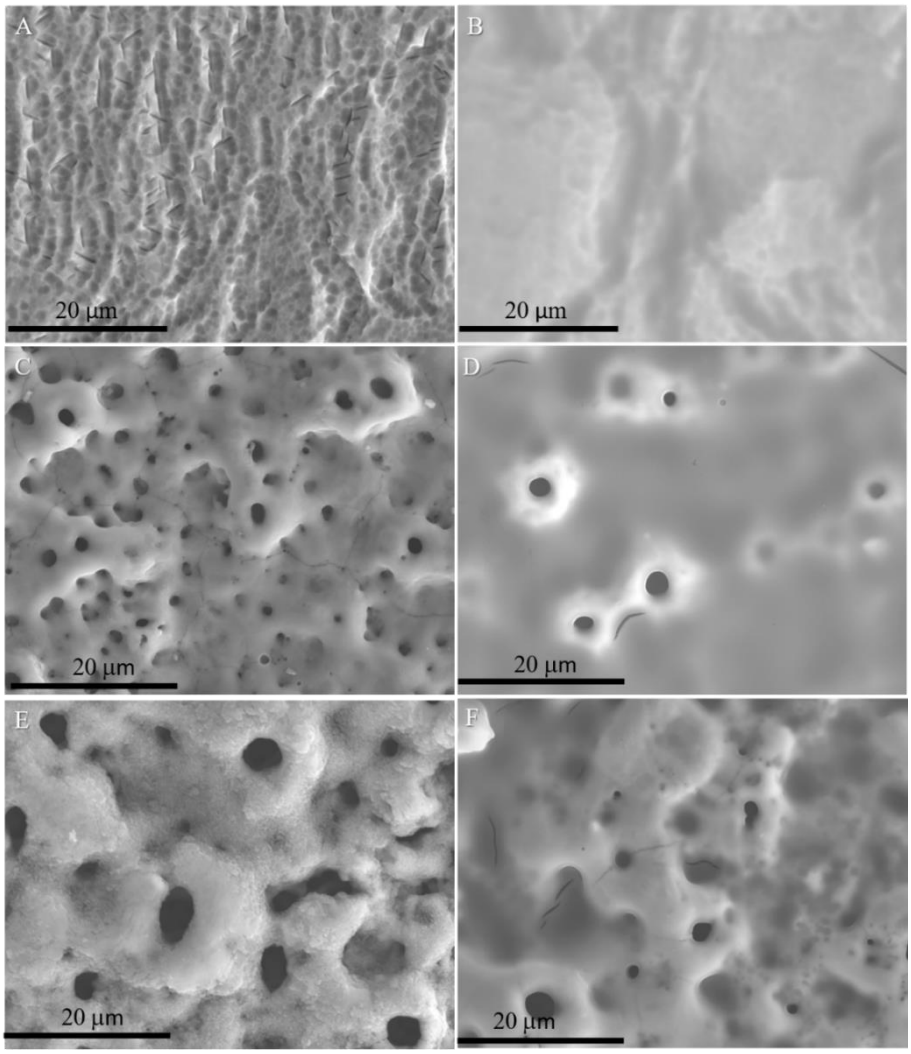

Figure 3.7. Plan view secondary electron micrographs of the substrate and coatings as received (left column) and impregnated with albumin (right column). (A, B) Ti Grade I; (C,D) PEO-90s; (E,F) PEO-600s.

BSA film is apparently thicker in the substrate and PEO-90s the surface, since the etching marks of the substrate (as a result of acid attack) and many of the pores (Figure 3.7 D) are completely covered. This observation correlates with ~40-50% reduction of the area roughness, S_a (Table 3.3). An increased roughness value is observed with PEO-600s, although BSA is uniformly covering the surface (Figure 3.7 F); BSA in this case apparently adapts to nanostructured

topography of PEO-600s surface possibly preventing the easy flow of the BSA into the valleys of the coating.

Table 3.3. Surface characteristics of the PEO coatings.

Parameter	Ti CP		PEO-90s		PEO-600s	
	A.r.*	+BSA	A.r.	+BSA	A.r.	+BSA
Roughness, S_a, nm	420 ±50	190 ±30	1050 ±50	640 ±140	1880 ±30	1760 ±40
Pore size, μm			0.4 - 2.0		0.4 - 6.2	
Surface porosity, %			9.7		7.2	
Transverse porosity, %			15.3		7.8	
Volume porosity, %			9.7-15.3		7.2-7.8	
Pore volume, nL/cm^2			49-77		108-117	

*A.r. - as received.

The coating cross-sections and corresponding black and white contrast footprints of the pores are presented in Figure 3.8. The quantification results of the image analysis in form of pore size, pore population density and surface and transverse porosity are summarized in Table 3.3. Morphological differences give rise to different volume porosity (considering surface and transverse porosity values). For instance, the thinner coating exhibits small pore size and relatively high transverse and surface porosity compared with the thicker coating. PEO-90s exhibit penetrating pore character and the presence of bottlenecked inner voids (Figure 3.8 A).

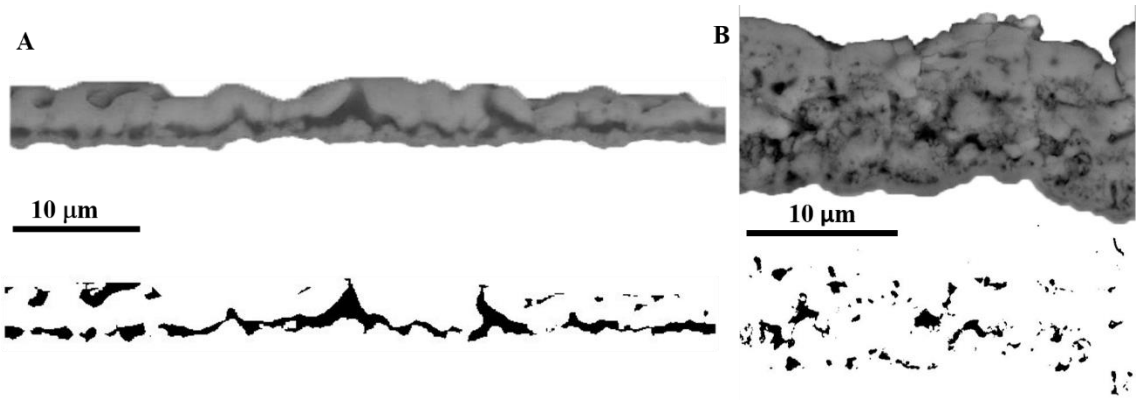

Figure 3.8. Backscattered electron micrograph of the coatings PEO-90s (a) and PEO-600s (b) with respective black-and-white contrast porosity footprints.

Wettability of the surface of a dental implant can determine protein absorption and its final implantation success. Figure 3.9 shows that both PEO coatings were more hydrophilic than Ti CP (~80º, Figure 3.9 C), with contact angles lying in the range of ~37º to ~45º (Figure 3.9 A-B). Contact angle value reduces as PEO treatment increases. Moreover, the wettability values before and after impregnation with BSA are presented in Figure 3.9 C; all BSA loaded surfaces revealed similarly hydrophilic properties, with the contact angles being in the range from ~37º to 49º. The contact angle for BSA-loaded Ti CP control dropped to half (80º to 40º). Contrarily, PEO-90s

slightly increased the contact angle value related to the filling by BSA of the coating pores and inner voids previously described.

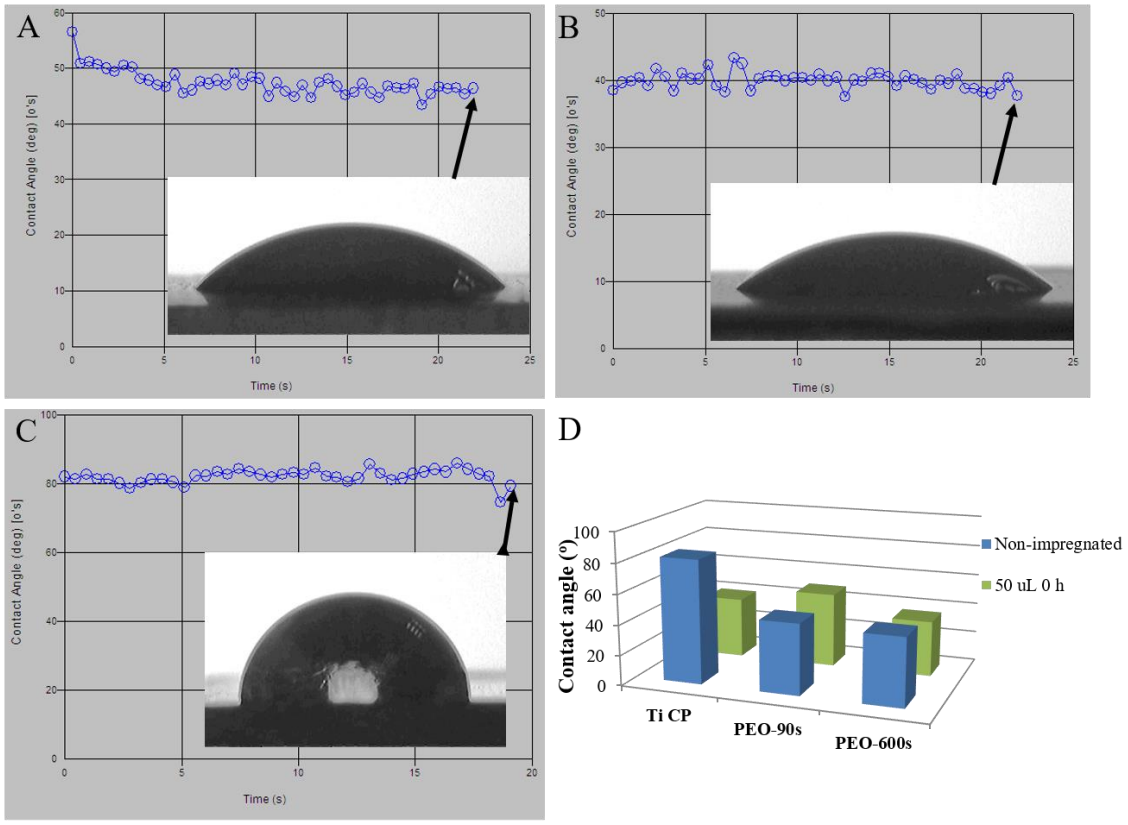

Figure 3.9. Variation of contact angle with time for BSA-free surfaces of PEO-90s (A) and PEO-600s (B) coatings and uncoated Ti CP substrate (C). Average contact angle of the materials before and after impregnation with albumin (D).

The next step was to estimated BSA delivery by Bradford Assay in Ti CP and coated Ti specimens at different time points, up to 48 h as final time. As expected, Ti CP samples have released the entire BSA load in 24 h (Figure 3.10), based on the evidence that at 48 h point the amount of the BSA found in the PBS for Ti substrate did not further increase (the slight decrease of the measured BSA at 48 h is attributed to the experimental error). The control samples are poreless and the protein would have had less interactions with the surface as there is no presence of Ca and P compounds. The liberated BSA amounted to 3410 μg. Considering that 4±1 μL of the drop was removed in the loading procedure, the expected remaining load is 3450 ± 75 μg, i.e. the measured value of 3410 μg of BSA falls well within the expected error and is further considered as a reference maximum load.

In PEO-90s very low BSA release was detected, corresponding to approximately 15% of the load, showing its ability to be used as protein carrier implant. Interestingly, PEO-600s exhibited an even faster BSA delivery than non treated Ti control samples in the first 4 h, reaching the

liberation of the ~70% of the load in the first 24 h, and the remaining amount of BSA at 48 h point.

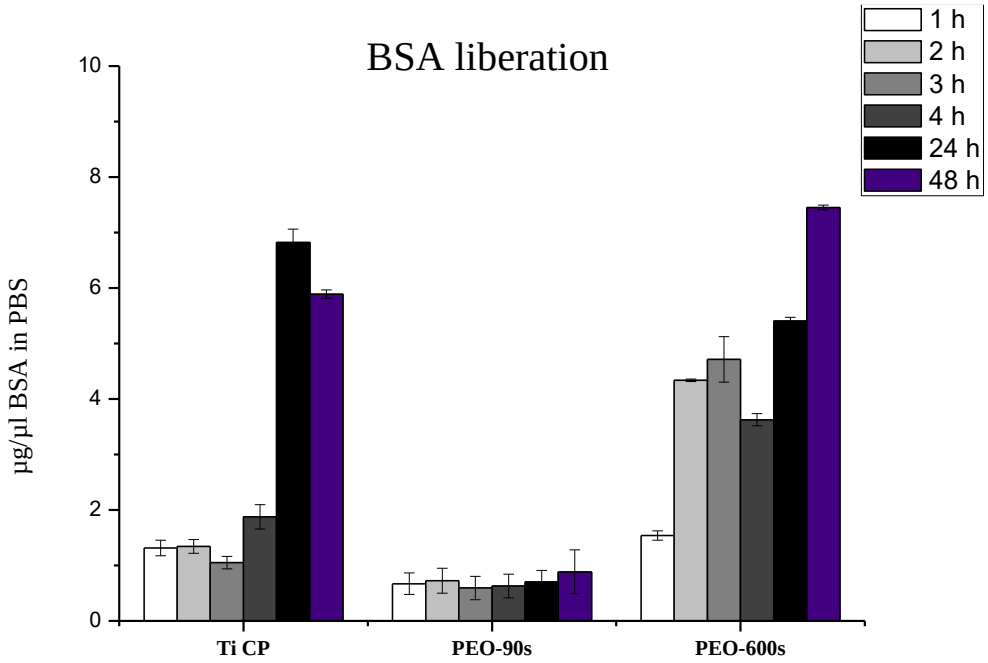

Figure 3.10. Albumin liberation from the materials impregnated with 75µg/µL of albumin during 48h of immersion in PBS. Initial content of albumin was 3750 µg/cm^2.

In vivo studies

After all the *in vitro* evaluation of the two coatings as potential implants a preliminary *in vivo* approach was developed. Dental titanium implants with PEO coatings were placed through the inferior maxilla in an adult pig (Figure 3.11 A,C). After 8 weeks, tissue samples were extracted, resin treated and stained with Levai Lazcko protocol, which allows histological discrimination between old and new bone tissue. At this time point, no adverse reaction or signs of implant rejection were detected as there was no presence of fibrous tissue or inflammation evidence. As it was expected, all the conditions PEO-90s and PEO-600s coatings or Ti CP controls implants were almost fully covered with bone matrix (Figure 3.11 B and Figure 3.12). Histological analysis of the PEO-treated implant area revealed a newly formed bone matrix around implant with a proper collagen distribution, with a similar osseointegration level that Ti CP controls. Likewise, osteoblastic populations with no aberrant phenotypes were observed (Figure 3.11 B). Bone-to-implant contact (BIC) analysis revealed no significant differences between the control and the PEO coatings (Figure 3.11 D). However, in this surgical model, a trend was identified for higher BIC values of the treated implants with 92.1 ± 6.9% and 89.6 ± 7.4% for PEO-90s and PEO-600s, respectively.

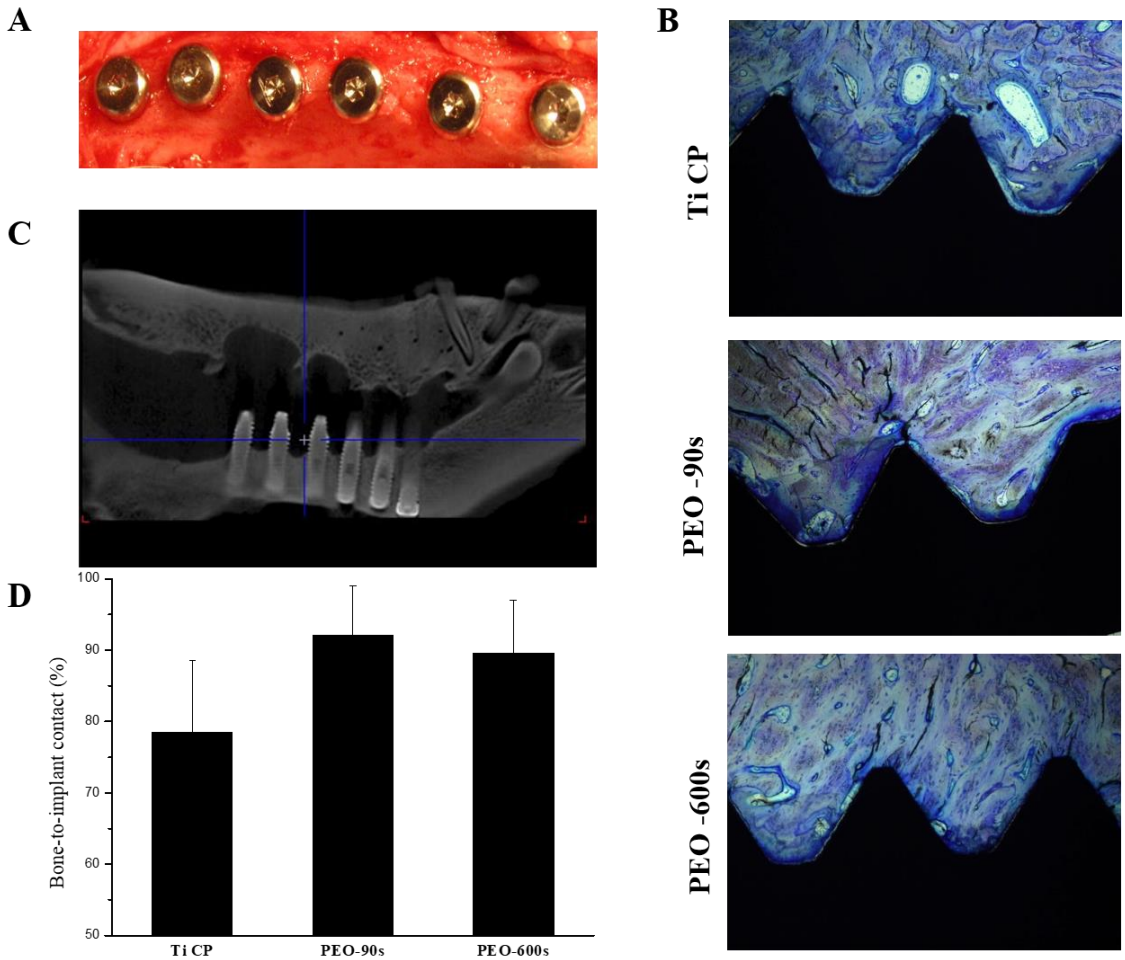

Figure 3.11. PEO-treated dental implants in pig's maxilla. A. Six dental implants (2 for each treatment) were placed in inferior area of maxilla, reaching medullar channel. B. Levai-Lazcko staining of histological sections of each dental implant and surrounding bone tissue. C. X-ray of dental implants localization after surgery. D.% of Bone-to-implant contact (BIC) of ROI.

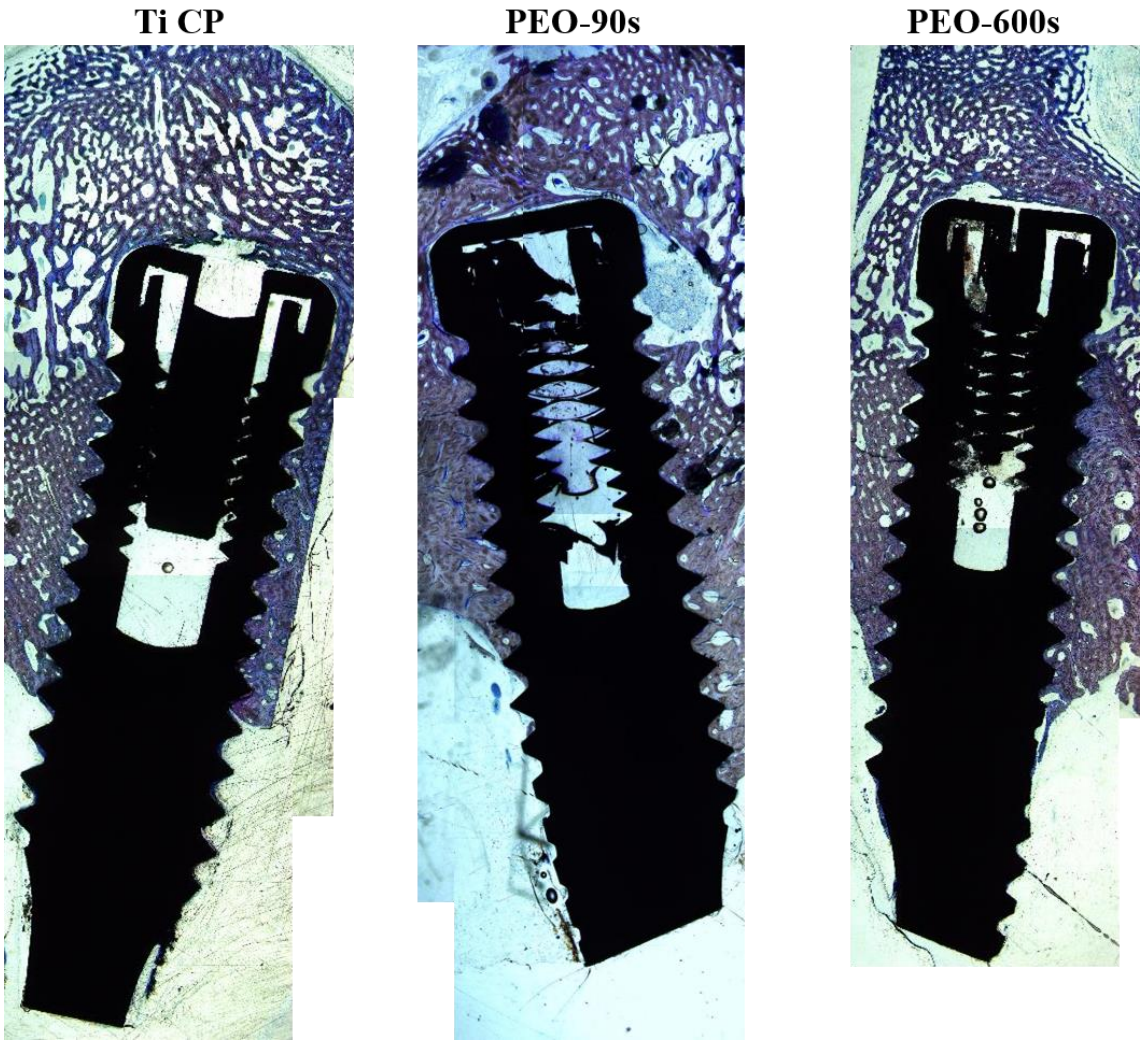

Figure 3.12. Levai-Lazcko staining of histological sections of total dental implant area and surrounding bone tissue.

1.1.2. Bioactive multi-elemental surface functionalization of titanium

PEO treatment for dental implants has emerged as an extremely favourable strategy to add diverse functionalities and obtain a 'smart' biomaterial. The inclusion of other bioactive elements into the coating components could provide a better osseointegration rate or even an antibacterial effect around the implant area. Ca and P have been widely studied and evaluated, and their effect has been analysed in the previous section with respect to Ti CP behaviour. On the other hand, elements such as Mg, Zn, F or Si can also promote bone homeostasis, augment matrix mineralization or promote angiogenesis. For instance, Si is known to have an important role in metabolic processes, formation and calcification of bone tissue [187]. Mg stimulates new bone formation, increases bone cell adhesion and stability [188, 189]. Zn is essential for mineralization, hormone activity, DNA synthesis and presents antibacterial effects [190, 191]. F has also antibacterial activity and an improved bone response [192].

However, in bone homeostasis osteoblasts have to interact with other cell types, including osteoclasts, to achieve a proper tissue regeneration. The osteoclasts are in charge of the remodelling of interfacial bone during the service lifetime of the implant and also includes the removal of necrotic bone at the interface. These phenomena are also regulated by surface features, such as surface composition, porosity or roughness [193]. Therefore, both cell types should be studied in order to biovalidate a potential commercial implant treatment.

In this Section electrolytes based on true solutions, which offer the benefit of easy technological maintenance compared with the suspension electrolytes described in Section 1.1.1, are used to develop PEO coatings on Ti CP. These electrolytes contain Ca and P as base and different combinations of Mg, Si, Zn and F. Microstructural and morphological characteristics of the formed coatings are studied and related to the osteoblastic and osteoclastic cell response.

Coating characterization

Figure 3.13 reveals topographic characteristics of the four formed coatings from the different electrolytes presented in methodologies section (Table 2.2). Optical and 2D micrographs (left and central columns) showed that the PEO coatings had a distinctive morphology for each type of electrolyte. The Ti-1PEO electrolyte with near-neutral pH resulted in a very homogeneous surface.

Table 3.4. Surface characteristics of the coatings.

Sample / Characteristics		**Ti-1PEO**	**Ti-2PEO**	**Ti-3PEO**	**Ti-4PEO**
Thickness (μm)		21.2±0.8	18.2±2.0	15.8±0.9	27.9±9.5
Roughness (μm)	R_a	1.02 ±0.01	1.07 ±0.01	1.33 ±0.03	2.29 ±0.03
	S_a	1.35	1.60	1.73	4.18
Population density of pores (pores/mm^2)		34326	32102	21966	25111
Pore area (μm^2)	Max.	35.5	22.0	35.6	27.1
	Min.	0.503	0.511	0.502	0.501
Contact angle (º)	**Ti CP** 83±12	40±4.9	42±1.7	48±1.3	9±1.3

Ti-2PEO presented black areas in the surface with no direct relation with the height of the coating. Ti-3PEO had relatively uniform topography and Ti-4PEO had the highest crater-like protuberances of all the formed coatings, (Figure 3.13, 3D-rendering) with ~55 μm of elevation. Diagrams of R_a are displayed in the figure with the profile line indicated in white in the optical micrographs. S_a values were obtained analysing the whole area of each 2D micrographs. The

values of R_a and S_a obtained are presented in Table 3.4, both values were the lowest of all coatings for Ti-1PEO (R_a=1.02 µm; S_a=1.35 µm) consistent with the surface characteristics described before. The incorporation of Mg into the electrolyte resulted in slight decrease of the roughness parameters. On the other hand, Ti-4PEO showed the highest values of the all coatings with the R_a= 2.29 µm and S_a=4.18 µm. This could be related, on the one hand, to the incorporation of F and formation of bulky Ca-P-F containing compounds; on the other hand, high alkalinity of the electrolyte (pH=12.28) and, consequently, highest conductivity (18.87 mS/cm) lead to larger and longer lasting microdischarges.

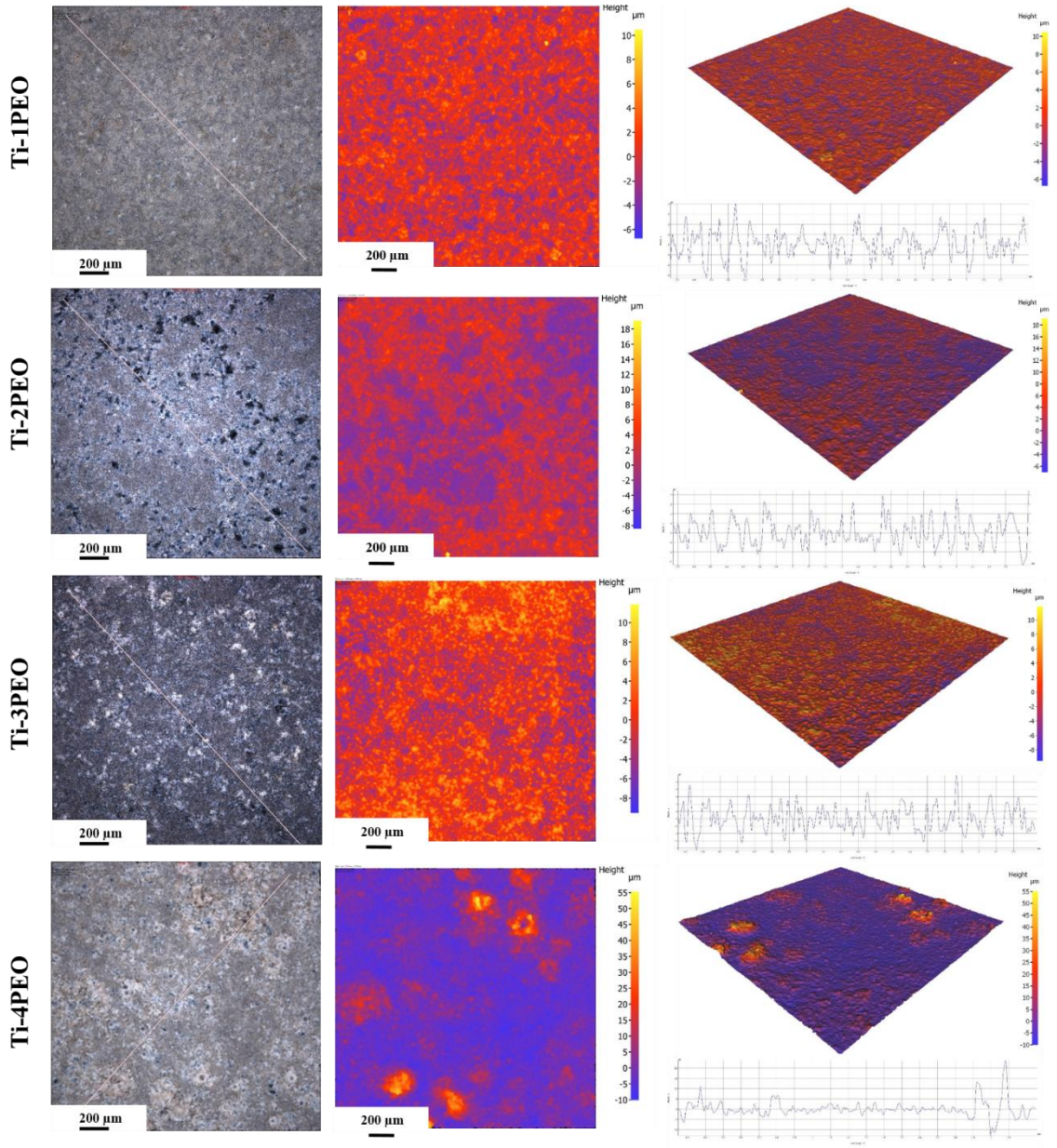

Figure 3.13. Optical micrographs (left column), variation of surface topography in 2D (centre column) and 3D (right column) rendering. R_a diagrams are also presented (right column).

The surface morphology was also studied by SEM (Figure 3.14), observing a characteristic porous pumice-like structure with pores localised at the centre of a small and rather flat craters. The porous structure is a consequence of gas ejection out of the discharge channel as well as gas evolution through molten coating material followed by fast solidification [74]. Ti-1PEO coating reveals numerous pores on the surface, with the highest pore density of all the coatings (Table 3.3, Fig. 1.14 a). On the other hand, coatings developed in electrolytes with pH in the range of 4-5 with presence of Zn, Si and/or Mg ions show a marked decrease either in the pore density (Ti-3PEO) or maximum pore area (Ti-2PEO) compared to the rest of electrolytes (Table 3.4).

Surface EDS analysis of Ti-1PEO coating (Table 3.5) revealed a surface Ca/P ratio of 1.40, that was slightly lower than that of stoichiometric hydroxyapatite (HA Ca/P=1.667) [194]. Electrolytes containing Si, Zn and/or Mg produced an incorporation of these elements in the range of 0.9-2.2 at. %., in Ti-2PEO Zn was incorporated in the smallest amount compared with Mg and Si, despite that its molar concentration in the electrolyte was equivalent with that of Mg and higher than that of Si. That may be related to factors such as the thermodynamics of the formation of the respective compounds in the coating and solubility of the species and compounds in TiO_2 matrix. Simultaneously, a decrease in Ca/P ratios down to 1.32 and 1.11 occurred in Ti-2PEO and Ti-3PEO coatings, respectively. Ti-4PEO coating revealed a Ca/P ratio of 2.90 which is overstoichiometric in comparison to HA.

Backscattered scanning electron micrographs of the coatings are shown in Figure 3.14 (f-i). The coatings comprised an inner barrier sub-micron thick layer and an outer layer; the latter in all coatings except Ti-2PEO disclosed a homogeneous and compact microstructure, with a minimal internal porosity (Figure 3.14 g). The Ti-2PEO and Ti-3PEO coatings revealed a reduction of the thickness (down to 15.8 μm) compared with Ti-1PEO coating (21.2 μm) which is in concordance with other works claiming that acidic electrolytes lead a lower coating growth rate [77]. In the case of Ti-4PEO coating (Figure 3.14 i) formed in alkaline electrolyte containing fluorides species, a 27.9 μm of thickness was achieved and the cross-section disclosed large cavities in the outer layer, which may be associated with greater gas generation as alkaline pH.

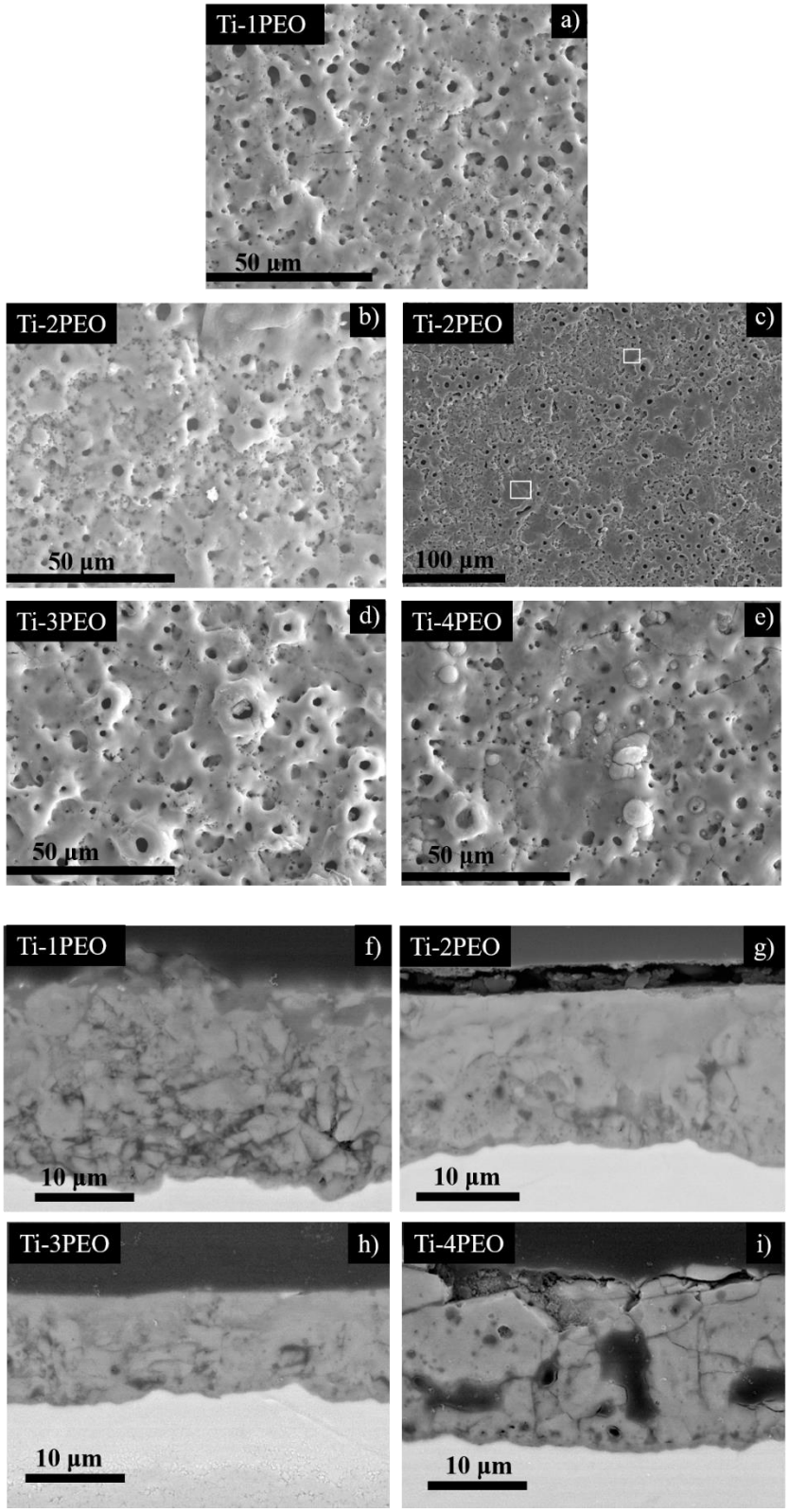

Figure 3.14. Secondary electron plan view micrographs of PEO coatings a-e). Backscattered electron cross-sectional micrographs of PEO coatings f-i).

Table 3.5. Area EDS analysis of the PEO coatings (at. %).

Sample / Assignation	% Atomic									Ratio		
	O	Na	P	Ca	Ti	Mg	Si	Zn	F	*Ca/P*	*Ca/Ti*	*P/Ti*
Ti-1PEO	65.5	-	4.0	5.6	25.0	-	-	-	-	**1.40**	0.22	0.16
Ti-2PEO	65.3	-	2.2	2.9	25.2	1.2	2.2	0.9	-	**1.32**	0.12	0.09
Ti-3PEO	65.3	-	3.6	4.0	23.1	-	2.2	1.8	-	**1.11**	0.17	0.16
Ti-4PEO	56.2	1.6	4.1	11.9	14.6	-	2.0	-	9.5	**2.90**	0.82	0.28

XRD analysis reveals the presence of anatase and rutile in all of the studied oxide layers, along with peaks of Ti proceeding from the substrate (Figure 3.15). Additionally, Ti-4PEO presents peaks for $CaTiO_3$, CaF_2, SiO_2 and bioactive compounds such as hydroxyapatite (HA). CaF_2 was formed as a consequence of the fluoride in the electrolyte and the PEO conditions. The presence of MgO in Ti-2PEO is associated with the oxidation during the PEO process of Mg cations added into the electrolyte. The oxidation of silicon species was also detected for Ti-2PEO and Ti-3PEO coating comprised small amounts of $Ca_3(PO_4)_2$ (apatite) and $CaTiO_3$.

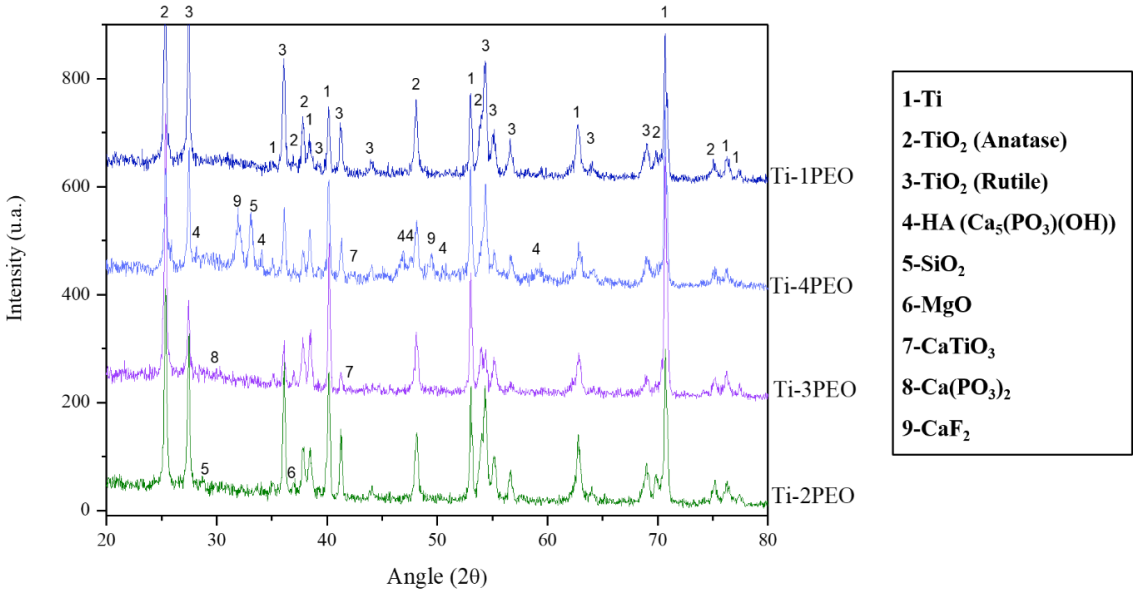

Figure 3.15. X-Ray diffraction patterns for the coatings (Ti-1PEO, Ti-4PEO, Ti-3PEO and Ti-2PEO).

Contact angle

Wettability of the PEO coatings and control Ti was evaluated (Table 3.4) as it can be a crucial surface characteristic for the final performance of an implant as already review before. The ceramic coatings were considerably more hydrophilic compared with Ti CP (~83°). Ti1-PEO, Ti2-PEO and Ti3-PEO showed comparable contact angles values oscillating between ~40º to ~48° (Table 3.4). Contrarily, fluoride containing coating (Ti4-PEO) contact angle decreased (9º) with a quick sinking of the drop.

Ion liberation

Table 3.6 gathers the values of ion liberation (Ca, Mg, P, Si, Ti and Zn) determined by ICP-OES from the different PEO coatings after 28 days of immersion in 0.9% NaCl and it is visually represented in Figure 3.16 NaCl solution was used instead of m-SBF in order to avoid difficulties related to the background presence of Ca and P in the latter, which leads to a complicated equilibrium between the released species and their precipitation as compounds of low solubility.

Bioactive elements were released from all the coatings, the highest amount of Ca was found for Ti-1PEO and Ti-4PEO; furthermore, Ti-1PEO stand up with the highest quantity of P liberated (approximately three-fold compared with the rest). Ti-4PEO exhibited higher Ti^{4+} liberation (up to 15 times higher) compared with other PEO coatings.

The kinetics of F^- ion release was studied due to its great importance as an antibacterial element [195]. Figure 3.16 shows the evolution of free F^- ions content in 0.9% NaCl released during 12 days of immersion from Ti-4PEO coating. Fluoride liberation is detected to diminish with the time. Besides its properties as antibacterial element which should be determine to assess sufficiency for bacteriostatic and/or bactericidal effect, the possible cytotoxicity of this level of F^- on cells participating in osteogenesis has to be studied.

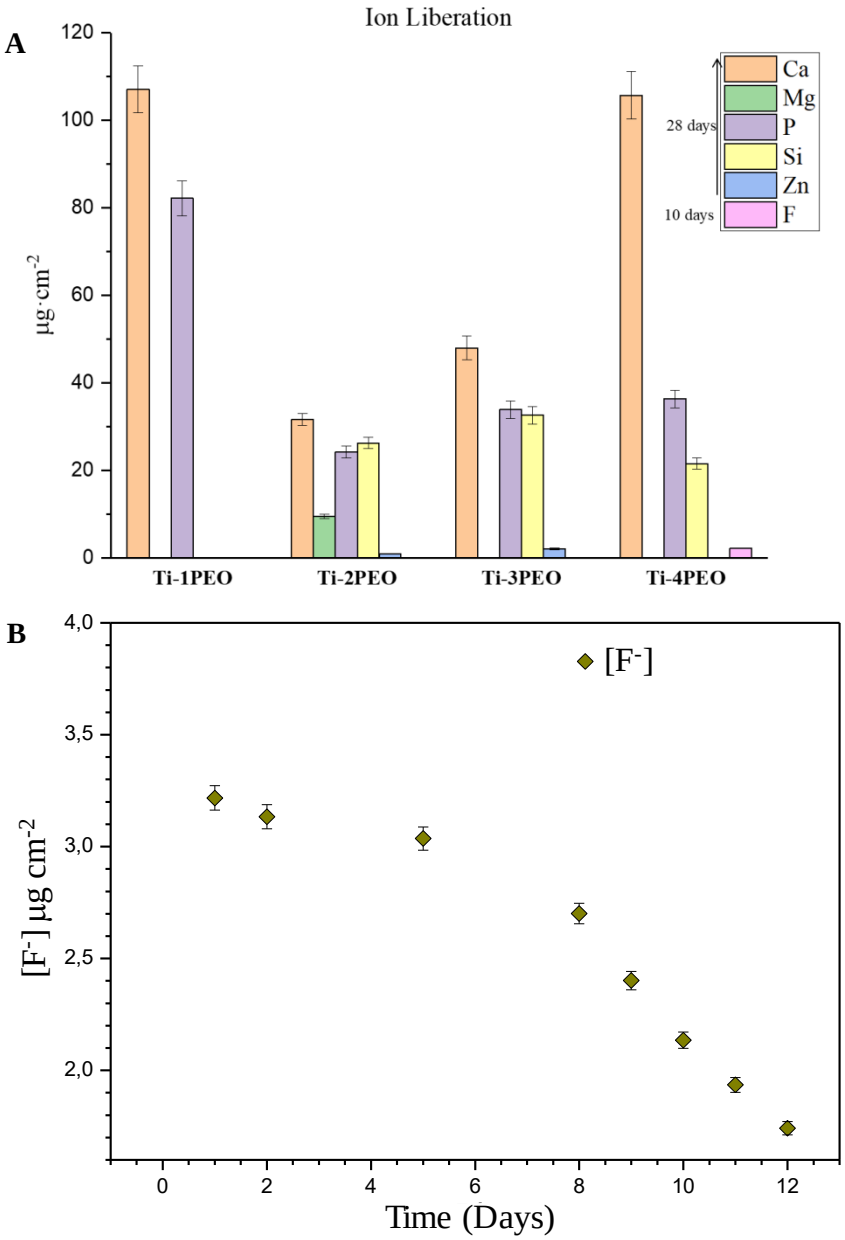

Figure 3.16. Ion liberation from PEO coatings after 28 days in 0.9% NaCl (A). Fluoride ion liberation at different time points from Ti-4PEO coating after 12 days of immersion in 0.9% NaCl (B).

Table 3.6. Ion liberation from PEO coatings after 28 days of immersion in 0.9% NaCl determined by ICP-OES.

Samples	*Elements (µg/cm²)*					
	Ca	**Mg**	**P**	**Si**	**Ti**	**Zn**
Ti-1PEO	107.060±5.4	-	82.147±4	-	0.074±0.01	-
Ti-2PEO	31.647±1.3	9.494±0.5	24.240±1.3	26.260±1.3	0.027±0.01	0.943±0.07
Ti-3PEO	48.000±2.7	-	33.920±2	32.640±2	0.026±0.01	2.048±0.2
Ti-4PEO	105.713±5.4	-	36.360±2	21.547±1.3	0.411±0.04	-

Osteoblasts and osteoclasts response

MC3T3 preosteoblastic cell line was seeded at a cell density of 2×10^4 cells per cm^2 over the materials (Ti CP and Ti-1PEO, Ti-2PEO, Ti-3PEO and Ti-4PEO coatings). For the differentiation process cells were allow to grow for 24 h, change to differentiation medium and cultured for 7 days. To be able to visualize the cells at end point a fluorescence staining of actin and Hoechst (Figure 3.17 a) was carried out and proved a proper monolayer formation and growth over all the analysed surfaces. Actin staining images showed a different disposition of the monolayer as the coatings topology differed, especially on Ti-2PEO where some cultured areas, corresponding to the raised and crater-like pore morphology, were less positive for the staining (Figure 3.11). However, these areas were positive for nuclei staining, demonstrating that osteoblastic culture colonized these zones as well. Likewise, the absence of staining was also detected in Ti-4PEO, related to protuberances in high areas, as appreciated in 3D pictures (Figure 3.11).

Following the evaluation of the culture by fluorescent markers a metabolic activity study was done after 7 days of culture (Figure 3.18). These results indicated that the PEO coatings were cytocompatible as all samples were similar in metabolic activity results to control Ti CP and in concordance with monolayer formation and cell layout results.

RAW 264.7 macrophages were seeded at $1.5x10^4$ cells/cm^2. The osteoclastogenesis process was also assessed by actin and Hoechst staining (Figure 3.17 b), the latter was done in order to determine the number of nuclei inside the formed osteoclasts which is a key factor for the establishment of the differentiation process. Besides, by cytoskeleton staining the presence of actin rings of the osteoclasts can be detected, this constitutes an excellent marker that can confirms their formation [196, 197]. Ti CP behaved as in the previously section: the images showed large osteoclasts, with many nuclei, spread all over the surface and also smaller ones fusing with others.

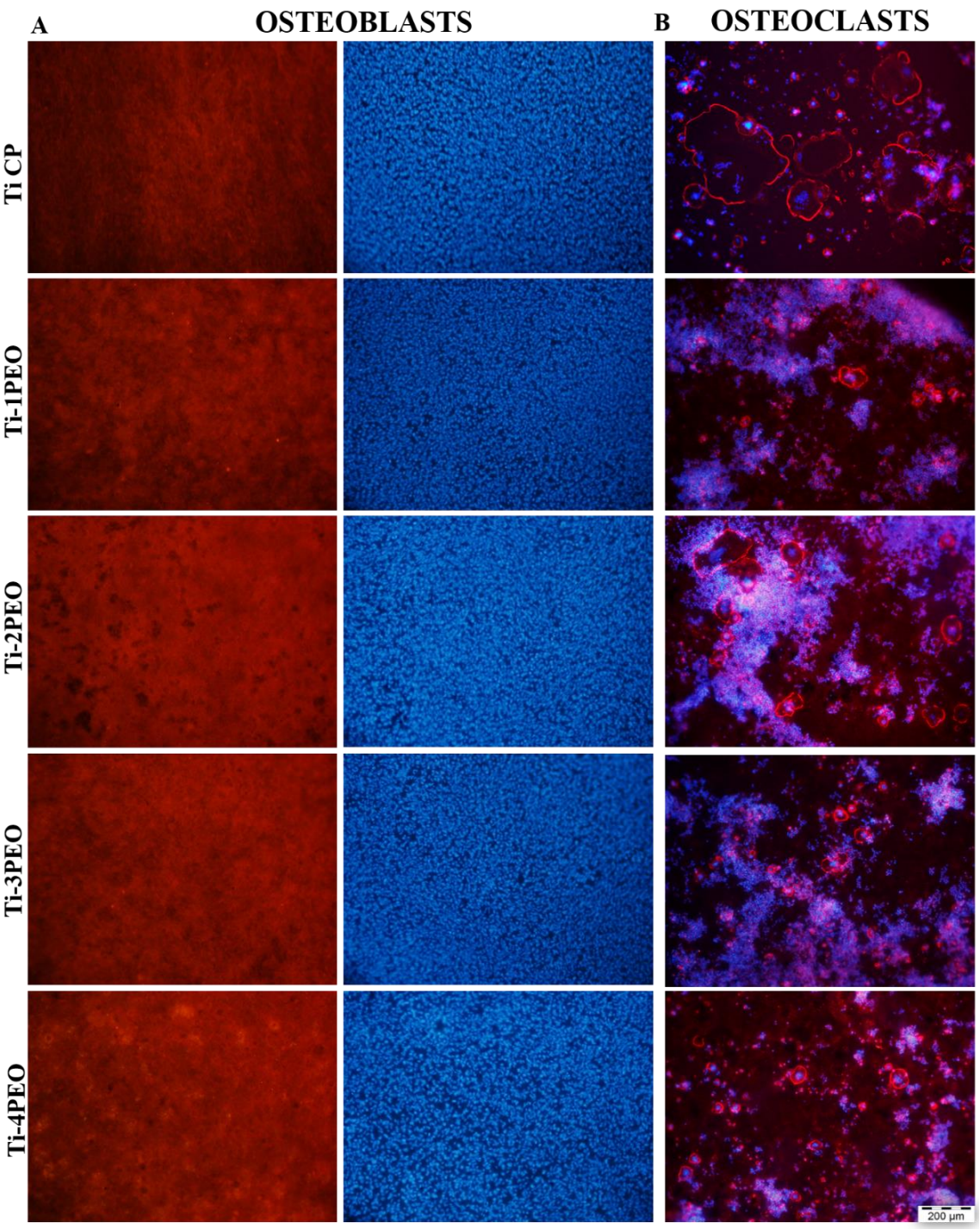

Figure 3.17. a) Evaluation of monolayer formation of the preosteoblastic cell line with an actin (red, left column) and Hoechst (blue, right column) staining performed at 168 hours; b) merge of actin and Hoechst staining of the formed osteoclasts over the surfaces.

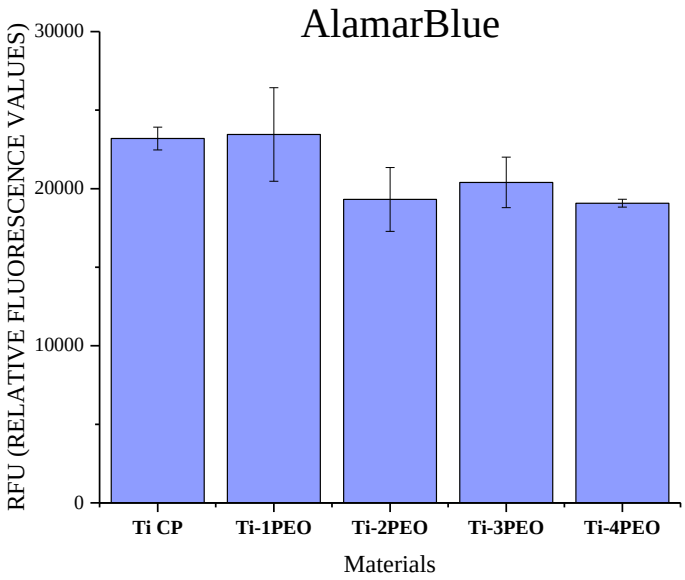

Figure 3.18. Metabolic activity (AlamarBlue assay) of MC3T3 differentiated cells over the materials at 168 hours.

Finally, aiming to evaluate the differences between materials in terms of matrix secretion as a result of the differentiation process an estimation of collagen secretion was obtained. Osteoblastic cultures growing over Ti CP and PEO coatings for 168 hours were assessed by Sirius red staining (Figure 3.19). A significant increase of collagen secretion was detected over all the PEO treated samples compared with the control Ti CP. The tendency observed for the absorbance values was preserved with no discrimination amongst the coated samples. This indicates that even though cytocompatibility studies showed similar results between Ti CP and the PEO coatings, the coated samples exhibit a greater bioactive effect in terms of promotion of a differentiated state.

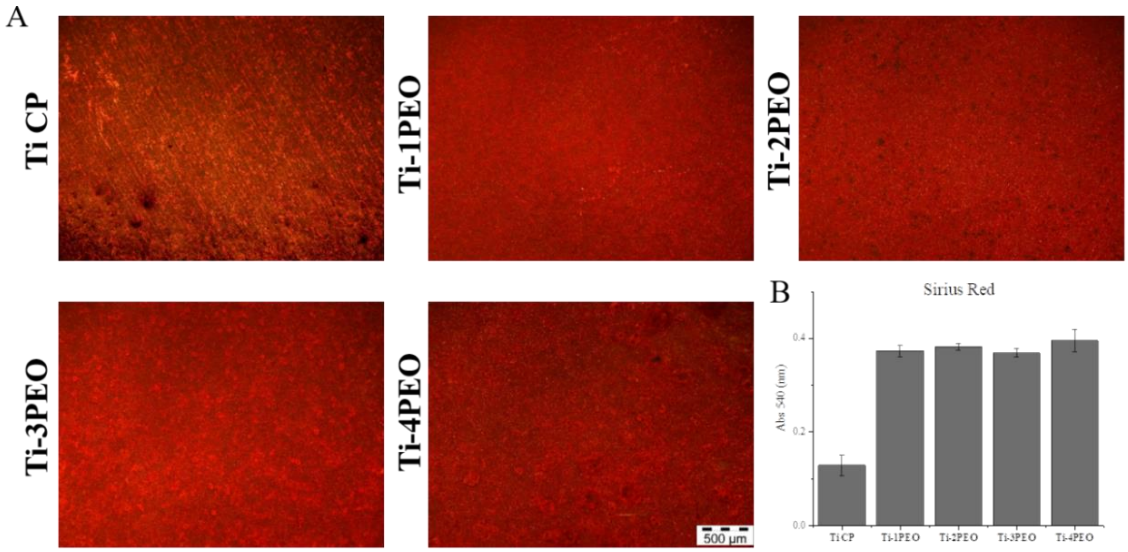

Figure 3.19. Collagen secretion staining and quantitative measurement: micrographs of the collagen staining over the samples after 168 h of culture (a); colorimetrical quantitative values of absorbance at 540 nm (b).

1.2. Orthopaedic applications

1.2.1. In vitro studies of anodised zirconium as a potential implant material

Demand on long-lasting orthopaedic prosthesis is continuously rising as population ages. New materials that can fulfil the desired mechanical properties, biocompatibility and increase the average life of a prosthesis are being investigated. Among this materials zirconium (Zr) and its alloys are considered as potential candidates due to their low electronic conductivity, high corrosion resistance and great biological response. Surface modification in cementless prosthesis could promote the bioactive surface to integrate the metal to the human body more efficiently. More specifically, anodizing forms an oxide layer on the surface of Zr modifying its chemistry and topography which may lead to improvement in its osseointegrative properties by mechanisms reviewed before in Section 1.3. Therefore, we aimed to disclose the interaction with all types of tissues present in orthopaedic surgical model in a more complete way. The materials were previously anodized with two different potential conditions (30 V or 60 V) over Zr using a phosphorous based electrolyte. Different cell types, including preomyoblastic, endothelial, preosteoblastic, macrographic cell models were evaluated in terms of cytocompatibility and growth. Bone tissue related processes such as osteoblast and osteoclast differentiation over the materials were also investigated in order to estimate its possible application as orthopaedic implant.

Surface characterization of anodized zirconium

In Figure 3.20 (A) the surface of as received zirconium (Zr 0 V, control material) is presented. Typically, native Zr is covered with a thin native oxide film of thickness of 10 nm of Zr suboxides when in contact with air. These kind of suboxides can not be resolved in SEM images. On the other hand, the anodized samples at different voltage (30-60 V) are presented in Figure 3.20 B-C. The formed anodic films are characterized by the presence of bright spots of submicrometrical oxide structures, this phenomenon is more apparent in Zr 60 V than in Zr 30 V. There is also a film growth with the increased potential in the nanometrical range. The incorporation of phosphate ions into anodic films growth in phosphoric acid has been already described [198]. Surface chemistry of anodized zirconium changes as the phosphate is incorporated into the film.

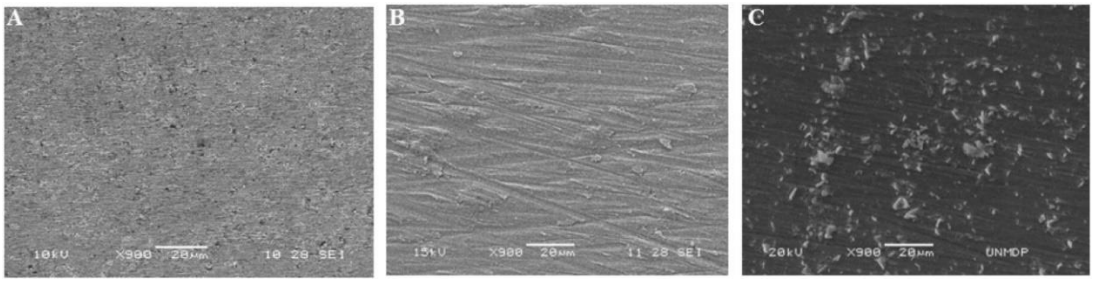

Figure 3.20. SEM micrographs of zirconium samples with different surface treatments. (A) control, Zr 0 V (B) Zr 30 V and (C) Zr 60 V.

In vitro response of premyoblastic C2C12-GFP cell line and endothelial C166-GFP cell line

In vitro biocompatibility of the materials was assessed in a preliminary study with two self-fluorescent cell lines. C2C12-GFP cell line is able to differentiate into myoblasts or, with concrete stimuli (e.g. BMP-2) or environment, can transdifferentiate into osteoblasts. Also, endothelial cells are important for bone tissue vascularization and can induce a quicker integration.

As it is described in Figure 3.21, micrographs were taken at 24, 48, 72 and 96 h to determine cell growth and adhesion to the material of the premyoblastic cells. At 24 h, cells growing over the three samples have an expanded morphology showing a suitable initial adhesion behaviour. Furthermore, in Zr 30 V and Zr 60 V it can be appreciated a cell alignment matching the anodized treatment pattern that it is maintained until the end point (96 h). Regarding cell growth, cells proliferated along the days with a resulting formation of a cell sheet monolayer on all the samples. In a similar way in Figure 3.22 endothelial cells after 48 h of culture have already formed a dense monolayer over the materials.

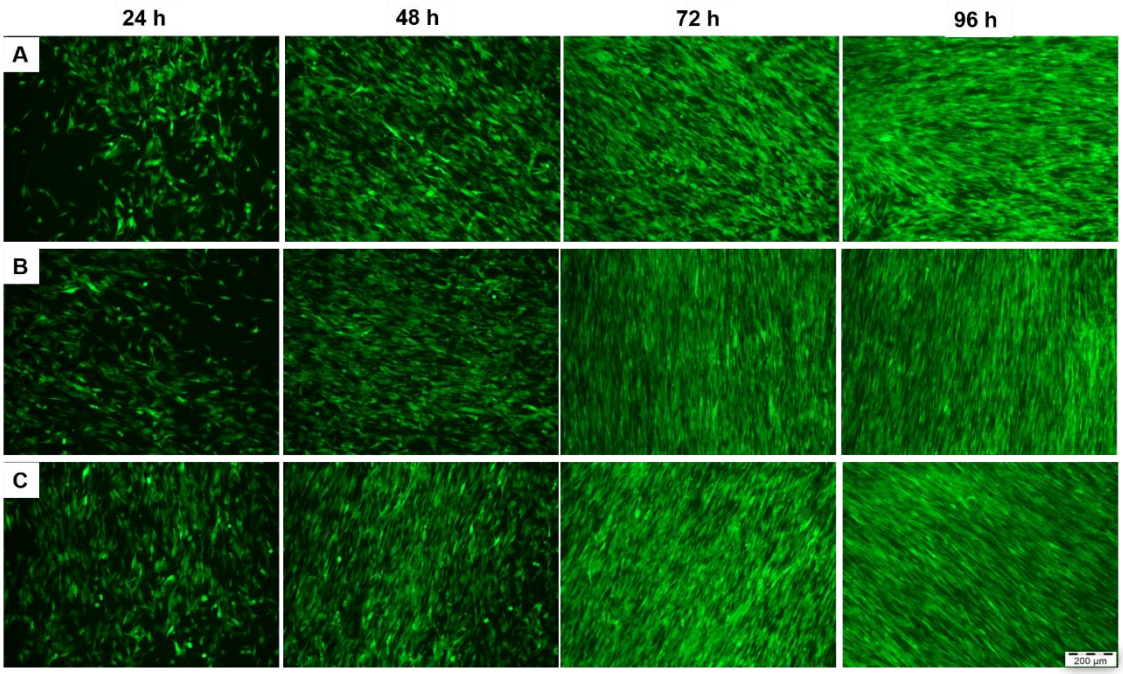

Figure 3.21. C2C12-GFP cells seeded on Zr 0 V (A), Zr 30 V (B) and Zr 60 V (C). Micrographs were taken at 24, 48, 72 and 96 h (end point). Cell alignment and tissue formation can be appreciated after 24 h.

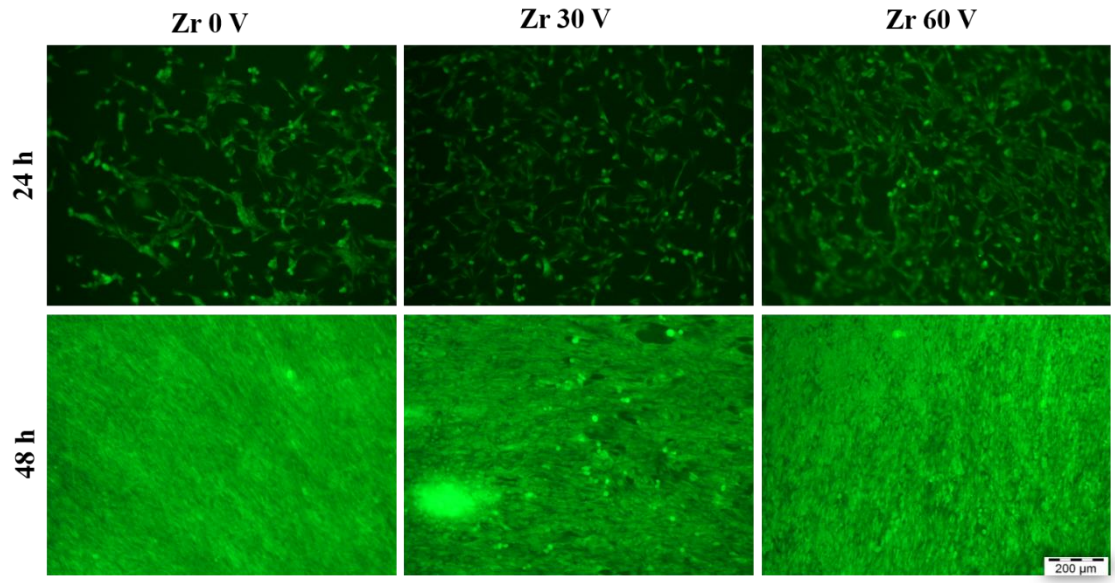

Figure 3.22. Fluorescence micrographs of endothelial cells (C166-GFP) growing over the Zr surfaces at 24 and 48 h.

In vitro response of osteoblastic MC3T3 cell line

The initial adhesion behaviour and spreading of MC3T3 are monitored at different time points. After culturing for 72 h, MC3T3 culture were attached and spread onto the surface as shown in Figure 3.23, establishing a dense monolayer after 120 h. The quantification of metabolic activity at 72 h and 168 h after seeding can be seen in Figure 3.24.

The Alamar Blue metabolic activity measurements showed that all conditions under study were biocompatible and they did not inhibit cell proliferation. While there is no remarkable statistical difference between the anodized conditions, Zr with the highest potential treatment (60 V) presents a sight tendency for enhanced metabolic activity. As it was detected with C2C12-GFP cell line, from merge micrographs it can be depicted that the osteoblastic cells were also aligned following anodized treatments (Figure 3.23, last row). The monolayer formation was also confirmed by SEM (Figure 3.25).

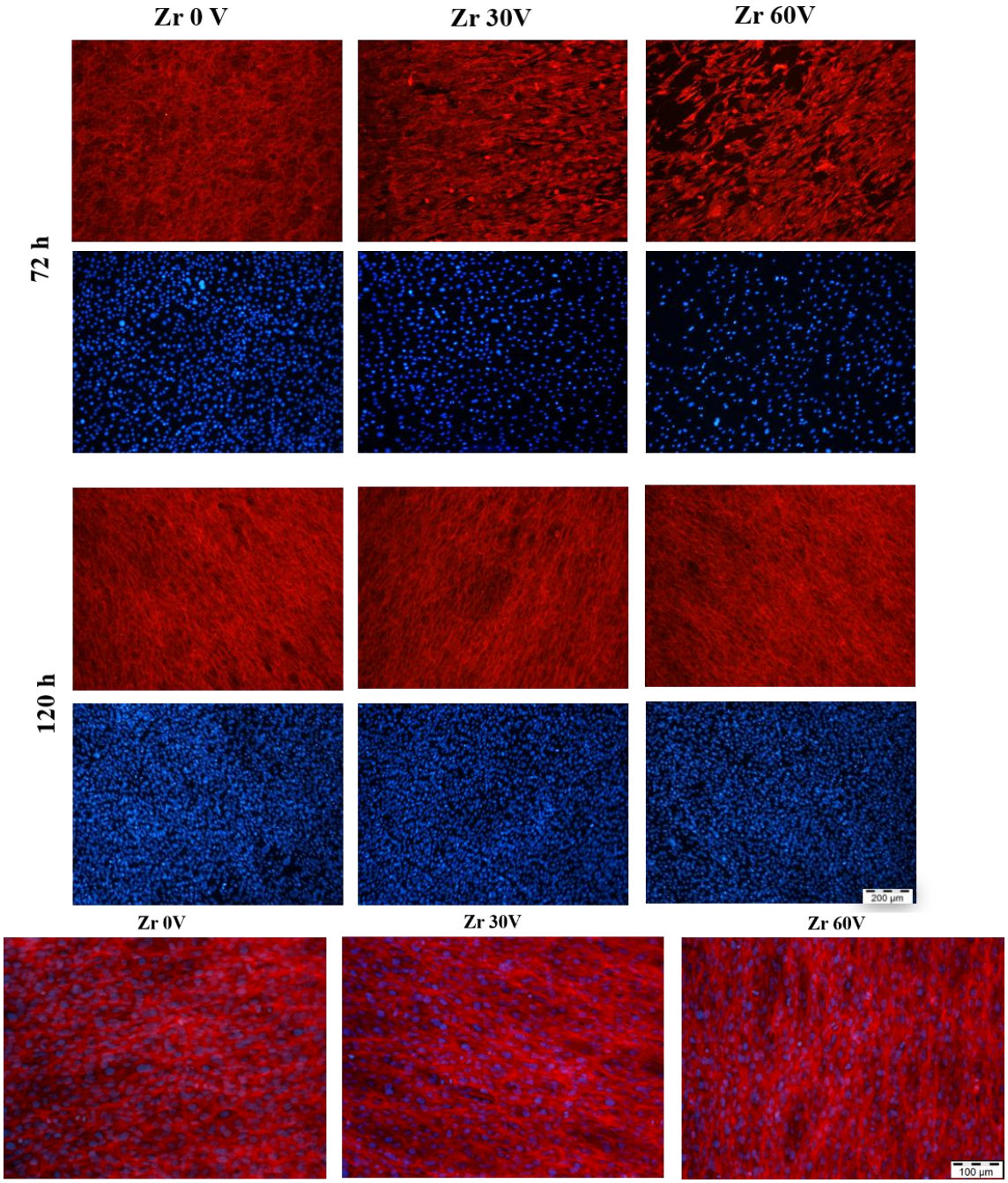

Figure 3.23. MC3T3 proliferation over zirconium surfaces: 72 h and 120 h after seeding. First and third row: actin staining (cytoskeleton). Second and fourth row: Hoechst staining (cell nuclei). Fifth row: merge magnifications of the osteoblastic monolayer.

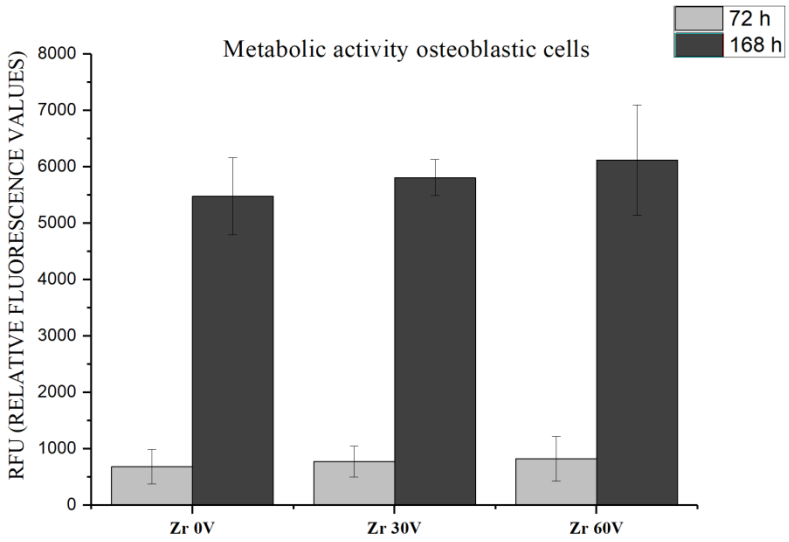

Figure 3.24. Metabolic activity (Alamar Blue) of MC3T3 cell culture at 72 h and 168 h after cell seeding. RFU (Relative Fluorescence Units).

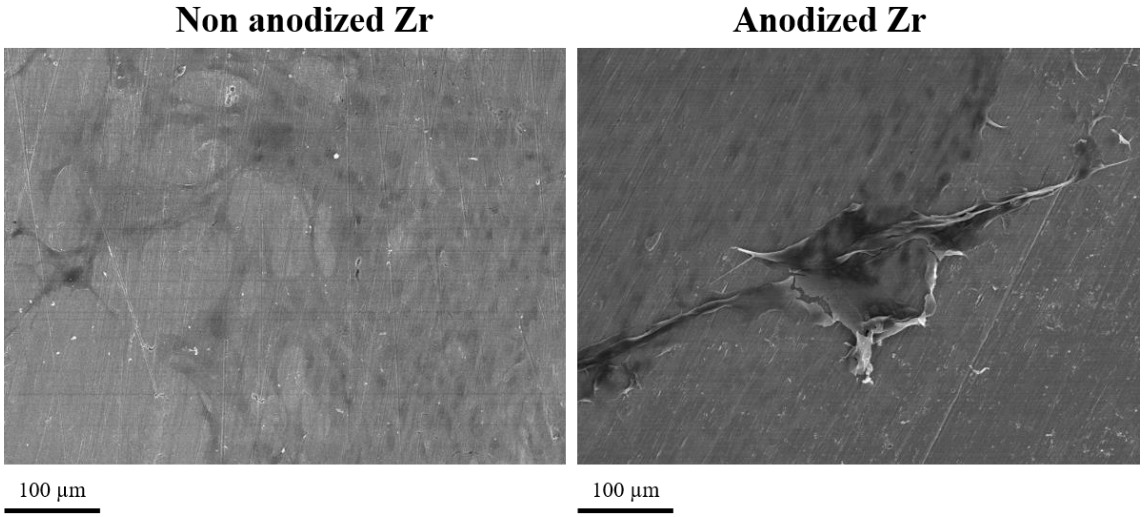

Figure 3.25. Secondary electron microscopy of osteoblastic cells growing over Zr surface after 120 h.

Immune system: macrophage cell behaviour

As already evaluated in Section 1.1.1 for Ti Grade I, RAW 264.7 cell line can constitute an excelent cell model for osteoclastogenesis evaluation and immune system response. As described, it can polarize into macrophagic M1 and M2 phenotypes, or fuse to form osteoclasts, bone resorbing cells. Cells were seeded over the materials without RANKL and as it was expected there was no osteoclast formation. Cells grew homogeneously in all samples (Figure 3.26).

In Zr 60 V macrophages are organized in lines with elongated morphology as the oxide treatment is displaced. This phenotype could correspond to a M2 polarized state, an optimal immune response for successful implant integration.

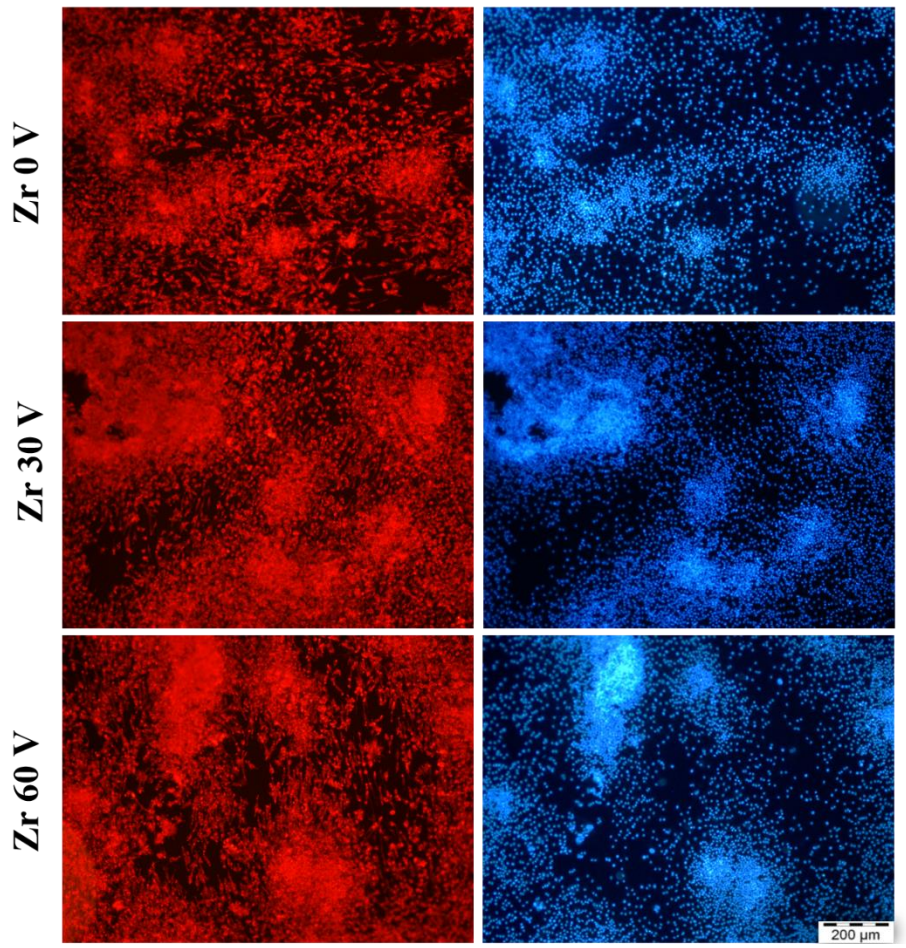

Figure 3.26. RAW 264.7 cells growing over the materials (Zr 0 V, 30 V and 60 V) after 120 h of culture. Left row: actin staining (red) and right row: hoechst staining (blue).

Osteoclast differentiation

Osteoclast formation induced by RANKL was achieved in all the samples (Figure 3.27 A) as it can be seen in actin images (first row in red). Actin rings are a differentation marker that can be easily detected as already developed in Section 1.1.2, these are expressed in order to seal the resorbing area to the biomaterial surface. Moreover, Hoechst staining (second row in blue) showed that the formed osteoclasts were mature as they have several nuclei. A major number of osteoclasts per area were detected in Zr 30 V and Zr 60 V evidencing an increased differentiation capacity over Zr treatments. Cell alignment is also present in the osteoclast cytoskeleton (Figure 3.27 B) at Zr 60 V, consistent with the anodic treatment oxide formation and phosphorous deposition.

Consequetly, an immunocytochemistry of TRAP was performed to obtain more information about the difference between the control material and the treated samples in osteoclast differentiation, (Figure 3.27 A). Zr 60 V was the selected sample for treated condition and as with actin ring

detection more osteoclasts per area were formed and even with an increased resorption ability as many lysosomal vesicles were detected (Figure 3.28 B).

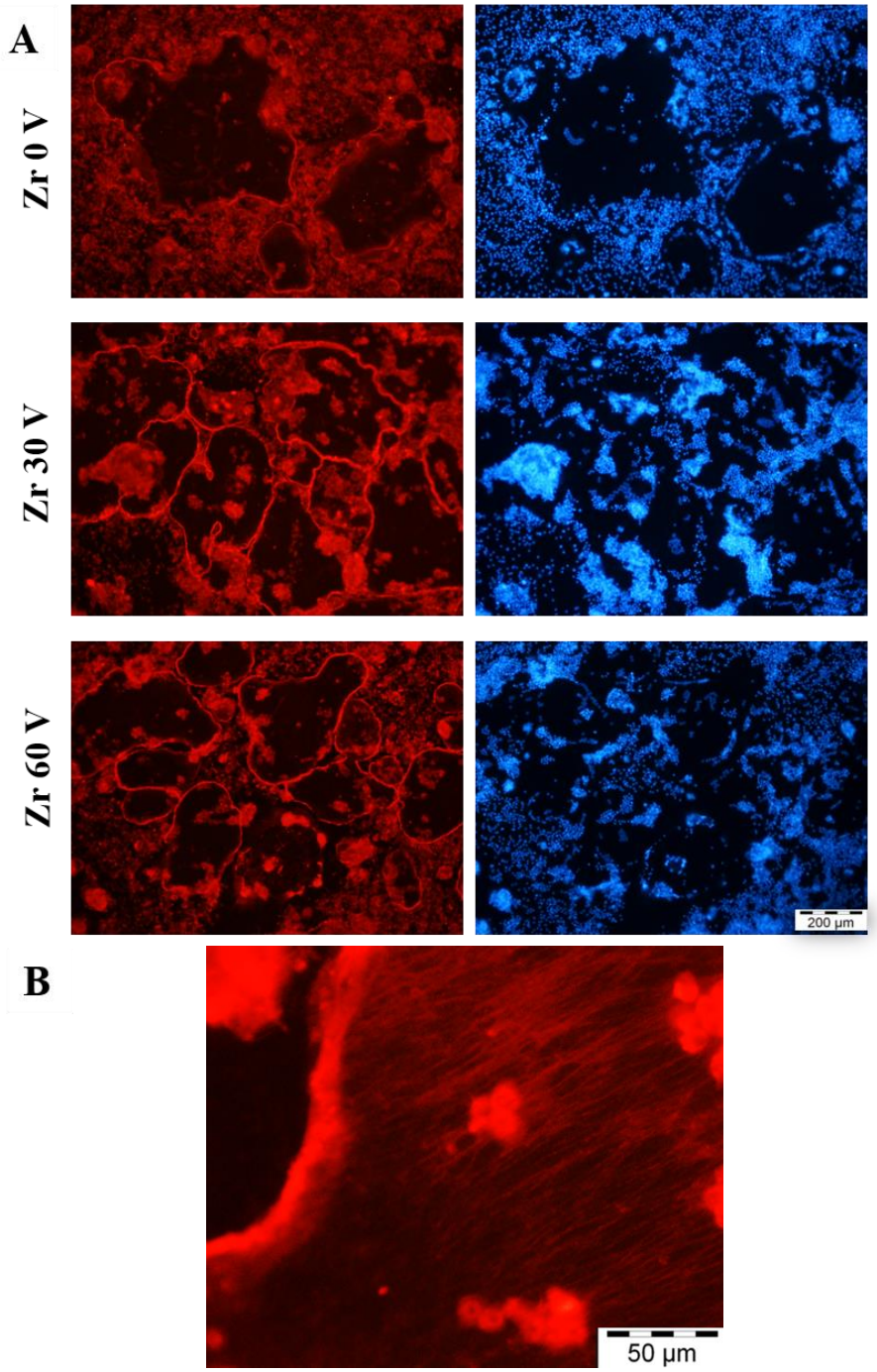

Figure 3.27. Micrographs of actin (red) and Hoescht (blue) of RAW 264.7 cells forming multinucleated osteoclasts over zirconium surfaces (A) . Detail of actin staining (400 ×) of an osteoclast growing on Zr 60 V (B) Filaments seems to follow the same orientation than the oxide treatment.

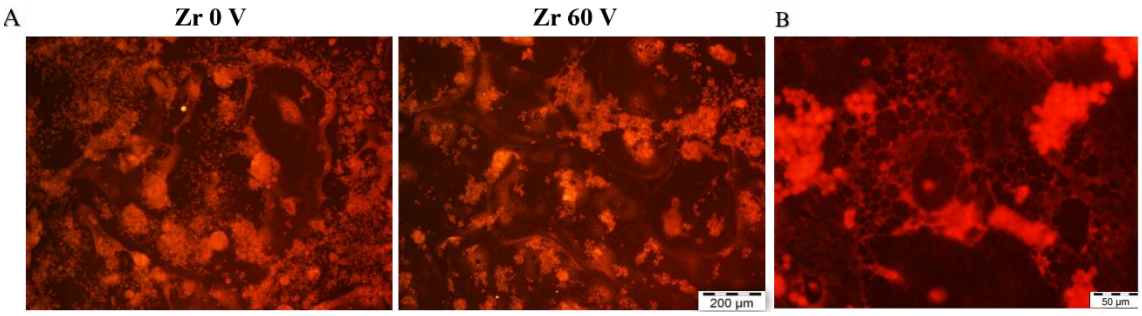

Figure 3.28. Immunocytochemistry of Tartrate resistant acid phosphatase. RAW 264.7 cells forming multinucleated osteoclasts over the Zr 0 V and Zr 60 V (A). B) Detail (200 ×) of Zr 60 V where osteoclasts are differentiated.

In this study, different cell lines were evaluated in terms of monolayer formation and adhesion over these surfaces as very little is known about their in vitro behaviour. Moreover, differentation processes such as osteoclastogenesis were also assessed showing an improved condition on the anodized materials. Their implications will be properly analyzed in the Discussion section.

1.2.2. Enhanced properties of Ti6AlV4 through PEO treatment: antibacterial activity and improved osteogenesis

As we have exposed, PEO treatments over Ti CP and Zr have shown improved properties in terms of eukaryotic cell activity. Ti6Al4V is one of the gold standard materials in orthopaedics applications, and this alloy could be also benefited of a similar approach. The main issue about the use of Ti6Al4V alloy is that its corrosion resistance is lower than that of the commercially pure Ti and may provoke possible cytotoxicity due to metal release. As a consequence, surface treatments to avoid these biocompatibility problems are being studied. Among them, PEO treatment of this material could reduce the negative properties reducing its corrosion and improving the osseointegration of the implant. A combined strategy using a Ca and P based coating with the incorporation of Si could promote osseointegration; Si-containing implants and ceramics such as Si-substituted hydroxyapatites and Bioglass™ bond to the bone in a more efficient manner than their Si-free counterparts, in consequence of the spontaneous formation of a biologically active apatite-like layer on their surface [187, 199]. Moreover, Si improves anti-corrosion properties of PEO-treated alloys and affects the rate of bone growth during the early stages of bone formation, significantly augmenting the up-regulation of osteoblast proliferation and gene expression [200]. Si-containing PEO coatings for biomedical applications have already been evaluated *in vitro* [201-205].

As has already been reviewed in previous sections, antibacterial properties of an implant are crucial to avoid an initial post-surgery infection or biofilm formation after implantation. Several antibacterial elements (Cu, Ag, Zn, Zr, etc.) inclusion into PEO coatings on Ti6Al4V alloy have

already been investigated [95, 98, 206, 207] and evaluated in terms of antibacterial activity. Fluoride, on the other hand, has proved an antibacterial effect on different bacteria strains [195] but has not been explored in PEO coatings on titanium.

Herein, the surface functionalization of Ti6Al4V alloy with Ca and P or Ca, P, F and Si-containing PEO coatings is evaluated. Osteogenesis processes (ALP and collagen secretion) and antibacterial properties against *Staphylococcus aureus* of the formed coatings are also assessed.

Coatings characterization

Ti6Al4V PEO coatings were obtained at different treatment times (90, 180, 300 and 600 s) with two different electrolytes (Table 2.2), PEO samples with a Ca and P based electrolyte, and PEO-Si/F samples from a Ca, P, Si and F based electrolyte. The surface morphologies and cross sections of the coatings prepared at different conditions are displayed in Figure 3.28 for PEO and Figure 3.29 for PEO-Si/F, respectively. Tables 3.7, 3.8 and 3.9 show the corresponding EDS point and area analysis (surface and cross-section) and surface characteristics. Coating thickness increases in the same fashion as treatment time (Table 3.9) reaching up to ~ 40 μm for PEO-Si/F electrolyte longer treatment.

PEO-90s and PEO-Si/F-90s samples result in uniform surfaces with reduced small porosity (Figure 3.28 A and Fig.1.29 A). In PEO-180s (Figure 3.29 C) bigger pores with a more uniform distribution are formed compared with PEO-Si/F-180s (Figure 3.29 C), which showed a more heterogeneous surface with protuberances (Figure 3.29 C). These features are more evident after PEO for 300 s, with some of the pores in the PEO-300s and the majority of the pores in PEO-Si/F-300s plugged with deposits associated with compounds derived from electrolytes species (Figures 3.28 E, 3.29 E, 3.28 G and 3.29 G). Huge mushroom-like prominences in the surface of both long treatment times coatings can be distinguished (Figure 3.28 G, 3.29 G), this feature results in an increment of surface roughness values (Table 3.9).

Backscattered scanning electron (BSE) micrographs of coating cross-sections permit a better visualization of the coating features and can be disclosed that all the coatings present a sub-micron size barrier layer adjacent to the substrate and a thick porous part that becomes denser with treatment time (Figures 3.28, 3.29).

Table 3.7. Local EDS analysis of the studied PEO coatings (at.%).

Sample	*% Atomic*							*Ratios*		
	O	**Na**	**Al**	**P**	**Ca**	**Ti**	**V**	***Ca/P***	***Ca/Ti***	***P/Ti***
PEO-90s	66.5	0.7	1.5	7.0	8.2	15.4	0.8	1.2	0.5	0.5
PEO-180s	65.9	0.8	1.0	7.6	9.2	14.8	0.6	1.2	0.6	0.5
PEO-300s	63.7	1.1	0.8	8.5	11.5	14.0	0.5	1.4	0.8	0.6
PEO-600s	64.4	2.2	0.4	11.3	17.3	4.6	0.0	1.5	3.8	2.5

Table 3.8. Local EDS analysis of the PEO-Si/F coatings (at.%).

Sample	*% Atomic*									*Ratios*		
	O	**F**	**Na**	**Al**	**Si**	**P**	**Ca**	**Ti**	**V**	**Ca/P**	**Ca/Ti**	**P/Ti**
PEO-Si/F-90s	64.3	1.6	1.1	1.2	2.0	5.8	10.4	13.0	0.6	1.8	0.8	0.4
PEO-Si/F-180s	60.2	6.3	0.9	0.8	2.1	7.3	13.0	9.0	0.3	1.8	1.4	0.8
PEO-Si/F-300s	57.4	7.9	0.9	0.8	2.2	8.2	14.1	8.1	0.4	1.7	1.7	1.0
PEO-Si/F-600s	56.8	9.7	1.1	0.7	2.3	8.0	14.7	6.5	0.3	1.8	2.3	1.2

Minimum pore size is comparable in both coatings and does not change much during PEO processing, while maximum pore size increases with treatment time, the effect being more pronounced in Si/F-free PEO coatings. This is a typical feature of PEO coatings and is related to longer lasting microdischarges as the coating thickness increases. The surface pore population density was evaluated only for the coatings with regular pore morphology (Table 3.9). The values were greater in Si/F-free PEO coatings compared with PEO-Si/F for all treatment times.

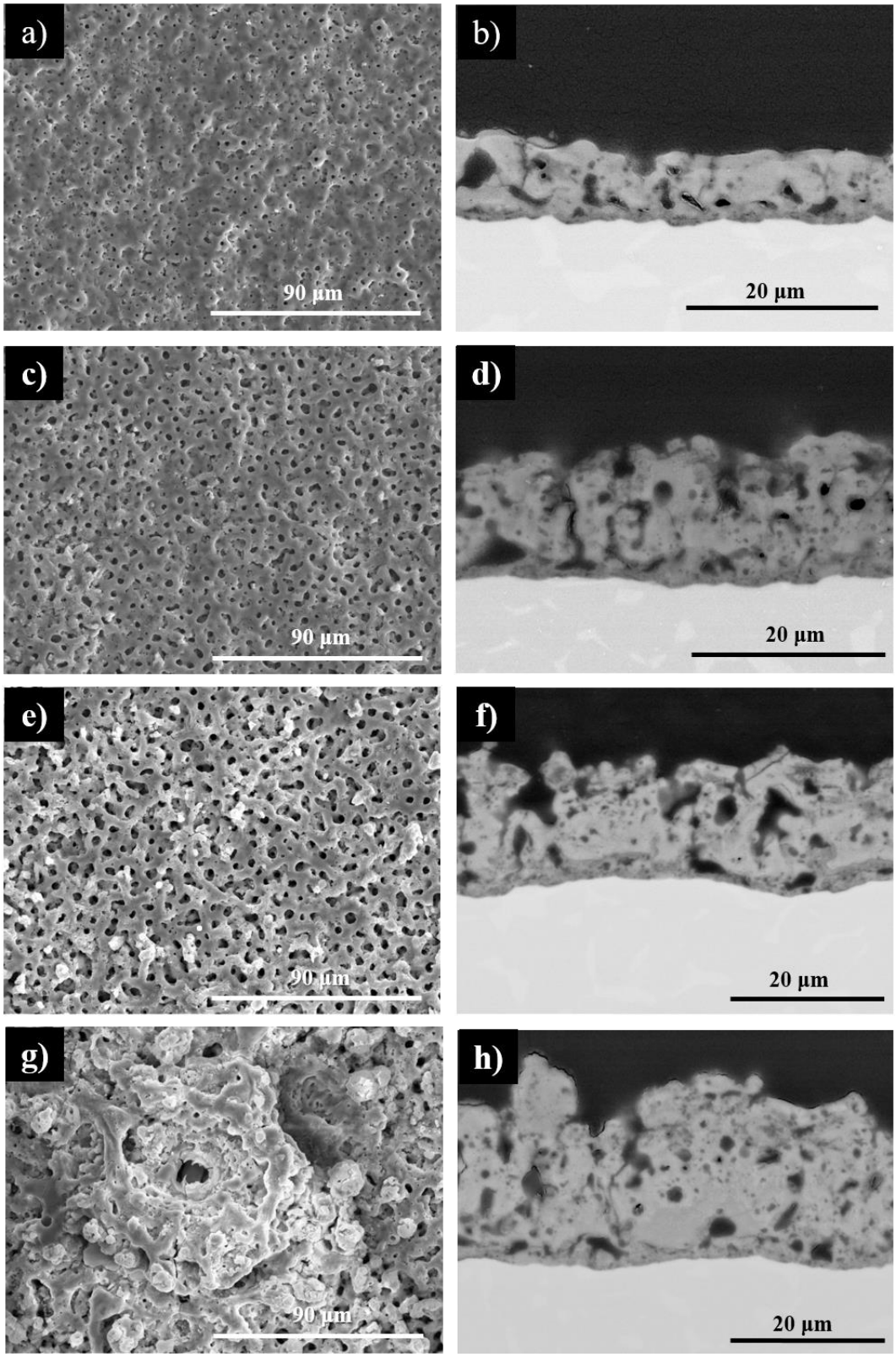

Figure 3.29. Secondary electron plan view micrographs and backscattered electron cross-sectional micrographs of the PEO coatings produced after 90 s (a,b), 180 s (c,d), 300 s (e,f) and 600 s (g, h).

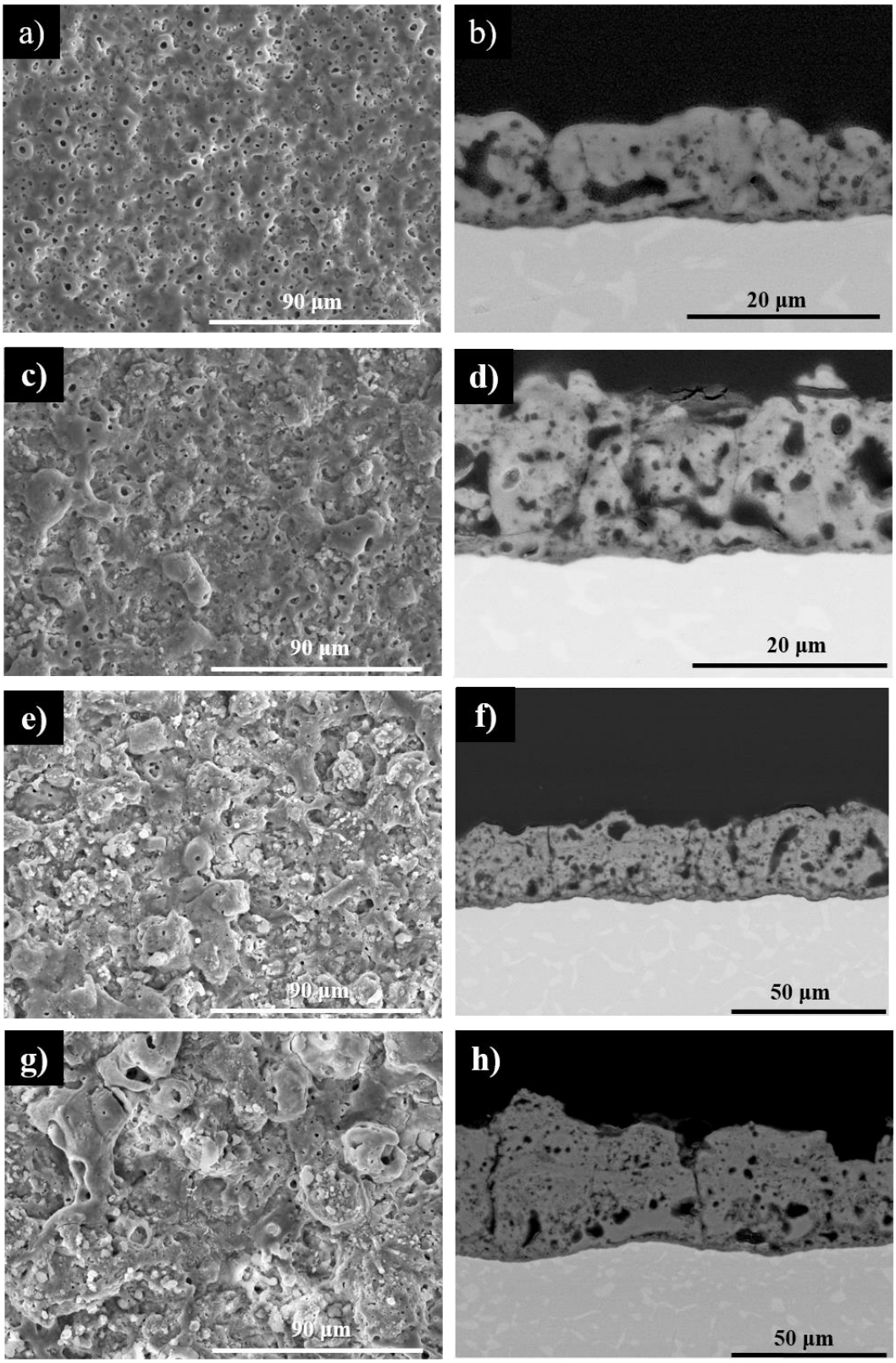

Figure 3.30. Secondary electron plan view micrographs and backscattered electron cross-sectional micrographs of the PEO-Si/F coatings produced after 90 s (a, b), 180 s (c, d), 300 s (e, f) and 600 s (g, h).

Surface area EDS analysis of the coatings (Tables 3.7 and 3.8) obtained by SEM revealed that bioactive elements (Ca, P, Si and F) were successfully incorporated from the electrolyte into the coatings. The greatest Ca/P ratio was found for coatings formed in PEO-Si/F electrolyte (~ 1.8 Ca/P, Table 3.7); Ca/P ratios in the surface of the coatings formed in PEO electrolyte were inferior and increased with treatment time from 1.2 to 1.5 (Table 3.7). These ratios can be compared with mineralized bone tissue that is known to have a Ca/P ratio of ~1.67 (hydroxyapatite stoichiometry).

Table 3.9. Surface characteristics of the studied coatings.

Coating / Characteristics		*PEO*				*PEO-Si/F*			
		90 s	*180 s*	*300 s*	*600 s*	*90 s*	*180 s*	*300 s*	*600 s*
Thickness (μm)		6.4 ± 1.1	12.7 ± 1.4	15.2 ± 1	27.1 ± 3.8	9.5 ± 1	17.2 ± 1.6	21 ± 1.5	40 ± 4.6
Roughness (μm)	*Ra*	1.1 ± 0.19	1.1 ± 0.2	1.4 ± 0.01	3.7 ± 0.40	1.3 ± 0.01	1.7 ± 0.06	2.9 ± 0.2	6.3 ± 1
	Rz	6.6 ± 0.9	6.8 ± 0.5	8.6 ± 0.05	24.2 ± 2.62	8 ± 0.2	16.7 ± 0.14	16.7 ± 0.14	36.6 ± 4
Pore size (μm^2)	*Max.*	4.2 ± 0.9	14.2 ± 1.3	28.1 ± 4.6	57± 20	7.7 ± 1.5	12.9 ± 4	24 ± 6.6	39 ± 4
	Min.	0.9 ± 0.5	0.7 ± 0.4	0.9 ± 0.4	0.6 ± 0.3	0.8 ± 0.3	0.6 ± 0.4	0.9 ± 0.6	0.78 ± 0.18
Surface pore population density (*pores/mm*^{2})		~65600	~64700	~45600	*	~30900	~43700	*	*

*Not evaluated due to the extremely heterogeneous surface morphology.

A XRD examination of PEO coatings (Figure 3.31) was performed in order to obtain information about the formed crystalline phases after the electrochemical treatment. From the diffraction patters can be depicted that for 90 s coatings rutile and anatase are the only phases present. As already observed in Section 1.1.1 for Ti grade I the rutile peak intensity increases with treatment time since it is a phase stable at high temperatures (>400ºC) and anatase-to-rutile conversion occurs as the duration and temperature of the plasma microdischarges increases with treatment time. Likewise, from 180 s treatment time other bioactive species such as hydroxyapatite (HA, $Ca_5(PO_4)_3OH$) and fluorapatite (FA, $Ca_5(PO_4)_3F$) start to appear in XRD spectrum (Figure 3.31 B), although in PEO electrolytes hydroxyapatite appears after 300 s (Figure 3.31 A). Hydroxyapatite and fluorapatite are widely described to promote bioactivity [208, 209].

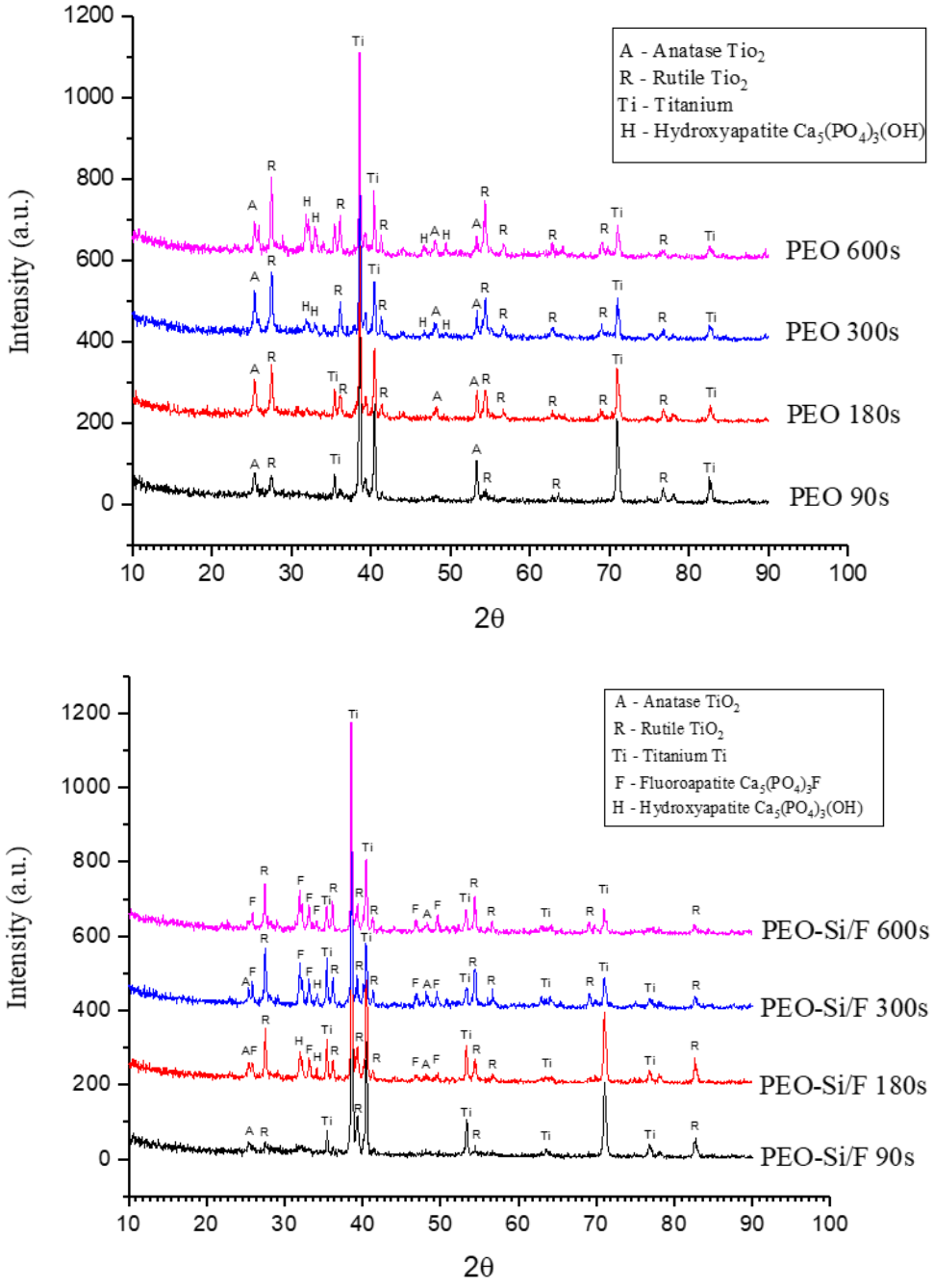

Figure 3.31. X-ray diffraction patterns for the coatings: PEO (a); PEO-Si/F(b).

Four types of coatings were selected for ion liberation studies, *in vitro* cell culture and antibacterial effect; 180 s coating for each electrolyte as an intermediate condition and 600 s as the thicker coating with a major % of bioactive species and crystalline phases.

Ion release

The release of bioactive elements from the coatings (PEO-180s, PEO-600s, PEO-Si/F-180s and PEO-Si/F-600s) was studied after immersion in 0.9 wt.% NaCl at 37ºC. F content, of great interest for the antibacterial properties of the implant, was measured by ISE at different time points for 30 days. This could constitute the most crucial period for its mechanism of action avoiding a post-implantation infection. The measured F^- content in the liquid diminished with immersion time from 32.7 μg/cm^2 to 18.6 μg/cm^2 in PEO-Si/F-600s and from 13.2 μg/cm^2 to 7.4 μg/cm^2 in PEO-Si/F-180s (Figure 3.32 B). The higher F^- release in PEO-Si/F-600s coating is related to its greater thickness and higher surface F content (6.3 vs. 9.7 at. %).

Table 3.10 and Figure 3.32 (A) present the ion liberation measurements obtained by ICP-OES after 60 days of immersion. Regarding the release of the remaining ions, a tendency is observed for Al, Si and Ti liberation from PEO-Si/F coatings as increases with anodizing time but remains in a similar range for Si/F-free PEO coatings. As for V, its release from the coatings is higher compared to the Ti alloy which no μg of this element were detected. Ti release can be considered insignificant from thin coatings (180 s) and uncoated Ti6Al4V and was higher from the thick coatings (~ 0.1 μg/cm^2), suggesting a good long-term electrochemical stability of the materials. Considering ~2 cm^2 implant area, the ion release amounts for Al, V and Ti is far below the cytotoxic values [210, 211]. PEO-Si/F-600s stands up as the PEO-coated sample with the highest amount of bioactive elements (Ca, P and Si) release of all the evaluated samples. High release of these elements is essential for osteogenic processes and bone mineralization, hence the generation of amorphous Ca- and P-containing phases must be taken in consideration in surface bioengineering by PEO as there are easily liberated to the microenvironment.

Table 3.10. Ion liberation from PEO and PEO-Si/F coatings after 60 days of immersion in 0.9 wt.% NaCl determined by ICP-OES.

Samples	*Elements (μg/cm^2)*					
	Ca	**P**	**Si**	**Ti**	**Al**	**V**
PEO 180s	74.3 ± 3.8	49.1 ± 2.5	0 ± 0	0.01 ± 0	0.2 ± 0.0	0.9 ± 0.0
PEO 600s	58.0 ± 3.2	53.6 ± 2.5	0 ± 0	0.1 ± 0.01	0.1 ± 0.0	0.9 ± 0.0
PEO-Si/F 180s	47.9 ± 2.5	29.0 ± 1.3	13.9 ± 0.6	0.01 ± 0	0.2 ± 0.0	0.9 ± 0.0
PEO-Si/F 600s	220.5 ± 12.6	105.8 ± 5.0	37.2 ± 1.9	0.1 ± 0.01	0.2± 0.0	1.0 ± 0.1
Ti6Al4V control	0 ± 0	0 ± 0	0 ± 0	0.01 ± 0	0.3 ± 0.0	0.0 ± 0.0

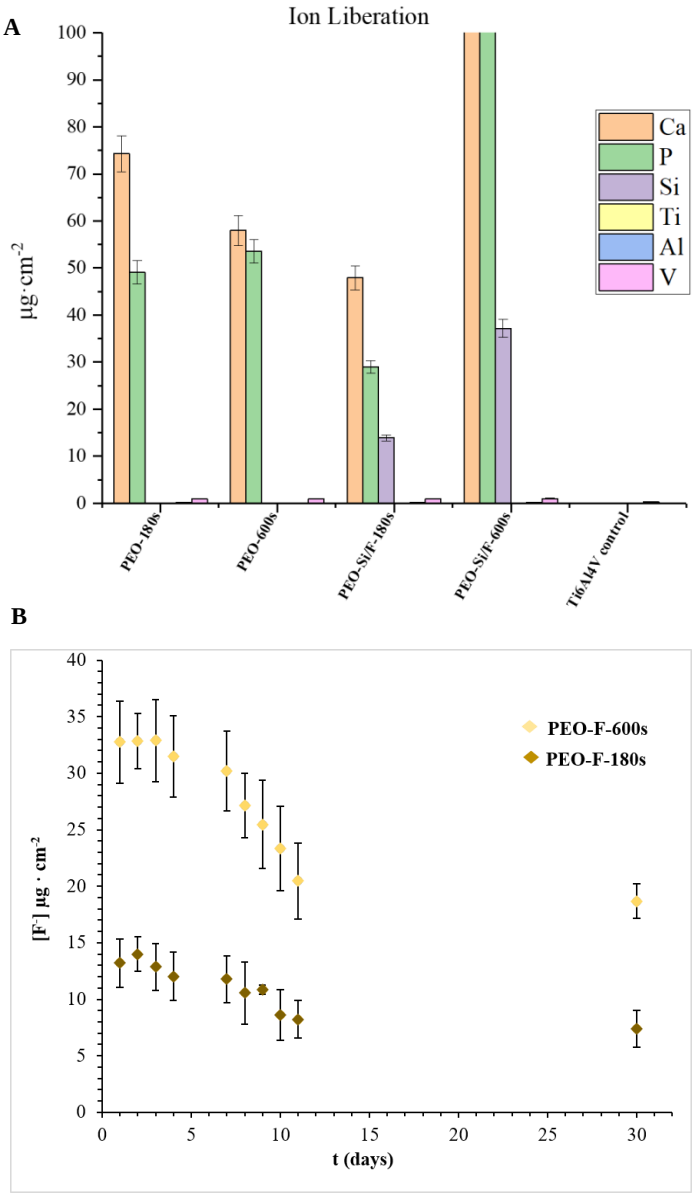

Figure 3.32. Ion liberation (Ca, P, Si, Ti, Al and V) from PEO and PEO-Si/F coatings after 60 days (A). Fluoride ion liberation from PEO-Si/F coatings after 30 days of immersion in 0.9 % NaCl (B).

Osteoblastic response

Based on characterization of the coatings 180 s and 600 s treatments were selected for *in vitro* cell studies. A proper osteoblastic response is expected from a potential new surface modified implant as it has been found that ions associated with Ti6Al4V alloy inhibited the normal differentiation to mature osteoblasts of bone marrow stromal cells [212] and in total hip replacement patients presented toxic effects [213].

In order to evaluate the osteoblastogenesis process over the selected samples, the preosteoblastic MC3T3 cell line was seeded over the samples at a cell density of 2×10^4 cells/cm^2 and allowed to grow for 24 h, then were change to the differentiation medium and allowed to differentiate for 168 h.

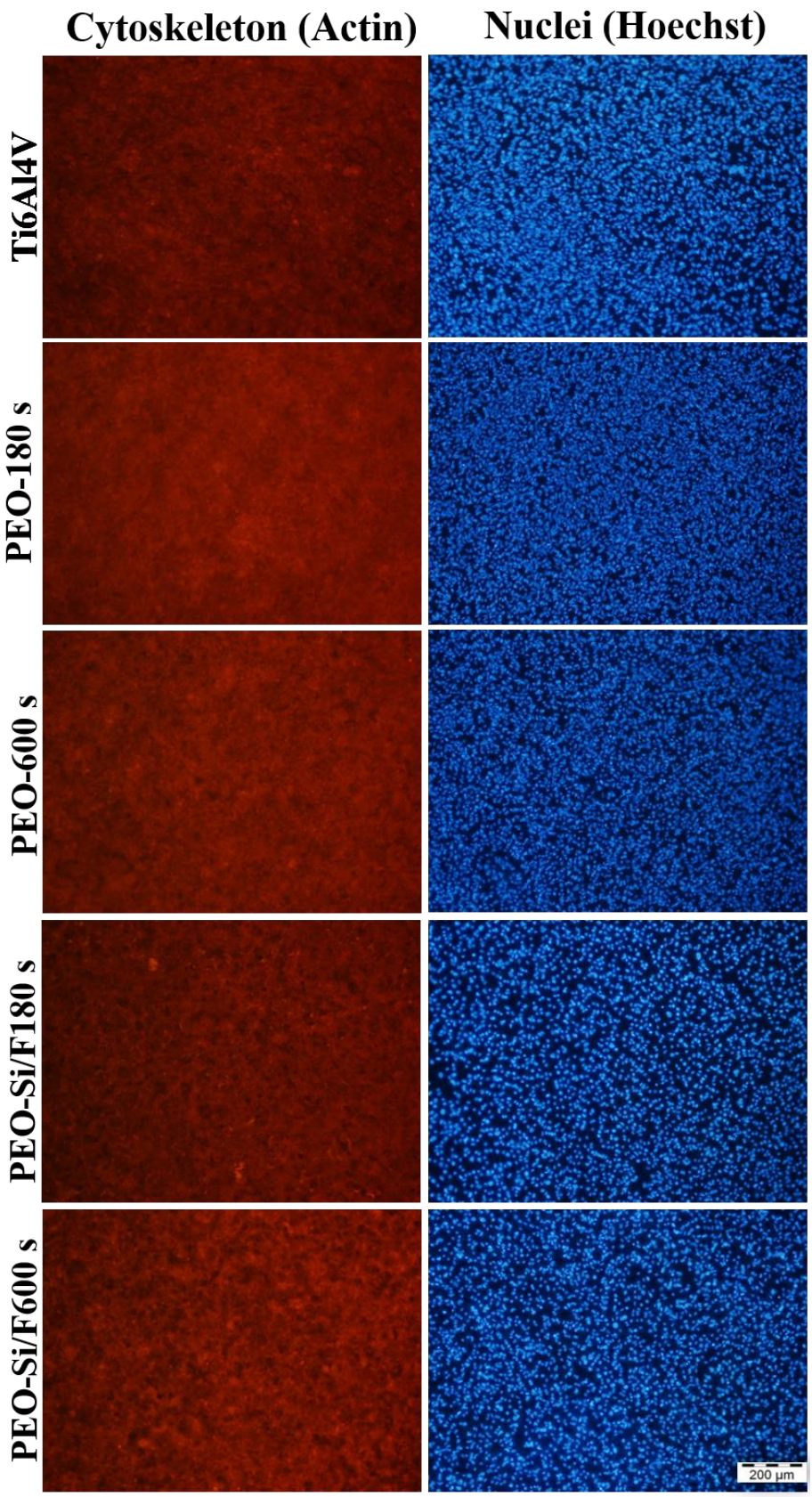

Figure 3.33. MC3T3 pre-osteoblastic cells are induced to differentiate over the Ti6Al4V alloy surfaces: an actin (red, left column) and Hoechst (blue, right column) staining was performed at 168 h in all the samples.

At end point of the culture (168 h), a cytoskeleton and nuclei staining was done to evaluate the growth and monolayer formation of cells proliferating over Ti6Al4V, PEO-180s, PEO-600s, PEO-Si/F-180s and PEO-Si/F-600s. An extended monolayer was observed in all the conditions with different nuclei disposition, the latter appear more separated in PEO-Si/F-180s and PEO-Si/F-600s. Still, actin staining of the cytoplasm discloses a denser monolayer in PEO coatings compared with the Ti6Al4V control (Figure 3.33). The metabolic activity results obtained from Alamar Blue assay at 168 hours show that all the coatings were cytocompatible, showing a similar response compared to the bare Ti4Al6V alloy. Following this first assessment an activity assay of an early bone matrix synthesis marker (ALP) was made after 168 h of differentiation stimulation of the preosteoblastic cell line. ALP was expressed over all of the samples and displayed no significant differences between the samples, nevertheless, over PEO-Si/F-180s the response was improved in comparison to control Ti6Al4V (Figure 3.34 B).

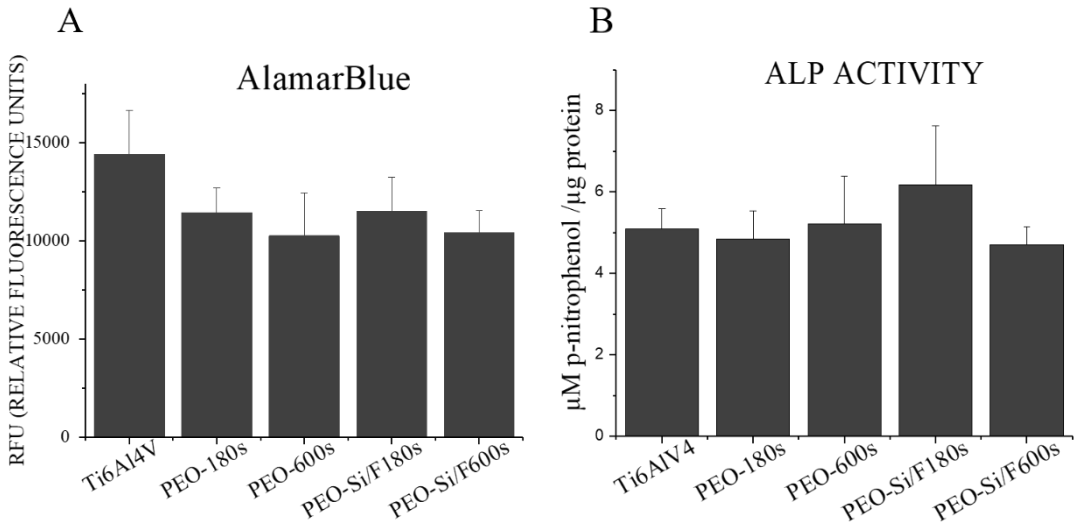

Figure 3.34. Metabolic activity at 168 h was evaluated by Alamar Blue on PEO coatings with and without Si/F (A); an early osteogenic marker ALP (alkaline phosphatase) activity was measured at 168 h on PEO coatings with and without Si/F (B).

Besides ALP, others makers such as collagen secretion can be used to evaluate the differentiation state of the culture. This fibrous structural protein serves as a scaffold for mineralization of the organic part of bone matrix and it is expressed when the cell differentiation is promoted. Sirius red staining absorbance values (Figure 3.34 B) revealed an increase in collagen secretion over all PEO-treated samples compared to the control Ti6Al4V alloy. The highest difference in collagen secretion is observed between the control sample and those obtained in the Ca and P-based electrolyte (PEO-180s and PEO-600s). In contrast, collagen secretion in Si/F-containing coatings was reduced, probably due to the previously described delay in monolayer formation.

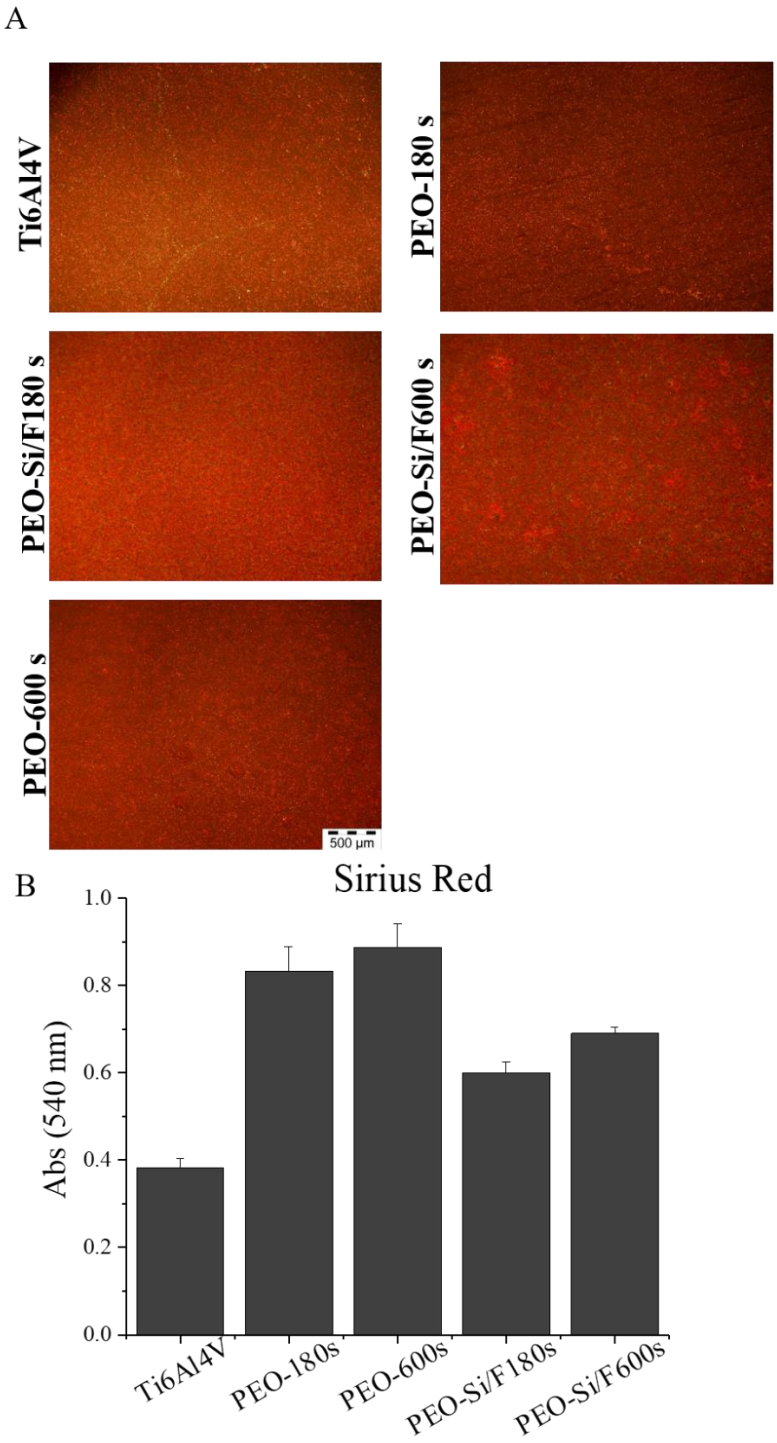

Figure 3.35. Collagen secretion staining and quantitative measurement: micrographs of the collagen staining over the samples (a); colorimetrically quantitative values of absorbance at 540 nm (b).

Antibacterial activity

The evaluation of antibacterial activity of PEO and PEO-Si/F coatings was done with *Staphylococcus aureus*, using it as model of a very common pathogenic strain in orthopaedic implants. Bacteria was inoculated onto the samples and cultured for 24 hours to allow the biofilm formation. After this time bacterial adhesion and antibacterial properties of the PEO coatings were

assessed by a Live/Dead staining. This technique allows us to discriminate between living (green) or dead bacteria (red) through fluorescence analysis. In Figure 3.36 depicts merge images of the staining (a), total bacteria surface coverage, % (b) and dead bacteria over surfaces, % (c).

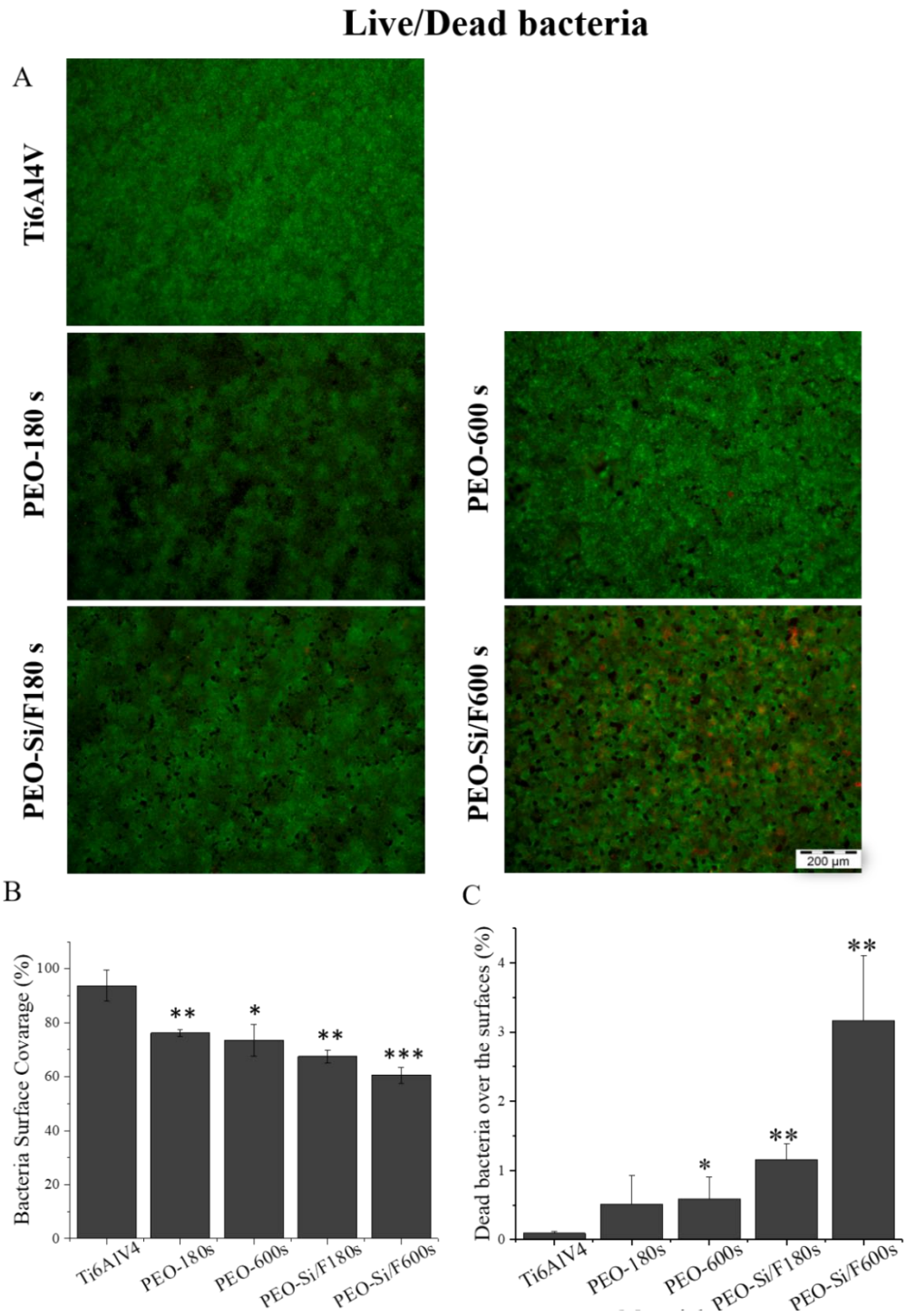

Figure 3.36. Live and dead merge staining of Staphylococcus aureus biofilm formation over the materials (Ti6Al4V, PEO-180s, PEO-600s, PEO-Si/F180s and PEO-Si/F600s) after 24 h of inoculation (a). Total bacteria surface coverage, % (b). Dead bacteria over surfaces, % (c). Green for live bacteria and red for dead bacteria. Live/Dead assay: image analysis. Significant differences stand for: *($p \leq 0.05$), **($p \leq 0.01$), ***($p \leq 0.001$).

A thick bacteria biofilm was developed on Ti6Al4V bare alloy. Related to PEO-180s and PEO-600s coatings lower bacterial densities were present (Figure 3.36 B), even though still a ~75% of surface coverage was detected. Fluoride containing coatings showed the lowest level of bacteria proliferation with PEO-Si/F-600s standing up with small clusters of dead bacteria bodies. Bacteria coverage area was down to ~60% with statistical differences compared to coating-free sample, moreover, the % of dead bacteria over the surface was the highest of all. A magnification of the state of the culture can be observed in Figure 3.37 indicating no bacterial growth inside the pores of both of the F-containing coatings.

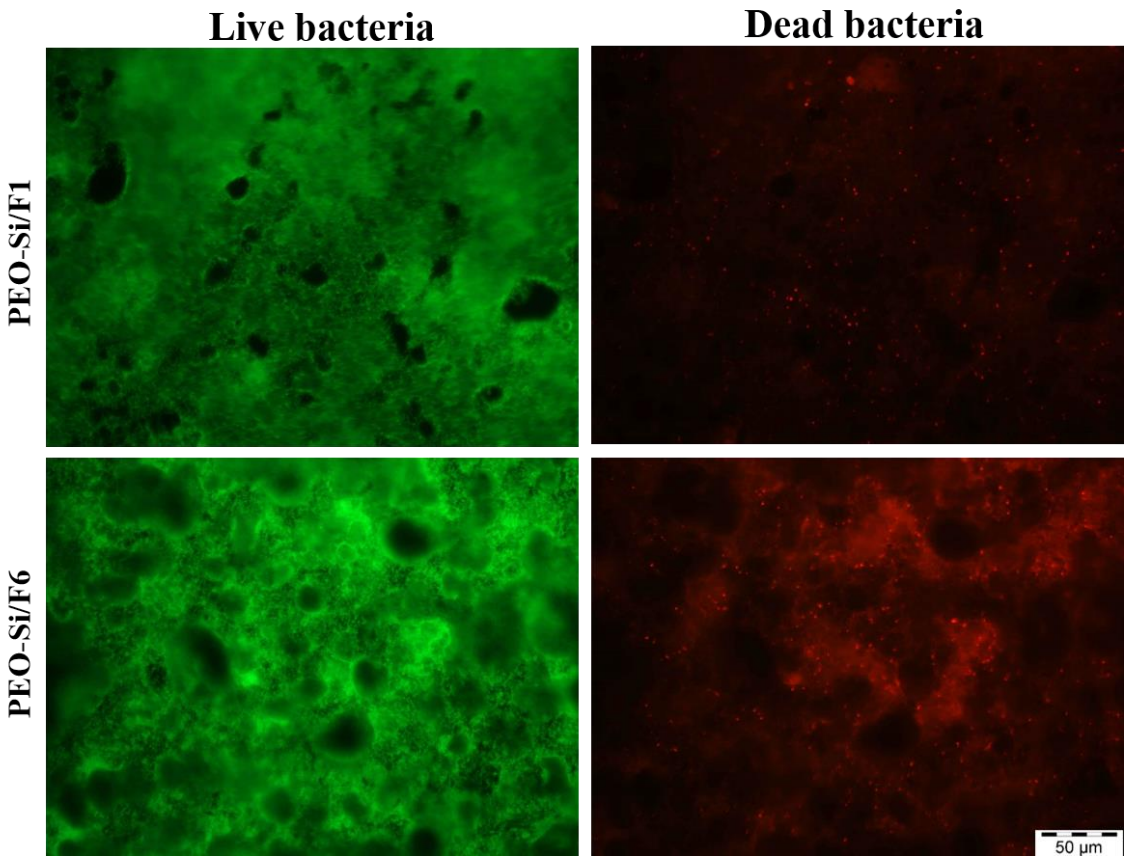

Figure 3.37. Magnification of the F-containing coatings showing no bacterial growth inside the pores. FITC filter for live bacteria (left column) and TRICT filter for dead bacteria (right column).

1.3. Discussion

In Section 1.1.1 a thin and a thick Ca and P-containing coatings were evaluated *in vitro* and *in vivo* over dental-oriented Ti CP surfaces. The rutile fraction increased with treatment time from 23% to 85% and the surface Ca/P ratio in the coatings also increased from 2.0 to 4.0. PEO treatments of shorter duration (90 s) come up with thinner coatings (5 μm in our case) and can diminish energy consumption with resultant important technological benefits such as reduction of implant manufacturing costs. However, PEO-90s presented higher pore population density, smaller pore size, lower roughness values and lower incorporation of Ca and lower Ca/P ratio; affecting its topographic and compositional features and in consequence the biological response of this coating.

In vitro studies revealed a good cell adhesion, expansion and proliferation of murine osteoblasts and osteoclasts over both of the PEO coated surfaces evaluated. Cell differentiation studies disclosed an increased ALP expression of osteoblasts (Figure 3.4) over the coating with Ca/P = 2.0 and 77% of anatase (PEO-90s), promoting bone matrix mineralization. It has been described that this molecular pathway regulates skeletal mineralization [214, 215]. ALP regulation might be a consequence in changes in wettability, phase composition, and elemental composition associated with the ion adsorption and release during immersion. PEO-90s is mainly composed of anatase which has been reported to be more bioactive than rutile with regards to osteoblast adhesion and proliferation *in vitro* [216].

On the other hand, osteoclasts were able to differentiate over PEO treatments (Figure 3.6) but with smaller extension compared with Ti CP. Moreover, a greater expression of TRAP for the coating with greater Ca/P ratio and lower pore population density was also found. This could be related to the fact that a range of roughness can promote the osteoclast formation and the greater amount of pores and smaller interpore distances leave little space for the osteoclast growth and expansion, cells cannot fuse with each other easily. Related to the roughness parameters, in other studies smooth surfaces (R_a 0.5 μm) such as PEO-90s (R_a ~0.59 μm) did not promote stable actin rings and mature osteoclasts, whereas rough surfaces (R_a ~4 μm) enhance larger sealing zones and osteoclastic activity [217]. Moreover, RAW 264.7 cells (macrophagic precursors) were also evaluated in absence of RANKL (Figure 3.5) and no significant phenotype change was present in PEO-coatings. These results showed that essential bone processes (matrix synthesis and resorption) occurred over PEO surfaces and were regulated *in vitro* by specific surface features such as elemental and phase composition.

After *in vitro* cell culture studies a drug loading mechanism of the formed PEO coatings was evaluated, using a model protein, bovine serum albumin (BSA), as an example of a potential drug or growth factor. Protein adsorption on the surface of bioceramics, especially the Ca-P based ones,

starts spontaneously and quickly after water adsorption and even before the cellular attachment. Protein adsorption is known to be affected by topography, porosity, composition, wettability, heterogeneity and surface potential [218].

However, in this study with the two evaluated coatings their capacity to retain albumin must be ascribed to the coating chemistry and is based on the interactions of the BSA with the elements/compounds present on the surface. PEO-600s with slightly reduced surface porosity and half transverse porosity than PEO-90s liberated the entire load in 48 h even quicker than Ti CP with no porosity, therefore, no clear correlation with surface or volume porosities of the coatings was found. In terms of wettability both PEO coatings presented a hydrophilicity similar to each other (45º and ~37º).

The differences in protein liberation could be explained by the differences in composition. PEO-600s presents a Ca/P ratio of 4.0 that exceeds by far the stoichiometry of any usual Ca-P-based bioceramic, whether amorphous or crystalline (e.g. tricalcium phosphate, hydroxyapatite, calcium phosphate etc). Hence, Ca and P ions must be mostly present in PEO-600s as dopants and can be easily liberated into the solution. If Ca and P function as anchor points of BSA, their fast release from PEO-600s explains the initial BSA liberation (Figure 3.10). It is known that Ca ions can be attracted and incorporated into albumin, ever since albumin is negatively charged in physiological solutions, attraction and adsorption of albumin to Ti is favoured by a bridge between the albumin and hydroxyl groups on the surface of Ti [219].

This system demonstrated the potential of PEO-treated surfaces to be further modified with other proteins, that could be used as drug carriers (antibiotics, anti-inflammatories, etc.) or growth factors such as BMPs. This BMP-guided regeneration strategy has been previously reported by our group with optimal results [220-222]. Furthermore, BSA unloading rate did not have a clear correlation with volume porosities of the coatings, majority of the loaded albumin was located on the coating surface. The observations suggest that PEO-90s coating with the slowest liberation rate is a potentially candidate for drug delivery in bone regeneration systems. Other strategy could be the use of PEO coatings with fast liberation rate (PEO-600s) to control initial inflammatory response after surgery, for fast anti-inflammatory drug delivery systems purposes.

Besides the incorporation of growth factors or proteins, antibiotics could also be embedded into the pores of the coating, designing the correct liberation time with a major release in the first post-surgery hours to avoid peri-implantitis of dental implants or biofilm formation around orthopaedic implants. Many examples can be found in the literature, as antibiotics such as gentamicin and ciprofloxacin have already been evaluated embedded in hydroxyapatite and eletrophoretically deposited on titanium implants [223]. Gentamicin liberation was also evaluated from TiO_2 nanotubes, that where formed over Ti films deposited by PEO on a Si substrate as possible drug

carriers [224]. Nanocomposite coatings were formed on Ti CP by PEO in a phosphate-based electrolyte containing ketoconazole (antifungal agent) and alumina nanoparticles [225].

Given that marked effect of the coating composition on the cell response and the coating's capacity to interact with model protein was observed *in vitro*, further validation of these coatings was carried out *in vivo*. In order to do so, Noricum implants (Ti grade IV) were coated with PEO-90s and PEO-600s systems. In their *in vivo* response in pig maxilla surgeries, both PEO-coatings showed high but not statistically different BIC values of $92.1 \pm 6.9\%$ and $89.6 \pm 7.4\%$ with higher mean BIC values than for machined Ti CP implants after 8 weeks. Also the Levai Lazcko staining (3.11 B) showed that bone matrix proteins (e.g. collagen) were present as osteoblasts adhere in the material have promoted their formation. Other PEO-coated dental implants have been evaluated *in vivo* by Sul and colleagues [85, 90-94] with improved results in contrast to machined implants. Oxidized implants have also been evaluated in human bone using microimplants to be close to the clinical situation. Ivanoff *et al.* [226] and Shibli *et al.* [227] investigated oxidized and turned implants as control. Both studies concluded that oxidized implants demonstrated more BIC values than turned surfaces. On the contrary, Kim *et al.* [228] used as controls blasted implants (with and without thermal oxidation) compared with oxidized surfaces in animal experiments, after 4 weeks BIC values of the oxidized group were greater than that of the blasted group. However, no statistically significantly different BIC values after 12 weeks were obtained. In general, oxidised implants exhibit stronger bone anchorage than machined implants, in animal studies as well as in human [58].

In our case an improvement of the BIC values could be expected also at the first weeks after the implantation as an improvement of the osteoinduction mechanisms as a consequence of the improved surface characteristics and presence of Ca and P. Ca and P enriched interface should enhance bone homeostasis, allowing osteoclast formation and function and improving final implant fixation. This short time evaluation including molecular biomarkers could provide a significant difference.

Regarding Section 1.1.2 results, electrolyte recipes were modified from those utilised in Section 1.1.1 resulting in true solution electrolytes (Table 2.2) in contrast to the colloid or particles suspension solutions. Use of true solutions is technologically preferable since it avoids the precipitation of the components and a constant requirement of electrolyte agitation. From a technological point of view this could benefit the possible bottom-up process for its possible applications as a surface treatment in dental implants. The incorporation of many species into the electrolyte and consequently into the coating is relatively new [229-231] and in most cases no *in vitro* response is evaluated.

All the potentially bioactive elements present in the electrolyte (Ca, P, Si, Mg, Zn and F) were successfully incorporated into the PEO coatings. However, there were differences in the morphology of the coatings which could be explained by the incorporation of these bioactive species in agreement with those found in other recent studies. For example, S. Lim *et al.* revealed that the presence of ions (Si and Sr) in the electrolyte affected the formation of pores during PEO by decreasing the pore size and increasing the number of pores [209]. J. Yu *et al.* reported a decrease in pore size and number of pores when Mg concentration in the electrolyte was increased [232]. The reduced porosity of the coatings obtained with multi-componential electrolytes must be related to the greater number of incorporated species and compounds. In contrast with the samples obtained by the suspension electrolyte (PEO-90s and PEO-600s), the obtained coatings with the true solutions and intermediate treatment time (300 s) promote the formation of more crystalline phases e.g. MgO, CaF_2, SiO_2, HA and apatite. However, Ti-1PEO based on Ca and P also only promoted anatase and rutile phases (Figure 3.15).

As for the wettability results, amongst all the evaluated materials Ti-4PEO stood out with the lowest contact angle value (~9º). This fact could be explained as it presents more protuberances, greater pores size and the highest roughness values (S_a and R_a). Thus, surface chemistry could also explained it as Ti4-PEO is the only coating that contains HA (Figure 3.15), which is known to have greater wettability values [233] than rutile or anatase. Moreover, this coating was also evaluated in terms of F^- release (Figure 3.16 B) showing a constant level during the first week (~3±0.25 µg/cm^2) and could be especially relevant to prevent a post-operatory infection around the implant.

After the coatings were characterized, osteoclasts formation was assessed over these surfaces. As seen in the previous section surface porosity can determine the expansion of the osteoclast and, as already observed, smaller osteoclasts were formed in PEO samples in contrast to control Ti. This fact could be related to the topography of the surfaces [217, 234], i.e. due to the porosity and roughness of the coatings. Regardless of the smaller size of osteoclasts over the PEO coatings, the sealing zones seemed denser and continuous than the actin rings formed over Ti CP, with a discontinuous morphology and a thinner aspect. It is known that bioactive elements can also modulate the osteoclast differentiation state [235-237], nevertheless, there are not studies that include all this elements combined. The larger osteoclasts (more than 20 nuclei) were found in Ti-2PEO of all PEO treated samples. On the other hand, the smaller osteoclasts were formed on Ti-3PEO, this could indicate that the incorporation of Mg into the coating promotes a more mature state. Mg is known to modulate osteoclastogenesis positively in a determined composition range [238]. Ti-4PEO showed the greatest number of osteoclasts per area although they were small, with less than 20 nuclei. Si could be modulating this characteristic as it has been described to influence osteoclastogenesis in some concentrations [236, 239-241]. Furthermore, Ti-4PEO had

the highest S_a (<4) and R_a (~2.3) values and presented areas with great protuberances (Figure 3.13) could also affect spreading, actin ring area and fusion of the osteoclasts [242].

MC3T3 preosteoblastic cell line cultured with differentiation medium was also evaluated in terms of monolayer formation, metabolic activity and collagen secretion. In contrast to the results of the previous section with ALP expression (Figure 3.4) where only slightly tendencies were found between Ti CP and PEO coatings, when the collagen secretion ability (Figure 3.19) was evaluated quantitatively much higher levels were found for PEO coatings. Collagen is the main component of the organic matrix and it provides a scaffold for a highly organized arrangement of oriented apatite crystals. It is considered a template for mineralization and deposition of the inorganic matrix. Therefore, if more secretion of collagen has been detected over the PEO coatings it can be considered a more mature state of differentiation.

Nevertheless, no differences between the four PEO samples were observed and it cannot be correlated with the ICP results (Table 3.6) which showed a differential liberation of Ca and P from Ti-1PEO compared with other coatings. On the other hand, liberation of Zn, Si and/or Mg could probably be compensating for the reduction of Ca and P in Ti-2PEO, Ti-3PEO and for reduction of P in Ti-4PEO and thus explain the similarities in collagen secretion. On the other hand, in order to discriminate the possible specific implications of these bioactive in early and late stages of bone matrix synthesis, more genetic expression osteoblastic markers should be evaluated.

All these results taken together could indicate that a modulated topography of the coatings and the incorporation of bioactive elements (Ca, P, Si, Mg, Zn and F) into the ceramic coating can favour an enhanced remodelling/osseointegration process [241, 243].

Orthopaedic implants

New candidate materials are still being investigated to be applied in orthopaedics. Oxidised Zirconium (Oxinium by Smith and Nephew) was introduced to the orthopaedic market in an attempt to reduce Polyethylene (PE) wear associated failures and increase the longevity of the prosthesis. Oxinium consists in a zirconium/niobium alloy (97.5% Zr:2.5% Nb) metal substrate which undergoes a surface transitions into a ceramic-like zirconium oxide outer layer when heated to 500 °C and it has been recently evaluated in under 50 years patients for total knee replacements with promising results [244]. A new knee replaced with this material is expected to last for 20–25 years considerably more than CoCr alloy and PE implants last (15–20 years) [23].

Pure Zr and Zr alloys have not widely been commercialized in the orthopaedics field due to its high cost and considerable higher density (6.5-6.7 g/cm^3) in contrast to Ti alloys (4.5 g/cm^3). Zr yield strength 230 MPa vs 758-1117 MPa of Ti alloys, making it less suitable for load-bearing

applications. However, Ti6Al4V presents a higher elastic/young's modulus (110-119 Gpa) than Zr (88 Gpa), more close to bone tissue, resulting in a diminished stress shielding process. Also, Zr possesses superior corrosion resistance and low wear in comparison to Ti alloys [245]. Alloying elements such as Al or V can be toxic in contrast Zr presents high biocompatibility.

Orthopaedic materials, such as Zr, also require surface modifications to improve their biocompatibility. The ability to "mimick" the biology of surrounding tissue or promote wound repair is thought to improve the integration of biomaterials and reduce the foreign body reactions. Zr anodizing provides a roughning of the surface by means of P deposition. Surface roughness can be classified based on the modified dimensions such as topography height, width, rigidity and spacing and patterns. Generally rough surfaces can modify cell adhesion [246, 247], density and spreading [248, 249], enhanced proliferation and differentiation [250]; still these responses are dependet on cell type and on the method of surface modification. In our study, premyoblastic, endothelial, osteoblastic and osteoclastic cells were evaluated over the Zr 0 V, Zr 30 V and Zr 60 V samples showing a preference for anodized surfaces. In all the cell types evaluated an aligned disposition was observed matching the oxide treatment. Premyoblastic, which are able to transdiffentitied into osteoblasts [251, 252], and osteoblastic cells can recognize the implant surface and are able to attach and proliferate fast over Zr samples as seen in Figure 3.21 and 3.22. Interestingly, anodizing of Zr samples induced cells to growth with a define direction. These results are in agreement with some reports that present an enhancement in osteoblast like cell attachment after 24 h on rough Ti, demonstrating that surface topography also caused the alignment of cells parallel to the 10 μm grooves presented on the metal surface [253]. Moreover, endothelial cells were able to formed a dense monolayer after just 48 h of cell culture, these cells are of high importance for the promotion of the vascularization of the tissue. Anodized surfaces could be providing an anchoring site (oxides and P, in this case) for protein binding favouring the cellular adhesion and proliferation and consequently, avoiding a poor osseointegration.

Moreover, a premilinar study with macrophage precursors for immune system evaluation of Zr samples showed no polarization to M1 states, a precursor of foreign body giant cell apparition, fibrous tissue formation and implantation failure [254]. In contrast, M2 elongated states were detected in Zr 60 V, a phenotype that will become a sign of implantation success. Related to the bone resorbing cells, a higher number of osteoclasts per area in anodized treatments was detected with denser and continuous actin rings that are in charge of sealing the resorptive area. Additionally, a "zipper like" actin-based (Figure 3.27) and more resorption vesicles were found on the anodized surfaces (Figure 3.28). The former feature suggests an improvement in multinucleated osteoclast fusion and an acceleration of the process. Additionally, osteoclasts actin filaments are aligned following the oxide treatment, showing an intimate contact between the material surface and bone cell populations. Osteoclasts are of great importance as can affect tissue

healing processes and regulate osteoblast proliferation and a correct matrix deposition rate. These results contrast with the observed on Ti grade I PEO in the previous sections where osteoclasts were smaller, R_a valuesof Zr are lower in comparison to PEO surfaces as in anodised samples the topographic changes are less appreciable with no porosity. As observed before, the presence of pores can modulate greatly the size of the formed osteoclasts. It is therefore evident that anodized Zr surface allows for bone cell adhesion and proliferation, affecting cytoskeleton alignment and permitting bone cell differentiation positioning the Zr as a promising candidate as permanent cementless implant.

Alternatively, Ti6Al4V is widely used daily in orthopaedic applications in contrast to Zr implants; the main concern about its use is the possible cytotoxicity of the alloying elements (Al and V) as a consequence of long-term wear. Moreover, there is also major problems associated with a possible post-implantation infection leading to the formation of biofilm around the implants. Therefore, another strategy different to drug loading proposed in Section 1.1.1 could be the incorporation of antibacterial elements into the core of the coatings, such as F in our case. In Section 1.2.2 Ti6Al4V PEO coatings are characterized and evaluated in terms of osteogenesis and antibacterial effects. The release of these elements from the coatings is crucial for their possible effect on the adjacent bacteria and a quick response at the very first moments of the bacteria colonization is desired. For this matter ion release from the coatings was evaluated, Figure 3.32 depicts the liberation of fluoride-containing coatings and as expected a higher release from the thicker coating was detected. This correlates with the EDS results (Table 3.8), PEO- Si/F-600s displayed the higher at.% of F. Moreover, the greater quantities liberated into the medium were detected at the first five days, a boost of F^- could be release from the coatings at the first stages of the implantation process. The discussion of the chemistry causing the decreasing trend of the F-release is beyond the main focus of this Thesis and can be found elsewhere [5]. In terms of cytocompatibility the optimal consumption amount recommended by the World Health Organization for an adult is 1.4-3.4 mg/d.

Other elements were also measured, including bioactive ones (Ca, P and Si) and substrate elements (Al, V and Ti). In order to relate the liberation results with their possible effect on osteoblastic cells, a linear backwards extrapolation of the ion release of the elements to the time point of 4 days of immersion in 0.9% NaCl can be done. For PEO-Si/F-600s coating with the highest ion release, the amounts of these elements would be: 0.026 $\mu g/cm^2$ Al, 0.08 $\mu g/cm^2$ V, 0.013 $\mu g/cm^2$ Ti, 15.75 $\mu g/cm^2$ Ca, 7.56 $\mu g/cm^2$ P, 2.66 $\mu g/cm^2$ Si and 31.48 $\mu g/cm^2$ F. These values suggest that a positive cell response with a potential antibacterial effect can be expected as the release of bioactive elements from the coating (Ca, P, Si, F) is noticeably higher compared to substrate elements.

Regarding the osteoblastic behaviour, actin and Hoechst staining depicted a more separated disposition of the cells in PEO-Si/F-180s and PEO-Si/F-600s (Figure 3.33). This feature might be associated to the greater roughness of the coatings containing Si and F (Table 3.8), therefore the cytoplasm distribution differs. As it has been described, PEO coatings form from fluoride containing electrolytes promote a more abrupt topography and as with electrolytes from Section 1.1.2 with bioactive species the porosity of the coatings is reduced with the incorporation of Si and F. In particular, in PEO-Si/F-600s unstained areas corresponding to the raised parts of the surface topography are observed, this could be a consequence of surface protuberances height is greater than the monolayer thickness.

Differentiation markers studies revealed no significant differences in ALP expression for PEO coatings, as observed before with Section 1.1.1 coatings, however PEO-Si/F-90s presented the highest values. In contrast, Sirius red staining corresponding to collagen secretion (Figure 3.35) showed an upward trend for PEO coatings compared with Ti6Al4V. This result is in agreement with the obtained in Figure 3.19 for Ti CP, observing in both scenarios an upregulation of collagen secretion.

As it is well known, osteoblasts differentiation process goes as follows; in Stage 1 the cells continue to proliferate and express fibronectin, collagen, TGFβ receptor 1, and osteopontin. subsequently in Stage 2 they exit the cell cycle and start differentiating, while maturating the extracellular matrix with ALP and collagen. Lastly, in Stage 3 matrix mineralization takes place when the organic scaffold is enriched with osteocalcin (promotes deposition of mineral substance). Osteocalcin is the second most abundant protein in bone after collagen [255].

Taking into account these facts and considering that the osteoblastogenesis process has been evaluated for 7 days, collagen secretion has been determined at the stage 2 where cells growing over PEO coatings could be accelerating the differentiation process. Moreover, in this cell model the mineralization processes do not take place until 14 days reaching the maturest state of differentiation around 21 days. For instance, Wang *et al.* have demonstrated that at 14 and 21 days there is a higher difference in differentiation markers (ALP, mineralization and collagen content) between the control Ti alloy and the PEO coatings obtained in a P-based electrolyte (3 at.%), also they reported comparable cell adhesion and proliferation values at 3, 5 and 7 days as obtained with our results [256].

These results indicate that fluoride in the coating does not bear an adverse effect on osteogenic processes and the use of PEO coatings for surface treatment of orthopaedic implants could help to avoid the negative features related to the osteogenic capacity that have been observed during the years with this alloy.

Furthermore, reduced bacteria colonization was obtained with PEO coatings with incorporated F (Figure 3.36). The most noticeable antibacterial effect was detected in the coating with the greatest content of fluoride (PEO-Si/F600s), the reduction of bacteria surface coverage obtained was down to 60% and death of ~3% of bacteria. Fluoride mechanism of action is based on the inhibition the biosynthetic metabolism of bacteria by enzyme inhibitor, e.g. glycolytic enzyme enolase. Membrane permeability to protons increases and F-ATPases function of exporting protons is compromised, leading to cytoplasmic acidification and acid inhibition of glycolytic enzymes. Therefore, fluoride induces the decrease of acid tolerance of the bacteria [257]. Other strategies reported in literature include multi-step treatments such as implants formed by selective laser melting were biofunctionalized by embedding silver nanoparticles in an oxide surface layer grown using plasma electrolytic oxidation (PEO) in Ca/P-based electrolytes proving antibacterial effect [258]. In contrast to F, Ag mechanisms of action are associated to their interaction with thiol (sulfhydryl) groups and by its union to important functional groups of enzymes. Moreover, Ag ions produce the release of K^+ ions from bacteria which is related with many important enzymes function [259]. Surface chemistry can also be tuned to obtain an antifouling/antiadherent surface.

Taking into account these results, new possible commercial or clinical uses of PEO-treated Ti alloys can be proposed. An orthopaedic implant functionalized with fluoride ions could be obtained in just a single step surface modification, providing bioactive properties and modulated topography, and, on the other hand, antibacterial effects.

Chapter 2: Biodegradable materials for orthopaedic and vascular applications

2.1. Bioactive multi-elemental surface functionalization of Mg-Ca alloy

New biodegradable materials are in constant research as for some applications there is no need for a permanent implant and avoiding a second surgery is of great interest. Mg alloys are highly biocompatible materials with emerging application in bone reconstruction plates (specially in children) and cardiovascular stents [260]. Ca-bearing Mg alloys (Mg−Ca) are good candidates as Ca constitutes a key element of human bone. While Mg−Ca alloys present good mechanical properties, their corrosion resistance is reduced. PEO technology has been proven as an outstanding technique to control magnesium corrosion rate [119] and also being able to upregulate cell response.

Functionalization of Mg0.8Ca alloy by PEO using electrolytes containing bioactive elements (Ca, P, F and Si) is explored in this Chapter. An evaluation of the liberation of the incorporated bioactive elements from the coated alloy and biovalidation of the materials by direct studies and extracts incubation using premyoblast, endothelial, osteoblast and osteoclast cell models is performed.

2.1.1. Coating characterization

PEO coatings were obtained on Mg0.8Ca alloy with four different electrolytes (Table 2.3). A Ca-P based electrolyte (PEO-B), two different Ca, P and F containing electrolytes (PEO-4F and PEO-8F) and a Ca, P and Si-based one (PEO-9Si). Aiming to gather information about the surface morphologies and transversal characteristics of the formed coatings SEM micrographs were obtained (Figure 4.1) with the indication of their respective surface area and local area EDS analysis (Table 4.1). The Ca-P based coating displayed the lowest thickness (~6 µm) and roughness value (R_a ~0.7 µm) (Figure 4.1, Table 4.2) whereas as a consequence of the incorporation of Si into the electrolyte the thickness of the coating was doubled (~13 µm). A homogenous pore size and protuberances among the pores were found for PEO-9Si (Figure 4.1), a structure that bears a resemblance to bone structure.

BSE images (cross-sections) depict a superior compactness and uniformity of PEO-9Si compared to the other PEO-coatings. As for its roughness, the value was comparable to PEO-B with a R_a of 0.84 µm. In contrast, F-containing coatings presented the same higher thickness value (~48 µm) but not the same morphology. On the one hand, in PEO-4F a two-layer morphology can be seen, the outer layer presents large dispersed cavities and the inner layer has abundant small pores (Figure 4.1). PEO-8F coating, on the other hand, displays just one relatively compact and regular layer. No defined pores were found on the surface therefore only transversal porosity was

analysed (Table 4.2); obtaining a maximum pore size value of 115 μm^2 and 30 μm^2 for PEO-4F and PEO-8F, respectively. Moreover, for PEO-8F surface microcracks were found, a phenomena associated with thermal stresses from a quick cooling process. For both fluoride-containing coatings the R_a value (4.3 μm and 3.6 μm) increased by nearly 5-6 times compared with the values of the other two coatings (~0.7 μm and 0.84 μm, Table 4.2). The values of microhardness depicted that the PEO-8F coating was ~1.5 times harder than PEO-9Si, indicating that both the composition and compactness of the coatings can modulate this parameter.

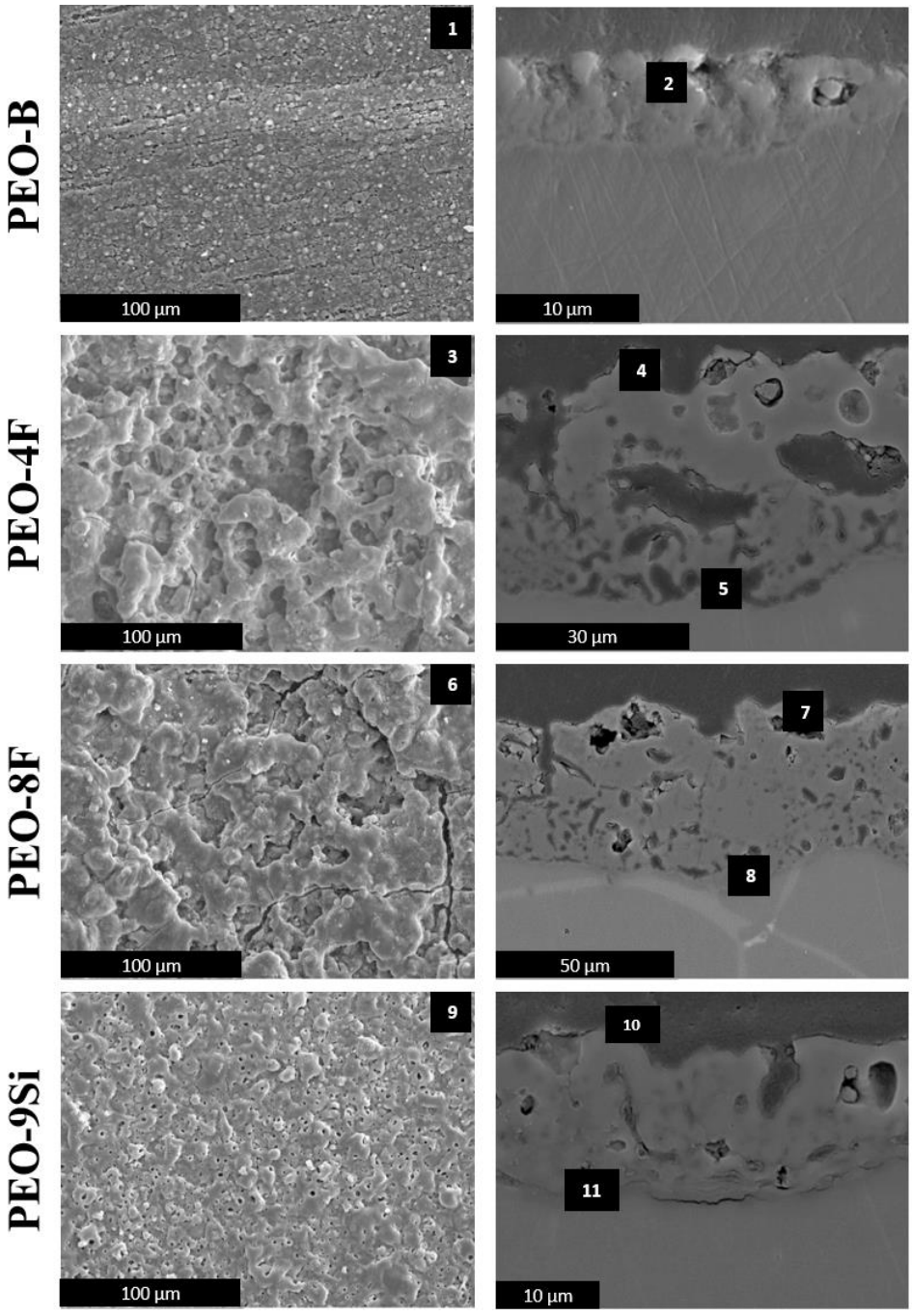

Figure 4.1. Secondary electron plan view micrographs and backscattered electron cross-sectional micrographs of the PEO coatings (PEO-B, PEO-4F, PEO-8F and PEO-9Si).

The elemental composition of the coatings was obtained by EDS (Table 4.1). All the electrolytes species were incorporated into the coatings. Ca and P was found in all the samples and F and Si were detected in the PEO-F and PEO-Si coatings, respectively. As for the Ca/P ratios in the F-containing electrolytes were found higher in the outer part with 1.3 and 1.5 for PEO-4F and PEO-8F coatings, respectively. Nevertheless, for PEO-9Si in the inner part (point 11) the Ca/P ratio was much higher (3.79) than in the surface area or outer part analysis with 0.45 and 0.16. The content of Si was found higher in the outer region of the coating (12.1 at. %). It is known that Si usually forms Si-rich top layers related to precipitation of amorphous SiO_2, as observed in aluminium PEO coatings [261]. F incorporation was found in a greater extent in the inner locations of PEO-4F and PEO-8F, getting up to ~24% and ~39%, respectively.

Table 4.1. Local EDS analysis of the coatings (at. %).

Coating / Location		*Elements*							*Ratios*
		Mg	**O**	**P**	**Ca**	**F**	**Na**	**Si**	***Ca/P***
PEO-B	**1**	48.8	44.7	3.3	2.1	-	1.2	-	0.66
	2	53.7	42.1	3.1	0.5	-	0.6	-	0.14
PEO-4F	**3**	22	50.2	7.1	9.1	8.6	2.8	-	1.32
	4	32.6	33.3	12	15.5	4.6	2	-	1.29
	5	54.7	15.7	5.5	0.03	24.1	0.1	-	0.01
PEO-8F	**6**	25.8	42.5	6.6	10.2	11.1	3.7	-	1.55
	7	33.7	33	8.8	12.4	8	4.1	-	1.41
	8	42.6	11.3	6.3	0.2	39.2	-	-	0.02
PEO-9Si	**9**	36.5	48	2.5	1.1	-	1.8	10.1	0.45
	10	41.1	42	3.3	0.5	-	1	12.1	0.16
	11	64.5	25.4	0.6	2.2	-	0.4	7	3.79

Table 4.2. Surface characteristics of the studied coatings.

Coatings		*PEO-B*	*PEO-4F*	*PEO-8F*	*PEO-9Si*
Roughness (μm)	R_a	0.7 ± 0.02	4.3 ± 0.3	3.6 ± 0.3	0.84± 0.01
	R_z	4.7 ± 0.2	24.2 ± 1.7	22.9 ± 1.9	5.6 ± 0.3
Surface Porosity (μm^2)	*Max.*	*	*	*	4.50
	Min.	*	*	*	0.3
Transversal Porosity (μm^2)	*Max.*	*	115.4	29.5	*
	Min.	*	0.9	0.9	*
Surface pore population density ($pores/mm^2$)		*	*	*	1.705 ± 0.31
Thickness (µm)		6.4 ± 0.7	47.5 ± 2.7	48.6 ± 4.0	12.7 ± 1.3
Microhardness (HV)		***	181.7 ± 42.4	358.2 ± 85.5	241.86 ± 56.8

* Not evaluated due to limitations of image analysis

** Not evaluated due to the technique limitation (too thin coating)

The crystalline formed structures were analysed by XRD (Figure 4.2) X-ray diffraction patterns show high intensity peaks of Mg coming from the base material in all the evaluated coatings. The materials were comprised of a MgO matrix and amorphous material was found (peak broadening between 25-35 2θ). In PEO-B hydroxyapatite (HA; $Ca_5(PO_4)_3(OH)$), $CaMg_2$ and $Ca(OH)_2$ were formed. PEO-9Si presented peaks for HA (with greater intensity than in PEO-B), Mg_2SiO_4 (forsterite), $Ca(OH)_2$ and $Ca_3(PO_4)_2$. Lastly, in both fluoride-containing electrolytes the formation of MgF_2, Mg fluorophosphate and $Ca_5(PO_4)_3F$ (fluorapatite; FA) was promoted. CaF_2 and $Ca(OH)_2$ peaks were also found for PEO-8F.

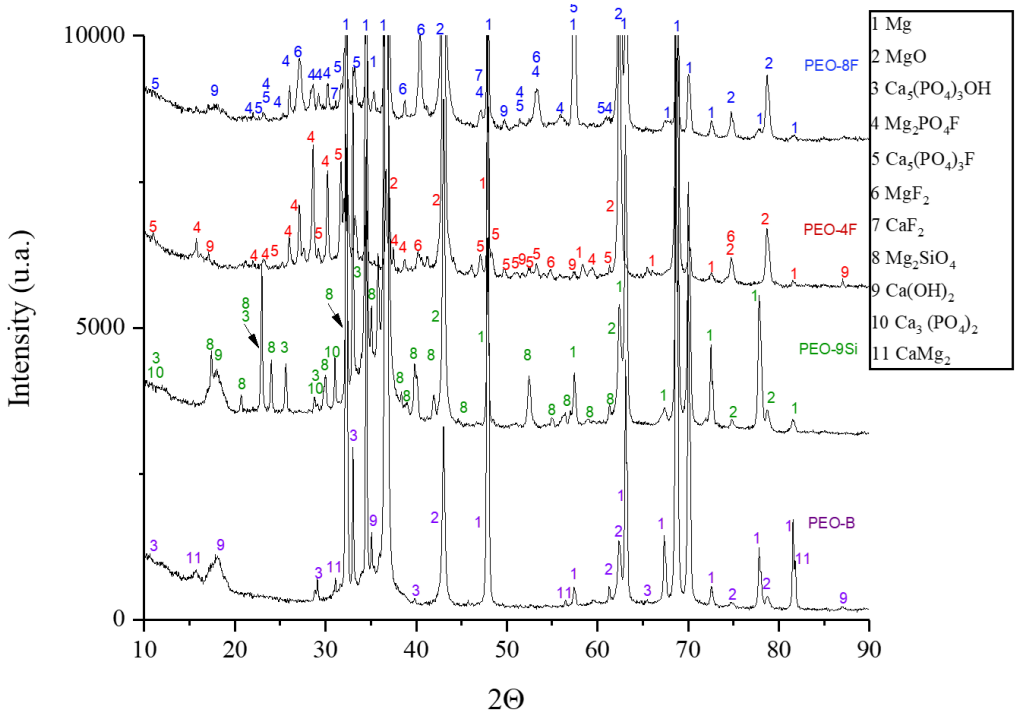

Figure 4.2. X-Ray diffraction patterns for the PEO coatings.

2.1.2 Ion release

After the coatings characterization, information about the possible liberation of the incorporated bioactive elements was sought. As these elements participate actively in cell metabolism and present other interesting properties (e.g. Ca and P are important for the formation of HA during bone matrix mineralization and F is known for its antibacterial properties [195]), their liberation into the media is of great interest. ICP-OES was used to evaluate Mg, Ca, P and Si ions, F was evaluated by ISE after their immersion in 0.9% wt.% NaCl at 37ºC during 5 days (Table 4.3). In order to evaluate the liberation of the Mg0.8Ca substrate, Mg and Ca was also measured for this condition.

The following findings of the ion liberation from the studied PEO coatings showed that the ion lixiviation is determined by the element content in the coating, the coating thickness and the structure of the compounds incorporated into the ceramic layer.

Table 4.3. Ion liberation from coatings after 5 days of immersion in 0.9 wt.% NaCl determined by ICP-OES.

Samples	*Elements (μg/cm²/d)*			
	Mg	**Ca**	**P**	**Si**
PEO-B	46.1 ± 4.4	2 ± 0.2	0.7 ± 0.1	-
PEO-4F	354.6 ± 35.1	11.4 ± 1.1	4.2 ± 0.4	-
PEO-8F	305.2 ± 30.7	15.9 ± 1.6	3.8 ± 0.4	-
PEO-9Si	70.3 ± 6.6	1.1 ± 0.1	1.1 ± 0.1	2.2 ± 0.2
Mg0.8Ca	65±419	5.2 ± 4.6	-	-

It can be assumed that the Mg release from the bare alloy comes from corrosion process (65±419 μg/cm^2/d). The high value of error is a consequence of pitting corrosion in some of the analysed specimens. Mg release from the PEO-B coated substrate is reduced (46 μg /cm^2/d) with a very small error, due to the corrosion protection provided by the PEO coating, which is in agreement with previous reports [119]. The Mg measured in PEO-B solution consist of both the ions produced by the electrochemical corrosion process and by chemical dissolution, i.e. lixiviation process. By increasing the thickness of the coating and obtaining a more homogenous barrier layer the corrosion resistance is enhanced. Therefore, chemical dissolution should explain the higher release of Mg from three other coatings as they all are thicker than PEO-B. The Mg release from the coatings matches their thickness and complex phase composition; the thicker coatings (PEO-4F and PEO-8F) that contain MgF_2 and $Mg_2(PO_4)F$ exhibited the highest liberation.

Likewise, Ca and P ion liberation was also improved in the F-coatings related to coating thickness and the presence of MgF_2, CaF_2 and FA. No significant differences between the ion release from PEO-4F and PEO-8F were found.

In addition, F^- liberation was measured after at 1 and 5 days of immersion (Table 4.4) using fluoride ion selective electrode. A decrease in the free F^- was observed with time. The greater liberation in day 1 from PEO-8F coating in comparison with PEO-4F is in agreement with its higher amount of fluoride.

Table 4.4. Ion liberation from coatings after 1 and 5 days of immersion in 0.9 wt.% NaCl determined by Ion Selective Electrode (ISE).

Conditions	***F (μg /cm²)***	
	1 day	**5 days**
PEO-4F	63.7 ± 1.0	12.7 ± 0.2
PEO-8F	118.9 ± 8.5	7.0 ± 0.5

2.1.3. Direct cell seeding studies

In order to evaluate biological behaviour, cell cultures were seeded over the following samples: non-coated Mg0.8Ca and commercially pure titanium as control materials; PEO-B, PEO-4F, PEO-8F and PEO-9Si coatings. Three different cell types were used: endothelial (C166-GFP), premyoblastic (C2C12-GFP) and preosteoblastic (MC3T3) murine cell lines. This selection covers a wide range of cell response as cell lineages react differently to the same topographic and bioactive characteristics.

Figure 4.3 depicts fluorescence micrographs of the three cell types growing on the materials at 120 h. C166-GFP and C2C12-GFP were evaluated daily thanks to their auto-fluorescence; both cell types were unable to grow and proliferate over control Mg0.8Ca. On the contrary, they formed a dense monolayer over Ti CP (the positive control), as expected. The premyoblastic cell line, C2C12-GFP, showed a good performance in all the coatings with a greater result in terms of monolayer formation in PEO-9Si. On the other hand, C166-GFP cells exhibited a differential behaviour over the PEO-coated materials. In PEO-4F these cells were not able to form a monolayer and in PEO-B the formed monolayer was unorganized. This correlates with the results presented in Figure 4.7, as the endothelial cells are very sensible to the fluoride content. In contrast, in PEO-9Si the cells were able to organize themselves following the surface topography.

An actin and Hoechst staining was performed in order to assess the cellular performance of MC3T3 cells over the surfaces. These cells successfully formed a monolayer in Ti CP, and, unlike endothelial and premyoblastic cells, a larger number of cells were able to survive in Mg0.8Ca. PEO-4F and PEO-8F coatings did not promote the monolayer formation, although higher number

of cells could be seen in PEO-8F, indicating that the decreased long-term liberation of fluoride from these coatings, compared with PEO-4F, determines this outcome, as predicted by the preliminary NaF cytotoxicity study (Figure 4.7).

Moreover, PEO-9Si demonstrated an improved preosteoblast growth, with a denser monolayer and higher number of stained nuclei, in comparison with Ti CP control. PEO-9Si was the only coating with a surface porosity (Figure 4.1) similar to the bone structure.

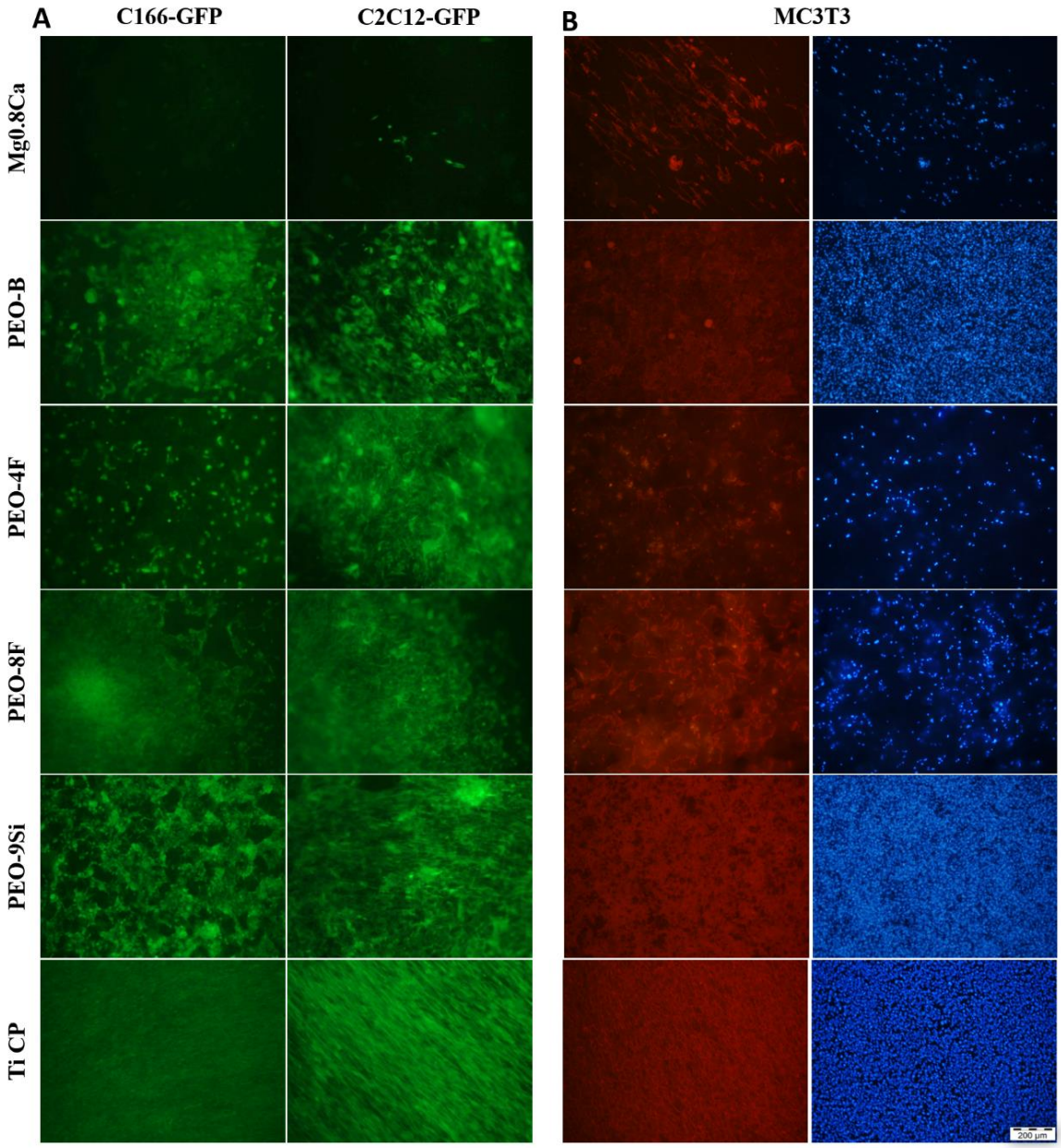

Figure 4.4. Cells growing over the PEO-coated materials and control materials, Mg0.8Ca and Ti CP, for 120 h. **A.** Self-Fluorescence micrographs of C166-GFP and C2C12-GFP cell lines. **B.** Actin (red) and Hoechst (blue) of MC3T3 preosteoblastic cell line.

In order to describe the cell-surface interaction over PEO coatings, SEM observation of premyoblastic cell line was carried out (Figure 4.5). After 120 h proliferating over PEO surfaces,

a C2C12-GFP monolayer was photographed in all samples (right row, Figure 4.5). To permit a deeper analysis, a magnification of selected areas (left row, Figure 4.5) allowed the identification of isolated cell morphologies and their interaction with surface features. In PEO-4F and PEO-8F, cells did not interact with the deeper areas of the uneven topography and appeared "hovering" over the surface, a situation that changed over PEO-B or PEO-9Si, where premyoblasts were tightly adhered and extended over the less rough topography. Specially, over PEO-B surface cracking was detected, as a result of the undercoating corrosion. Oppositely, PEO-9Si did not showed this morphology, showing a non-altered state (Figure 4.5), and allowing interaction with premyoblastic lamellipodia and filopodia.

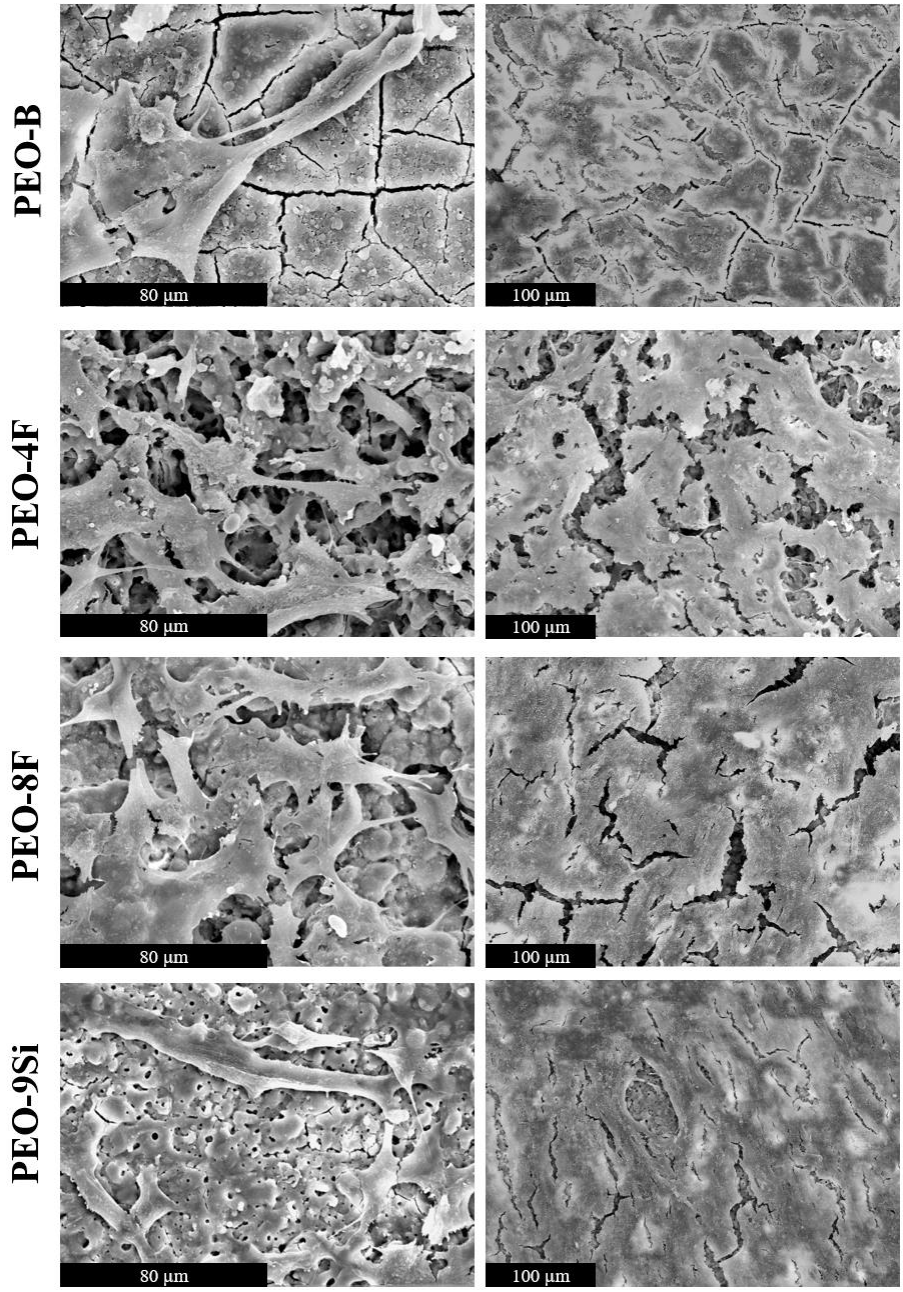

Figure 4.5. Secondary electron micrographs of C2C12-GFP preomyoblastic cell line spreading in the PEO-coated Mg0.8Ca alloy after 120 h of culture.

It is well-known that both surface topography and bioactive elements can modulate cell behaviour. Aiming to evaluate the possible cytotoxicity and bioactivity of this elements, the PEO-coated and non-coated substrate were immersed in complete DMEM for 5 days mimicking cell culture conditions (37ºC, 5% CO_2 and 95% humidity). The resulting extracts were then used for cytotoxicity, differentiation and co-culture studies. Extracts provide a simplification of the conditions, since there is no pH modification and element concentration with time, and providing a superior reproducibility of the *in vitro* cell studies.

When the immersion in this medium was completed, the samples were collected and evaluated by optical profilometry (Figure 4.6). Moreover, roughness parameters of the surfaces after the incubation were also acquired (Figure 4.6). The bare alloy showed a layer containing corrosion products ($Mg(OH)_2$ typically) and deposits from the enriched DMEM solution (these could include both inorganic and organic components, e.g. FBS proteins) obtaining an increment in R_a and S_a values (~1.3 and ~2.3 µm, Figure 4.6). Also some pitting was found with a depth of 40 µm, formed due to the corrosion process (Figure 4.6, centre row 2D simulation). PEO-B revealed a Ra value of 0.5 µm (slightly reduced than before the immersion) and a S_v of 28.5 µm corresponding with the deep pitting point. On the other hand, PEO-4F and PEO-8F samples presented high roughness values similar to those measured before the incubation, with a slight increase in R_a for PEO-4F, as some areas revealed detachment and/or loosening of the top part of the coating. From 3D rendering it could be depicted that the detached areas reached up to 29.5 µm deep (S_v), which correlates with the thickness of the outer coating layer as observed in Figure 4.2. PEO-8F and PEO-9Si with a more homogeneous surface maintain the as-received surface characteristics.

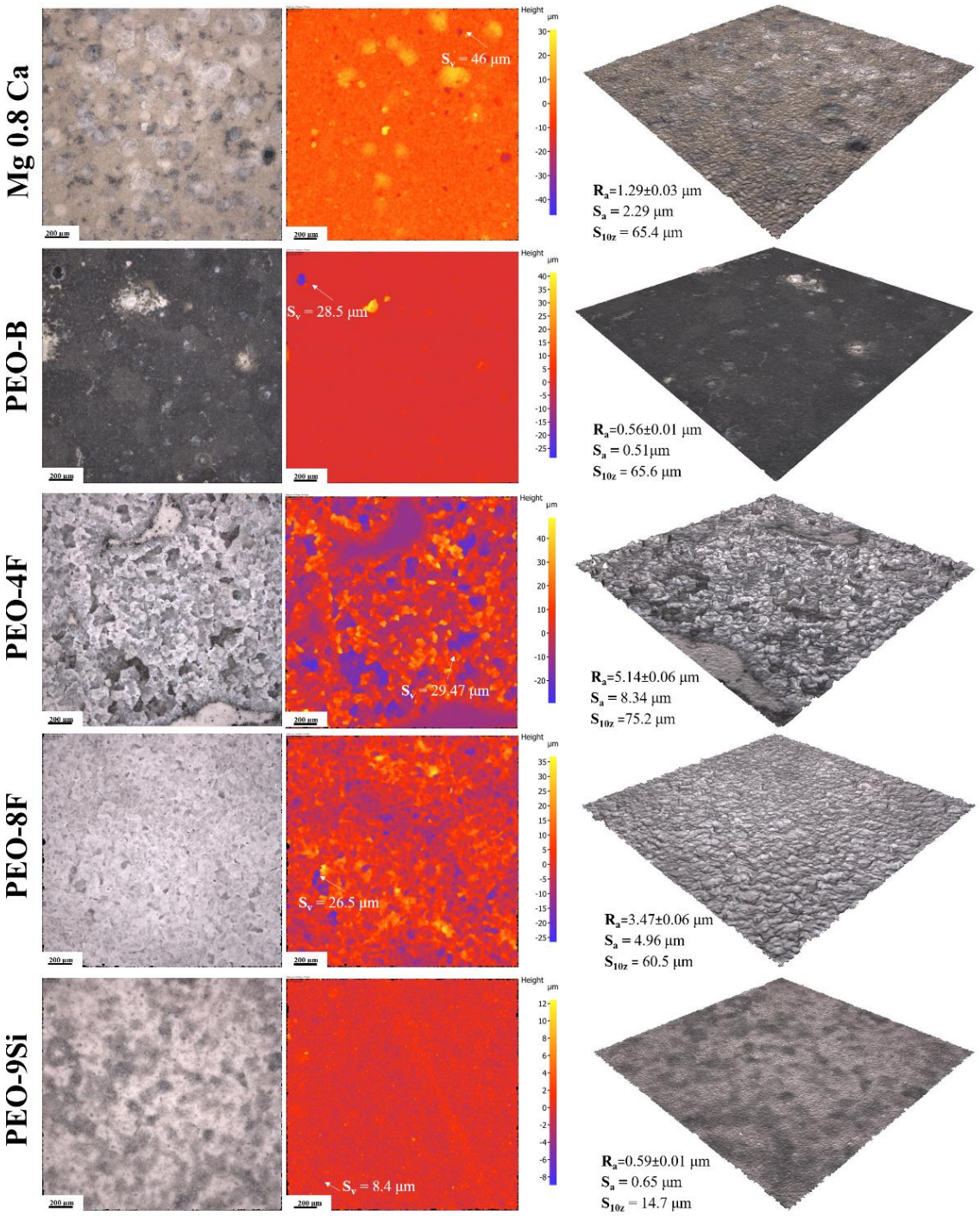

Figure 4.6. Optical micrographs, variation of surface topography and 3D-rendering of the surface of non-coated and coated Mg0.8Ca after 5 days of exposure in DMEM.

2.1.5. Extracts studies

Firstly, a preliminary analysis of the influence of NaF in cell response was done using a range of concentrations, as it has been described that liberated F^- can result toxic in certain concentrations (Figure 4.7). As expected, endothelial cells were more sensible [262], showing a tolerance limit of ≤1.0-1.75 mM. Premyoblastic cells exhibited the most robust behaviour of all the evaluated

cell lines, starting to be affected at a concentration >2.5 mM NaF. The preosteoblasts (MC3T3) were in an intermediate situation.

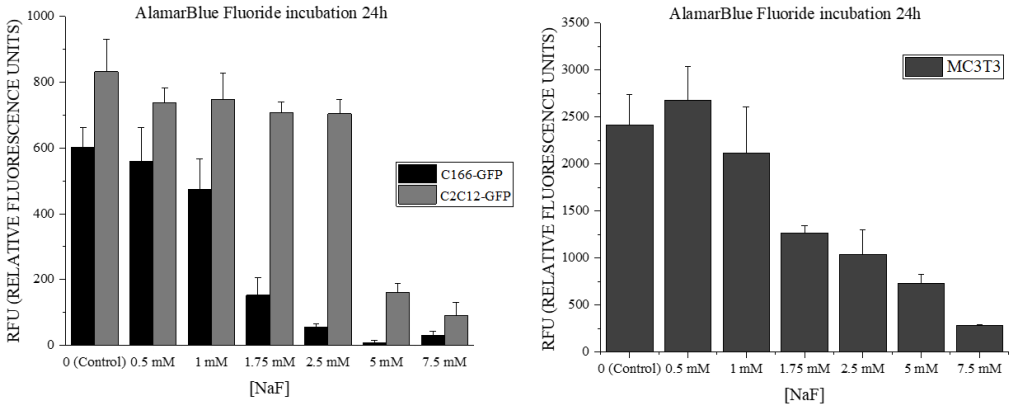

Figure 4.7. NaF cytotoxicity study with C166-GFP, C2C12-GFP and MC3T3 cell lines.

Before their evaluation in differentiation conditions the obtained extracts were studied in terms of cell growth and metabolic activity levels with premyoblastic and endothelial cell types. Two dilutions were chosen based on highly unfavourable concentrated extract (1:2) and highly favourable (1:10) conditions. 1:10 extract was selected mimicking the physiological state with a pH≈7.4. On Figure 4.8 A micrographs of the culture state of C166-GFP and C2C12-GFP cell lines after 5 days with the 1:2 extract are shown. With Mg0.8Ca condition both cell types were highly disturbed and were not able to proliferate. In contrast, Si-containing coating exhibited the best biological performance of all the PEO-coatings with dense monolayer formation (even though the pH≈8.0), and the higher metabolic activity levels in both endothelial and preomyoblastic cells with significant differences compared to Mg0.8Ca. PEO-8F extract with C166-GFP cells turn out to be the only condition without significant differences compared with the uncoated sample

Incubation with 1:10 extracts resulted in the formation of a monolayer for both cell lines and all the evaluated conditions after 5 days of culture (Figure 4.9 A). This is related to the absence of alkalinisation of the culture medium. In addition, an increase in metabolic activity can be detected with these highly favourable dilute conditions (Figure 4.9 B), especially with PEO-9Si extract with the premyoblastic cell line with statistical significance. PEO-4F and PEO-8F extracts contained ~1.5 times greater amount of Mg and 2-3 times greater amount of Ca than the Mg0.8Ca and showed a superior performance. Lastly, the PEO-9Si extract, containing ~26 ppm of Mg, ~0.4 ppm each of Ca and P and 0.8 ppm of Si, exhibited the greatest of all metabolic activity.

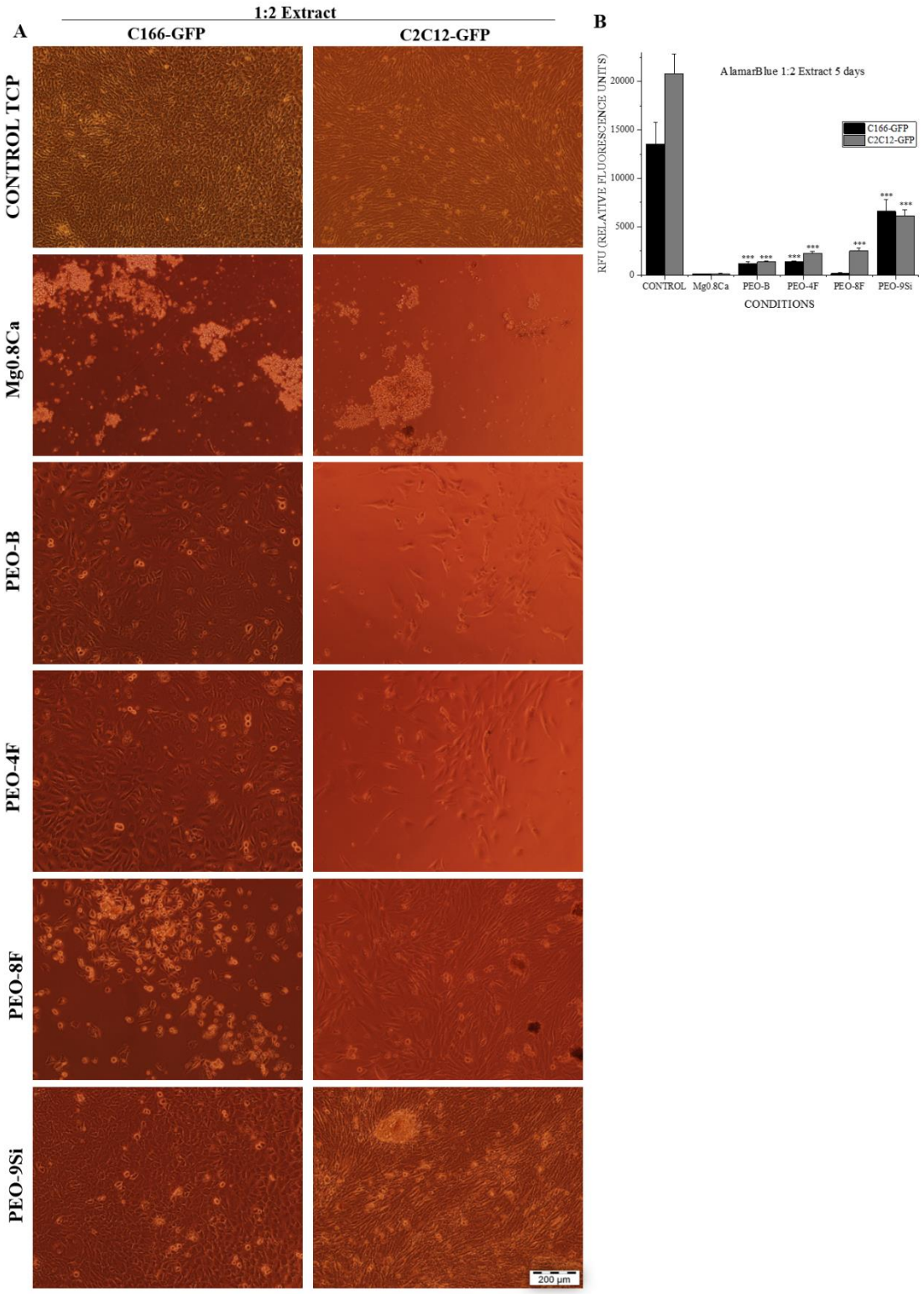

Figure 4.8. Extracts cytocompatibility. **A.** Micrographs of C166-GFP and C2C12-GFP cells after 5 days in contact with 1:2 extracts. **B**. AlamarBlue results at day 5 of both cell lines incubated with extracts 1:2. Significant differences stand for ***($p \leq 0.001$). Each extract condition is compared with control bare material for each cell line.

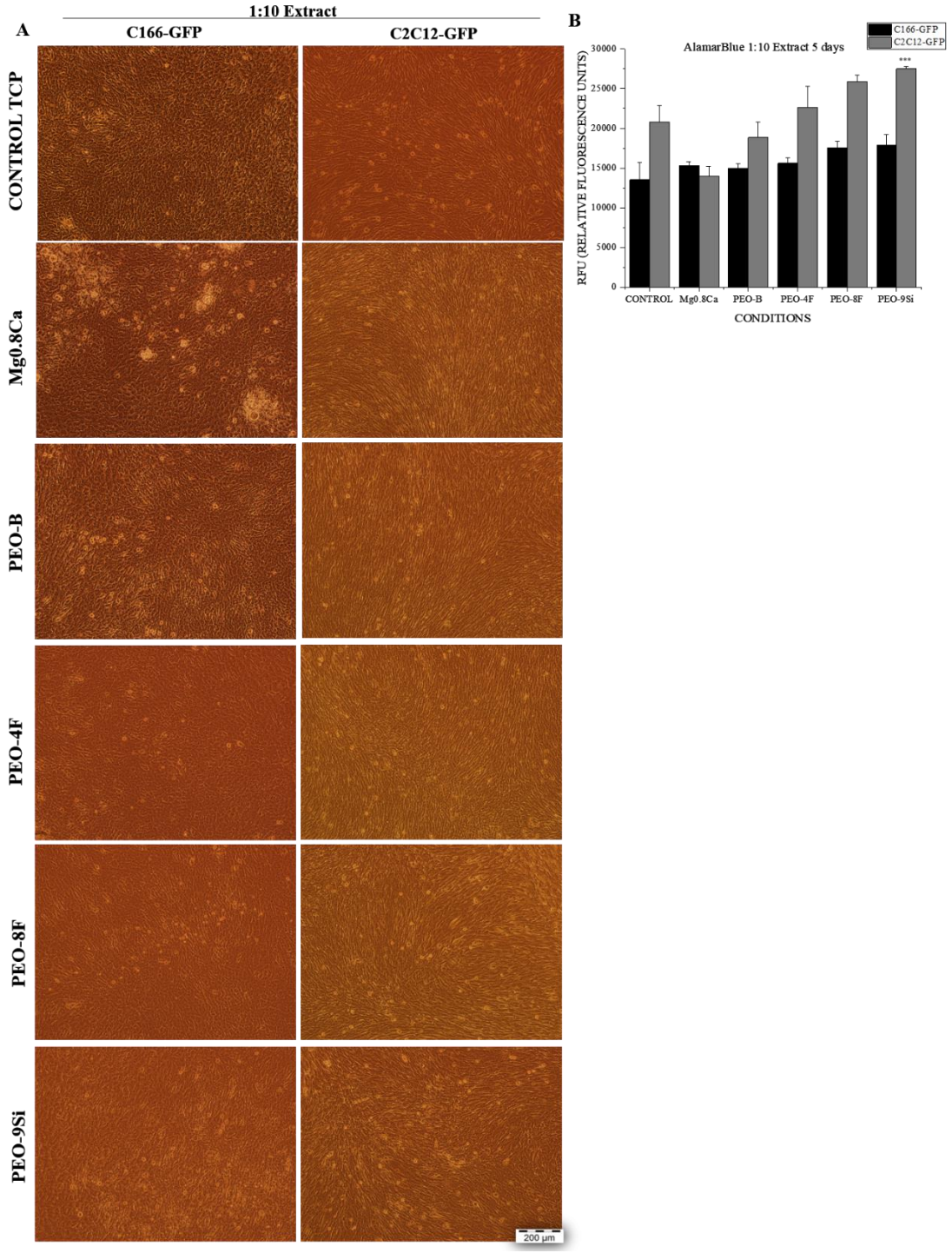

Figure 4.9. Extracts cytocompatibility. **A.** Micrographs of C166-GFP and C2C12-GFP cells after 5 days in contact with 1:10 extracts. **B**. AlamarBlue results at day 5 of both cell lines incubated with extracts 1:10. Significant differences stand for ***($p \leq 0.001$). Each extract condition is compared with control bare material for each cell line.

Differentiation evaluation in extracts

With regards to predict organism response in presence of PEO implants, bone cell activity has been analysed using MC3T3 preosteoblasts and RAW 264.7 osteoclast precursor as *in vitro* models. In this study, incubation of cells in presence of different 1:4 extracts were carried out in order to evaluate cell differentiation under these conditions. This dilution has been reported previously [182], and ensures a coating-derived ion concentration in the culture media similar as the one detected in the ion liberation analysis (Tables 2.4 and 2.5).

Thus, MC3T3 preosteoblasts were incubated following these conditions during 7 days and a metabolic activity measurement was performed (Figure 4.10). Next, osteoblastic culture was incubated again for another 7 days in differentiation medium (14 days end point), and collagen secretion (Figure 4.11) and calcium deposits formation (Figure 4.12) were analysed. In the first stage of this experiment, PEO coating extracts did not provoke significant changes in cell metabolic activity, demonstrating that pH alkalinisation at 1:4 dilution did not disturb cell processes. In fact, pH values of the extracts at day 7 were higher in Mg0.8Ca extract than in the other samples (pH 8.6 versus pH 8), showing that osteoblastic cells are less sensible to this kind of pH changes. Regarding differentiation process, collagen was secreted in all conditions as Sirius Red analyses revealed. This protein presented a nodular disposition at end time, especially in case of PEO-9Si extract (Figure 4.11 C). In addition, all conditions allowed calcium deposits formation and therefore matrix mineralization, revealed by Alizarin Red staining at day 7 and 14 (Figure 4.12). In presence of PEO-9Si extracts, calcium deposits were rounded and bigger. For these reasons, it can be suggested that Si can play a positive influence in osteoblastic differentiation, increasing or accelerating this process.

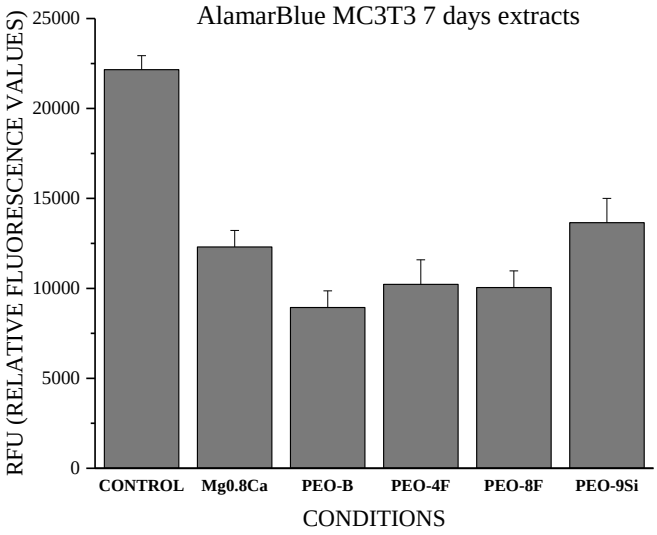

Figure 4.10. Metabolic activity levels at day 7 of MC3T3 cell line incubated with extracts 1:4.

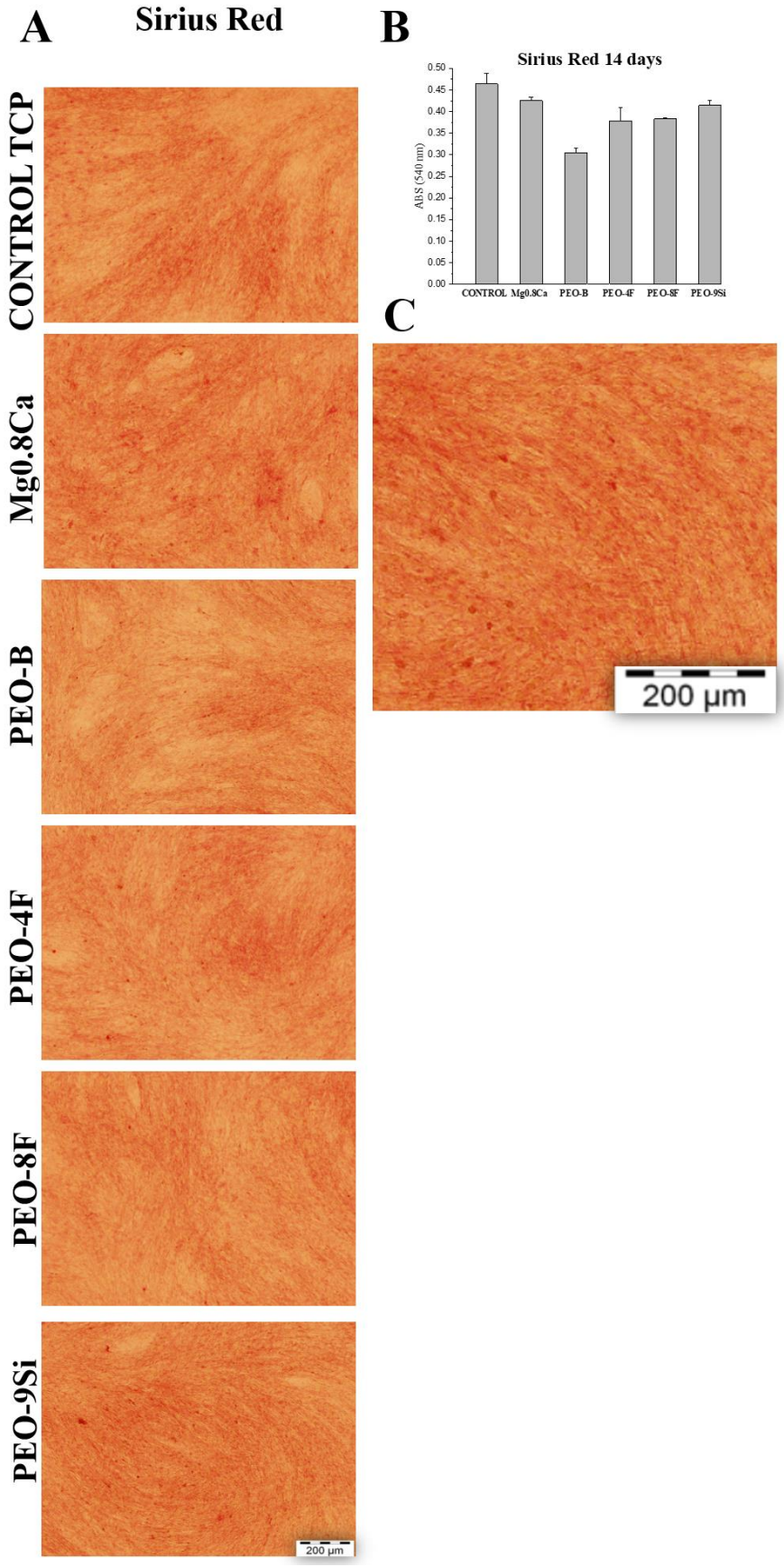

Figure 4.11. **A.** Sirius red staining after 14 days of culture **B.** Colorimetric quantification **C.** Detailed morphology of PEO-9Si staining.

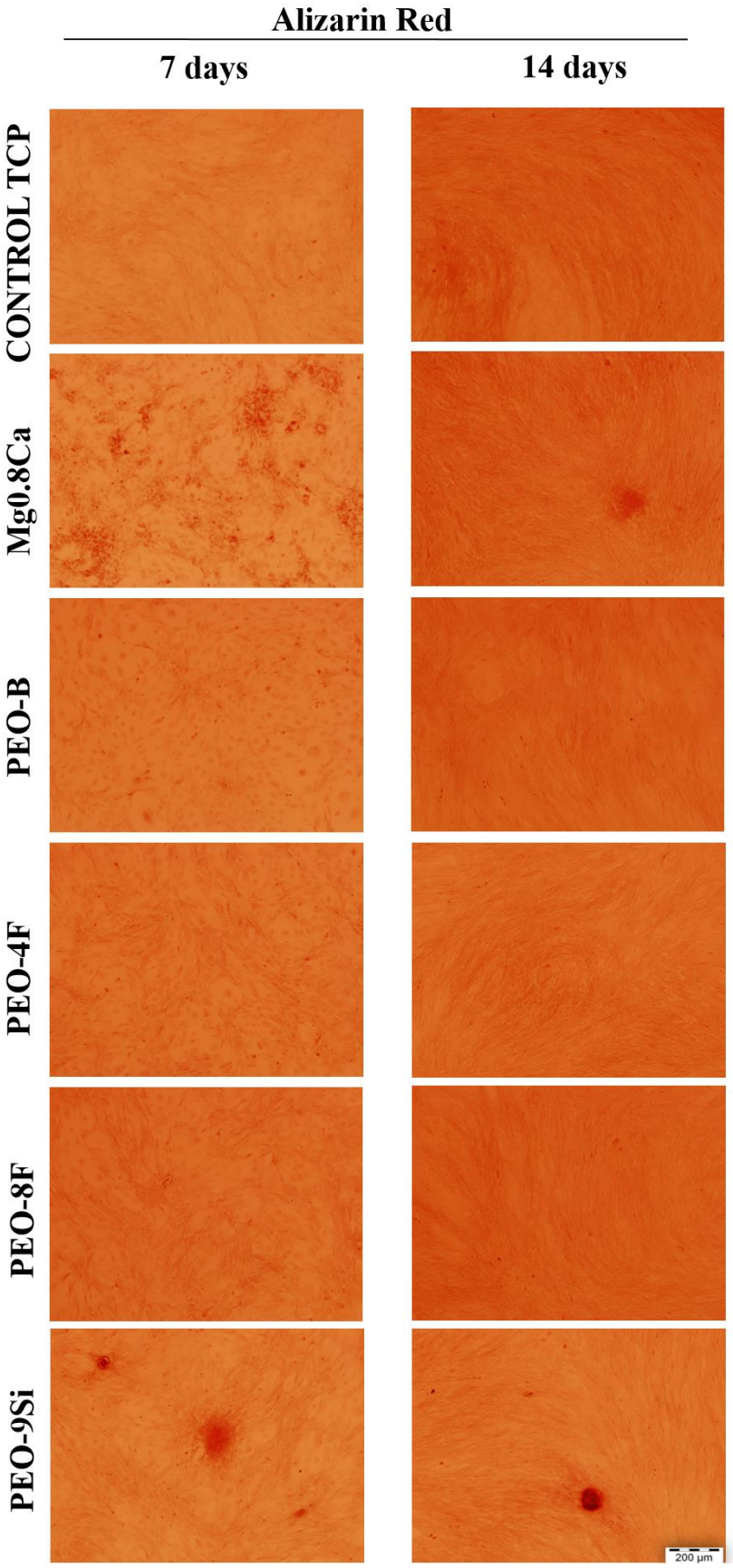

Figure 4.12. Mineralization study. Alizarin red staining of MC3T3 cells after 7 days of 1:4 extract incubation and 14 days of culture.

In a second stage, osteoclastogenesis process was also evaluated with a similar perspective. This phenomenon can directly affect bone regeneration after a lession, one of the most important applications of Mg implants. To achieve this goal, RAW264.7 macrophagic precursors were incubated in presence of these extracts supplemented with RANKL, a key regulator molecule of osteoclastic formation [178]. TRAP staining revealed at day 5 the formation of osteoclasts under described conditions (Figure 4.13), showing osteoclasts in all PEO extracts incubation. Contrarily, in presence of Mg0.8Ca extract, only small osteoclasts were detected, a fact that can be due to the high pH values of this dilution (pH=8.6). It has been previously described that acidic environment is needed for fusion and expansion of mature osteoclasts [263, 264]. In addition, some extracts such as PEO-B and PEO-4F showed less osteoclasts and a high presence of mononucleated precursors in comparison with samples such as PEO-8F or PEO-9Si, where osteoblasts were more numerous. This fact can be a consequence of a higher corrosion protection of these coverings in comparison with other samples.

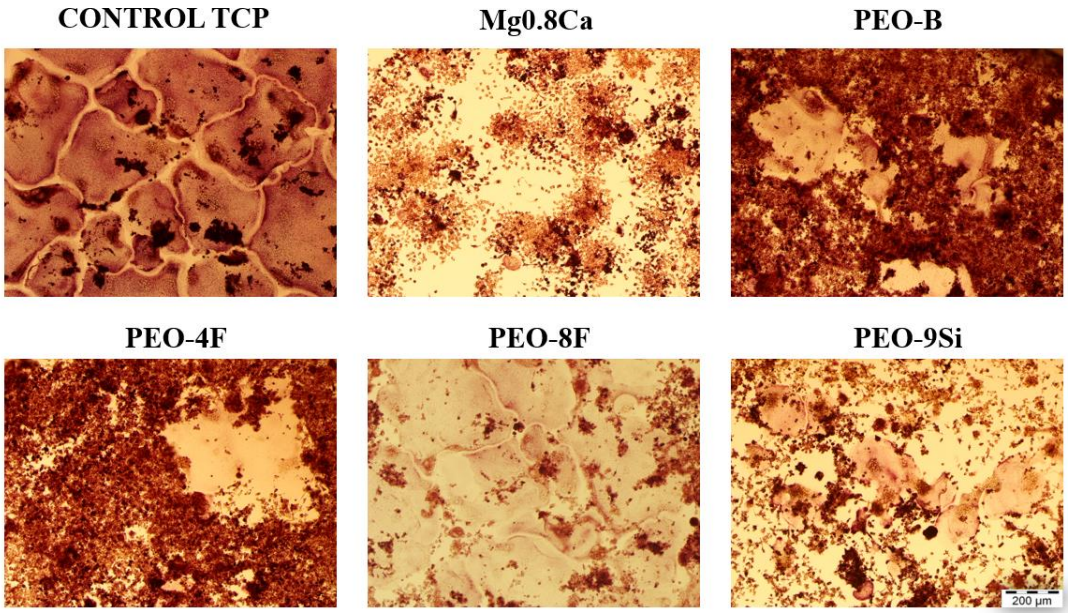

Figure 4.13. TRAP staining. Osteoclast differentiation after 5 days of incubation in 1:4 extracts (the medium and RANKL refreshed after day 3).

Direct Co-cultures of Osteoblasts and Osteoclasts

As it has been reviewed before, bone remodelling after an injury or an implantation surgery is a consequence of a cross-talk communication between bone cell populations, where osteoblasts and osteoclasts are involved. Bone homeostasis requires a well-balanced microenvironment, where chemical and biological factors play a crucial role in organism regeneration. In order to obtain a first approach of the effect of PEO samples in this scenario, a direct co-culture of both RAW264.7 macrophagic precursors and MC3T3 preosteoblasts was performed in presence of 1:4 extracts during 5 days. In Figure 4.14, micrographs of co-cultures are shown, using actin and Hoechst staining and a specific osteoclast marker (TRAP). As a result, in all PEO coated extracts mature osteoclasts with a high number of cell nuclei were found, together with osteoblastic cells. In comparison with previous cultures without bone producing cells, osteoclastogenesis was promoted, an observation that has been already documented. As with osteoclasts study, the medium was changed at day 3 without extract and RANKL was refreshed in order to rescue the "physiological state" [265]. However, in presence of Mg0.8Ca extract, osteoclastogenesis process was delayed as described before (Figure 4.13). No clear differences were found between PEO-B, PEO4-F and PEO8-F, a situation that changed in PEO-9Si extract. In this co-culture, a huge number of large osteoclasts covering the surface were found, as can be identified through TRAP staining. Besides, a close presence of osteoblasts around the formed osteoclasts was detected (Figure 4.15), where a clear difference between the actin ring of the multinucleated osteoclasts (left) and osteoblasts cytoskeletons (right) was observed. In summary, PEO coatings allowed an optimal activity of both cell lines, permitting cell proliferation and differentiation.

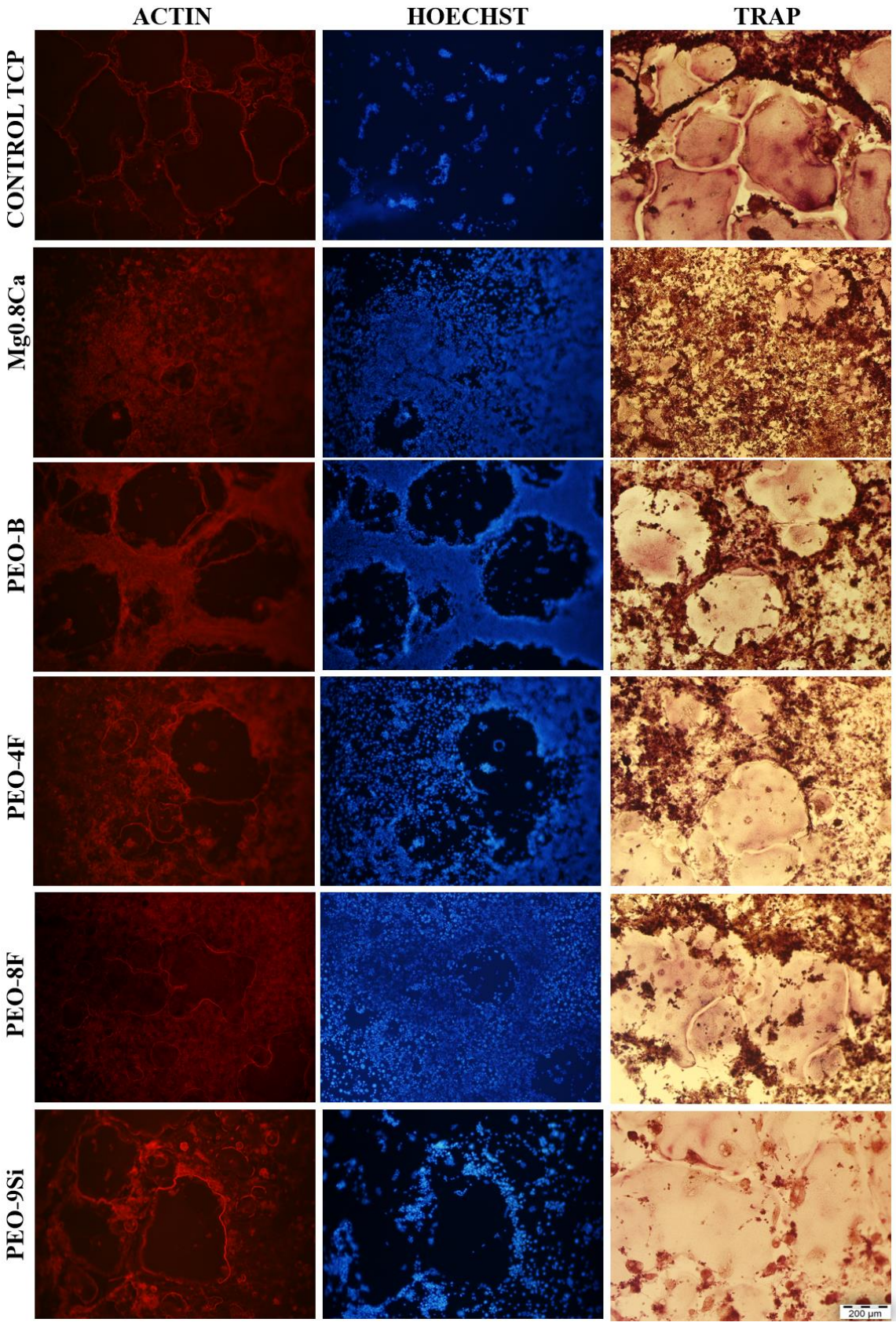

Figure 4.14. Direct co-cultures of osteoblasts and osteoclasts (MC3T3 and RAW 364.7 cells) with extracts 1:4. Left row - actin cytoskeleton staining, centre row - nuclei staining by Hoechst, right row - TRAP staining for resorption marker expression.

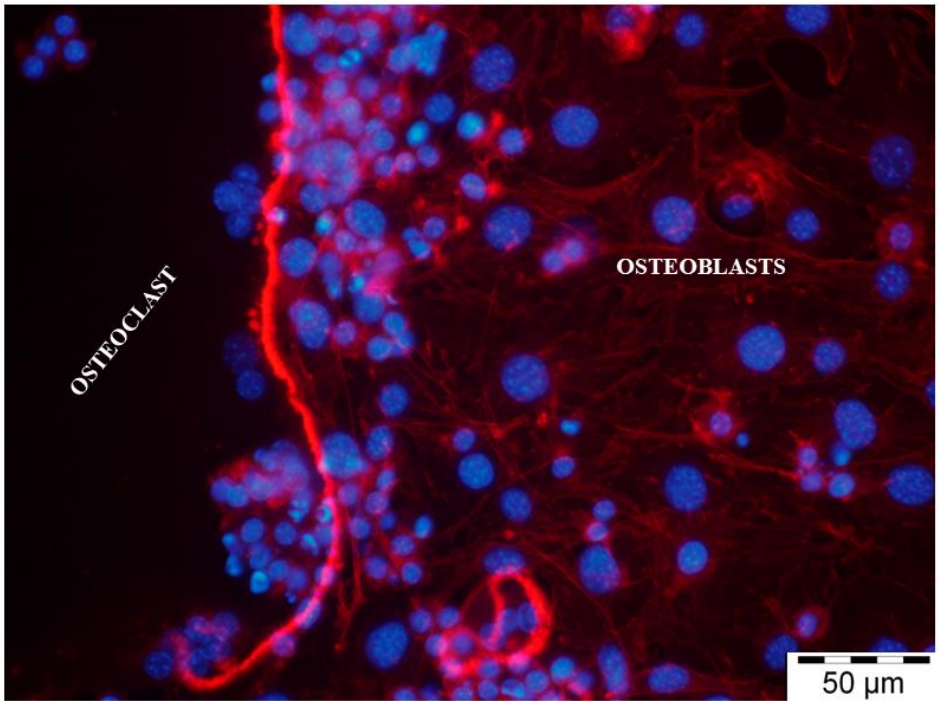

Figure 4.15. Merged of actin and Hoechst staining of co-cultured RAW 364.7 and MC3T3 cells with 1:4 PEO-9Si extract.

2.2 Hybrid ceramic-polymeric functionalization of Mg-Ca alloy

PEO surface modification of Mg has been proved as a promising approach in order to reduce the corrosion rate and avoid high alkalinisation around the tissues. Also, it can be described as a 'smart' biomaterial, since functionalization can be achieved through adding of bioactive species and topographic features of interest into the coating. However, the formation of micropores and cracks as a consequence of PEO discharges enables aggressive ions to migrate through the layer and react with the Mg alloy accelerating the corrosion mechanism and therefore, liberating H_2.

A polymeric coating over the already formed PEO ceramic layer could prevent the described event and could even provide other functionalities to the implant. Even though polymeric materials lack of good mechanical properties for these applications, a post-treatment strategy after Mg functionalization can be implemented. PCL is a bioresorbable semicrystalline poly(α-hydroxyester) and biocompatible polymer of a hydrophobic nature. It degrades slowly by hydrolysis in aqueous media. Moreover, a biodegradable polymer such as PCL can retain drugs such as sirolimus, everolimus or paclitaxel that are being used to avoid thickening of lumen induced by stents [266] or growth factors (BMPs, VEGF to improve bone regeneration). From a similar point of view, many examples can be reviewed. Xu *et al.* [267, 268] prepared PLLA and PCL coatings of both high molecular weight and low molecular weight on pure Mg, revealing that both films significantly improve cytocompatibility and suppress the pH increase of the medium during Mg degradation. Other study [269] also reported that PLA and PCL coatings on

high-purity Mg improve the corrosion resistance. Lastly, Zeng *et al.* [270] used a 5 μm phosphate based PEO and a PLLA coating on a Mg alloy proving a decreased corrosion rate and good cytocompatibility.

Scaffold porosity of a polymer layer can be considered a key feature as the pores guide the cells to proliferate into the desired 3D shape of the defect and promote vascularization of the tissue, apart from being essential for an adequate diffusion of nutrients and oxygen which is vital for cell survival and proliferation. The honeycomb topography has been described to interact with cell surface integrins and to influence cell proliferation, migration and differentiation processes [40].

The strategy proposed herein is the use of a biodegradable polymer (PCL) over PEO-9Si selected from the previous section as it presents the most favourable results in terms of biological effect. Additionally, a BFs approach to fabricate microstructured PCL over the PEO-Mg interface is also implemented. A hierarchic coating approach with different layers combining the benefits of a Mg core, ceramic PEO-based layer that provides corrosion protection and bioactive species, and an added value of polymeric 3D scaffold is proposed.

2.2.1. Coatings characterization

After the PEO process, the materials were sterilized and coated with PCL at a concentration of 20 mg/mL. Triplicate samples were used for BF approach. Following the final processing of the samples the proposed implants were characterized by SEM. Figure 4.14 depicts backscattered electron (BSE) cross-sectional micrographs of the formed coatings; a hybrid double-layer polymeric-ceramic coating was formed over the Mg0.8Ca alloy. A Ca/P/Si-based PEO layer was coated with PCL (Figure 4.16 a, b), sample Mg-PEO-PCL. Based on the same strategy, PCL was deposited and BFs were carried out in order to fabricate a microstructured polymer surface (Figure 4.16 c, d), Mg-PEO-PCL-BF. PEO coatings were formed around ~13μm, as it has already been described in Section 2.1, and PCL coating ranged between 25-30 μm. A porous structure can be distinguished in Mg-PEO-PCL-BF related to the polymer microstructuration.

Top view images of the polymeric coatings are presented in Figure 4.15. For Mg-PEO-PCL (Figure 4.17 a) a non-porous surface can be observed with some globular-like structures, that have sealed and completely obscured the original PEO porous morphology (Figure 4.1, PEO-9Si coating). Figure 4.17 b-d shows the porous structure formed by the BFs method with different pore size (2-30 μm). In Figure 4.17 d PEO structure can be detected inside the pores with local EDS analysis (Table 4.5, point 1) confirming the presence of Ca, P and Si elements. On the surface of PCL (Table 4.5, point 2) almost no presence of bioactive elements (Ca, P and Si) was detected and a large amount of detected C was consistent with the PCL structure.

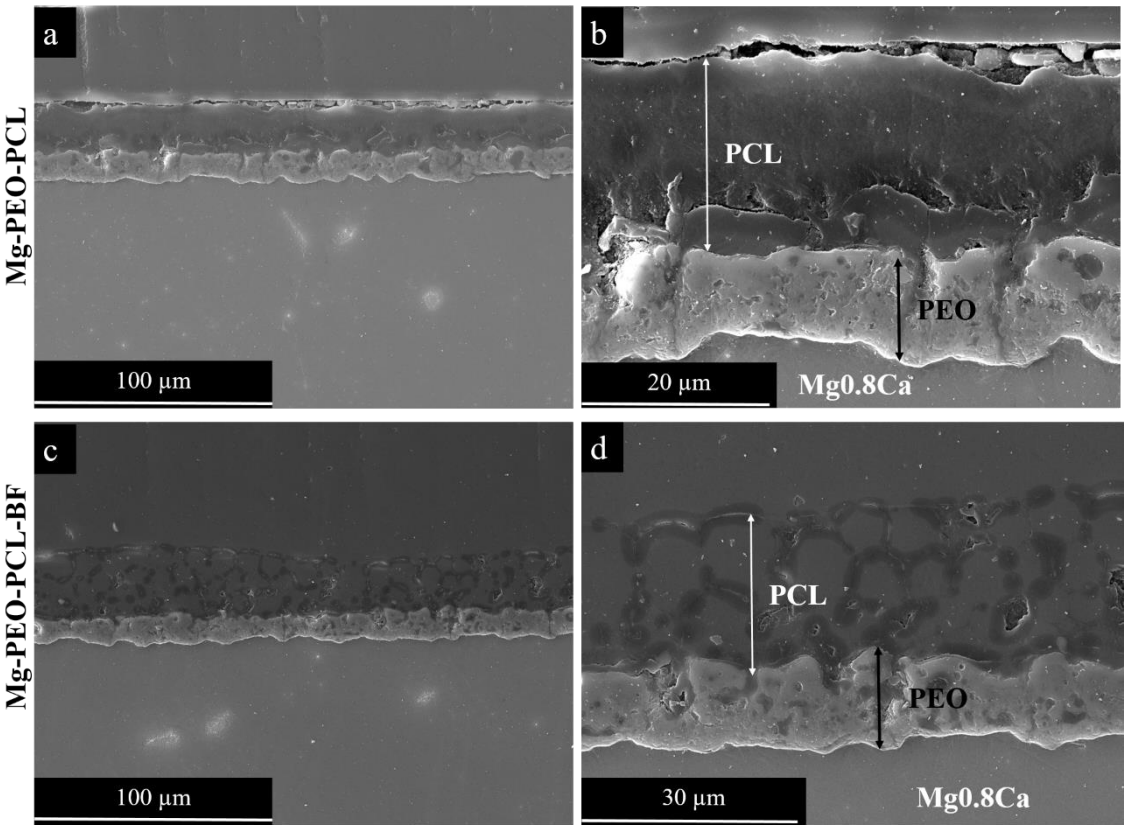

Figure 4.16. Backscattered electron cross-sectional micrographs of PEO-PCL coatings on Mg0.8Ca alloy.

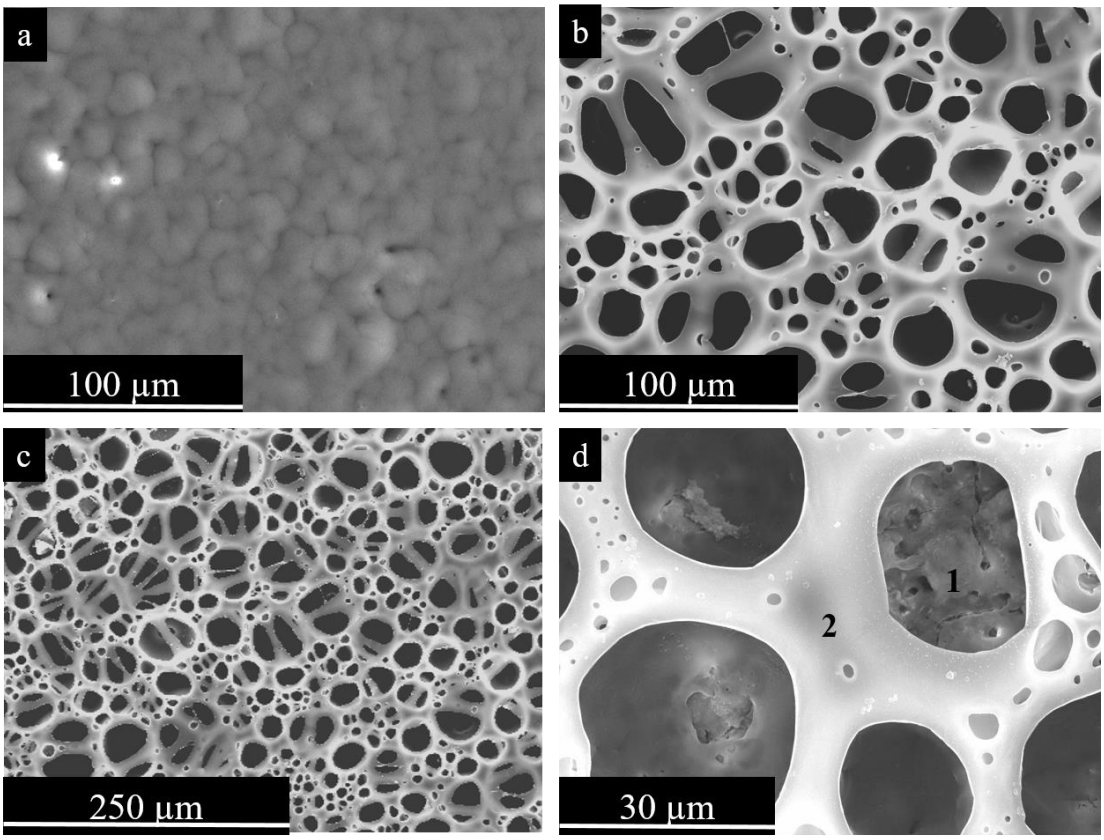

Figure 4.17. Secondary electron plan view micrographs of PEO-PCL coatings. a) Mg-PEO-PCL; b-d) Mg-PEO-PCL-BF.

Table 4.5. Local EDS analysis (at. %).

Sample / Assignation		*% Atomic*					
		O	**C**	**Mg**	**Ca**	**P**	**Si**
Mg PEO PCL BF	**1**	64.8	24	5.9	0.7	1.5	3.4
	2	66.9	32.8	0.2	-	-	0.1

Table 4.6. Surface characteristics of the studied coatings.

Sample / Characteristics	**Mg-PEO**	**Mg-PEO-PCL**	**Mg-PEO-PCL-BF**
Thickness (μm)	~13	~32	~35
R_a (μm)	0.84 ± 0.01	0.41 ± 0.01	8 ± 0.30
R_z (μm)	5.6 ± 0.3	2.70 ± 0.1	36 ± 0.6
Contact angle (º)	34.1 ± 4.6	82.9 ± 1.6	106.3 ± 1.8

By using optical profilometry the variation of the surface topography in 2D and 3D rendering were obtained for both materials (Figure 4.18). As already seen by SEM the Mg-PEO-PCL planar surfaces were formed with a R_a value of 0.41 μm (Table 4.6). In contrast, Mg-PEO presented a higher R_a value due to the surface porosity after PEO (Table 4.1). Regarding Mg-PEO-PCL-BF, surface porosity can be detected with average pores down to 30 μm. As a result of the formed microstructure the R_a value increased up to 8 μm (Table 4.6).

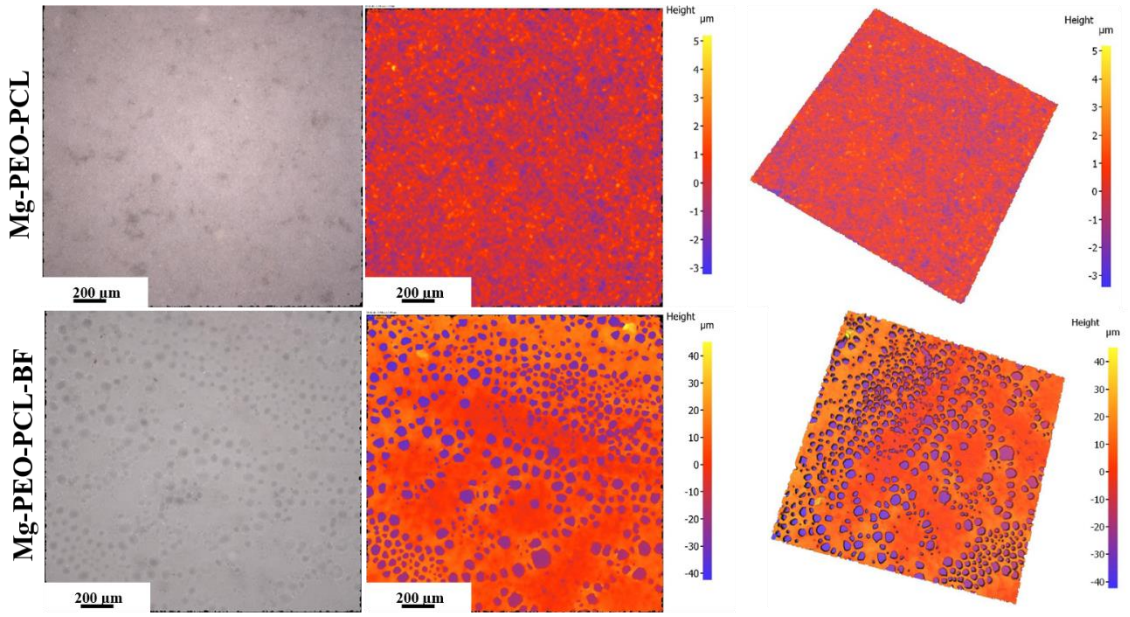

Figure 4.18. Optical micrographs (left column), variation of surface topography in 2D (centre column) and 3D (right column) rendering.

In terms of wettability, Mg PEO is a high hydrophilic surface with a contact angle of 34.1º (Table 4.6). However, when it is coated with PCL there is an increment of the contact angle up to ~83º, indicating a less hydrophilic surface. After the porosity is induced by the BF method, the polymeric structure becomes hydrophobic (106.3º), this can be explained by the Cassie-Baxter theoretical model proposed for rough and/or chemical heterogeneous surfaces. PCL is a hydrophobic polymer and when the surface becomes porous the air is supposed to stay inside the pores consequently increasing its contact angle. As a consequence of this air a small area of contact is present between the water droplet and the surface [271].

2.2.2. Biological evaluation

After the coatings characterization was performed, a premyoblastic cell line (C2C12-GFP) was seeded over at a cell density of 3×10^4 cell per cm^2 the materials using Ti CP as a positive control for cell growth. A daily track of cell expansion and growth over the materials was done with an inverted fluorescence microscope (Figure 4.19), this was possible because of the self-fluorescence characteristics of this cell line. In all three evaluated materials cells were able to adhere (after 24 h) and to proliferate during the evaluated time (96 h).

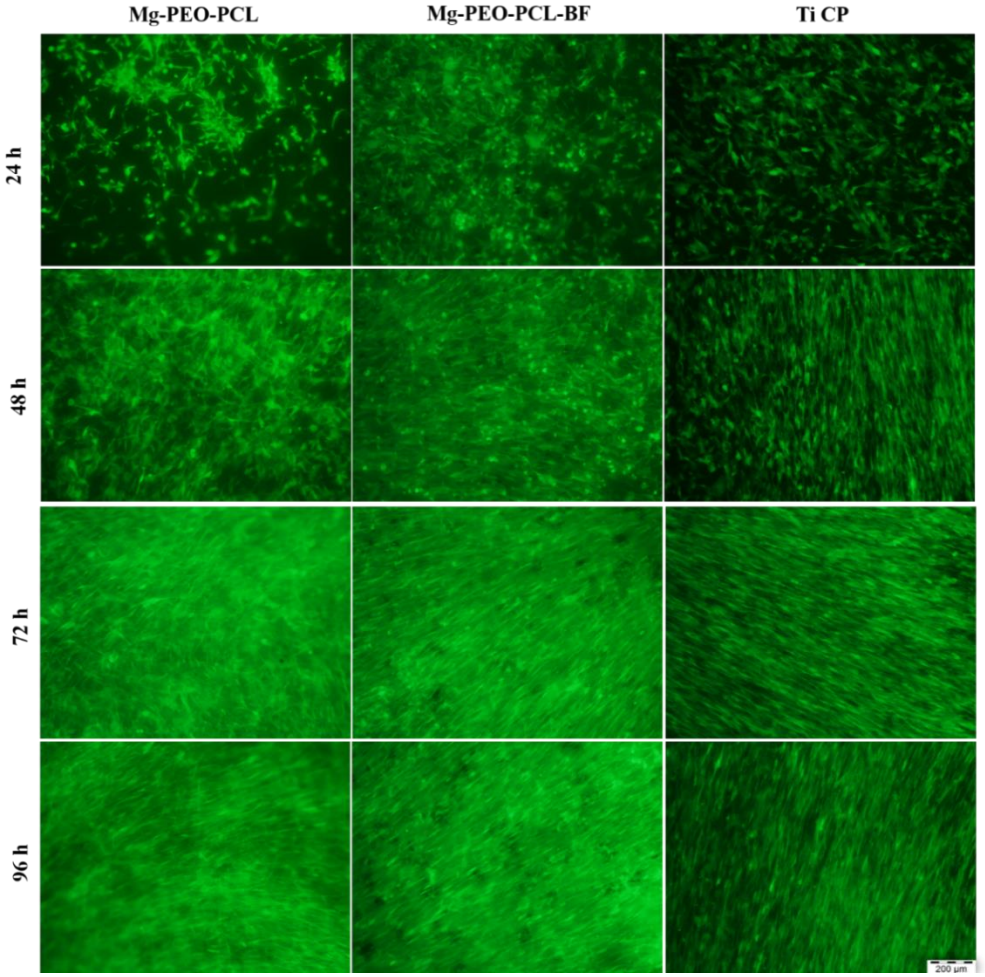

Figure 4.19. Premyoblast cells growth over the materials (Mg-PEO-PCL, Mg-PEO-PCL-BF and Ti CP).

No significant differences in terms of cell proliferation were observed between the planar Mg-PEO-PCL and the microstructured sample. The change in the wettability property towards a more hydrophobic material did not seem to be affecting cell adhesion and later proliferation. However, as displayed in Figure 4.20, cells were found growing at different depth levels of Mg-PEO-PCL-BF. Two areas of the surface are presented (Figure 4.20, first row) with a more visible porosity and the same areas with another focus (Figure 4.20, second row). Inside the pores a more rounded morphology of the cells was appreciable and an elongated fibroblast-like morphology on the surface.

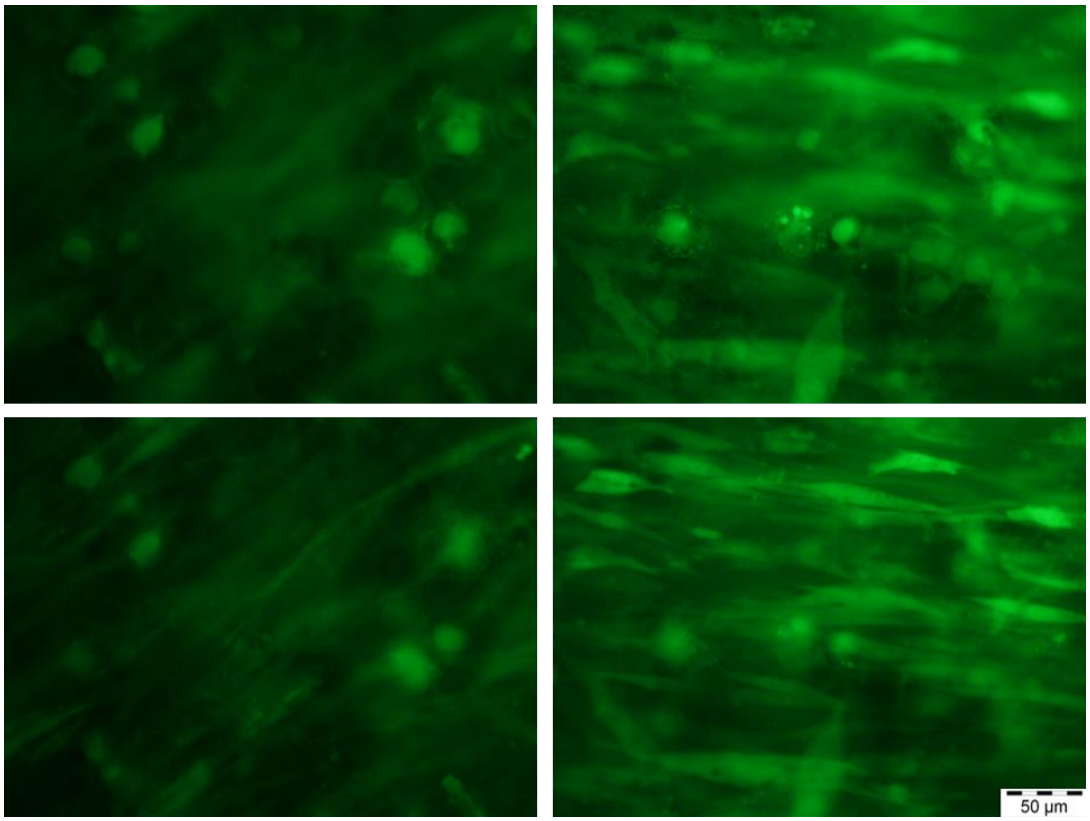

Figure 4.20. Magnification of cells growing over Mg-PEO-PCL-BF at different depth levels of the coating.

In order to closer evaluate this observed phenomenon SEM micrographs were taken (Figure 4.21). Figure 4.21(a) depicts a formed monolayer over the Mg PEO PCL BF, in agreement with the previous observation by fluorescence pictures. In Figure 6 b-d detailed magnifications show how the premyoblastic cells extend and reach through the pores with filopodia evidencing their growth all over the porous surface structure. The presence of pores throughout the scaffold may facilitate the flow of nutrients, oxygen and waste products. Adequate substance flow is an extremely important requirement for cell survival and function in the cell culture medium and in case of transplantation. Inside the pores more bioelements can be found and favour certain biological response (proliferation, differentiation, etc.).

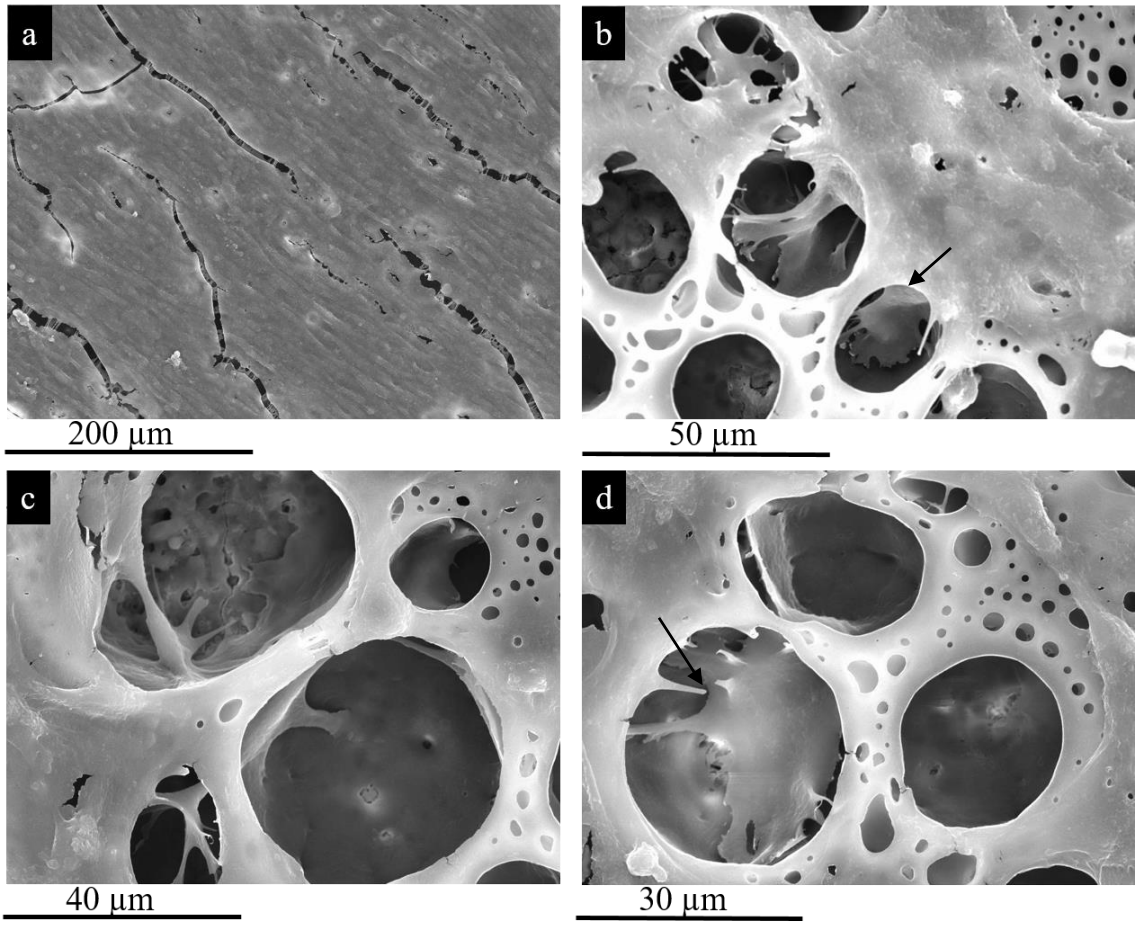

Figure 4.21. SEM micrographs of C2C12-GFP cells after 96 h growing over Mg-PEO-PCL-BF. a) Monolayer formed over the hybrid material, b-d) magnifications of cells growing inside the formed pores.

3.3 Discussion

Biodegradable materials are required to have bioactive properties. For non-load bearing applications a biomaterial capable of being resorbed physiologically and promote a biological response must be chosen and designed wisely. Mg alloys are already being used for some of the orthopaedic and cardiovascular devices, however, surface modifications should be made to better control their degradation rate and spread their use for a wider range of applications. To that end, in this chapter Mg0.8Ca alloy was used and four different types of PEO coatings were obtained. All the bioactive elements present in the electrolyte were successfully incorporated into the coatings, similarly to what have been demonstrated in case of PEO of Ti in the previous chapter. The addition of Si into the electrolyte has been reported to favour more homogeneous coatings and the stabilization of the HA in the coatings [272]. In the present work, DRX disclosed the formation of forsterite (Figure 4.2) that could have been formed by reaction between MgO and SiO_2 within temperature range of 1100-1400ºC [273]; its presence may have contributed to the enhanced compactness and mechanical properties of the coating (e.g. microhardness). It is worth mentioning that forsterite has also been related with an improved corrosion resistance of PEO coatings on other Mg alloys [274], although investigation of the corrosion resistance of the materials is beyond the scope of the present Thesis.

In regards to the NaF, its addition into the electrolyte composition leads to thicker and rougher PEO coatings as it has been reported previously [119]. The inclusion of F has been linked with the passivation of the surface of the alloy [275] as a result of MgF_2 formation and, therefore, enhanced ceramic layer growth. These phenomena can be explained by formation of fluoride-based compounds which are being assisted by plasma microdischarges. In addition, the increase of NaF concentration (from 4 g/L to 8 g/L) gives rise to a more compact coating with reduced transversal porosity, two times greater microhardness and larger amount of crystalline phases (Table 4.2, Figure 4.2). A greater incorporation of F in PEO-8F (Table 4.1) coating is associated with a higher concentration of F^- ions in the electrolyte. Moreover, F-containing samples presented bioactive crystalline phases such as FA which is reported to have similar activity to the HA present in bone tissue [208, 276]; the presence of both FA in PEO-4F and PEO-8F and HA in PEO-B and PEO-9Si is an indicator of potential bioactivity of the coatings.

After the coatings were characterized and the bioactive elements incorporation was confirmed, the ion liberation of Ca, P, Mg and Si was measured by ICP (Table 4.3) showing consistent liberation with the compositional surface area EDS analysis of the coatings (Table 4.1). Mg alloy, which also contains Ca, possibly will also contribute to the liberation of Ca into the medium, since non-coated substrate released between 2.1-9.3 $\mu g/cm^2/d$ of Ca (Table 4.3). Fluoride liberation was also measured by ISE and, similarly to the trend observed in F-containing PEO coatings on

Ti6Al4V and Ti grade I, there is a reduction of free F^- in the solution with time. This may be attributed to the fact that other liberated ions from the coating can react with F^-, resulting in formation of precipitates with low solubility product values such as MgF_2, CaF_2, $Mg_2(PO_4)F$ and $Ca_2(PO_4)F$. Nevertheless, the maximum F^- release (118.9 µg/cm^2) measured in this work would be within the acceptable intake (1.4-3.4 mg per day of F^-) as long as the implant area does not go beyond ~10 cm^2. An initial burst of F^- could be expected after the implant makes contact with the physiological medium avoiding a possible initial bacteria colonization.

Initial cell biocompatibility was assessed by direct seeding studies and, as expected, cells (endothelial, premyoblastic and preosteoblastic) were not able to proliferate over the bare alloy (Figure 4.4). The high alkalinisation around the material and the formation of bubbles reduce the biocompatibility of the material. Nonetheless, premyoblastic cells presented the higher number of cells growing over the material and this could be explained by their greater resistance to the alkalinisation of the medium that occurs as a result of corrosion of magnesium. These results corroborate the reports of osteoblastic cells being able to perform in higher pH media [263, 277].

In relation to PEO coatings bioactivity, F-containing coatings showed a reduced monolayer formation of the preosteoblastic cells in contrast with PEO-B and PEO-9Si, which may be due to the presence of fluoride as well as the greater roughness of both coatings with R_a values around 4 µm (Table 4.2). The latter fact contrasts with the good performance of the preosteoblastic cells in terms of monolayer formation in the smoother surfaces with R_a values less than 1 µm (Table 4.2), suggesting that a less uneven topography is preferential for the ability to form a monolayer. As for endothelial cells, there was a differential behaviour between F-containing coatings as PEO-8F coating did not seemed to be disturbing them to the same extent as PEO-4F, which could be explained by the phenomenon observed during the F^- liberation measurements (Table 4.4) as the decrease of free F^- in the media with time is steeper in case of PEO-8F allowing the cells to form a monolayer. Premyoblastic cells were the most robust cell line evaluated and all the cell lines presented the best performance with PEO-9Si even with better results than Ti CP positive control. PEO-9Si also stood out with the best performance in extracts biocompatibility studies with significant statistical results for C2C12-GFP in both 1:2 and 1:10 conditions. Si is considered a favouring element in angiogenesis processes [278] explaining the good behaviour of PEO-9Si coating and suggesting the possible positive implications after implantation of the material in the vascularization of tissues. Moreover, the implication of Si in bone metabolism and promotion of bone regeneration has been widely described [187, 279] and the present findings are in agreement with other works where Si has been incorporated into a biomaterial and the same cell line was used [279].

Interestingly, in 1:2 extracts (Figure 4.8) similarly poor results were obtained for Mg0.8Ca and PEO-8F showing very low biocompatibility with the endothelial cell line (C166-GFP). Whereas in case of Mg0.8Ca this is related to the high pH of the extract, for PEO-8F this could be explained by the fluoride cytotoxicity observed for C166-GFP (Figure 4.7), as PEO-8F has the highest release of F^- at short times. The F^- concentration in the PEO-8F 1:2 diluted extract can be estimated as ~44 ppm or ~2.3 mM, which is above the F^- tolerance limit determined initially.

In regards to the tendencies observed in the differentiation studies, PEO-9Si extracts favoured the differentiation markers, e.g. calcium deposits were rounded and bigger (Figure 4.12). Si can play a positive influence in osteoblastic differentiation, increasing or accelerating this process. Moreover, in the co-culture studies PEO-9Si favoured the osteoclastogenesis process among all the evaluated conditions. It is known that an acidic environment is needed for fusion and expansion of mature osteoclasts [263, 264], which may explain why PEO-9Si which produced less changes in the pH favoured the differentiation processes.

In regards to the composition, the incorporation of elements, such as Ca, P, Si and F, into the ceramic PEO layer can promote different biological responses: i) Ca and P are essential part of bone mineralization; ii) F can provide antibacterial properties and even favour osteogenesis process [280], although it can affect endothelial cells negatively in concentration dependent manner [262]; iii) Si promotes vascularization and bone regeneration. Along with the action of the Mg itself, these elements can favour bone regeneration processes or other biological processes. For instance, besides its implication in bone tissue, Ca is important in signalling. It is known that positively charged Ca^{2+} and negatively charged phosphate ions are two primary signalling elements of cells. Ca^{2+} binds to thousands of proteins to produce changes in localization, association, and function [281]. Moreover, endothelial Ca decreases with age and its signalling in endothelial cells is essential to vasomotor control.

Si is a vital structural component of arteries and its concentration is reduced with age inducing a bigger risk of lesions and plaque formations, therefore can be an interesting approach for stents design. For instance, in a high cholesterol diet, Si supplementation diminishes the incidence of artherosclerotic lesions in blood vessels [282]. Atheromatous arteries contain approximately 10 times less Si than in healthy subjects.

Concerning the final applications, the findings of this Thesis indicate that PEO technology offers a versatility for the design of implants with different set of elements that can be chosen in accordance with the needs of the tissue that is being regenerated.

Hybrid ceramic-polymer functionalization

Among all the PEO-based Mg samples, PEO-9Si had an outstanding biological behaviour of all the evaluated coatings presenting interesting characteristics for bone regeneration and stents applications. Therefore, this coating was selected for the next step of functionalization where a biodegradable polymeric coatings was used to add, among other characteristics, additional corrosion protection. It is known that a top polymeric layer slows the degradation of Mg [269] (corrosive species have to diffuse towards the Mg substrate through and additional layer hence corrosion becomes slower) and provides longer structural integrity of the device, making sure that the reconstruction plate (or stent) will not fracture prematurely. However, corrosion studies considering this premise should be implemented in the future.

Furthermore, a 3D polymeric structure obtained by BF approach can favour the free diffusion of nutrients and gases to the cells, and waste products away from the cells. Figure 4.21 shows how cells interact in different levels, even reaching the PEO structure on the bottom of the pores where bioactive elements can be available. In another study by other authors, PCL honeycomb films were obtained with different porosity ranges promoting the adhesion of preosteoblastic MC3T3-E1 cells, and enhanced spreading and proliferation with better efficiency than the flat films with higher number of focal adhesions and enhanced integrin expression. ALP activity and calcium content were found favoured by the honeycomb porosity and mostly by the presence of smaller pores (3.5 μm) [283]. In our results, a higher cell alignment with the porous sample after 48 h of cell growth (Figure 4.19) can be depicted compared with the flat condition (Mg-PEO-PCL) and observed with more detailed in Figure 4.20, where the cells growing on the surface present a more elongated state and more rounded inside the pores.

As already seen in our results (Table 4.6) the PCL porous films were more hydrophobic than the flat PCL used as control. According to the study that applied the Cassie and Baxter model to predict the water angle values this can be attributed to the air pockets that are produced between substrate surface and water droplets when water droplets are much larger than the dimension of the structures present on substrate surface [283].

Hierarchical materials (e.g. metallic/ceramic/polymeric) usually offer improved properties compared to the single components. Different studies have determined that the combination of the porous substrates with other materials result in a biomaterial with enhanced properties for different application as in bone regeneration. More specifically, porous films form by BF method have been reported to improve cell adhesion to the biomaterial as a consequence of adsorption of ECM proteins, modulated topography or improved cell entrapment within the pores, as well as the mechanical properties or substance flow through the material [40].

Potential as drug-eluting carrier

In a future application of the hybrid Mg/PEO/BF PCL material demonstrated in this Thesis, drugs or growth factors could be retained in the outer BF PCL layer in order to promote a pharmacological response. Porous films are able to adsorb proteins in a site-specific manner, and to store them inside the pores as described in Figure 1.11. Moreover, PCL by itself has been described as good drug carrier and possible drug-eluting stent. As reviewed in Section 1, intimal hyperplasia produces restenosis (re-narrowing) of the vessel lumen following vascular intervention and drugs such as paclitaxel, rapamycin (Sirolimus) or everolimus are being used to avoid it, all them are hydrophobic drugs. For instance, a study has shown that non-constrictive perivascular PCL cuffs are able to release paclitaxel or rapamycin for 3 weeks. Their application reduced intimal thickening of the treated femoral arteries by 75% and 76%, respectively [284]. Other study, with rapamycin-loaded PCL delivery system revealed a substantial reduction of neointima (scar tissue that forms within tubular anatomical structures such as blood vessels) [285]. Other strategies include different layers with a metal as the core material such as the pre-coating with PCL or PLCL to a Mg alloy (AZ31) and an external top layer of PDLLA sirolimus loaded. This layering strategy showed an improved Mg corrosion resistance, and it has been proposed as an important foundational procedure for the development of a coronary scaffold with Mg alloys [286]. However, a different alloy should be used as there are concerns about the use of alloying elements such as Al for biomedical applications.

On the other hand, related to enhancement of bone repair/regeneration processes, growth factors incorporation into the polymeric top layer could be investigated. As such, in [287] 3D printed HA was coated with PCL with BMP-2–loaded nanoparticles (PLGA and poly(vinyl alcohol)) resulting in optimal cellular cytocompatibility, no cytotoxicity, and improved bone regeneration in a rabbit calvarial defect model.

Hydrophobic drugs (sirolimus, everolimus, paclitaxel) could be easily embedded in PCL, whereas hydrophilic ones such as growth factors for bone regeneration (BMP-2) can be incorporated into the PCL with nanoparticle carriers. Another strategy could consist in the incorporation of hydrophilic brushes into PCL; using the BF strategy these segments can be situated inside the pores of BF favouring the interaction with the hydrophilic therapeutic agent, which could be retained inside the pores by electrostatic interactions.

Therefore, a combination of the highly protective and degradation rate controlling PEO ceramic layer with PCL BF top coat that successfully supports a scaffolding cell structure as demonstrated in the present study, is a step to creation of a hybrid 3D hierarchic implant material with hierarchic structure that can be used as a drug carrier.

Chapter 3: Functionalized microporous polystyrene supports for tissue engineering

As evaluated in the previous section BF strategy can be used to provide a microstructure and even a tridimensional coating. This technique can also be applied with other polymers, not only PCL, as has been discussed in the Introduction. Polystyrene (PS) is a very common polymer used in many applications (test tubes, petri dishes, diagnostic components and medical devices) and as cell culture substrate. We propose the use of PS as a model surface that could provide the base for the development of potential antimicrobial and at the same time biocompatible implants. Our main goal is to not only provide a porous surface, as achieved in Section 2.2, but also functionalize it, i.e., modify the surface chemical composition. The proposed strategy is based on the copolymerization of blends of PS and other polymeric cues with potential antibacterial properties. Previous studies already demonstrated the recognition of proteins and selective bacterial adhesion of *Escherichia coli* with polystyrene-*block*-poly(acrylic acid) diblock copolymer and homopolymer (PS) functionalized with polypeptide sequences [131].

Herein, two strategies of anti-bacterial functionalization are being investigated. i) A homopolymer (PS) and a block copolymer (either polystyrene-*b*-poly(dimethylaminoethyl methacrylate) (PDMAEMA) or a quaternized polystyrene-*b*-poly(PDMAEMA) functionalization of the pore cavity with a determinate pore size that can only affect bacteria and not mammalian cells. ii) Similar strategy with different chemical composition in the pore cavity (poly(acrylic acid) or the antimicrobial peptide Nisin anchored to this group. An endothelial cell model (C166-GFP) and *S. aureus* were used as mammalian cell and pathogenic bacteria models, respectively. Furthermore, this kind of functionalization strategy could be imparted to other types of polymers and tissue engineering applications.

3.1. Surface functionalization with selective antibacterial effects

3.1.1. Porous films characterization

The porous films selected for this study were prepared using polymer blends consist of a PS-*b*-PDMAEMA or PS-*b*-PDMAEMAQ block copolymer and high-molecular-weight polystyrene.

The amphiphilic block copolymer PS_{42}-*b*-$PDMAEMA_{16}$ was prepared and then quaternized to provide quaternary ammonium salt groups. These positive quaternary ammonium groups have been described to present antimicrobial properties. In order to produce microporous surfaces with pore diameters in the range of 3−7 μm (i.e., beyond the diameter of *S. aureus* and inferior to the endothelial cell size) the relative humidity and polymer concentration were fixed to 95% and 30

mg/mL. It is already widely accepted that pore size and distribution of films prepared using the breath figures approach directly influence several parameters, including the polymer concentration, the relative humidity. When polymer blends are being used such as in this scenario the relative amount of the components also matter [40, 126].

Table 5.1. Composition (wt. %) of the porous films prepared and evaluated as selective antimicrobial surfaces.

	PS (wt. %)	**PS_{42}-*b*-$PDMAEMA_{16}$ (wt. %)**	**PS_{42}-*b*-$PDMAEMAQ_{16}$ (wt. %)**
PS	100	0	0
PSD305	95	5	0
PSD31	90	10	0
PSD32	80	20	0
PSDQ305	95	0	5
PSDQ31	90	0	10
PSDQ32	80	0	20

The samples were prepared using either 5, 10 or 20 wt. % of block copolymer quaternized and nonquaternized (Table 5.1). With the purpose of evaluating the formed porous structure SEM micrographs were taken at different magnifications (Figure 5.1) as the different compositions can modulate pore size and distribution. For the nonquaternized 10 and 20 wt. % (PSD31 and PSD32) the detected pore sizes did not differ significantly when the block copolymer content increased. The quaternized ones (PSDQ31 and PSDQ32) also maintained the same tendency but with a slightly increment for PSDQ32 pore size. In contrast, PSD305 (5 wt. % of nonquaternized block copolymer) showed an ordered array of pores, while PSDQ305 presented superior pore sizes (~ 5.1 μm) and a heterogeneous size distribution. Regardless, all the pore sizes ranged (3.1-5.1 μm) below the diameter of mammalian cells, which can be an essential feature for their antimicrobial performance. Therefore, all the evaluated samples were selected for biocompatibility studies with endothelial cells and for antibacterial activity against *S. aureus*.

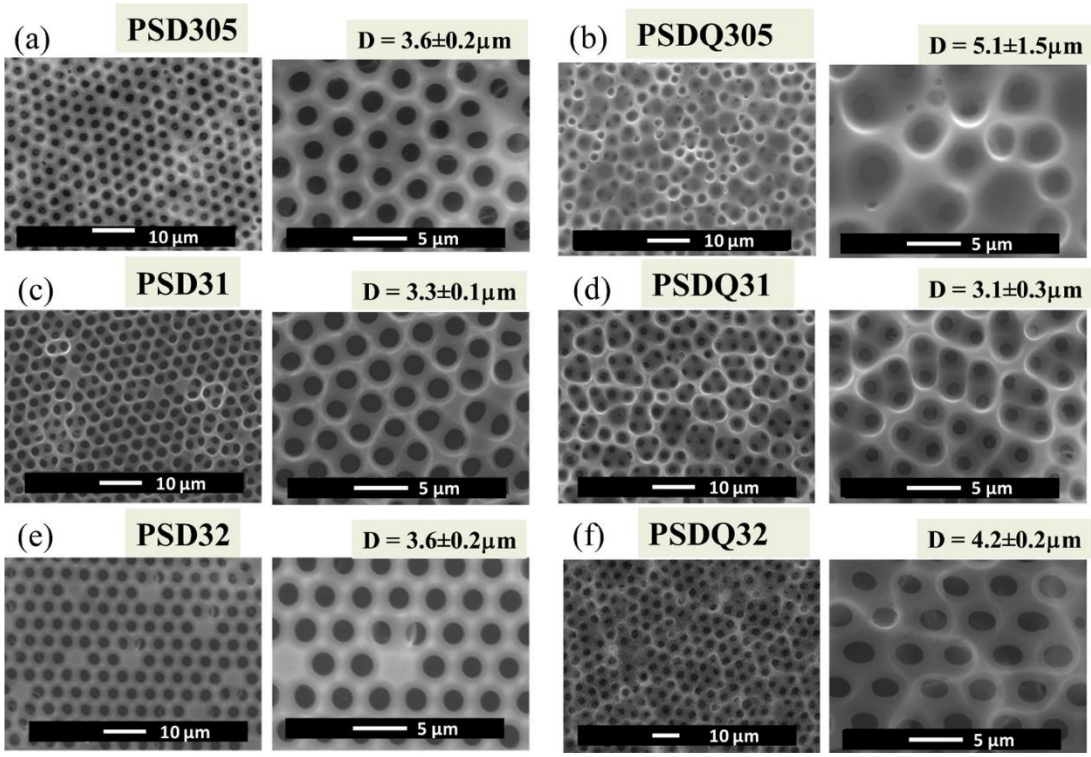

Figure 5.1. Comparison of the porous films obtained using either the non quaternized or the quaternized PS_{42}-*b*-$PDMAEMA_{16}$ diblock copolymer. The concentration of block copolymer in the blend was varied: (a, b) 5 wt. % (PSD305 and PSDQ305), (c, d) 10 wt. % (PSD31 and PSDQ31), and (e, f) 20 wt. % (PSD32 and PSDQ32). Q stands for quaternized (corresponding to the right column images). The total polymer concentration was set at 30 mg/mL for this experiment. The average diameters of the pores and the standard errors are shown in µm.

After ensuring that the appropriate pore size was obtained by BF method, a characterization of the inner cavities was carried out by confocal Raman to confirm the selective funcionalization. Chemical composition of two areas, pore wall and the surface, were obtained (Figure 5.2). A signal at 2789 cm^{-1} at Raman spectra is present exclusively in PDMAEMA. Figure 5.2.d illustrates the confocal Raman spectra of the pore wall and at the surface of the film, a cross is added for the exact position in which the spectra were acquired (Figure 5.2 b). The PDMAEMA signal is observed in the spectra acquired inside the pores, suggesting a selective enrichment of the diblock copolymer in this particular area. In Figure 5.2 c a mapping of the surface composition in the same cross-sectional profile is showed. The red colour stands for the presence of polystyrene, therefore the observed violet colour inside the pore can be related to changes in the chemical composition provided by the block copolymer confirming a selective disposition of PDMAEMA.

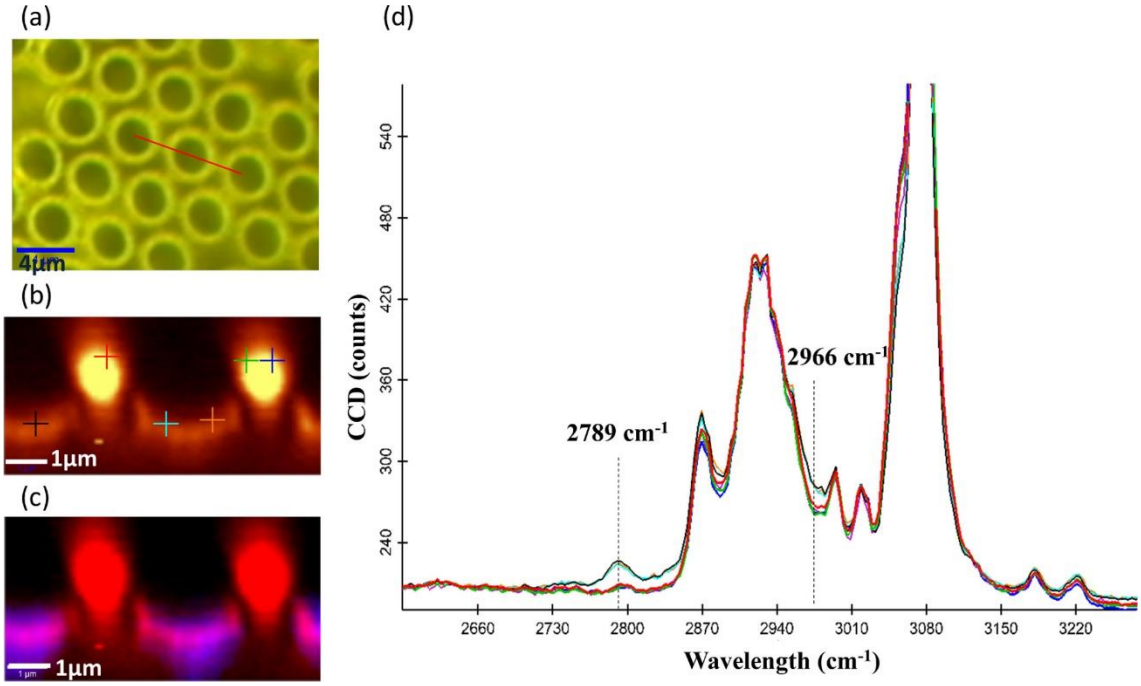

Figure 5.2. Raman confocal analysis of a porous film prepared using the nonquaternized PS_{42}-*b*-$PDMAEMA_{16}$ diblock copolymer 20 wt. % and PS (sample: PSD32). (a) Optical image of the porous surface. (b) Cross-sectional profile marked with crosses indicating the position in which the Raman spectra of (d) have been measured. (c) Cross-sectional profile to identify variations in the chemical composition inside the pores (violet) formed mainly by the diblock copolymer and outside the pores (red) indicating the presence of polystyrene.

Confocal Raman analyses were also performed on the films obtained using the quaternized block copolymer. In Figure 5.3 a numerous different signals can be detected (indicated in green) in the block copolymer (i.e., 3024 cm^{-1}) compared to the representative signals of polystyrene (i.e., 1009 cm^{-1}). Moreover, the characteristic carbonyl band of the diblock copolymer at 1734 cm^{-1} is also present. Similarly to the films prepared using the nonquaternized block copolymers, Figure 5.3 c depicts the composition of a pore with colour red outside the pore, indicating PS, and an enrichment of the block copolymer inside the pore (in blue).

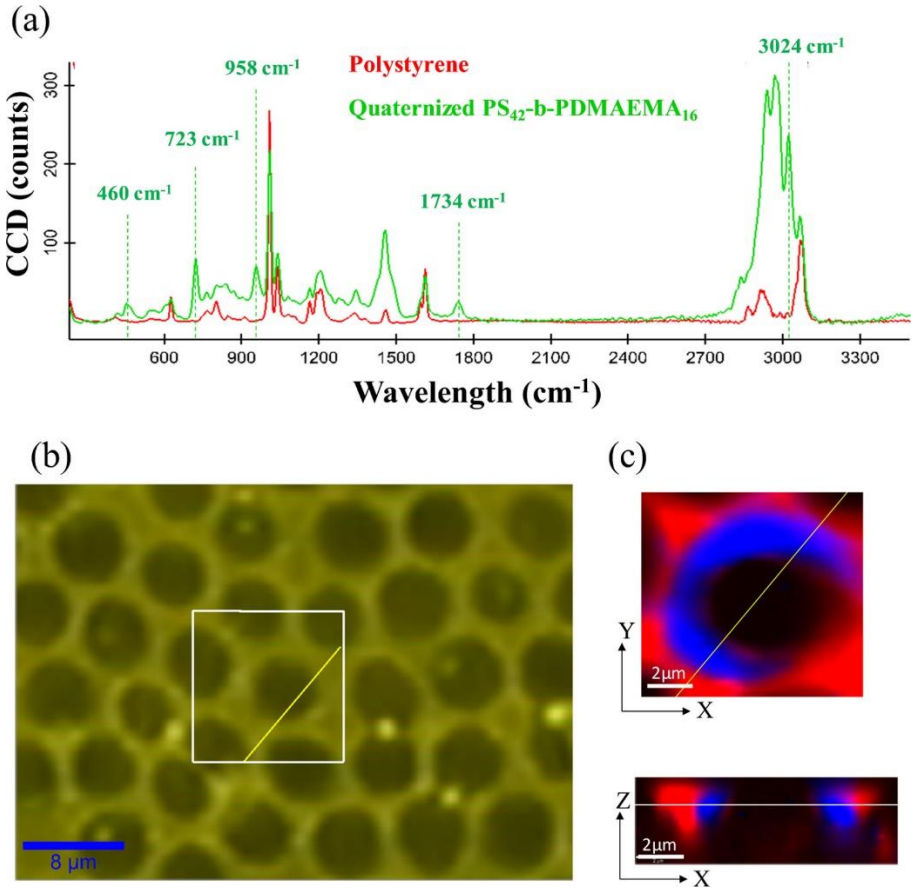

Figure 5.3. Comparison of the porous films obtained using quaternized PS_{42}-*b*-$PDMAEMAQ_{16}$ diblock copolymer (20 wt. %) and PS (80%) (sample: PSDQ32). (a) Raman spectra of the blend components, i.e., polystyrene and the quaternized block copolymer. (b) Optical image of the porous surface and (c) cross-sectional profiles in the Y−X-axis (above) and in the Z−X-axis indicating the presence of quaternized block copolymer inside the pores.

3.1.2. Biocompatibility studies

All the porous samples with different compositions (PSD305, PSD31, and PSD32), their quaternized variants (PSDQ305, PSDQ31, PSDQ32) and a control surface PS were assessed in terms of biocompatibility with the endothelial cell line (C166-GFP) after their selective functionalization was confirmed. Cells were seeded with a density of 1.5×10^4 cell per sample and after 96 h hours of culture the cell metabolic activity was measured (Figure 5.5) and fluorescence micrographs of the cytoskeleton and nuclei of the cells growing over the films were also taken (Figure 5.4). In all of the samples a cell monolayer was formed, however on PSD32 surfaces with a major percentage of copolymer a less expanded morphology was observed with a rounded morphology (Figure 5.4 f). In addition, the metabolic activity levels were also lower in contrast with PSD31, PSD305 and PSDQ31, PSDQ305, respectively. Over these two nonquaternized surfaces the endothelial cells showed similar metabolic activity and proper monolayer formation. In contrast, quaternized variants revealed a reduced cell support capacity with lower metabolic activity values.

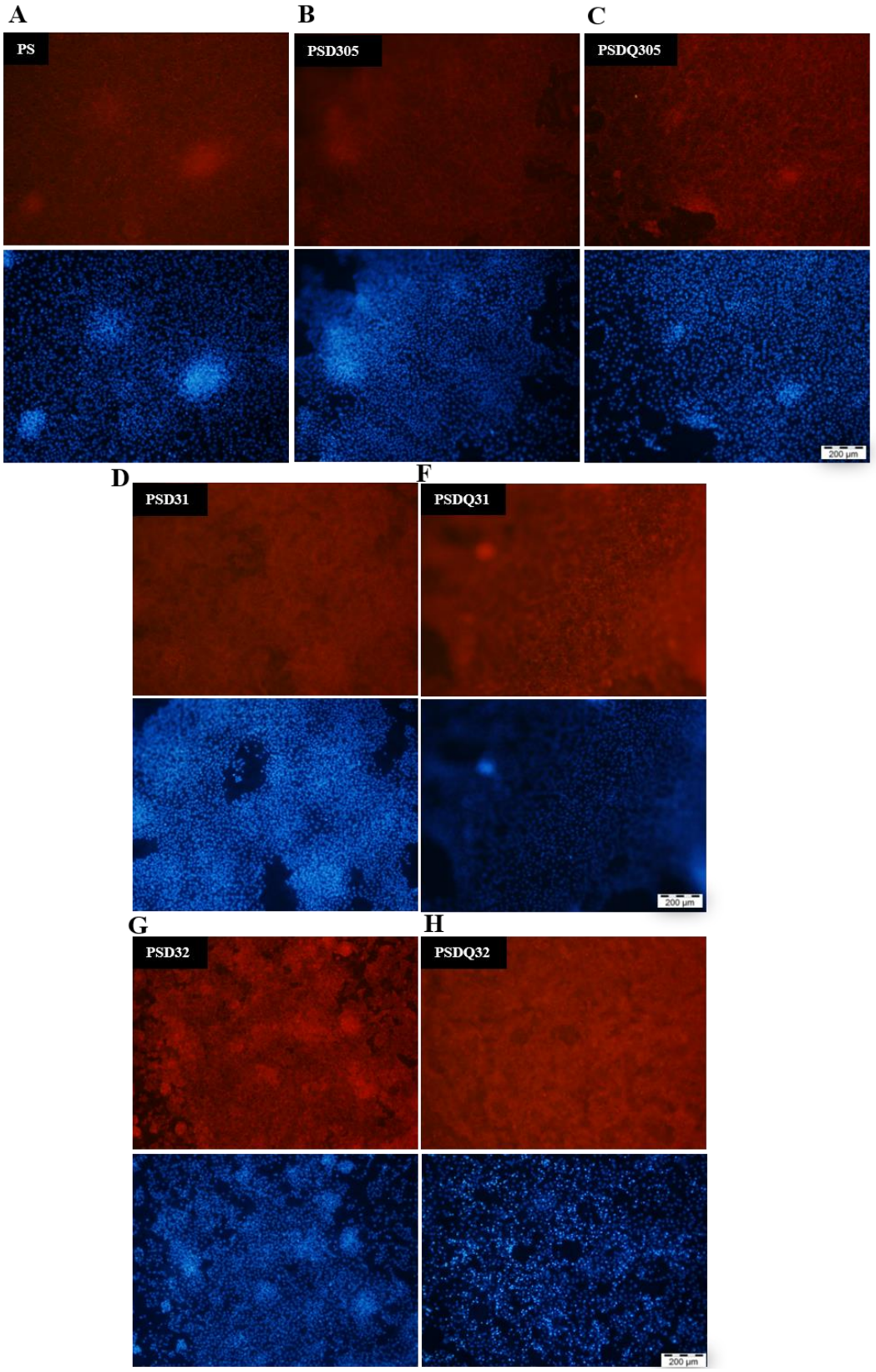

Figure 5.4. Cell adhesion tests using (actin staining (red), and Hoechst (blue)) after 96 h of culture: (a) PS, (b) PSD305, (c) PSDQ305, (d) PSD31, (e) PSDQ31, (f) PSD32, and (g) PSDQ32.

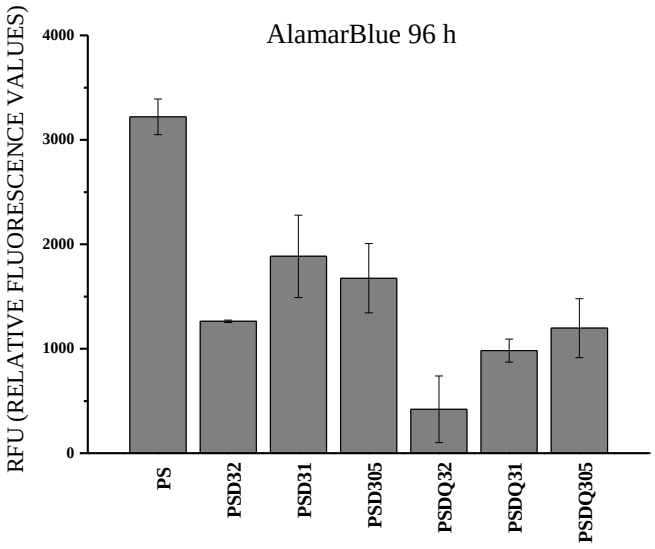

Figure 5.5. Metabolic activity measurement after 96 h of culture.

3.1.3. Antibacterial evaluation

Following mammalian cell evaluation, *S. aureus* was selected as model bacteria. This type of bacteria was of particular interest because it easily becomes resistant to antibiotics (e.g. Methicillin-resistant *S. aureus*) causing many hospital-acquired infections. Our control, PS, did not present any bactericidal activity during the 48 h. In a similar way, the nonquaternized films (PSD32, PSD31 and PSD305) showed none to very limited bactericidal activity with PSD32 after 48 h incubation time. In contrast, as expected the quaternized porous films revealed a significant bactericidal activity. Figure 5.6 displays a clear tendency in the effect of the increased percentage of the quaternized block copolymer and the incubation time on the bacterial survival. In PSDQ305 with the lowest % of quaternized PDMAEMA, a remarkable effect is distinguished only after 48 h. Oppositely with the highest concentration, PSDQ32, a bactericidal effect was detected since the beginning at time 0 h.

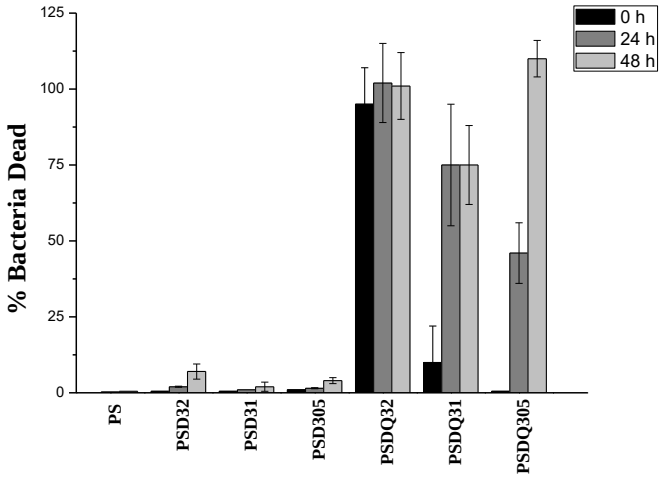

Figure 5.6. Quantification of the percentage of bacteria dead for each experimental condition. The quantification was performed by counting the number of cells stained in red or in green using ImageJ.

3.1.4. PAA and Nisin functionalization

The second approach uses an antimicrobial cue, poly(acrylic acid) (PAA), a potent antimicrobial polymer [288] with an antimicrobial peptide, the bacteriocin Nisin [289, 290]. This peptide is FDA approved and is considered a safe peptide with known potential for clinical use with proven prevention of the growth of drug-resistant bacterial strains, such as methicillin-resistant *Staphylococcus aureus*, *Streptococcus pneumoniae*, *Enterococci* and *Clostridium difficile* [290]. This peptide was covalently anchored at the surface of the formed pores by chemical coupling between the carboxylic acid groups (present in the PAA chains) and the amine terminal group of the Nisin amino acid sequence.

Porous film characterization

A polymer blend consisting of a 20% of amphiphilic block copolymer (PS-*b*-PAA) and 80% of a polymer matrix (PS) was dissolved in chloroform. In order to obtain the BF structure, the polymeric solution (30 mg/mL) was deposited onto a glass wafer and evaporated at room temperature under a saturated vapour atmosphere (99% RH). The obtained samples consisted on a variable hydrophilic to hydrophobic ratio; using larger (PS_{42}-*b*-PAA_{47}) and shorter (PS_{42}-*b*-PAA_{25}) PAA segments in comparison to the PS block. Furthermore, another block copolymer was selected with a similar hydrophilic-to-hydrophobic ratio of PS_{42}-*b*-PAA_{25} but with different molecular weight (PS_{23}-*b*-PAA_{12}).

Figure 5.7 reveals SEM images of the formed porous films; PS/PS_{42}-*b*-PAA_{47} with a larger hydrophilic block (PAA) in comparison to the hydrophobic block (PS) produced porous surfaces without order with an average pore sizes around 10 μm. On the other hand, PS/PS_{23}-*b*-PAA_{12} and PS/PS_{42}-*b*-PAA_{25} films prepared using higher hydrophobic blocks resulted in a highly order porous structure. Even though there are not significant differences in their topographic features of the block copolymers with larger molecular weight, these samples might present longer PAA segments reoriented towards the inner part compared to PS/PS_{42}-*b*-PAA_{47} with lower molecular weight. This stands as a key fact for their antibacterial performance ensuring the required interaction between the functionalized pore and the bacterial membrane.

As already introduced, Nisin was immobilized in the selected samples (PS/PS_{23}-*b*-PAA_{12}, PS/PS_{42}-*b*-PAA_{25} and PS/PS_{42}-*b*-PAA_{47}) using the amine terminal group usually more reactive that will ensure an oriented homogenous immobilization of the peptide and the carboxylic groups of the pores.

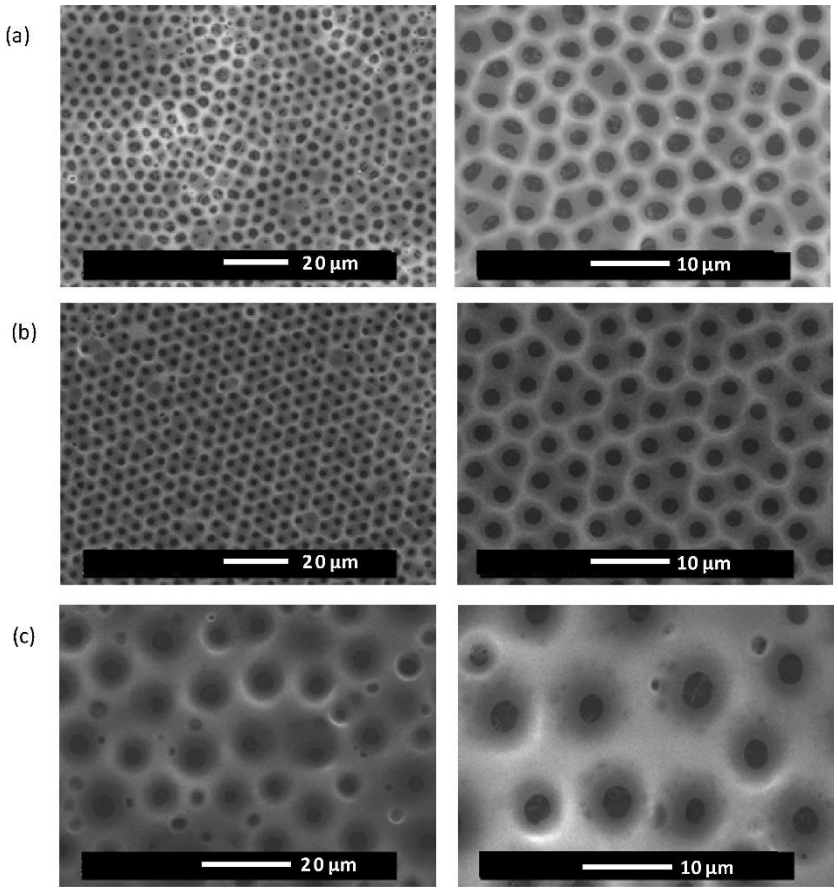

Figure 5.7. Influence of the block copolymer composition on the porous morphology. The microscope images were obtained from blends employed is formed by 80% of PS and 20% of (a) PS_{23}-*b*-PAA_{12}, (b) PS_{42}-*b*-PAA_{25} and (c) PS_{42}-*b*-PAA_{47}. The polymer concentration was fixed at 30 mg/mL and the relative humidity employed is around 99%.

After the characterization of the surface topography, the chemical distribution of the carboxylic functional groups provided by the PAA block was assessed by Confocal Raman Microscopy as already exposed with the first strategy consisting in DMAEMA functionalization. The obtained Raman spectra of the inside (blue) and the outside (red) of the pores are presented in Figure 5.8 (representative spectra from several records). Moreover, in order to compare with PS and with a PS-*b*-PAA block copolymer (PS_{42}-*b*-PAA_{47}) both spectra have also been included. The presence of a carbonyl group signal at ~1720–1730 cm^{-1} turned out to be the most significant difference between the pure PS and the block copolymer. PAA segments will present the signal and its localization in the porous structure can be predicted. Therefore, the spectra recorded inside of the pores showed a signal due to the carbonyl groups indicating the presence of the diblock copolymer in this area, while outside the pores the acquired spectra were comparable with the spectrum of pure PS. These results confirmed that inside the pores there is an enhancement in the hydrophilic block (PAA) and the surface of the film is mainly formed by pure PS.

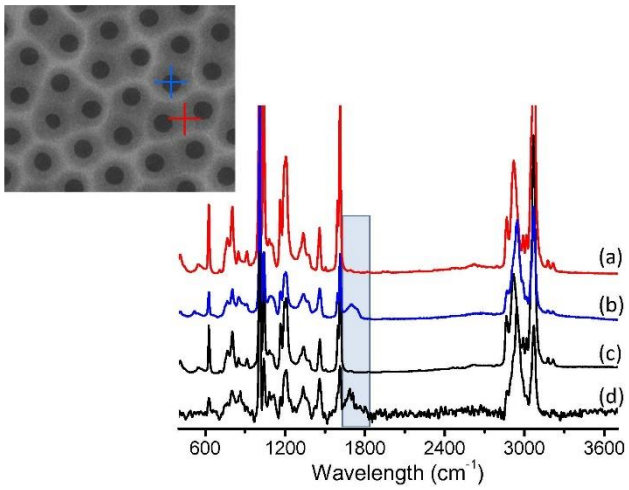

Figure 5.8. Confocal Raman spectra of porous films prepared using 20% of PS_{42}-*b*-PAA_{47} and 80% of PS measured outside the pores (a) and inside the pore (b). For comparative purposes, Raman spectra of pure polystyrene (c) and the block copolymer PS_{42}-*b*-PAA_{47} (d) have been equally included.

Regarding the samples with Nisin incorporation, the films were evaluated by FT-IR. The FT-IR spectra of Nisin (Figure 5.9 a) reveal two large signals in the region between 1000 and 2000 cm^{-1}, 1050–1200 cm^{-1} signals are in agreement with the aliphatic residues of the aminoacids. However, the aliphatic residues signals are overlapped with other signals in the treated and non-treated porous films spectra. A broad band is observed in the region 1580–1720 cm^{-1} assigned to the amide bands present in the polypeptide chains [291, 292]. This fact can also be depicted in the surfaces where Nisin was bonded (PS/PS_{23}-*b*-PAA_{12} or PS/PS_{42}-*b*-PAA_{47}, Figure 5.9 c and e), nevertheless for blend PS/PS_{42}-*b*-PAA_{47} the band is more evident suggesting that larger PAA hydrophilic chains are capable to immobilize larger amount of Nisin.

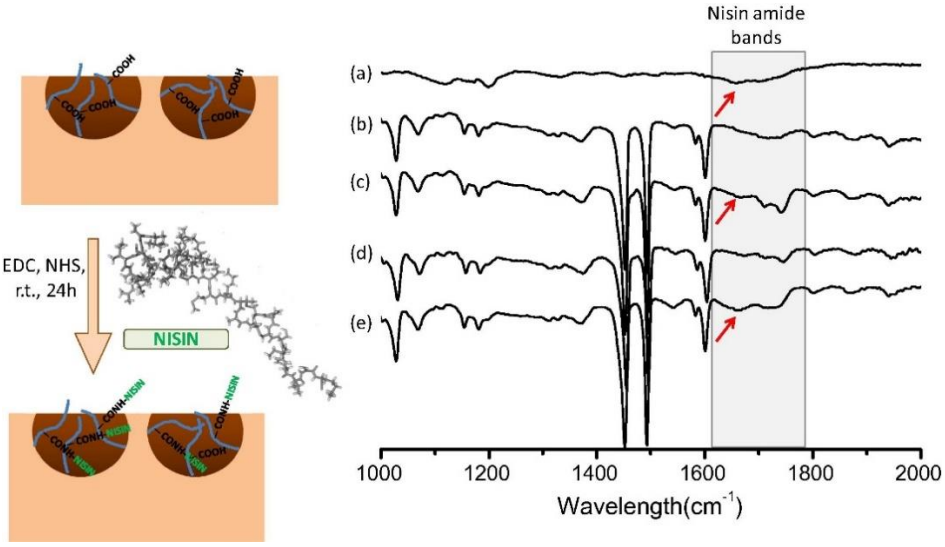

Figure 5.9. Left: scheme of the immobilization of Nisin onto the poly(acrylic acid) functionalized surfaces. Right: IR spectra of (a) Nisin, (b) microstructured films obtained from blends of PS/PS_{23}-*b*-PAA_{12}, (c) microstructured films obtained using PS/PS_{23}-*b*-PAA_{12} treated with Nisin, (d) microstructured films obtained using PS/PS_{42}-*b*-PAA_{47}, (e) porous film prepared using PS/PS_{42}-*b*-PAA_{47} treated with Nisin.

3.1.5. Biocompatibility studies

Subsequently after the porous films characterization with confirmation of selective disposition of PAA segments and Nisin immobilization biocompatibility studies were performed using the same murine endothelial C166-GFP cell line as in the first approach (DMAEMA). Simulating the prior conditions (same cell density and cell culture methodology) cells were allowed to grow over the films for 96 h. Pure PS presented an almost 100% confluent culture (Figure 5.10.A), with an outstretched cell morphology showing an excellent cell adhesion. Likewise, with PS/PS_{23}-*b*-PAA_{12} film (Figure 5.10.B) good cell monolayer formation with a slight increase in cell density was observed. On the other hand, over PS/PS_{42}-*b*-PAA_{25} (Figure 5.10.D) and PS/PS_{42}-*b*-PAA_{47} (Figure 5.10.F) surfaces a confluent monolayer was developed but with a reduced adhesion to the surface as cells were growing heterogeneously with high-density cell clump areas. Figure 5.11 reveals the metabolic activity of the culture cells after 96 h, all three PAA functionalized samples present comparable metabolic activity values as the greater value obtained in PS/PS_{42}-*b*-PAA_{47} has a high error.

As described with the previous samples, the poly(acrylic acid) surfaces with immobilized Nisin also allowed a good monolayer formation. Nisin treated films promoted the growth of a homogeneous cell culture over PS/PS_{42}-*b*-PAA_{25}N and PS/PS_{42}-*b*-PAA_{47}N samples (Figure 5.10 E and G). Moreover, from Hoechst staining disclosed an increased growth in PS/PS_{42}-*b*-PAA_{25} treated with Nisin, later on confirmed with the metabolic activity measurements with the highest value of all the evaluated samples (Figure 5.11).

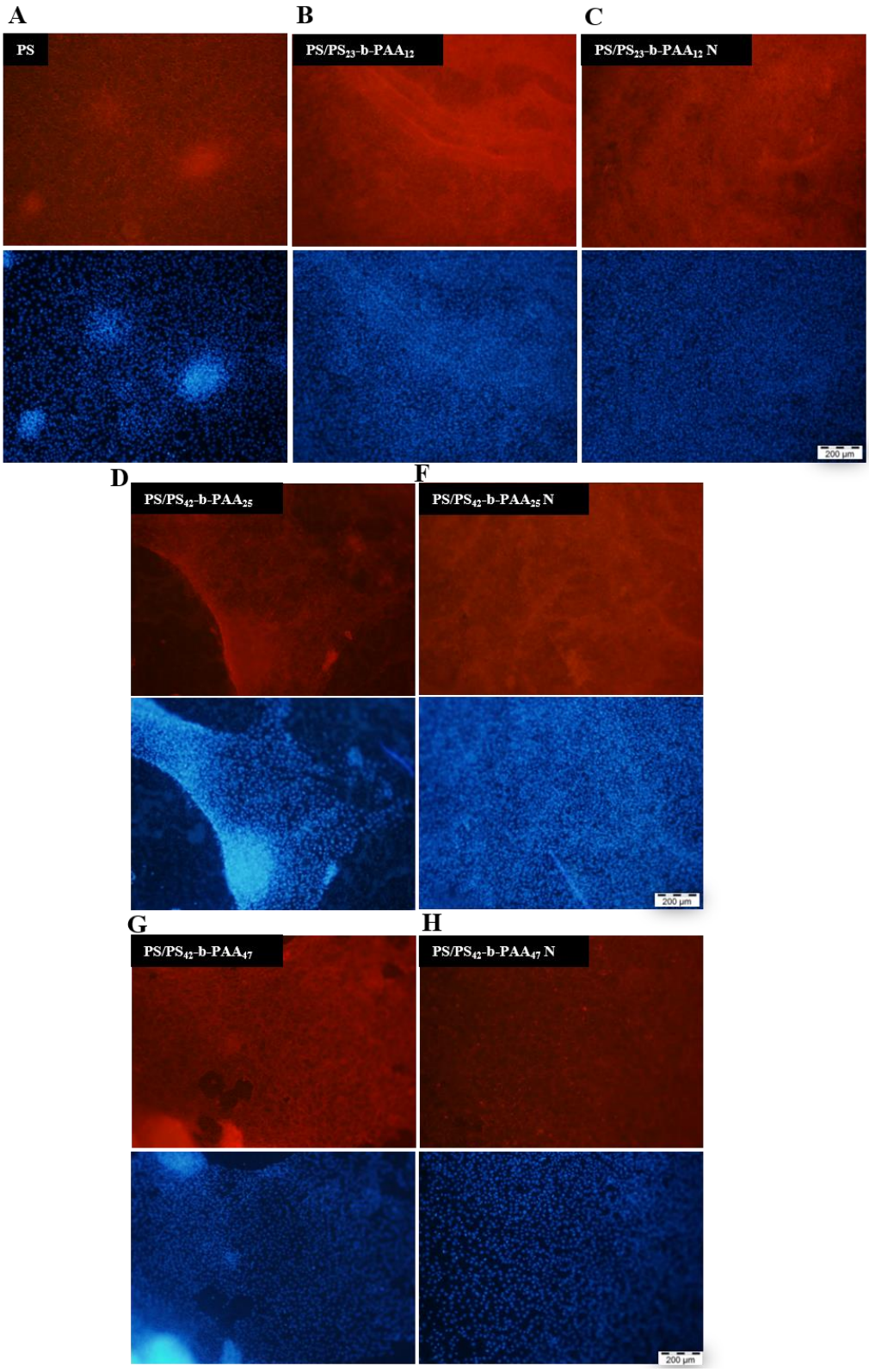

Figure 5.10. Fluorescence images obtained by Hoechst (blue) and actin staining (red). The fluorescence images of the surfaces were obtained upon 96 h of culture on different microporous functional surfaces: (a) 100% PS (b) PS/PS_{23}-*b*-PAA_{12}, (d) PS/PS_{42}-*b*-PAA_{25} and (f) PS/PS_{42}-*b*-PAA_{47}, (c) PS/PS_{23}-*b*-PAA_{12} and treated with Nisin, (e) PS/PS_{42}-*b*-PAA_{25} and treated with Nisin and (g) PS/PS_{42}-*b*-PAA_{47} and treated with Nisin.

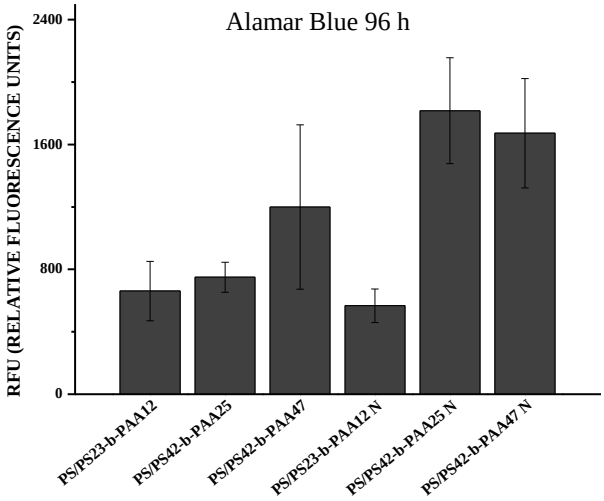

Figure 5.11. 96 h of culture on different microporous functional surfaces: PS/PS_{23}-b-PAA_{12}, PS/PS_{42}-b-PAA_{25}, PS/PS_{42}-b-PAA_{47}, PS/PS_{23}-b-PAA_{12} and treated with Nisin, PS/PS_{42}-b-PAA_{25} and treated with Nisin and PS/PS_{42}-b-PAA_{47} and treated with Nisin.

3.1.6. Antibacterial evaluation

S. aureus was also used in this section for the evaluation of the formed porous coatings. Percentage of live and dead bacteria under each experimental condition was quantified after 0, 24 and 48 h using Image J (Figure 5.12). PS control did not show bactericidal activity over time. Nonetheless, when the PAA was introduced in the composition remarkable bactericidal properties to the surfaces were provided PS-*b*-PAA di-block copolymers exhibited after 24 h incubation full bactericidal activity with 100% of the adhered bacteria being killed with no direct relation to the PAA content. Unexpectedly, the Nisin functionalized surfaces did not display significant bactericidal activity at any surface composition and incubation time not even at 48 h.

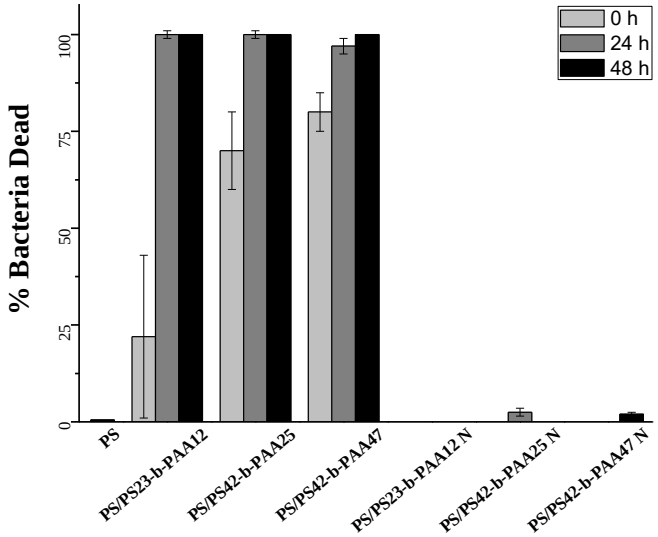

Figure 5.12. Quantification of the % of bacteria dead at different times 0, 24 h and 48 h on the different porous surfaces tested. The quantification was performed by counting the number of cells stained in red or in green using Image J.

3.2. Discussion

New materials with selective antifouling (no bacteria adhesion) or bactericidal (bacteria death) properties are being constantly investigated. In tissue engineering applications one of the main concerns is the possible implant or medical device contamination. BF method can provide not only a mouldable microporous structure, as described in the previous chapter, but can also introduce added functionalities, e.g. antibacterial motifs/cues incorporation into the interface. The proposed strategy (Figure 5.13) is based on bacteria size being between 1 to 5 μm (*S. aureus* employed in these studies has 1 μm diameter), whereas mammalian cells are several times larger (from 10 to 20 μm). Obtaining functionalized pores in that range (for instance, between 4 and 6 μm) could prevent the contact of the cells with the inner part of the pores.

Quaternized DMAEMA functionalization

Confocal Raman allowed us to ascertain the chemical composition inside/outside the pores for both PSD and PSDQ (Figure 5.2 and 5.3) and, in agreement with other studies [293-295], during the pore formation, the hydrophilic groups (DMAEMA) of the diblock copolymer were able to readjust around the pore surface. This orientation is a result of the solvent and the water droplet evaporation, due to which a heterogeneous surface chemical composition with localized positioning of the diblock copolymer is obtained.

The antibacterial strategy is based on quaternary ammonium groups; these groups are being used due to their excellent efficiency in killing on contact. The negatively charged groups present in the bacterial cell wall are described to interact with the ammonium groups [296, 297]. Other antibacterial quaternary polymers have been reported to be biocompatible with Caco-2 human epithelial cells in a range of concentrations keeping their minimum bactericidal concentrations [298]. However, it has been reported that these groups can also reduce the biocompatibility of a material, as mammalian cells have a net negative plasmatic membrane charge too [297, 299]. Therefore, to limit the contact between these antimicrobial groups and mammalian cells, these functional groups were placed inside the pores, thus remaining only accessible to bacteria.

It is known that the monolayer formation of the endothelial cells could also differ as a consequence of change in the porous structure and not only due to the chemical composition. Quaternized samples seemed to present more differences in height (Figure 5.1). An intermediate condition (PSDQ31) can be proposed as a potential material that provides a compromise between mammalian cells biocompatibility and antibacterial effect from shorter times than PSDQ305 (Figure 5.6). This strategy could be used with other polymers and evaluated with other cell types with bigger and smaller size.

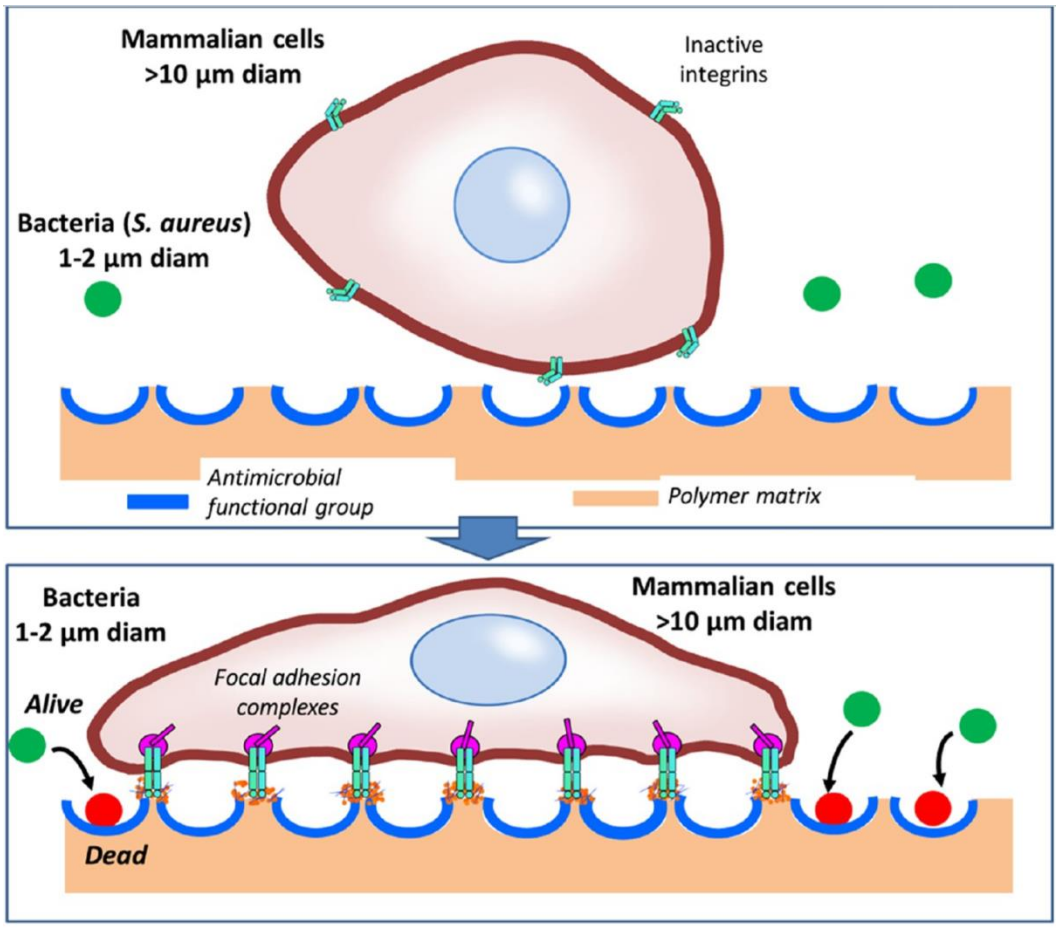

Figure 5.13. Illustration of the strategy proposed to fabricate functional porous surface selective against bacteria. Mammalian cells interact only with the inner part of the pores, and focal adhesion complexes are established through integrin activation. In contrast, bacteria may enter inside of the cavities and be affected by antimicrobial functional groups.

The proposed functional microporous surfaces presented excellent antimicrobial properties when the polymer is in its quaternized form. Interestingly, quaternary ammonium groups are hidden from the cell contact in this design. As a result, the developed materials presented simultaneously high biocompatibility with mammalian cells and antimicrobial activity against *S. aureus*.

PAA and Nisin functionalization

Confocal Raman Microscopy was used to ensure the incorporation of PAA inside the pores (Figure 5.8) confirmed a preferential reorientation inside the pores due to the affinity of the hydrophilic segments of the block copolymer (PAA) by the condensed droplets during the solvent evaporation. Therefore, BF approach allows us to rearrange the chemical disposition locating the hydrophilic parts inside the pores with tailored pore size by adapting polymer concentration, % of polymeric blends, humidity, etc. Additionally, Nisin, a potent antimicrobial peptide, was successfully anchored into the film by the covalent bond and confirmed by FT-IR.

Nisin incorporation in PS/PS_{42}-*b*-PAA_{47} and PS/PS_{42}-*b*-PAA_{25} favoured the metabolic activity results of the endothelial cells compared with the same samples without the peptide (Figure 5.11). Nisin could be interacting with serum proteins and promoting the adhesion of proteins, and in consequence enhancing cell proliferation. In a physiological state ingested nisin is inactivated by trypsin and pancreatin and will have no effect on the gut microflora.

In terms of bactericidal activity, the films with PS/PAA diblock copolymers presented an outstanding performance with all the bacteria killed at end point (Figure 5.12). Similar results were obtained by Günther *et al.*, where microphase separated PAA based block copolymers were able to kill bacteria and prevent from biofilm formation [288]. In contrast, Nisin incorporated films did not present bactericidal activity at any time point. This unexpected result can be explained considering the mechanisms of action of Nisin.

It is known that this peptide possesses two domains: the first domain binds with high affinity to the lipid II molecule, which is a precursor molecule in the synthesis of the cell wall of bacteria. The second region is the membrane-embedded pore-forming domain [300]. Therefore, Nisin inhibits bacterial growth by producing pores in cell membrane and disturbing cell-wall biosynthesis through specific lipid II interaction [301]. Nisin has to be in its oligomerized form to be able to permeabilize the pores. In this scenario the amount of Nisin and surface coverage density might not be enough to achieve an efficient bactericidal activity. On the other hand, Nisin is covalently achored to the PAA, thus the peptide may not have the flexibility to rearrange on the bacteria surface to achieve the active state. At the same time, the functionalization of PAA carboxylic groups with Nisin peptide may neutralize the groups responsible of the bactericidal activity of the PS-*b*-PAA/PS surfaces, causing inert surfaces. For instance, the PEGylation of Nisin via the amine group of the lysine side-chain resulted in an inactive molecule. It was theorized that the amino group of the lysine residue is required to bind to the pyrophosphate of the lipid II molecule resulting in its activity loss [302].

Interestingly, in the porous films prepared using PS/PS_{42}-*b*-PAA_{25} cells were able to grow on the surfaces and form perfect monolayers whereas their bactericidal effect is exceptional. Figure 5.14.A depicts the proposed action mechanism. Bacteria killed on contact with the poly(acrylic acid) surface are located inside the pores (red colour in Figure 5.14 B). Oppositely, Nisin functionalized samples did not present any antibacterial behaviour. This clearly evidences that bacteria are able to enter in the pores and interact with the PAA groups. Some dead bacteria can also be observed outside of the pores. This clearly indicates that *S. aureus* made contact with the pore inducing death by the interaction with the antimicrobial moiety and after that are able to diffuse outside of the pores.

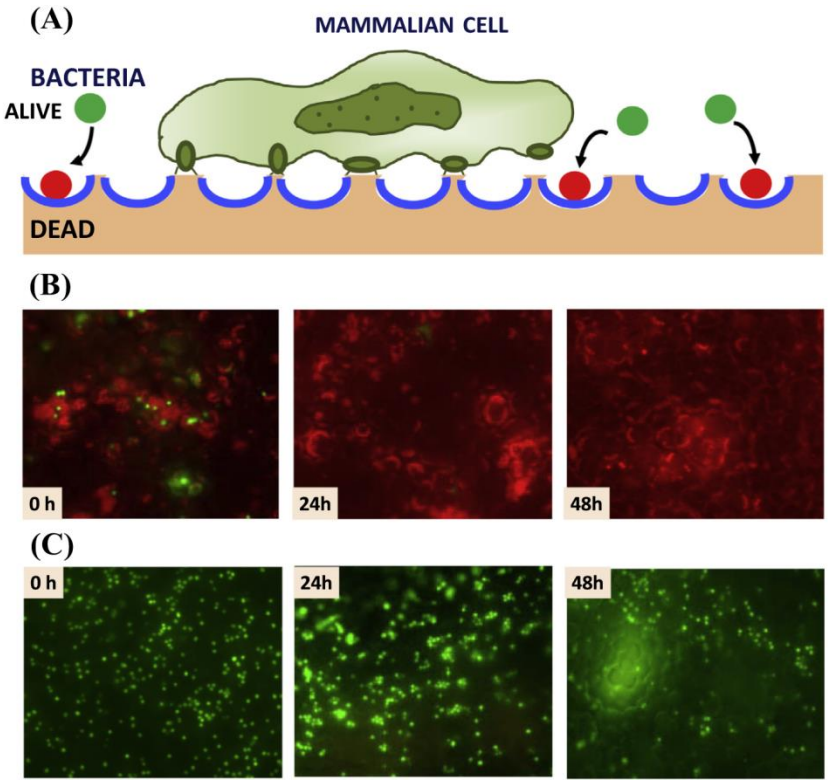

Figure 5.14. (A) Mechanism of action of the porous bactericidal surfaces. A schematic representation of the differential interaction of the large mammalian well with the main surfaces and the smaller bacteria cells with the pores that display the bactericidal properties due to the PAA composition. (B) Images of 20% PS_{42}-*b*-PAA_{25}/80% PS and (C) 20% PS_{42}-*b*-PAA_{25}/80% PS/NISIN surfaces incubated with bacteria in which dead bacteria are stained in red 0, 24, and 48 h after adhesion. Magnification images show the preferential distribution of the dead bacteria in the pores of the surfaces.

BF obtained PS-PS/PAA films did not show cytotoxicity in C166-GFP cell line, allowing endothelial culture to adhere and proliferate. Nisin treatment did not decrease biocompatibility of these samples and even promoted in some cases a better performance, motivating a homogenous cell distribution with a proper cell monolayer formation.

Chapter 4. Cell sheet engineering for bone regeneration

As it has been mentioned in Introduction (Section 1.4), cell sheet engineering could become a valuable strategy to improve the integration and reduce the immune system reaction to a biomaterial implantation. Bone cells coupled to implants by monolayer transplantation could favour a better implantation success. New strategies in tissue engineering include the incorporation of different components to a biomaterial e.g. a metallic core, a ceramic coating, a polymeric top layer and a cell monolayer, providing different desired characteristics.

In this thesis, the vinyl-lactams based hydrogels developed by FUPOL have been evaluated as supports for bone cell manipulation. Although the ultimate goal is to cover the metallic implants described in previous chapters with transplantable bone cell sheets detached from these hydrogels, this chapter is devoted to preliminary studies focused on the design, optimization and evaluation of the hydrogels as bone cell supports.

Previous studies have shown, on the one hand, that murine cells may adhere and proliferate onto the surface of VP-based hydrogels, and that they detach upon mechanical agitation [161]. On the other hand, thermosensitive VCL-based hydrogels exhibited higher cell growth stimulation and a better control on the detaching since it happens upon decrease of the temperature. Besides, it has been shown that the incorporation of ionic charges to the VP-based hydrogel do not have a strong influence on their performance over murine cells but it does have an antifouling effect on preliminary tests with bacteria [162].

Focusing on bone cells, which may respond specifically to certain chemical and topographical cues, it may be interesting; i) To explore the performance of VCL-based hydrogels when ionic charges are incorporated to the formulation, as a preliminary study to their use in the culture of bone-related cells. Surface chemistry modification could provide an improvement in cell growth and transplant capacity. ii) To study the influence of surface structuration, that is wrinkling, on the culture of bone-related cells.

4.1. VCL-based hydrogels as thermoresponsive platforms for cell transplants

4.1.1. Surface functionalization of VCL hydrogels

This kind of smart hydrogels respond to specific stimuli (temperature changes). VCL-based hydrogels can be functionalized with groups on its surface by methacrylate incorporation into the polymer blackbone, as it has been done with VP-based hydrogels. Different ionic methacrylates M (Table 6.1) were used based on a previously optimized formulation for VP-based networks [161, 162], via molar substitution of VP by VCL. VCL without ionic M (sample 8) and VP with SO_3^- from previous works [161] (sample 1) were used as control platforms. We chose endothelial

cells as a quick monolayer formation model over the hydrogels as a consequence of the previous evaluation with VCL and the growth time over the hydrogels was reduce to 72 h. It is known that this model builds a cell monolayer with a strong attachment to the substrate through specific protein complexes [303]. Besides, endothelial cells are important for vascularization of the tissues, including bone tissue. Therefore, the present aim was to evaluate the hydrogels functionalization (charged groups) in a preliminary study and to assess the possible transplant potential as mechanical properties can change with this functionalization.

Table 6.1. summarizes the structures of the precursors, the used methacrylates and the structure of the crosslikers. The two crosslinkers used are a dimethacrylate (C1) and a divinyl compound (C2), which are being used simultaneously.

Table 6.1. Characteristics of the hydrogels studied in this work.

	1	2a	2b	3a	3b	4a	4b	5a	5b	6a	6b	7a	7b	8a
ID cartoon														
Vinyl-lactame														
M	*M-SO_3^-*	*M-SO_3^-* 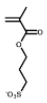		*M-N^+* 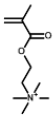		*M-SO_3^-/ M-N^+* 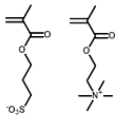				*M-N^+-SO_3^-* 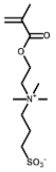		*M-PO_3^--N^+* 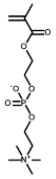		No *M*
(*VP* or *VCL*)/*M* molar ratio	6/1	12/1	6/1	12/1	6/1	12/1[a]	6/1[a]	6/1[a]	6/1[a]	12/1	6/1	12/1	6/1	12/1
VPTT		39	40	37	39	35	35	33	35	36	33	35	34	37
Swelling S at 37 °C	87	90±3	89±1	83±2	91±2	71±1	69±1	87±1	87±2	68±2	61±1	75±1	82±1	63±2
Structures of the crosslinkers	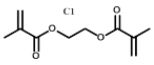 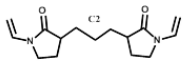													

Five different ionic M were evaluated: M-SO_3^- (samples 2 a/b), M-N^+ (samples 3 a/b), M-SO_3^-/ M-N^+ (samples 4 and 5 a/b), M-N^+-SO_3^- (samples 6 a/b) and M-PO_3--N^+ (samples 7 a/b). Sample variations a) or b) were prepared to study the influence of the ionic load and stand for the molar VCL/M ratio, a) corresponding to 12/1 with half moles of M and b) to 6/1. Samples 5 did not change in molar ratio but in charge distribution, 5a with higher negative charges and 5b with higher positive charges. The other obtained hydrogels were positive (samples 3), negative (samples 2), zwitterionic (samples 6 and 7) and pseudo-zwitterionic (samples 4). Their Young's moduli, as acquired by compression tests, oscillated between 90 and 400 KPa, consistent with the typical values for soft hydrogels [304].

4.1.2. Hydrogels characterization

All the new prepared hydrogels display thermosensitivity (Figure 6.1), swelling of the samples changes along with temperature. Graph on the left presents control VCL (sample 8) and samples 2-5, right graph contains samples 6-7. The VCL/M ratio and ionic monomer (M) changes seem to have a strong influence on the degree of thermosensitivity (change in swelling capacity), nevertheless, not on the VPTT values (Table 6.1). Similar VPTT values (near 37ºC) were measured for all the samples constituting a physiologically relevant interval. In order to obtained a cell culture approved platform it is important to stay in the physiological range. Moreover, these values are similar to that reported in literature for pure VCL systems [305].

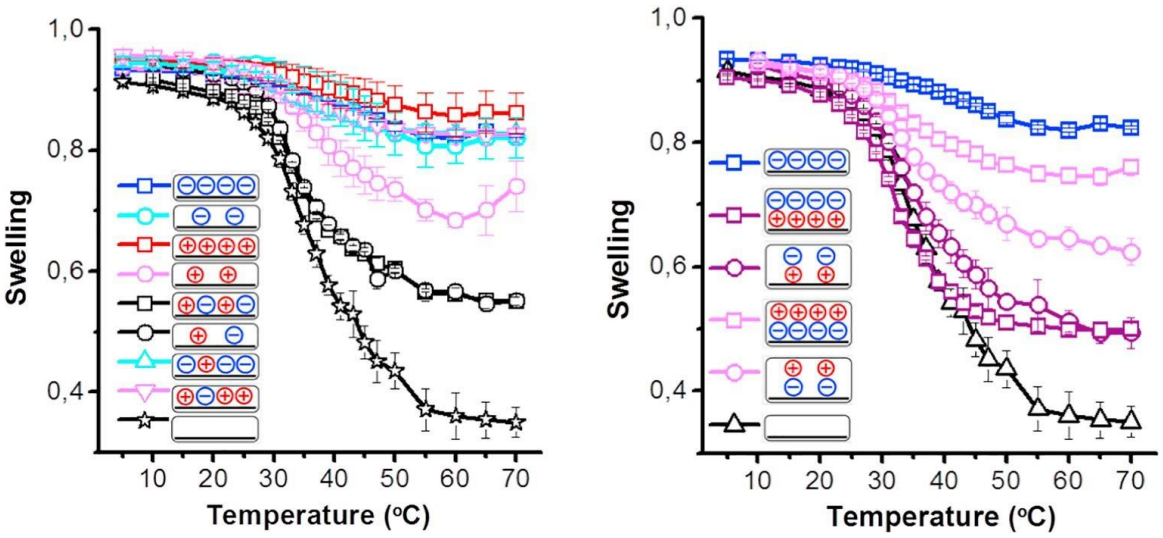

Figure 6.1. Swelling versus temperature for all hydrogels studied in this work.

From the swelling behaviour a similar swelling below the VPTT (volume phase transition temperature) can be depicted for the samples (0-30ºC). Under the VPTT the samples are in their 'hydrophilic' state, where the network is probably in its swelling maximum (the maximum determined by the crosslinking density). In contrast, above the VPTT the type and amount of M seems to be critical for the swelling behaviour and for the volume contraction. Control sample 8 with no ionic component M reveals the major reduction in swelling as the temperature increases, showing a more contractile behaviour from 0.9 to 0.35. A tendency is observed when the ionic components are incorporated, thermosensitivity capacity is reduced in a composition dependent manner (influence on swelling is stronger for the hydrogels with a VCL/M molar ratio of 12/1 when compared to the networks with a 6/1 ratio). Moreover, the hydrogels containing single charges (negative-samples 2, or positive-samples 3) or excess of one type of charge (samples 5) exhibit less volume changes than the systems incorporating stoichiometric amounts of charges. The latter systems are the zwitterionic sulfobetaine (samples 6), the zwitterionic phosphorylcholine (samples 7), or the pseudo-zwitterionic systems (samples 4). All these differences are less appreciable at the culture temperature (37 °C) which is an intermediate

temperature, swelling values at this temperature are available in Table 6.1 ranging between 61-90.

4.1.3. Cell growth and transplant potential evaluation

The characterized hydrogels were evaluated in terms of monolayer formation over the hydrogels and transplant potential, using as it has been mentioned before endothelial murine cells. Hydrogel charge has an important role both in the modulation of the cell adhesion and proliferation. Likewise, cell detachment can also be modulated by the charge which is also a crucial step in order to employ the materials for cell manipulation and tissue engineering purposes. It is known that different ionic charges can modulate cell adhesion through surface processes including both serum protein adsorption and early cell attachment [306]. Moreover, it has already been stablished that the type and amount of charge can strongly influence the thermosensitivity potential mainly in terms of water uptake and volume change.

Cells were allowed to grow during 72 h, at 37 °C above the VPTT of the hydrogels. This temperature is below the VPTT in order to induce the hydrogel conformation change and favouring water uptake. The temperature was controlled using a thermoprobe. The formed cell monolayer or adhered cells detach as the hydrogel swells and is transplanted onto a TCP surface. The endothelial cell monolayer is formed quick and thanks to its self-fluorescence the hydrogels were observed using fluorescence microscopy, placing them upside down into another TCP (Figure 6.2 and 6.3 F-labelled micrographs). Hydrogels were not transparent at 37ºC after the M incorporation, therefore no simple optical microscopy evaluation could be implemented. In order to study cell detachment, the same protocol was used as in the previous section. 'T' images represent the culture state of the transplant after 48 h, the culture was observed using optical microscopy (Figure 6.2 and 6.3).

All VCL-based hydrogels allowed cell adhesion and proliferation in contrast with VP (sample 1) that with such short culture time presented reduced clusters of cells, in agreement with previous studies [161]. This VP-based material was capable of inducing a rapid cell detachment or cell sheet transplantation through simple mechanical agitation after 7 days of culture [161]. Cell monolayer was formed at 72 h in most of the VCL-based samples. Nonetheless, there were differences in the cell adhesion and proliferation with composition variation. For instance, samples 2b and 3b that are hydrogels with higher load of negative and positive charge, respectively, presented different behaviour. Sample 2b had a homogenous cell distribution over all the seeded area with high cell density and sample 3b a marked decrease in cell growth. In the latter case, cell clusters are formed instead of monolayers. When the amount of load charge of the hydrogels diminishes the opposite scenario is found, negatively charged sample 2a showed a

poorer cell growth and the positive charged 3a presented a better cell growth than that in the above discussed samples 2b and 3b. The uncharged control (sample 8) endothelial cells displayed the best behaviour and compared with samples 2 and 3 a denser cell monolayer was formed (image 8-F). Regarding the transplant potential of the samples, the anionic sample 2b and neutral sample 8 exhibited the best performance with similar values of metabolic activity after transplantation (Figure 6.5) and significantly higher ones than those of positive samples 3a and 3b, which actually presented the lowest values of the transplants. In addition, when the hydrogel was analysed after the detachment process cellular remnants attached to the positive-charged surfaces were found (Figure 6.4, images 3a-D and 3b-D). Sample 2a, with less anionic load than 2b, presented an intermediate metabolic activity (Figure 6.5). Even though metabolic activities (Figure 6.5) of samples 2b and 8 after transplantation exhibited similar values, if we look at the transplant micrographs (Figure 6.2) sample 8 presented a complete detachment with a monolayer, while detachment from sample 2-b was incomplete and patchy. Moreover, after the transplantation some rounded cells remain adhered to the hydrogel (Figure 6.4, image 2b-D). Hydrogel 8 without ionic charge was the only sample that was completely transparent below the VPTT. Transparency of the substrate provides an interesting technological advantage; cells can be directly observed by invert optical microscopy without any manipulation.

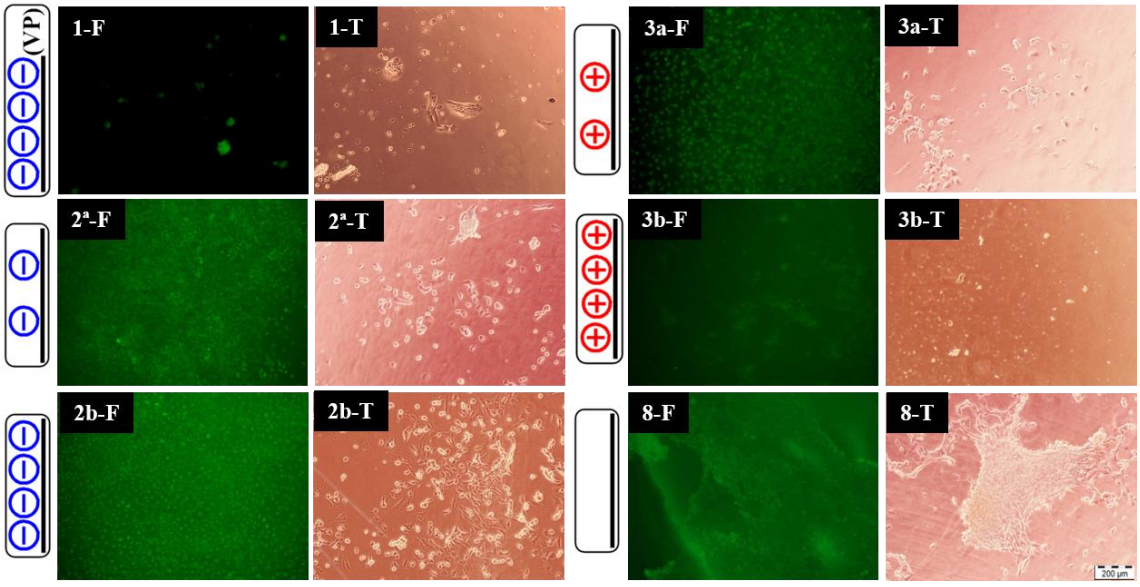

Figure 6.2. The label 'F' corresponds to images of cultures on the hydrogels 1, 2, 3 and 8 after 72 hours obtained by fluorescence microscopy. label 'T' indicates images of transplanted cells after 48 hours obtained by optical microscopy.

Different results were found when the positive and negative charges were combined (Figure 6.5). Cells grown over the pseudo-zwitterionic formulation (samples 4) or the sulfobetaine zwitterion (samples 6) presented higher cell proliferation and higher metabolic activity that in positively

charged samples 3. On the other hand, the cell growth was comparable or greater than the anionic and neutral hydrogels 2 and 8. It seems that there is an influence of the composition for samples 6 since samples with lower ionic load (6a) showed a diminished effect of surface charge on cell adhesion and proliferation when compared with sample 6b. As for the transplant potential, it was found outstanding for some of these samples (such as the 6b) and in agreement with the cell growth over the platforms. The cell transplant of sample 6b presented a conserved ECM and cell junctions and the higher metabolic activities levels of all the samples. Furthermore, very few and small cell clumps were detected over the hydrogel after detachment, indicating an optimal detachment process (Figure 6.3, image 6b-D). In a similar way, hydrogels 6a, 4a and 4b showed minor cell aggregates adhered to the surface after the detaching process (Figure 6.3, images 6a-D, 4a-D and 4b-D). In terms of thermosensitivity, zwitterionic samples 4 or pseudo-zwitterionic samples 6 presented higher volume change but still inferior to the neutral sample 8, where a better preservation of the cell monolayer is obtained.

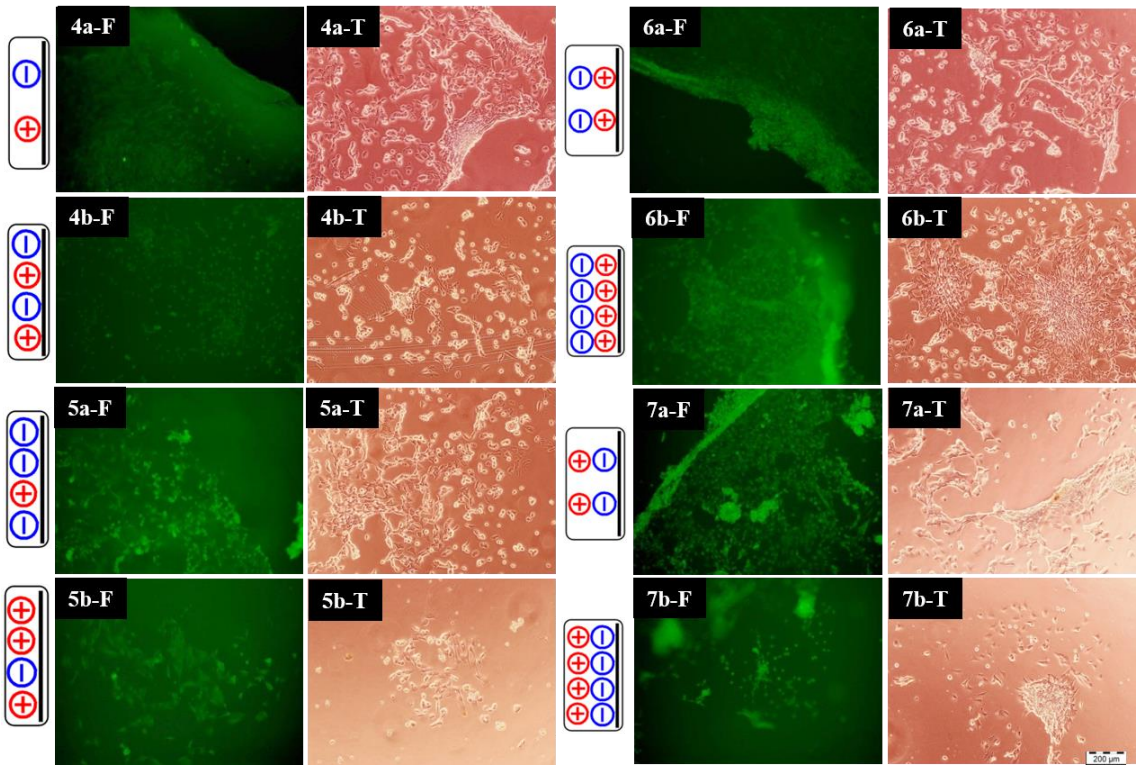

Figure 6.3. Labels 'F' correspond to images of cultures over the hydrogels 4, 5, 6 and 7 after 72 hours obtained by fluorescence microscopy. Labels 'T' are images of transplanted cells after 48 hours obtained by optical microscopy.

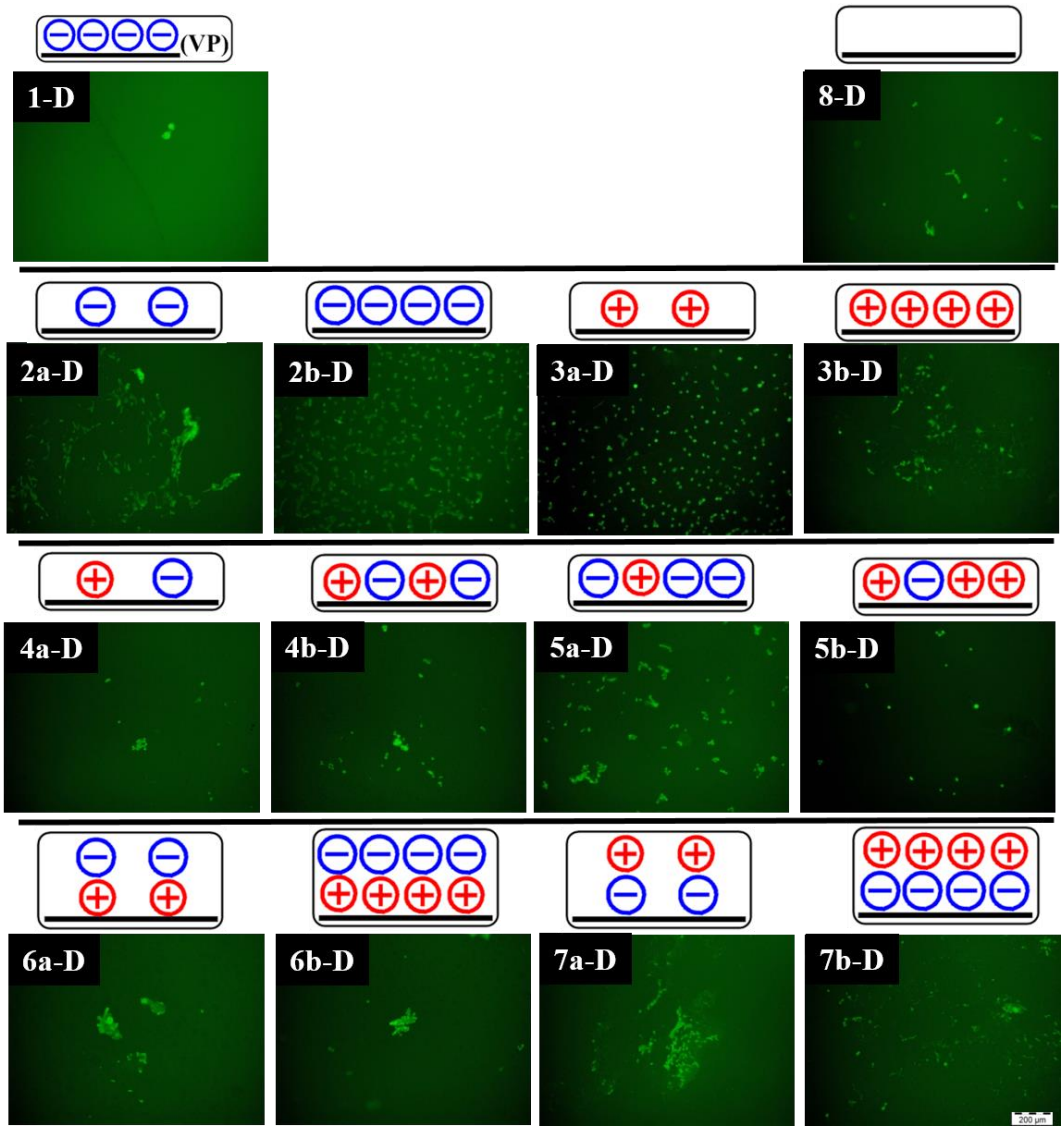

Figure 6.4. Fluorescence microscopy images of the surfaces of the VCL-based hydrogels after the detachment process.

Lastly, the remaining samples displayed different behaviours. Sample 5a, which has an excess of negative charge, presented an enhanced cell growth in comparison to sample 5b (excess of positive charge) however none of them achieved a complete monolayer. Moreover, the behaviour is similar to the negative and positive samples 2 and 3, respectively. Both samples 5 showed a low volume change upon change of temperature, this feature could explain the fact that no conserved monolayer in the TCP was found for sample 5a after the transplant. Low volume change induces an unstructured monolayer detachment. On the other hand, the behaviour of samples 7 were similar to the positive samples 3 with low metabolic activity levels (i.e. for sample 7b few cell aggregates were detected).

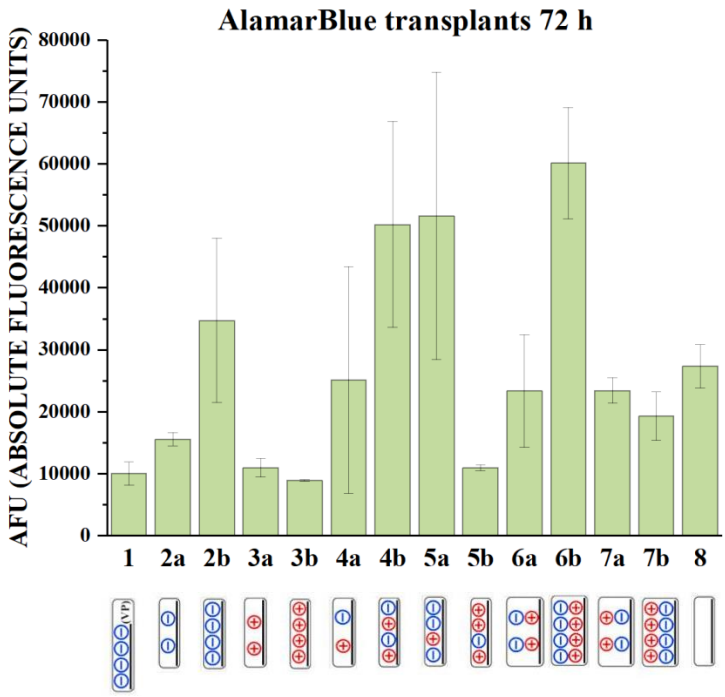

Figure 6.5. AlamarBlue metabolic activity for the different evaluated hydrogels after 72 h of growth on TCP.

4.1.4. Evaluation of selected VCL-based support with bone-related cells

The uncharged sample 8 from the previous study was selected to carry out additional studies with bone related cell models, i.e., a preosteoblast cell line (MC3T3) and a macrophagic cell line (RAW 264.7) to biovalidate the possible used of VCL platforms for cell transplants. The endothelial cell line (C166-GFP) has been used as well for comparative purposes. Macrophages are responsible for immune system reaction and osteoclasts precursors (with the presence/stimuli of RANKL). Preosteoblasts can form a monolayer and induce mineralization and bone matrix secretion (e.g. collagen). Besides, endothelial cells are important for vascularization of the tissues, including bone tissue.

All cell lines were seeded at a cell density of 1.5 $\times 10^4$ cells per cm^2. Cells were cultured over the hydrogels during 96 h at 37 °C above the VPTT of VCL. Cell monolayer formation was monitored during the days with an optical microscope as VCL-based hydrogels are transparent above the VPTT. After 96 h the cell detachment from the hydrogels was assessed, VCL-based hydrogels were gradually cooled down to 20 °C using cold culture medium as described in the previous Section. Figure 6.6 depicts the culture state (24 and 96 h) over the hydrogels for the three cell lines evaluated. Endothelial and preosteoblastic cell lines were able to form a dense monolayer after 96 h of growth, on the other hand, the macrophages were able to proliferate and spread all over the hydrogel's surface. Macrophages are the main effector of the innate immune response, these cells that do not form a monolayer but from 24 h of culture these cell type present a well

adhere morphology. Moreover, micrographs of the cell transplants after 24 h of growth on TCP are also presented in Figure 6.6, an outstanding performance was obtained by C166-GFP (endothelial cells). Denser areas in the centre of the well constitute the main focus of the transplant where cells have started to proliferate and expand.

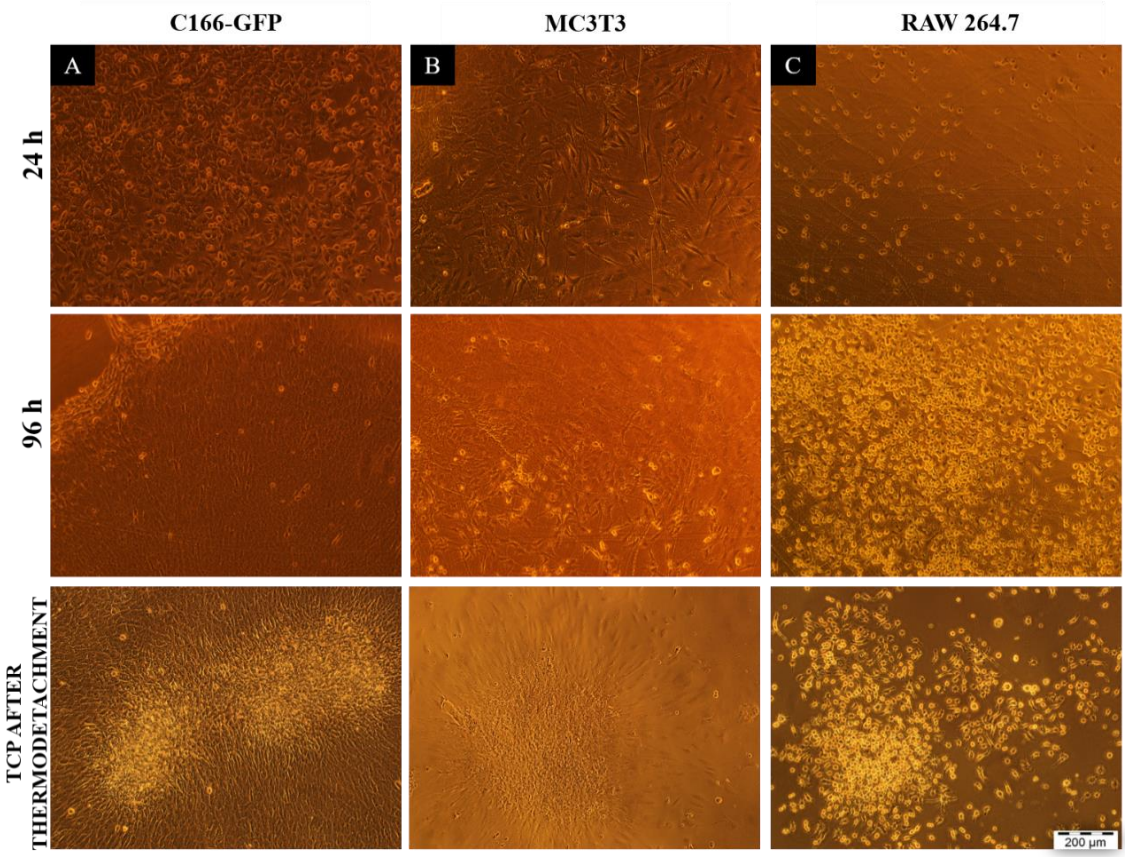

Figure 6.6. Endothelial (A), preosteoblastic (B) and macrophagic (C) cell types growing over the VCL-based hydrogel during 24 h (first row) and 96 h (second row). Micrographs of the culture state on TCP after 24 h of the thermodetachment process (third row).

Preosteoblastic cells with a higher doubling time (38 h) than endothelial cells (18 h) presented a smaller area of transplant but still there was a well formed monolayer. Lastly, macrophages (RAW 264.7) were also transplanted from the VCL platforms. As already developed during this work, RAW 264.7 macrophages are a good preosteoclastic cell model. Therefore, this cell line was also evaluated preliminary in presence of RANKL and rounded multinucleated cells were formed over the hydrogels detected by Hoechst staining (Figure 6.7).

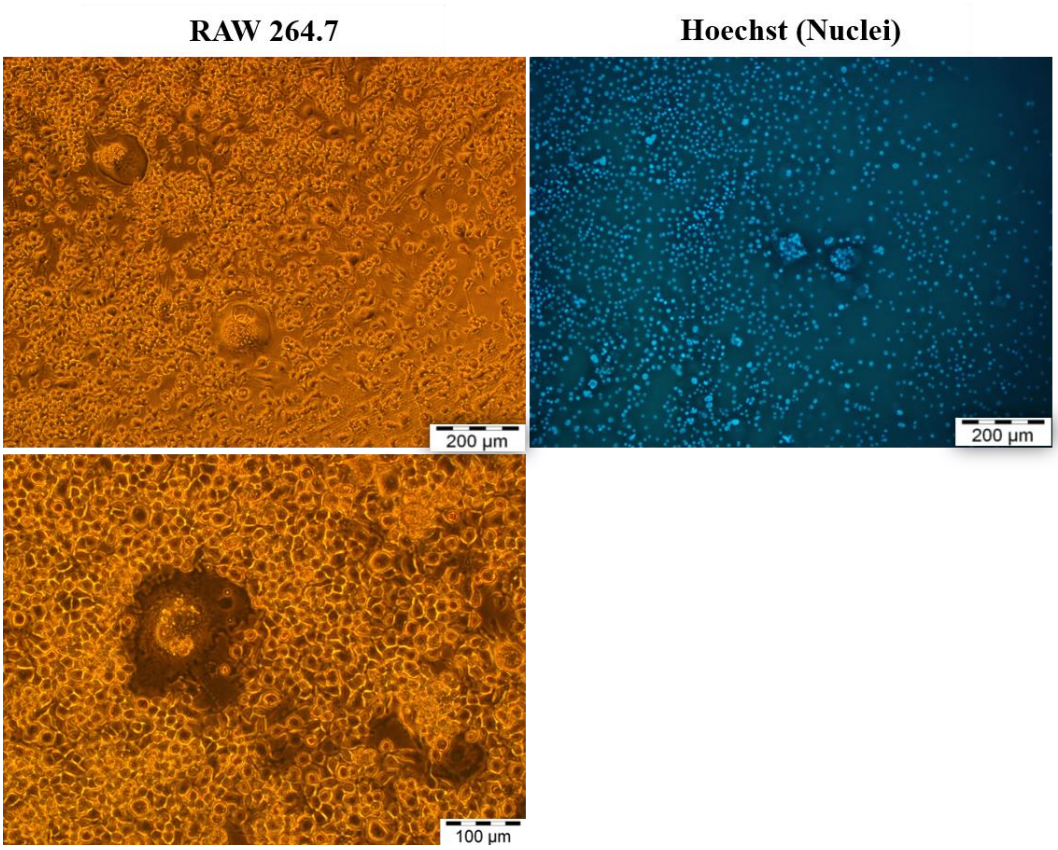

Figure 6.7. Preosteoclastic cells (RAW 264.7) growing over the hydrogel with RANKL factor on medium. Bright light images on the left column and Hoechst (nuclei) staining on the right.

4.2. Wrinkle VP-based hydrogels on PC supports as potential cell transplant platforms

VP-based surfaces with different ionic charges allow cell transplant upon mechanical agitation as it has have been described previously [161]. These kind of surfaces can also be modified in order to control topography (form wrinkles) (in addition to the ionic surface charge) and, in consequence, improve the performance of the materials. Also, these surfaces can be supported on other materials (PC) [163]. These features can affect cell adhesion and proliferation of different cell lines and cell detachment can be modulated by these surface modifications. For this purpose, this strategy was investigated herein with endothelial cell line (C166-GFP) to evaluate the influence of wrinkling of VP-based hydrogels functionalized with different ionic charges (negative positive and pseudo-zwitterionic) on the cell growth and cell detachment.

4.2.1. VP-based hydrogels on PC supports characterization

A polycarbonate film (PC) was used as substrate and a polypropylene (PP) cover was located on top separated by a precise distance using a PDMS spacer, the monomer (VP), crosslinking agent,

photoinitiator and Millipore water were introduced in this space as described in [163]. The elapsed time between the initial contact feed mixture and PC prior to the UV-irradiation step was varied between 0 and 20 min. After this time samples were irradiated using UV-vis light (365 nm) for 40 min to accomplish a complete photopolymerization. Table 6.2 summarizes the obtained surfaces with the anionic monomer (M-SO_3^-) with four different delay times (0 to 20 min) and variable water/VP ratio corresponding with N samples. P samples correspond with the positive charged monomer (M-N^+) and PZ samples with the pseudozwitterionic surface modification (M-SO_3^-/ M-N^+).

Table 6.2. Experimental conditions for the fabrication of the ionic microwrinkled surfaces. N: negatively charged, P: positively charged and PZ: pseudozwitterionic. For each of the four series, four hydrogels were obtained with delay times (defined as the time elapsed between the incorporation of the photosensitive mixture and the start of the UV-irradiation) of 0, 5, 10 and 20 minutes (labels correlates with this order).

	Monomer/s	**Water/VP ratio (v/v)**
N-1 to N-4	M-SO_3^-	1.05
N-5 to N-8	M-SO_3^-	1.50
P-1 to P-4	M-N^+	1.50
PZ-1 to PZ-4	M-SO_3^-/ M-N^+	1.50

Figure 6.8 presents 2D optical images and 3D rendering profilometry images for the series prepared using the different monomers using the experimental conditions described in Table 6.2. Furthermore, Figure 6.9 discloses the wrinkle characteristics of the samples such as period and amplitude of the samples obtained from Figure 6.8. Delay time is directly related to the size of the wrinkled formed, even though significant differences can be observed depending on the monomers employed. When the same quantity of Millipore water was used and all the parameters were kept constant (temperature, irradiation time and monomer/crosslinker composition) the mixture formed using both two monomers formed larger wrinkles (period up to 80 µm and amplitude up to 17 µm). In contrast, the wrinkles obtained with positively charged (M-N^+) or the negatively charged (M-SO_3^-) monomers resulted in smaller wrinkles. On the one hand, with M-SO_3^- wrinkles with periods of up to 25 µm and amplitudes up to 8 µm in period were detected. On the other hand, when M-N^+ was used wrinkles below 60 µm and amplitudes below 15µm were formed. Moreover, in delay times below 5 min (samples N5-6, PZ1-2 and P1-2) nearly flat surfaces were obtained.

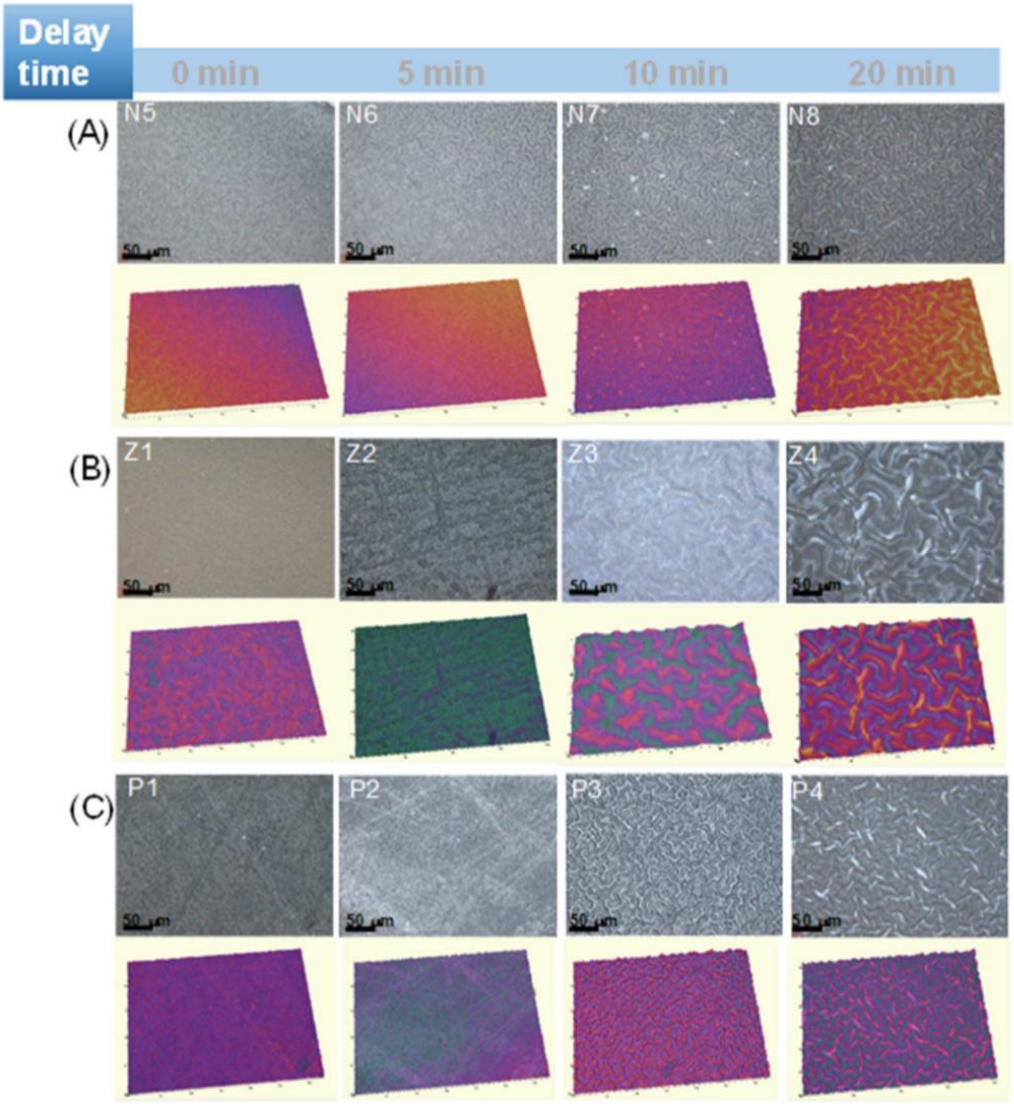

Figure 6.8. Profilometry images of wrinkled hydrogel/PC surfaces. In (A) the photosensitive mixture only contains M-SO_3^-. The delay time was varied between was varied between 0 and 20 thus leading the samples N5-N8. (B) was prepared also varying the delay time but using an equimolecular amount of M-SO_3^- and M-N^+ (samples PZ1-PZ4). Finally, (C) exclusively involves the use of M-N^+. (samples P1-P4).

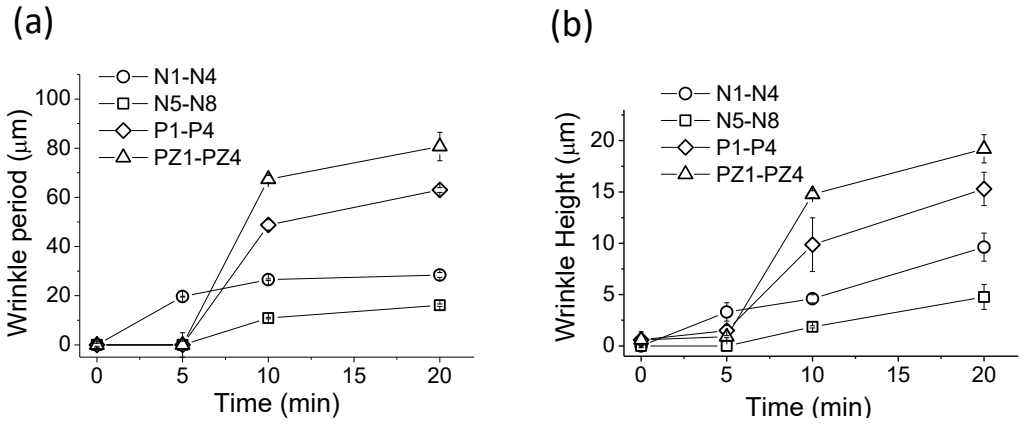

Figure 6.9. Evolution of the wrinkle dimensions as a function of the conditions and the type of monomers employed.

Optical profilometry gives information about morphology and wrinkle characteristics, in order to obtain data about chemical composition and distribution over the surface Confocal Raman was used (Figure 6.10). Particular signals associated to either PC or the hydrogel formed were obtained and the chemical distribution was determined of each component. Red colour stands for PC and blue colour areas point out the presence of VP-based hydrogel. The wrinkled surfaces positively (P-samples) or the negatively (N-samples) charged resulted in the formation of a thin (3-4 µm) layer of hydrogel (Figure 6.10. a and b) on top the PC surface. The hydrogel is arranged in a gradient structure as its amount decreases progressively with the depth. Oppositely, PC quantity gradually increased with the depth.

A different scenario was found for the pseudozwitterionic wrinkled surfaces prepared using a equimolecular amount of both monomers. Figure 6.10. c reveals a combination of both colours in the top layer therefore, indicating distinct chemical composition than the other surfaces. Micrometre size domains rich in hydrogel are embedded in areas rich in PC without any particular orientation. Therefore, with these results it can be depicted that PZ samples presented a mixture of both hydrogel and PC while P or N samples the surface top layer was predominantly composed of VP-based hydrogel.

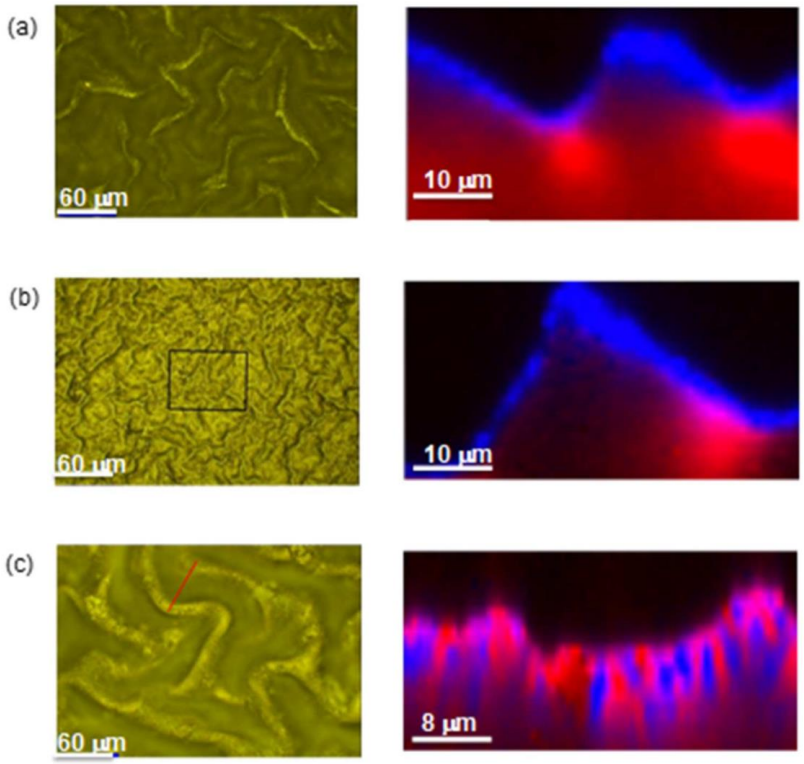

Figure 6.10. Optical image of the wrinkled surfaces (left) and Confocal Raman Z-cross sectional profiles (right) of the wrinkled surfaces prepared using the monomer M-SO_3^- (a), the monomer M-N^+ (b) and the mixture of M-SO_3^- and M-N^+ (c). Whereas the red colour is associated to the presence of PC, the blue colour areas indicate the presence of hydrogel.

4.2.2. Biological evaluation of wrinkled surfaces: biocompatibility

The different surface charge wrinkled surfaces (negative M-SO_3^-:N; positive M-N^+: P; equimolecular amount of M-SO_3 and M-N^{+-}PZ) were evaluated with endothelial cells line in terms of cell growth and transplant potential. Anionic VP-based hydrogels have been assessed as cell culture and transplant platforms with good biological behaviour [161]. Cell adhesion was described to be delayed over VP hydrogels compared to both TCP [161, 162] and VCL-based hydrogels as already exposed in the previous section.

Endothelial cells were seeded at a cell density of $1.5 \times 10^4/cm^2$ and left to grow over the surface for 72 h, after this time small clusters of autofluorescent cells on the surface of all samples were detected (Figure 6.11 A). No monolayer formation was observed and cells presented rounded morphology. Some of the cell clusters were placed into the wrinkles, particularly over N and P surfaces. No clear differences were qualitatively detected between samples in terms of cell growing.

Then, PC-hydrogel cultured samples were evaluated for their potential for cell detachment. VP-based hydrogels [161] were capable of cell sheet transplantation without using any chemical agents (trypsine, EDTA…etc). As already disclosed, cell to cell and cell to extracellular matrix junctions can be conserved and different cell types can be simply transplanted onto another surfaces such as implants to favour a quicker recovery or enhanced biological response avoiding immune system reactions.

Similarly to VCL hydrogels protocol, these surfaces were inverted and placed into a new TCP well permitting cell contact with the polystyrene surface but without temperature stimuli. Endothelial cell transplants were induced from all wrinkled samples (Figure 6.11 B). After 72 h (starting when the platforms were turned around) of growth over the TCP, cell cultures from the anionic surfaces (N) presented higher confluence levels than positive charged surfaces (P) or the pseudozwitterionic surfaces (PZ). The latter two exhibited a reduced cell expansion after transplant. Moreover, a quantitative measure of cell viability was obtained for all the transplants measuring their mitochondrial metabolic activity. Metabolic activity levels (Figure 6.11 C) were in agreement with the previous observations, higher values were measured for N surfaces and low for P and PZ.

In consequence, N samples with the anionic M with different wrinkle amplitude were selected to further analyse the influence of the topographic features in the cell response and transplant potential.

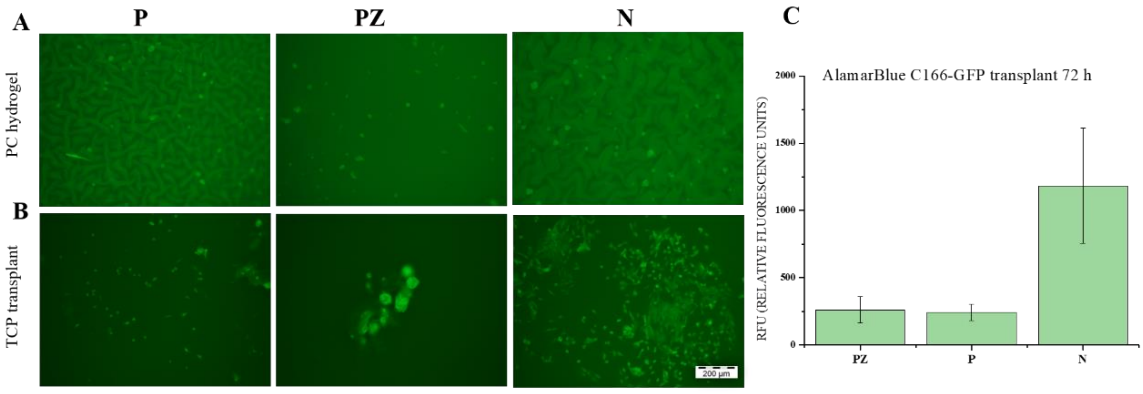

Figure 6.11. A. Fluorescence images of the PC-hydrogel substrates (positive M-N^+: P; equimolecular amount of M-SO_3 and M-N^+: PZ; negative M-SO_3^-:N) upon 3 days of endothelial C166-GFP cell culture growth. B. Fluorescence images of the cell transplants on TCP at 72h after transplantation process. C. Metabolic activity analysis of transplanted cultures.

4.2.3. Biological evaluation of negative-charged surfaces with different wrinkle periods

In order to analyse the cell response to different wrinkle periods different negative-charged supports were selected (N-large:50-70 µm; N-intermediate: 30-50 µm; N-small: 7-17 µm). Other two bone-related cell types with different sizes have been used for this evaluation: i) MC3T3 preosteoblasts, that can spread to more than 70 µm of diameter over a substrate; ii) RAW 264.7 macrophages, which are less adherent small cells with a diameter near 7-10 µm. Between the two sizes endothelial C166 GFP cells can reach up to 40-50 µm of diameter, approximately.

Firstly, cell adhesion and growth over wrinkled surfaces were explored (Figure 6.12). N-large samples with the wider wrinkle amplitude permitted the adhesion of preosteoblastic, endothelial and macrophagic cell lines all over the hydrogel top layer, including the depth areas of the wrinkles (Figure 6.12 and Figure 6.13). Figure 6.13 was included for sake of clarity as at this magnification preosteoblastic cells can be more easily distinguished. This cell line developed an extended morphology, whereas macrophages proliferated in clusters all along the surface, finding some colonies even in the depth areas. Over surfaces with intermediate wrinkle periods of ~ 48 µm (N-intermediate), the preosteoblastic and macrophagic cultures proliferated comparably. As for the endothelial culture no clear differences between topographical modifications were found, these cells proliferated in cell clusters over all the evaluated wrinkled surfaces.

At the same time, the smaller wrinkle periods (7 µm) exhibited a good performance for all the tested cell lines. Bright field micrographs at three different magnifications have been also added (Figure 6.14) to illustrate the interaction of the wrinkled topography with the non self-fluorescent cell cultures. Cells can be seen easily in N-intermediate and N-small samples including cell clusters disposed in the depth areas.

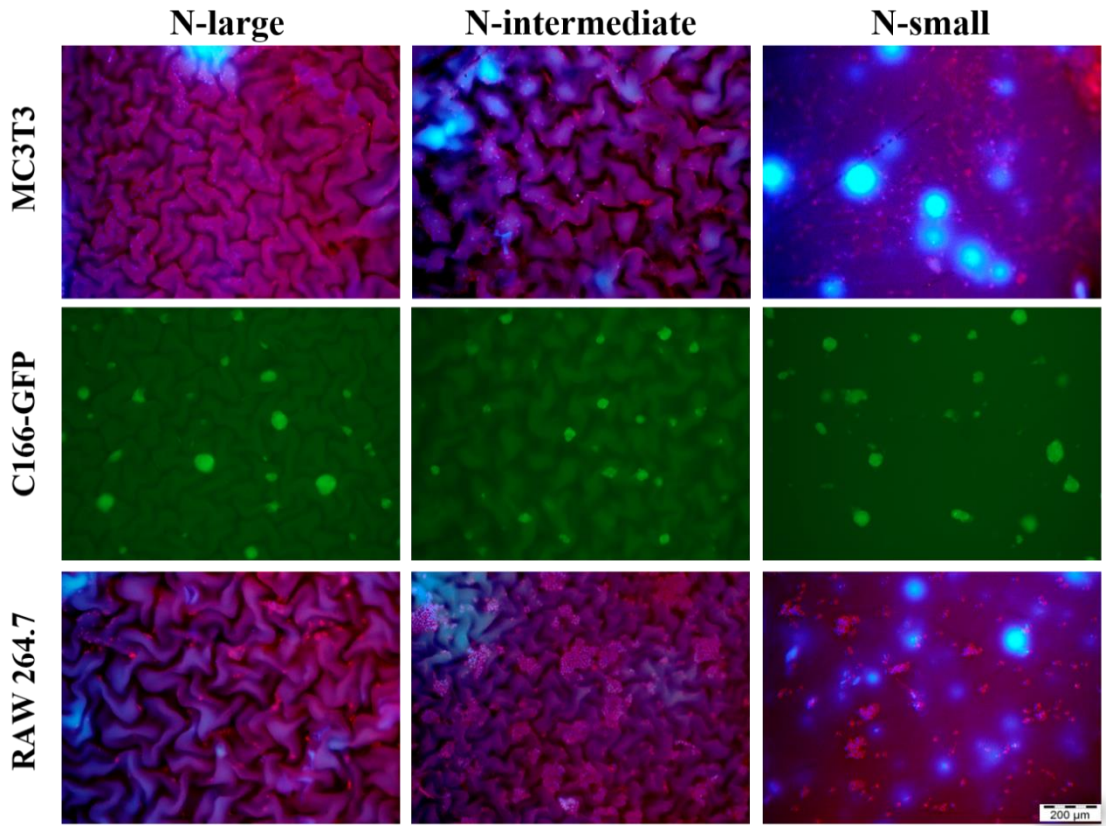

Figure 6.12. Cell adhesion and proliferation over negative-charged wrinkled surfaces (N-large:50-70 µm; N-intermediate: 30-50 µm; N-small: 7-17 µm) 96 h after seeding. First and third line: actin (red) /Hoechst (blue) staining (merge). Second line: GFP autofluorescence.

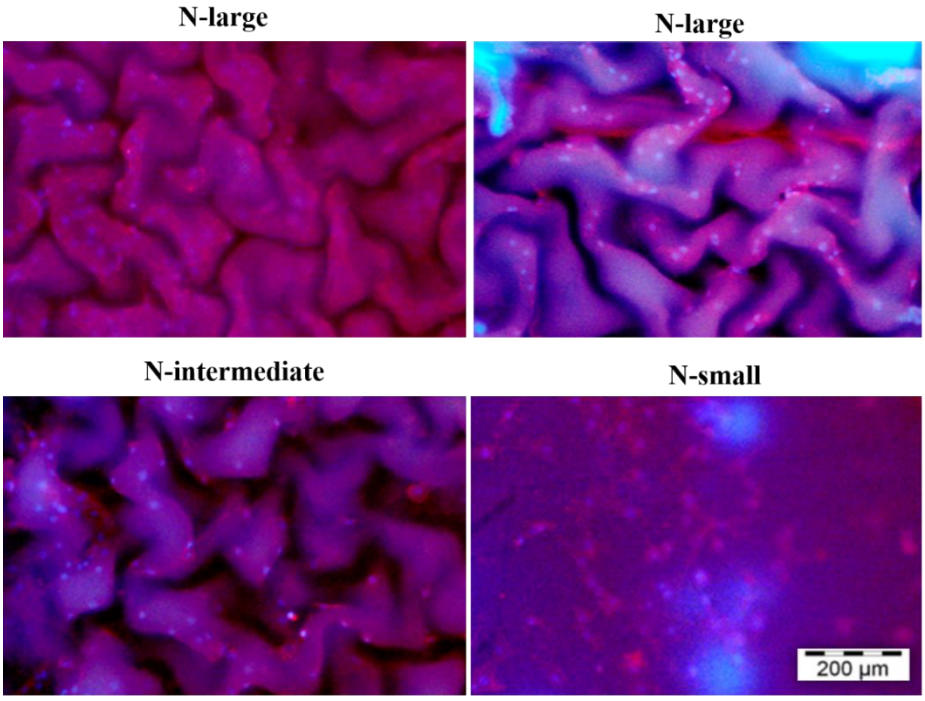

Figure 6.13. Cytoskeleton (actin; red) and cell nuclei (Hoechst; blue) of MC3T3 osteoblastic culture over wrinkled PC-hydrogel surfaces.

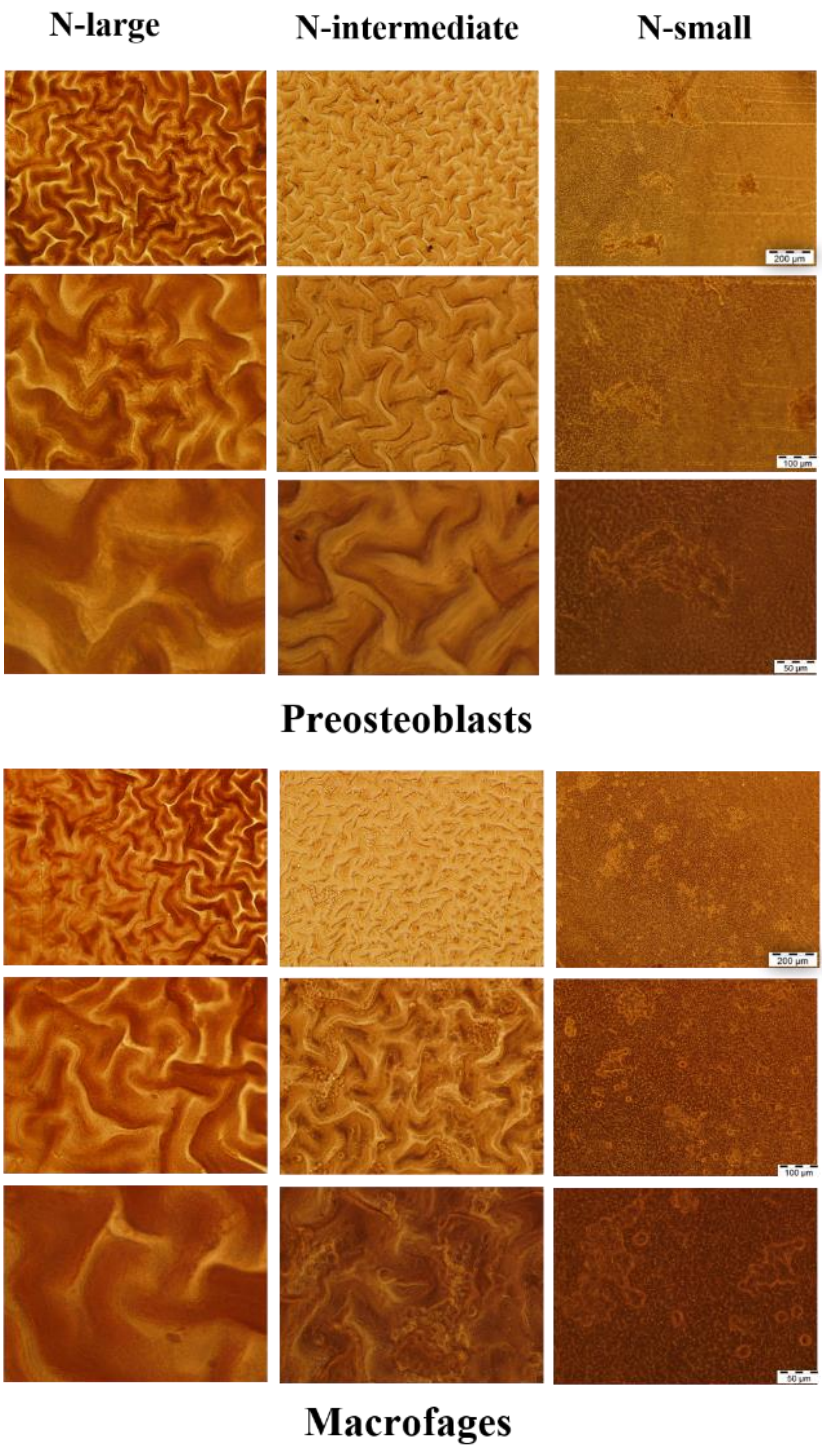

Figure 6.14. Bright field images for MC3T3 and RAW 264.7 cultures at 96 h over wrinkled surfaces.

Subsequently, N-large, N-intermediate and N-small samples were evaluated in terms of transplant potential following the previous protocol. Figure 6.14 contains the micrographs of the three cell lines after 72 h of transplantation. For all three surfaces cells were found adhere to the TCP surface, however interesting differences have been distinguished amongst them. For instance, the osteoblastic cells observed over the hydrogels (Figure 6.12) were not fully transplanted onto TCP with high degree of heterogeneity and the lowest metabolic activity values (Figure 6.15). Despite

this result the endothelial clusters detected over the hydrogels were effectively transplanted, and cells were able to attach and spread over the new substrate with a characteristic radial distribution (Figure 6.14). This phenomenon was observed mainly in N-intermediate and N-small surfaces with also the higher metabolic activity levels for this cell lineage. As for the macrophages transplants, the higher proliferation levels were found for this cell line as it has the lower doubling time (11 h) of all the evaluated cell lines. Moreover, its low adherence characteristic can favour the detachment from the surfaces. Nevertheless, the N-intermediate and N-small samples favoured higher transplant success with greater metabolic activity values.

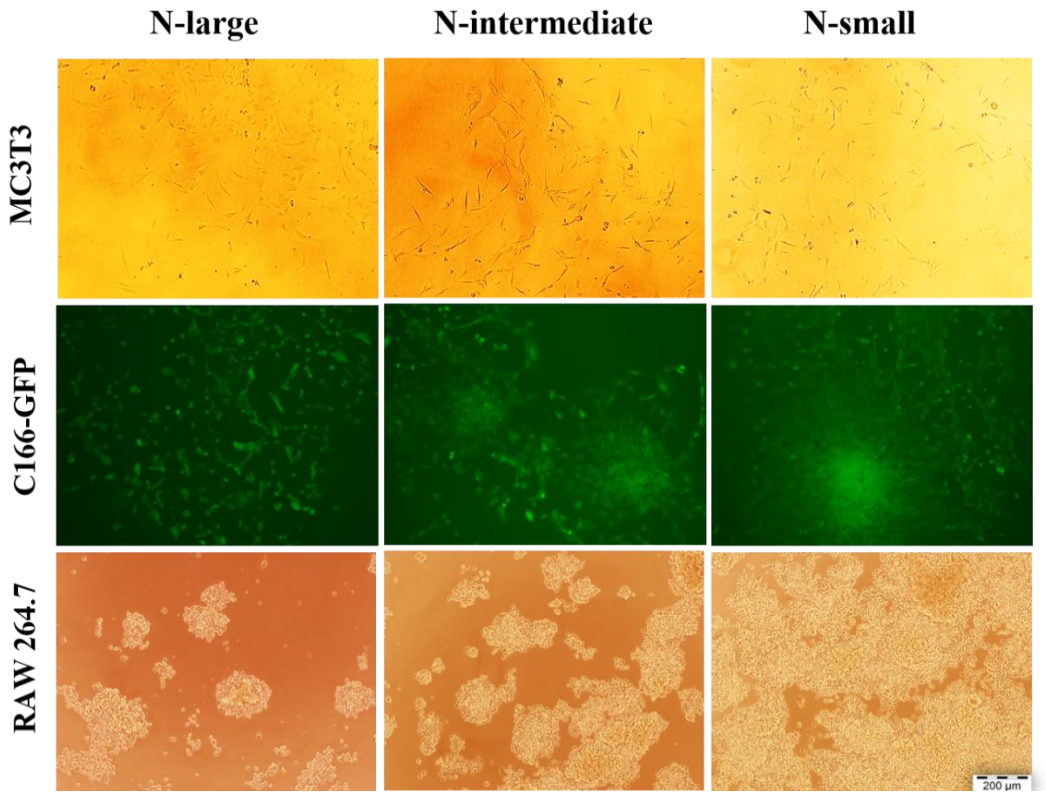

Figure 6.15. Cell transplants from PC-hydrogel supports (72h since transplantation process).

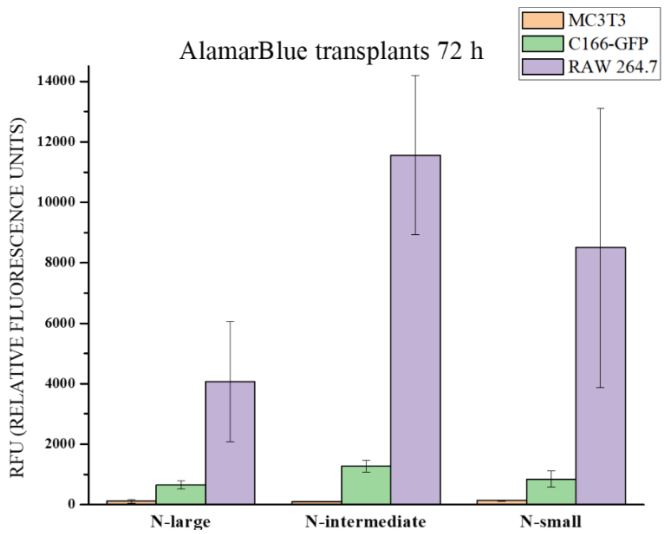

Figure 6.16. Metabolic activity (Alamar Blue) of cell transplants (72h since transplantation process).

4.3. Discussion

Cell sheet engineering could become a valuable solution for the incorporation of cells into biomaterials and promoting quicker tissue regeneration. VCL-based hydrogels are of great interest in this field for their possibility to be used as thermosensitive guided transplant supports. Compared with PNIPAM thermosensitive supports that need to be grafted into other materials, our VCL platforms are prepared as hydrogel free and can be easily handled to be transplanted into other materials.

An ionic functionalization of the evaluated hydrogels was investigated with endothelial cells; charged groups were added modifying the surface chemistry of the hydrogels. Previous studies developed with sample 1 (VP-based) revealed that the incorporation of anionic groups improved cell adhesion [161]. Herein, the anionic VCL-based sample 2b presented better cell adhesion and proliferation than the anionic VP-based hydrogel (sample 1) (Figure 6.2). This result is in agreement with the widely described low adhesive nature of pVP and the superior hydrophobicity and cytoadhesive properties of the VCL-based materials above the VPTT [307], coinciding with the culture temperature.

Moreover, non-charged VCL presented an outstanding performance in comparison to VP hydrogel at such short times. The inclusion of positive, negative, zwitterionic or pseudo-zwitterionic charges was explored with the aim of improvement in adhesion, monolayer formation and transplant potential. Regarding positive charges, literature examples [308, 309] indicate that this kind of surface charge favours negatively-charged blood serum protein adsorption and in consequence cell adhesion. Nevertheless, quaternary amines have also been described to decrease proliferation [310] and as such, can be used as an antibacterial strategy, as discussed in Chapter 3. On the other hand, zwitterionic and pseudozwitterionic constituents have shown an anti-adhesive behaviour [311]. This property could be beneficial when the detachment takes place in the ‘hydrophilic’ state below the VPTT favouring a proper monolayer delivery.

In general, we have seen that charge inclusion in VCL hydrogels affected cell adhesion, proliferation and detachment. Differences in detachment can be related with a recent study of Liu on thermosensitive supports with either positive and negative charges using L929 fibroblastic cell line [310]. It was proposed that positive charge surface attraction force to negative charged cells possibly will predominate over cytoskeletal tensile force, affecting in a negative way cell detachment, whereas minor amounts of negative charge could favour hydration and consequently improve cell detachment. In our results, samples 7 and 5b with positive charges presented low levels of metabolic activity (Figure 6.5) after the transplant and cell remains and residual debris

were still attached mainly to the samples 7. This phenomenon can be associated to cell contact with the positive groups (Figure 6.4, images 7a-D and 7b-D).

As a matter of fact, negatively charge surfaces with 6:1 VCL/M ratio, such as 2b, 5a and globally neutral systems (with the negative charges exposed) 6b seemed to be more beneficial for endothelial cells. However, in terms of detachment there appears to be differences related to the swelling capacity of the hydrogels. 6b sample with a good monolayer formation over the hydrogel, the higher metabolic activity levels of all the transplants and a maintenance of the integrity of the monolayer stands among all the evaluated hydrogels. This hydrogel was the methacrylate-modified sample that was closer to the uncharged condition (sample 8) at 37ºC in terms of swelling behaviour. Sample 8 is the hydrogel which reveals a dramatic volume expansion upon decrease of the temperature, whereas anionic samples 2b and 5a exhibited a slight volume change (Figure 6.6). This expansion, linked to a vast water uptake, may be responsible for the greater detachment performance of samples 8 and 6b.

The present findings suggest that in future studies, other groups related to bone mineralization and ones with better transplant outcome, such as M-N^+-SO_3^- sample 6b, should be evaluated with osteoblasts or other cell models (e.g. mesenchymal stem cells).

Non charged hydrogels were selected to carry out a preliminary evaluation of bone related cell lines. They showed a good behaviour of all of them with differences in monolayer expansion that could be explained by their different doubling times and differences in adhesion. Moreover, when RANKL was added multinucleated cells were observed over the hydrogels; though further studies should be complemented in order to discern the potential osteoclastic behaviour of these cells over the ionic charged materials or the integrity of these cells after a transplant. Differentiation factors incorporation into the medium where cells are being cultured over the hydrogels could stand as an interesting strategy to pre-stimulate them. For instance, pre-stimulated mesenchymal stem cells or preosteoblastic cells could be transplanted into an implant favouring osteoinduction mechanisms.

The majority of the synthetic hydrogels lack of osteoconductivity (bone-bonding ability) or osteoinductive (osteogenesis induction). Hence, in order to obtain a more mature state of differentiation prior to cell transplantation hydrogels should be complemented by their mineralization. The positive characteristics of the hydrogels can be improved with excellent osteoconductive and mechanical properties of calcium phosphates/apatites. Several approaches have been investigated since incorporation of incorporation of inorganic materials into the hydrogel matrix by direct blending and grinding coprecipitation or polymer-controlled mineralization. Related to the latest, the hydrogel mineralization induction can be achieved by the

functionalization of their side chains or backbone polymers with negatively charged moieties such as carboxyl ($COOH^-$), hydroxyl (OH^-), or phosphate (PO_4^{3-}) groups. Negatively charged groups strongly induced apatite formation but the positively charged group did not, the apatite formation initiated via calcium ion-adsorption upon complexation with a negative surface-charged group may be dominant in biomaterial calcification where ionic species directly contact the biomaterial surface in body fluids [312]. The anionic domains attract Ca^{2+} that leads to an ionic saturation that causes the CaP precipitation. Silanol (SiOH) along with the other groups increases the ability of apatite formation as they provide a nucleation site on the substrate. In the apatite nuclei on the substrate calcium and phosphate ions can be deposit from the surrounding fluid [313, 314].

Wrinkle VP-based platforms

As attempted in the previous Section with VCL-based hydrogels similar surface charges were introduced over PC supported VP-based hydrogels (N: M-SO_3^-, P: M-N^+, PZ: mixture of M-SO_3^- and M-N^+). Moreover, this strategy was similarly explored in support-free VP-based hydrogels with good result in cell proliferation and transplantation rate for all conditions tested (N, P and PZ) [161]. However, in the results presented here, P and PZ samples did not reach optimal values, suggesting that other factors added to this system can likewise modify the biological behaviour, such as, for instance, hydrogel immobilization and distribution in the PC support or wrinkling formation. As with VCL hydrogels, the negative charged surfaces (N samples) were selected as the platforms with best endothelial cell behaviour.

The negative charged supports with homogenous distribution of VP on the surface were chosen to be evaluated with three different cell lines. The possible influence of distribution in the PC support can be considered negligible in this case; as seen in Figure 6.10 these VP-based PC supports present a top layer with mainly hydrogel presence in contrast to PZ samples with a mixture of VP and PC. Nevertheless, topographic modifications as a result of the wrinkle formation can modulate the biological response and the possible transplant. Differences in cell behaviour between cell lines were found and could be related to cell size or specific adhesion mechanisms. In other studies with wrinkled hydrogels tested as cell culture platforms similar morphologies were found, in a recent study [315] it was exposed that human mesenchymal stem cells stayed rounded with low spreading into hexagonal patterns of PHEMA hydrogels. Furthermore, Zhao *et al.* [316] produced multicellular spheroids into microcaves of wrinkled PHEMA hydrogel films. Taking into account these results, the endothelial and macrophagic clusters detected in the depth areas of our PC-VP supports can be explained by the topographic changes and the negatively charged hydrogel molecular interaction with cell culture, as seen in previous studies with unsupported hydrogels [162]. In general, N-intermediate and N-small platforms seemed to be favouring a better transplant outcome for both endothelial and

macrophagic cell types that present a smaller cell size than preosteoblasts. However, MC3T3 cells did not presented differences in transplant efficiency between the different wrinkled surfaces.

VCL-based hydrogels with topographic modifications could also been explored in the future and the incorporation of topography into the hydrogel could provide added functionalities or the formation of more complex structures. Nevertheless, very little is known about the influence of topographic changes of the hydrogel in the transplantation processes. For instance, a thermosensitive hydrogel micropatterned with different pattern sizes (25 and 80 μm) was evaluated in terms of formation of cell sheet with a striated structure including extracellular matrix (ECM) and myoblasts [317]. Nevertheless, in this latter case [317] the pattern size did not seemed to have influence on alignment of cells on the cell sheet.

Taking into account the results presented in this thesis, both VCL and VP platforms could be used and functionalized for bone tissue regeneration purposes. However, more studies concerning other bone cell types (mesenchymal stem cells, hematopoietic stem cells, osteoblasts, osteoclasts and macrophages) should be implemented in the future. This should include evaluation of differentiation markers (collagen synthesis, mineralization, ALP for osteoblasts and TRAP or actin rings detection for osteoclasts) after the transplants performed over control TCP and other target materials (Ti, Zr, Mg, etc.), followed by evaluation of cells from patients with respect to their growth or viability ratios.

5. Outlook for formation of hybrid functionalized biomaterials for tissue engineering: General Discussion

Nowadays, life expectancy is continuously increasing (Figure 7.1) with the corresponding medical issues associated (organ failure and traumatic injuries diminishing the quality of life). Population aging implies that our tissues and organs are forced to serve for a longer time than they were able to stand without any medical intervention. People want to live longer but also to live with higher quality of life. Healthcare systems change fast and a change of healthcare model from replacement to regeneration is being seen with the upraise of tissue engineering and regenerative medicine. Different effects, such as loss of elasticity in the skin, failures in cell division leading to tumour formation, loss of bone mass, metabolic syndrome, thickening and loss of elasticity in arterial walls leading to arteriosclerosis or heart failure and development of illnesses related to immune system malfunction, increase with aging. Bones and joints suffer from ageing wear and tear; many illnesses (osteoporosis, osteoarthritis, multiple myeloma, Paget's disease, among others), are still a challenge. One of the biggest challenges is osteoporosis with millions of people affected and diminishing their quality of life.

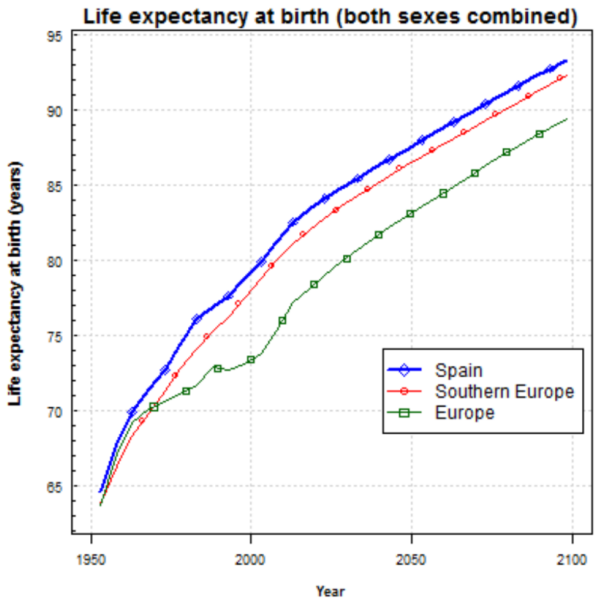

Figure 7.1. Adapted from United Nations, Department of Economic and Social Affairs, Population Division (2017). World Population Prospects: The 2017 Revision.

It has been estimated that each year all over the world severe bone lesions cause hundreds of millions of medical procedures. Moreover, bone defects can be different depending on their anatomical location, magnitude, form and also, the quality of the adjacent tissues. This latter fact relays on the origin of the bone damage (accident, diseases such as osteoporosis, tumorigenic conditions) and likewise other physiological parameters of the patients can be key for the final

choice of materials. Besides the selection of the biomaterial, their functionalization also must be designed according to specific needs of different age groups and medical conditions. Other pathologies, such arthrosclerosis in some scenarios require the inclusion of a stent after a coronary, intracranial or other blood vessels angioplasty; drug-eluting capacity is a desirable functionality for stents, as it helps to avoid possible restenosis. The selection and design of this kind of materials must also take into account the patients' medical condition, age, etc. The relevance of the functionalization for tissue engineering relays on the very different diseases and conditions observed in young to elderly population. Potential of regeneration diminishes gradually as life goes on, children are more capable to induce a quick regeneration and for instance, after menopause women can present osteopenia and imbalanced bone homeostasis.

Biomaterials have been used in medical applications for a very long time with visible progress since 1940s and with a greatly increased use in therapeutic medical technologies and implant devices in the past years. The survival half-life of prostheses based on bio-inert materials is about 15 years depending on the clinical applications. Therefore, permanent implants are now required to last longer and to provide new functionalities. The choice of the right material depends mainly on the application and new biodegradable, biomimetic and smart materials are being investigated, such as new composite systems for instance, the combination of hydrogels with solid phases such as degradable polymeric structures or bioceramics [30]. Such purport to achieve a synergistic biological activity added to the mechanical reinforcement.

For this purpose, in this Thesis different routes to creation of novel hybrid biomaterials have been explored in order to obtain a hierarchic material with multiple functionalities. The three key steps of functionalization proposed in the present work consist, firstly, in the choice of adequate permanent or temporary material based on the application (Figure 7.2). Load-bearing applications for implant dentistry or orthopaedics require a permanent implant selection (Ti CP, Ti alloys or Zr). Other applications where a second surgery should be avoided require temporary biodegradable materials (Mg). Furthermore, at this stage an *in situ* modification of the core material is proposed to be implemented by means of electrochemical treatments based on anodizing. It is demonstrated that anodizing of the implants can lead to the formation of smart ceramic coatings where bioactive inorganic species (Ca, P, Si, Zn, Mg and F) and stable phases (HA, FA, etc.) are incorporated; these elements can be slowly released post-implantation to favour biological responses. More specifically, PEO can modulate coating thickness, porosity, roughness and other topographic features.

In the second step of functionalization, a top layer polymeric material for both types of core material, either permanent or temporary, can be included. This stage also offers an option of the incorporation of drugs or growth factors directly into the PEO coatings. The possibility of direct

protein loading onto these porous ceramic coatings and the unloading mechanisms have been evaluated during this Thesis. It has been demonstrated that options of a quick or a prolonged release from the coating are possible and can be selected depending on the requirement of the final application. For instance, for an initial burst of antibiotics into the implanted area a quicker model, such as offered by PEO-600s system, can be of interest whereas a growth factor delivery should be more prolonged in time, for which purpose the PEO-90s system is more adequate. However, further studies with other proteins or antibiotics should be implemented in the future including the non-analysed PEO materials with bioactive components, nevertheless, a similar behaviour should be expected from this kind of materials.

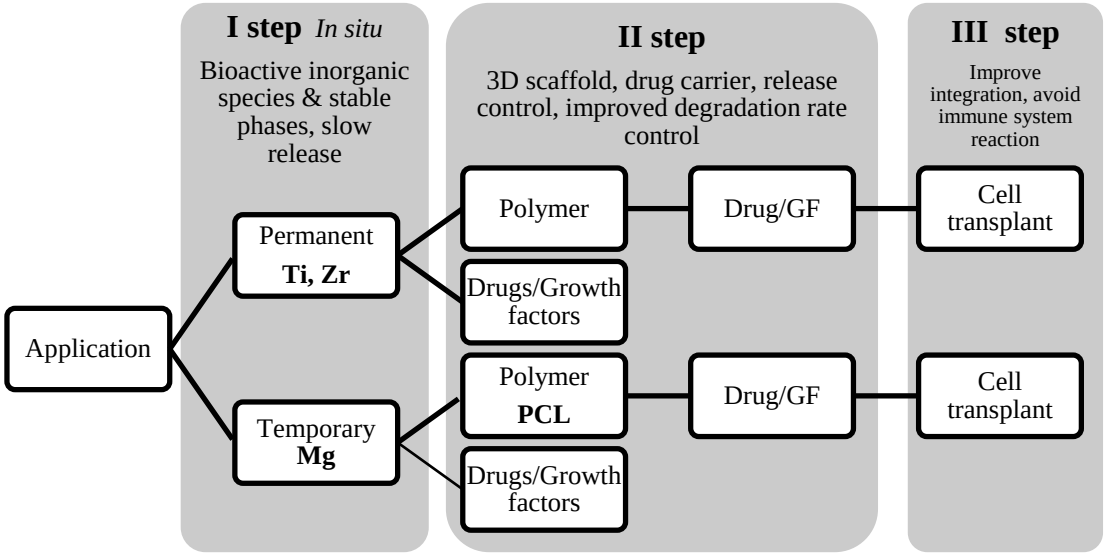

Figure 7.2. Proposed strategy to obtain a hierarchic biomaterial.

On the other hand, materials such as anodized Zr implants, a with a featureless, homogeneous surface morphology of the anodic film, would need a polymeric coating for the inclusion of active pharmaceutical agents; the choice of this polymeric material can be based on the release rate, degradation rate or the hydrophobic or hydrophilic nature of the active agent of interest. In a similar way, biodegradable Mg alloys after PEO process can be coated with a polymeric layer such as the PCL-based layer evaluated in the Thesis. In this particular scenario, besides the inclusion of drugs, a great advantage is obtained through a polymer layer, as corrosion rate of the Mg alloy is reduced and a sealing of the possible formed cracks on the PEO coatings can be achieved. In our results, it has been revealed that besides the expected protective characteristics of the polymeric coating, a 3D structure on PCL can be also be formed favouring cell behaviour. This structure can be achieved by BF approach, a technique that has likewise been used to selectively functionalized the formed pores with antibacterial motifs in a PS-based substrate. This kind of covalent functionalization can eliminate the necessity of the loading of the surface with antibiotics and thus reduce the number of steps involved in the functionalization process.

In the third envisaged step, a cellular component could be included into the hierarchical biomaterial aiming to enhance the integration of the implant and reduce the immune system reaction. This reaction could be reduced as compatible cells or patient's own cells can be incorporated into the implant. In addition, the transplanted cells could be previously differentiated or co-cultured with different cell types.

The following discussion analyses further the impact of the output of this Thesis in regards to the features concerning all three steps of multifunctionalization on the future outlook of the hybrid biomaterials development.

Step I: Functionalization by electrochemical treatments

Table 7.1. summarizes all the studied base materials belonging to step I. From a general vision it can be said that all the bioactive species present in the electrolyte can be successfully incorporated into the ceramic coating in all the evaluated materials. It is evident that modifying the experimental conditions different Ca/P ratios, stable phases, roughness and coating thickness can be modulated. All anodized surfaces presented an outstanding performance in cell behaviour and could be selected as a desirable surface modification.

The main issue addressed in Chapter 1 is the improvement of the osseointegration capacity and therefore avoiding of the post-implantation failure and reduction of the healing period. Orthopaedic and dental implant fixation depends on both bone-implant contact and bone formation around implant. The findings of the Thesis demonstrated that by means of osteoconduction mechanisms mediated by a variety of bioactive components incorporated in situ into the ceramic layer-modified surface, bone-to-implant contact can be improved and accelerated as cells implicated in the readjustment of the area are easily induced to adhere and start secreting bone matrix on the surface of the material and other biological factors to stimulate migration and proliferation. Another topic that has been addressed is the osteoinduction mechanism that can be triggered by the implant. The Thesis provided evidence that undifferentiated and pluripotent cells are stimulated to differentiate into the bone-forming cell lineage and induce osteogenesis by in situ modified surface composition.

This latter feature should be further implemented in the following steps by including growth factors or other active components, or rather implemented on cell culture over hydrogels for the monolayer formation.

Table 7.1. Anodized metallic materials from Chapter 1 and 2.

	Section 1.1.1	Section 1.1.2	Section 1.2.1	Section 1.2.2	Chapter 2
Material/alloy	Ti grade I Ti grade IV	Ti CP I	Zr	Ti6Al4V	Mg0.8Ca
Anodizing conditions	+490/-60 V AC 400 mA/cm^2 90s /600 s	+490/-30 V AC 300 mA/cm^2 300 s	30-60 V DC 60 min	+490/-30 V AC 300 mA/cm^2 90-600 s	+430/-50 V AC 138 mA cm$^{/2}$ 300 s
Ca/P ratio in the coating	2-4	1.1-2.9	-	1.2-1.8	0.45-1.55
Elements/Species	Ca;P	Ca;P;Si;Mg;Zn;F	P	Ca;P;Si; F	Ca;P;Si; F
Coating thickness, µm	5-15	16-28	-	6-38	6.4-48
Electrolyte	Suspension	Solution	Solution	Solution	Suspension
Formed phases	Anatase Rutile	Anatase; Rutile HA; apatite; MgO; SiO_2;CaF_2; $CaTiO_3$	ZrO_2	Anatase; Rutile HA;FA	MgO; $CaMg_2$; $Ca(OH)_2$ HA; apatite; MgF_2, Mg fluorophosphate:CaF_2; forsterite;
Roughness (R_a), µm	0.6-1.3	1.1-2.3	0.4-0.7	1.1-6.3	0.7-4-3
Water contact angle, °	40-45	9-48	-	-	-
Studied cell types	Osteoblasts, macrophages and osteoclasts	Osteoblasts and osteoclasts	Premyoblast, endothelial, osteoblast, macrophages and osteoclasts	Osteoblasts	Endothelial, premyoblasts, osteoblasts, osteoclasts and co-cultures

Step II: Functionalization by polymer and/or active agent

Step II constitutes an interesting approach to adding new functionalities to the implant material. Among them is the ability to incorporate antibacterial properties into the biomaterial. Microorganism colonization is still a key failure point for all of the biomaterials and, therefore, limits their use for a particular biomedical application. Elimination of the infection after a biofilm has been formed on a biomaterial remains still a challenge and in most of the cases the implanted device has to be removed and replaced.

With respect to the development of biomaterials with antibacterial strategies, three different approaches that could be utilised for permanent implants in dentistry and orthopaedics have been evaluated during this Thesis:

1. Incorporation of inorganic antibacterial elements into the coating composition (PEO with F or Zn) that that constituted part of Step I.

2. Protein loading mechanisms into the implant (Step II).

3. Copolymerization with antibacterial motifs (quaternized PDMAEMA or PAA) (Step II) thus avoiding the extra step of drug loading into the polymeric or ceramic layer.

Successful implementation of Breath Figures strategy I onto polymers such as polystyrene (PS) and degradable polymers such as PCL applied into an already formed ceramic coating with 3D structure (PEO) offers a double sided benefit for the future development of hybrid biodegradable materials. On one side, BF PCL is used as a protective coating, sealing the cracks and pores that otherwise could induce quick corrosion mechanisms of the Mg alloy. On the other side, following the functionalization strategy depicted in chapter 3, an added value is introduced into the coating making it a ‘smart coating’ with not only topographical changes (introducing porosity and roughness by the BF method) but also modulating the surface chemistry of underlying ceramic coating, which supplies the bioactive species to the cells that are anchored to it through the pores of the BF PCL.

The demonstrated strategy of *in situ* co-polymerization of antibacterial groups in polymers saves time and reduces the number of biomaterial fabrication steps. Additionally, this strategy is selective against bacteria over mammalian cells and there is no depletion of the antibacterial agent, hence there is no need to control its release as, for instance, in case of the surface imbued with drug. The strategy proposed with the incorporation of Nisin, although turned up to be unsuccessful, have revealed the importance of adding sufficient quantity of the peptide per unit of area and of the availability of the effective domain. As a follow up of this work, other strategies where the covalent union could be disrupted by pH changes or hydrolysis can be envisaged as feasible approaches to fixation and release of the agents that require an internalization by cells.

The possibility of loading and unloading of the 1st Step surface treatment (PEO) with a model protein has been confirmed in Chapter I, demonstrating that, in case of PEO coatings, surface chemistry rather than topography governs the binding and release rate of the protein. This is a positive indicator of the potential suitability of this kind of ceramic surface for incorporation of growth factors or other therapeutic agents. Among the former, BMPs stand as the bone regeneration main promoters, mainly BMP-2 has been widely proposed and there is a commercial product within already on the market (INFUSE® Bone Graft). Other strategies using Chitosan as a polymeric carrier for BMP-2 and either beta-tricalcium phosphate core material or calcium phosphate salts incorporation have been already evaluated [221, 318]. Nevertheless, other growth factors such as EGF (epithelial growth factor), TGF-β (transforming growth factor beta) and FGF (fibroblast growth factor) and PDGF, alone or in combinations, present positive effects on MSC survival or MSC-mediated bone formation. Other bioactive small-molecular-weight compounds such as icariin or simvastatin also favour stem cell–mediated bone formation [30]. VEGF also, has been used to favour the vascularization of tissues. In other specific situations, therapeutic agents such as chemotherapeutic drugs to disrupt tumour growth can also be desired. After a tumour resection (e.g. osteosarcoma), there is a huge need to promote tissue regeneration while remaining cancer cells needs to be killed. A combined therapy, including fast release antitumoral drugs and slow release for other growth factors, could be observed with this approach. Finally, the topic of drug-eluting stent applications has already been approached in Chapter 2 discussing the kinds of drugs that could be used and the different strategies of their inclusion.

Step III: Cell sheet engineering as a strategy to add cellular components

In the context of this Thesis cell sheet engineering has been explored as a potential way to improve the osseointegration of the implants. Cells (e.g. mesenchymal stem cells) from the patient, an autologous donation, could be induced to differentiate (treated with growth factors or other biological agents) over the hydrogel, also with cocultures of different cell types, and form a monolayer. As discussed previously, materials can be used as drug reservoirs; more specifically vynil-lactams hydrogels could be also loaded with growth factors or other active agents in order to trigger a specific response in the transplantable cells.

Regarding the first application proposed on this Thesis, cultured cells could be transplanted into the dental implant that will seal the screw, using a strategy similar to the one that has already been applied in wound healing and bone regeneration using PRP that derives from the centrifugation of the patient's own blood and contains growth factors that influence wound healing.

The possible outcome of the use of this strategy in future hybrid biomaterials would be a decreased immune system response and therefore, a reduced possibility of fibrotic encapsulation. Bone tissue could be formed around the implant favouring the osteoconduction mechanism. The

need for a trigger of osteoinduction mechanisms will not be so important as patient's own cells will be already differentiated over the implant.

This step can *be in vitro* tailored, adjusting cell populations or degree of differentiation, and according to the patient specific needs (osteoporotic or low implant integration success situations, as examples). After this process the cultured cells containing extracellular matrix could be transplanted into the implant. It has been demonstrated how the extracellular matrix contributes to accelerate tissue regeneration, as basic tissue architecture is already present and contain biological factors and other microenvironmental signals that enhance cell activity.

Depending on the area that would be needed to be coated with a cell monolayer or embedded with cells in the particular case of orthopaedic implants this approach could have limitations from a technological point of view. Despite this fact it still could be applied for some specific parts of the implant or for concrete patients (osteoporotic or low implant integration success such as BRONJ disease). These limitations can be solved adjusting cell culture platform design to the implant morphology, maybe through the help of 3D-printed VCL hydrogels. This strategy is now being developed by our group.

There are challenges that remain to be addressed in regards to the application of this approach onto the ceramic layer coated implant. On the hand, monolayer adhesion onto the PEO interface of the Ti implant and its integrity should be evaluated. Topographic features such as pores, interconnectivity, surface chemistry or wettability could influence the posterior cellular behaviour. On the other hand, the 3D structure of the implant should be taken into account for the success of the monolayer adhesion. In this Thesis, the cell lines evaluated over the hydrogels were at the same time evaluated over PEO-based materials, following the bottom-up approach. Successful behaviour observed in both types materials suggests that a similarly good response may reasonably be expected when a monolayer formed on a hydrogel would be transplanted onto a possible implant.

Concerning the biodegradable implant materials, a cell monolayer transplanted onto a coated Mg implant as third, final level of functionalization, could also constitute an additional strategy to delay the initiation of corrosion complementary to the ceramic and polymeric coating strategies evaluated individually and in combination in this Thesis. This concept could be used to create a biological film/organic coating/inorganic coating system that has the advantage of the fact that the transplanted cells from the VCL hydrogels (non-charged and sufobetain-zwitterionic) preserve the ECM proteins and therefore can easily adapt to the top polymeric layer (PCL). The monolayer will adhere onto the BF formed structure of the PCL layer and a more controlled degradation of the implant could be achieved.

To summarize, using tissue engineering principles this work has screened and validated different strategies for the design and fabrication of hybrid and smart biomaterials. By addressing the main components of tissue engineering, i.e. metallic, ceramic, polymeric and cell component materials individually and in combination, various steps of the possible route to fabrication of hybrid hierarchical biomaterials tailored to the needs of the patient have been demonstrated. Nowadays, clinical practice requires a change of paradigm, where patient needs determine therapeutic strategy. This approach not only would improve tissue regeneration and wound healing, but also a more efficient health system that can face the challenges of the actual society.

6. Conclusions

Electrochemical treatments for permanent implants

In situ simultaneous functionalization of chemistry, microstructure and topography of the alloys used for dental and orthopaedic applications was carried out employing plasma electrolytic oxidation technique and validated *in vitro* with respect to cells participating in bone homeostasis.

PEO treatments on Ti CP presented optimal characteristics for use as a surface treatment in implant dentistry. In the first stage two Ca- and P-based coatings with a thickness of 5 μm and 15 μm were achieved on plates and commercial dental implants with short and long treatment times. Stable phases were formed comprising a mixture of anatase and rutile; with treatment time both rutile fraction and the surface Ca/P ratio in the coatings increased, from 23% to 85% and from 2.0 to 4.0, respectively. Cell culture studies depicted good cell adhesion, expansion and proliferation of murine osteoblasts and osteoclasts over both PEO coating surfaces without signs of cytotoxicity. Moreover, ALP expression results with osteoblasts were improved over the coating with Ca/P=2.0 and higher anatase content, indicating the start of bone matrix mineralization. Osteoclast differentiation was also assessed and was found in both PEO surfaces. A superior level of TRAP expression was detected for the coating with Ca/P=4.0 and lower pore population density. Therefore, crucial bone processes (matrix synthesis and resorption) occurred over PEO surfaces and could be controlled *in vitro* by modulating surface parameters. These two coatings were also evaluated in terms of a model protein (albumin) loading and unloading capacity. The loaded albumin was found to be forming a film on the surface. Furthermore, it was found that the release rate did not depend on the coating porosity but was related to the interaction of the protein with the surface cationic and anionic groups. As a result, the thinner coating disclosed a slow liberation rate whereas the thicker coating with overstoichiometric Ca/P ratio of 4.0 in its composition released all the BSA load in 48 h. Lastly, an *in vivo* evaluation on a porcine maxilla model depicted that after 8 weeks a stronger bone matrix deposition at the implant-tissue interface was found for PEO coatings and higher BIC values of 92.1 ± 6.9% and 89.6 ± 7.4% compared to Ti CP.

Subsequently, a new approach regarding the inclusion of other bioactive elements into the ceramic coatings for dental implant application and their interaction with osteoblasts and osteoclasts was investigated. Four different coatings were obtained by combinations (minimum 2 and maximum 5) of different bioactive elements (Ca, P, Si, Mg, Zn and F) with a thickness variation of 15-27 μm. The coatings were obtained from technologically advantageous transparent electrolytes, as opposed to electrolytes with suspended precipitated particles. All the bioactive elements were successfully incorporated into the coating and crystalline phases such as hydroxyapatite, apatite,

SiO_2, MgO, CaF_2 and $CaTiO_3$ besides anatase and rutile were formed. Liberation of the bioactive elements into the physiological serum over 28 days of immersion ranged from ~1 μg/cm^2 (for Zn) to ~100 μg/cm^2 (for Ca). The formed PEO coatings permitted osteoblast proliferation and differentiation processes, determined by collagen secretion quantification with three times greater quantity of collagen than Ti CP. Osteoclast formation was detected in all the coatings as actin rings were clearly present on the surface, nevertheless variances in number, size and density between samples were found. Even though smaller osteoclasts were formed in PEO coatings, the sealing zones were denser and continuous whereas in Ti CP actin rings with a discontinuous morphology and a thinner aspect were detected.

A similar strategy was employed on Ti6Al4V for orthopaedic applications using a Ca/P-based transparent electrolyte with added Si and F for four different treatment times (90, 180, 300 and 600 s) obtaining thicknesses ranging within 6.5-40 μm. The Si/F modified electrolyte at longer treatment times encouraged the anatase-to-rutile transition and the formation of bioactive stable phases such as HA and FA. Elevated release of the incorporated bioactive elements (Ca, P, Si, F) was measured reaching up to 220.5 μg/cm^2 for Ca. Osteoblasts adhered, proliferated and differentiated over the PEO samples with no evident negative effect from the fluoride present in the coatings. Collagen secretion levels were also found to be much higher than for the control condition. The greatest antibacterial effect was detected for the PEO coating with the highest amount of fluoride (9.7 at.%) with a decrease in bacteria surface coverage down to 60% and death of ~3% of bacteria.

Conventional anodizing was employed as a way of surface morphology and composition modification of pure Zr, in order to explore the potential use of Zr in orthopaedic applications. The selected anodizing conditions resulted in the formation of ZrO_2 and P deposition on the surface following a structured pattern. This pattern affected cytoskeleton alignment and monolayer disposition of the evaluated cell lines (premyoblastic, osteoblastic, endothelial). Moreover, bone cell differentiation processes were detected with an improved osteoclasts formation on the anodized surfaces detected by actin rings and TRAP. Zr 60 V with higher amount of P was found to be more beneficial for all the evaluated cell types.

It has been demonstrated that *in situ* surface functionalization of titanium alloys with inorganic bioactive species by plasma electrolytic oxidation is a viable option for generation of implants with osteoconductive, osteoinductive, osseointegrative and antibacterial properties. Anodizing process on Zr was validated as a promising surface modification and material selection to be used as a permanent cementless implant.

Biodegradable implants for temporary applications

New biodegradable materials were formed with a Mg alloy as core element, employing two levels of functionalization: (i). *in situ* electrochemical modification by PEO that enabled simultaneous generation of corrosion protective layer that featured porous bone-like morphology and incorporated several bioactive species, followed by (ii) deposition of a biodegradable polymer layer of PCL employing a Breath Figures technique. After each step of functionalization, the materials were validated *in vitro* using both direct seeding and studies in incubated extracts with respect to four key types of cells involved in bone regeneration or in blood vessel regeneration: preosteoblastic, premyoblastic, macrophagic and endothelial.

At the first step, four ceramic coatings were manufactured on Mg0.8Ca alloy by PEO from Ca- and P-containing electrolytes with added Si or F. Stable bioactive phases (HA and FA) were obtained in all the coatings and ions (Mg, Ca, P, Si and F) were liberated from the crystalline and amorphous components of the coatings. It was demonstrated that surface characteristics of PEO coatings (porosity and roughness) can be modified by changes in the electrolyte chemical composition. The rougher coatings with greater fluoride content promoted an unstructured disposition of the preosteoblastic and endothelial cell monolayers. On the other hand, the Si-containing material presented an enhanced bioactivity in all the evaluated cell lines which was related to its chemical composition, favourable surface characteristics and enhanced protective properties, associated with its elevated compactness. Regarding the extract studies, the most concentrated extracts compromised the viability of the endothelial cells and premyoblasts, however for all coatings a better response was found in comparison with Mg0.8Ca uncoated control. The PEO coatings-derived highly diluted extracts with pH≈7.4, matching that of the control cell culture medium, had a tendency to enhance the metabolic activity, PEO-9Si extract especially standing out for premyoblastic cells, which was linked with the presence of ~1 ppm of Si in the extract. Differentiation studies revealed that osteoblastic differentiation was allowed and an improved performance of the Si-modified PEO extract was found with respect to by collagen secretion and mineralization, compared with other functionalized materials, which were Si-free and contained F. As a consequence of the alkaline pH, deliberately adjusted by the extract dilution to be at the upper cell survival limit, the obtained extracts compromised the first stages of the osteoclastogenesis process. Nonetheless, at the final stages it was capable to be recover and exhibited cell differentiation. PEO-8F and PEO-9Si favoured the formation of a greater number of large size osteoclasts similar to the control TCP, which indicates that favourable surface composition was able to ensure the robust cell performance even in the harsh initial conditions. Osteoblasts and osteoclasts co-culture studies exposed an exceptional behaviour of PEO-9Si extract of both cell types.

At the second step PCL polymeric layer was used as a top layer coating over the PEO ceramic layer and by breath figures approach a porous 3D structure was accomplished with good cell adhesion to the hydrophobic surface. Surface roughness was reduced by the PCL coating, compared with that of the initial ceramic coating, and increased again with the introduction of porosity. The contact angle increased when the porosity was created. Cells were found to be colonizing the inner pores and anchoring themselves to the underlying ceramic coating structure where higher amount of Ca, P, Mg and Si were detected. The findings suggest that tailored PCL-PEO-coated Mg hierarchical structures as biodegradable implants with bioactive properties could become excellent candidates for applications in bone reconstruction plates or cardiovascular stents design.

PS functionalization for tissue engineering purposes

New biomaterials design requires introduction of different characteristics in order to achieve a multiple function among which antibacterial properties are of enormous interest. For this matter, PS films were selective functionalized by BFs methodology resulting in microporous structures with antibacterial properties. This polymer was chosen as a versatile prototype to validate the proposed strategy. These films were formed in a single step by blending polystyrene and an amphiphilic diblock copolymer (either PS-b-PDMAEMA or PS-b-PDMAEMAQ or PS-b-PAA diblock copolymers). The pores diameters were selectively obtained in a range between 3-5 µm under mammalian cells size (10 µm). It was revealed that the diblock copolymer stays preferentially in the pore and the surface is composed mainly by PS. Therefore, the antimicrobial cues were selectively localized in the pores only reachable to the bacteria. PS-b-PDMAEMAQ or PS-b-PAA showed an improved bactericidal activity as bacteria were readily killed. PAA groups were described to interact with the bacterial membrane with a fast kill-on-contact effect, this effect was found to be associated with the concentration of PAA groups on the pore surface. However, when PAA was further functionalized with Nisin, these surfaces were nearly inactive against *S. aureus* indicating that the previous PAA effect was neutralised. On the other hand, the evaluated endothelial cell model presented good biocompatibility as these cells were able to grow and proliferate on these surfaces. It has been proposed that due to the significantly superior size cells do not contact the pores and, in consequence, there is no exposure to the antimicrobial groups. Therefore, selective functionalized surfaces with effective antimicrobial properties were obtained in one single step.

Breath figures strategy has been validated to selectively functionalize polymeric platforms and provide antibacterial/bactericidal properties to the material avoiding mammalian cell damage.

Cell sheet engineering as a promising strategy to improve biomaterials implantation

Hydrogels based on vinyl-lactams, VCL and VP, were evaluated in terms of suitable platforms for cell sheet engineering applications. Moreover, surface chemistry modifications by methacrylate inclusion of ionic moieties were made in order to improve the transplant potential. VP hydrogels were successfully supported on PC and topographic changes (wrinkles) were induced. Different bone related cell types (preosteoblasts, macrophages and endothelial) were evaluated to assess the adhesion, proliferation and transplant potential of the formed hydrogels.

Firstly, the hydrogels were functionalized with a large variety of ionic moieties (anionic, cationic, zwitterionic, pseudo- zwitterionic) and evaluated with the endothelial cell line. Cell response was found dependent on surface charge. In general, positive hydrogels displayed a suboptimal cell behaviour and transplant potential. Endothelial cell culture is promoted by anionic, mixtures of anionic and cationic or sulfobetain zwitterion ionic groups. Nevertheless, globally neutral systems (neutral hydrogels or with sulfobetain zwitterion) exhibited the best cell behaviour in terms of monolayer formation and cell transplant integrity. These surfaces are the more hydrophobic (less water content) at 37 °C (when compared to other ionic hydrogels) and the interaction with proteins/cell adhesion is favoured. Moreover, these samples presented the higher volume change favouring a quick transplantation and the obtainment of complete cell monolayers. The non-charged hydrogel, studied as a control material and evaluated firstly, is the only evaluated hydrogel that presents transparency, a key characteristic. On the other hand, the sulfobetaine zwitterion hydrogel was the best ionic material with great potential to be used as a platform for cell harvesting and transplant. In a next step, thermosensitive VCL-based hydrogel without charge were evaluated with three different cell lines with excellent monolayer expansion for endothelial and preosteoblastic cells and improved proliferation and colonization of the surface by the macrophages. All three cell types were successfully transplanted into TCP with a temperature drop off. Moreover, when the macrophagic cells were cultured with RANKL over the VCL hydrogels some multinucleated cells were detected.

VP-based hydrogels were evaluated as support-free and supported on PC. On the latter a thin hydrogel layer was deposited with a wrinkled structure changing the monomer composition with either negative, positive and pseudo- zwitterionic (neutral). Preliminary tests were performed with an endothelial cell model showing a preferential behaviour in terms of cell adhesion, growth and transplant potential for the negatively charged monomer wrinkled surfaces. Nonetheless, all the evaluated platforms permitted cell adhesion and proliferation. Negative charged platforms were further selected to be evaluated with endothelial, macrophagic and preosteoblastic cell types with three different wrinkle periods (small, intermediate and large). Macrophages and endothelial with smaller cell size presented best results in terms of spontaneous transplantation with the

intermediate and small wrinkled periods platforms. Osteoblasts did not present significative differences between the samples and a low efficiency transplant.

These results indicate that vinyl-lactam based platforms can be used for cell sheet engineering applications with either mechanical or temperature stimuli. This approach could be implemented on several biomaterials applications.

7. References

[1] E. Martínez Campos, A. Santos-Coquillat, B. Mingo, R. Arrabal, M. Mohedano, A. Pardo, V. Ramos, J.L. López Lacomba, E. Matykina, Albumin loaded PEO coatings on Ti - Potential as drug eluting systems, Surface and Coatings Technology, 283 (2015) 44-51.

[2] M.R. Katunar, A. Gomez Sanchez, A. Santos Coquillat, A. Civantos, E. Martinez Campos, J. Ballarre, T. Vico, M. Baca, V. Ramos, S. Cere, *In vitro* and *in vivo* characterization of anodised zirconium as a potential material for biomedical applications, Materials Science and Engineering C, 75 (2017) 957-968.

[3] N. Vargas-Alfredo, A. Santos-Coquillat, E. Martínez-Campos, A. Dorronsoro, A.L. Cortajarena, A. Del Campo, J. Rodríguez-Hernández, Highly Efficient Antibacterial Surfaces Based on Bacterial/Cell Size Selective Microporous Supports, ACS Applied Materials and Interfaces, 9 (2017) 44270-44280.

[4] E. Martínez-Campos, A. Santos-Coquillat, M.E. Pérez-Ojeda, A. Civantos, C. Elvira, H. Reinecke, C. García, V. Ramos, J. Rodríguez-Hernández, A. Gallardo, Thermosensitive hydrogel platforms with modulated ionic load for optimal cell sheet harvesting, European Polymer Journal, 103 (2018) 400-409.

[5] A. Santos-Coquillat, R. Gonzalez Tenorio, M. Mohedano, E. Martinez-Campos, R. Arrabal, E. Matykina, Tailoring of antibacterial and osteogenic properties of Ti6Al4V by plasma electrolytic oxidation, Applied Surface Science, 454 (2018) 157-172.

[6] A. Santos-Coquillat, E. Martínez-Campos, M. Mohedano, R. Martínez-Corriá, V. Ramos, R. Arrabal, E. Matykina, *In vitro* and *in vivo* evaluation of PEO-modified titanium for bone implant applications, Surface and Coatings Technology, 347 (2018) 358-368.

[7] N. Vargas-Alfredo, E. Martínez-Campos, A. Santos-Coquillat, A. Dorronsoro, A.L. Cortajarena, A. del Campo, J. Rodríguez-Hernández, Fabrication of biocompatible and efficient antimicrobial porous polymer surfaces by the Breath Figures approach, Journal of Colloid and Interface Science, 513 (2018) 820-830.

[8] R. Langer, J.P. Vacanti, Tissue engineering, Science (New York, N.Y.), 260 (1993) 920-926.

[9] R. Langer, D.A. Tirrell, Designing materials for biology and medicine, Nature, 428 (2004) 487.

[10] M.E. Gomes, M.T. Rodrigues, R.M.A. Domingues, R.L. Reis, Tissue Engineering and Regenerative Medicine: New Trends and Directions-A Year in Review, Tissue engineering. Part B, Reviews, 23 (2017) 211-224.

[11] C.J. Bettinger, R. Langer, J.T. Borenstein, Engineering substrate topography at the micro- and nanoscale to control cell function, Angewandte Chemie (International ed. in English), 48 (2009) 5406-5415.

[12] J. Yang, M. Yamato, C. Kohno, A. Nishimoto, H. Sekine, F. Fukai, T. Okano, Cell sheet engineering: Recreating tissues without biodegradable scaffolds, Biomaterials, 26 (2005) 6415-6422.

[13] J. Patterson, M.M. Martino, J.A. Hubbell, Biomimetic materials in tissue engineering, Materials Today, 13 (2010) 14-22.

[14] J.A. Hubbell, Biomaterials in tissue engineering, Bio/technology (Nature Publishing Company), 13 (1995) 565-576.

[15] Tissue Engineering Market Size, Share & Trends Analysis Report By Application (Cord Blood & Cell Banking, Cancer, GI & Gynecology, Dental, Skin/Integumentary, Orthopedics), And Segment Forecasts, 2018 - 2025, in.

[16] V. Campana, G. Milano, E. Pagano, M. Barba, C. Cicione, G. Salonna, W. Lattanzi, G. Logroscino, Bone substitutes in orthopaedic surgery: from basic science to clinical practice, Journal of materials science. Materials in medicine, 25 (2014) 2445-2461.

[17] B.V. Slaughter, S.S. Khurshid, O.Z. Fisher, A. Khademhosseini, N.A. Peppas, Hydrogels in Regenerative Medicine, Advanced materials (Deerfield Beach, Fla.), 21 (2009) 3307-3329.

[18] A. Khademhosseini, R. Langer, A decade of progress in tissue engineering, Nature Protocols, 11 (2016) 1775.

[19] S. Ohba, F. Yano, U.-i. Chung, Tissue engineering of bone and cartilage, IBMS BoneKEy, 6 (2009) 405-419.

[20] I. Kulinets, 1 - Biomaterials and their applications in medicine, in: S.F. Amato, R.M. Ezzell (Eds.) Regulatory Affairs for Biomaterials and Medical Devices, Woodhead Publishing, 2015, pp. 1-10.

[21] J.P. Vacanti, R. Langer, Tissue engineering: the design and fabrication of living replacement devices for surgical reconstruction and transplantation, Lancet (London, England), 354 Suppl 1 (1999) Si32-34.

[22] T.J. Keane, S.F. Badylak, Biomaterials for tissue engineering applications, Seminars in Pediatric Surgery, 23 (2014) 112-118.

[23] Q. Chen, G.A. Thouas, Metallic implant biomaterials, Materials Science and Engineering: R: Reports, 87 (2015) 1-57.

[24] S.F. Amato, 4 - Clinical development and endpoint strategies for biomaterials and medical devices, in: S.F. Amato, R.M. Ezzell (Eds.) Regulatory Affairs for Biomaterials and Medical Devices, Woodhead Publishing, 2015, pp. 47-66.

[25] X. Wang, S. Xu, S. Zhou, W. Xu, M. Leary, P. Choong, M. Qian, M. Brandt, Y.M. Xie, Topological design and additive manufacturing of porous metals for bone scaffolds and orthopaedic implants: A review, Biomaterials, 83 (2016) 127-141.

[26] A.J. Salgado, O.P. Coutinho, R.L. Reis, Bone Tissue Engineering: State of the Art and Future Trends, Macromolecular Bioscience, 4 (2004) 743-765.

[27] D.W. Hutmacher, Scaffolds in tissue engineering bone and cartilage, Biomaterials, 21 (2000) 2529-2543.

[28] V.I. Sikavitsas, J.S. Temenoff, A.G. Mikos, Biomaterials and bone mechanotransduction, Biomaterials, 22 (2001) 2581-2593.

[29] A.M. Parfitt, The cellular basis of bone remodeling: the quantum concept reexamined in light of recent advances in the cell biology of bone, Calcified tissue international, 36 Suppl 1 (1984) S37-45.

[30] M. Maisani, D. Pezzoli, O. Chassande, D. Mantovani, Cellularizing hydrogel-based scaffolds to repair bone tissue: How to create a physiologically relevant micro-environment?, Journal of Tissue Engineering, 8 (2017) 2041731417712073.

[31] A.K. Nair, A. Gautieri, S.-W. Chang, M.J. Buehler, Molecular mechanics of mineralized collagen fibrils in bone, Nature Communications, 4 (2013) 1724.

[32] R. Florencio-Silva, G.R.d.S. Sasso, E. Sasso-Cerri, M.J. Simões, P.S. Cerri, Biology of Bone Tissue: Structure, Function, and Factors That Influence Bone Cells, BioMed Research International, 2015 (2015) 421746.

[33] S. Bose, M. Roy, A. Bandyopadhyay, Recent advances in bone tissue engineering scaffolds, Trends in biotechnology, 30 (2012) 546-554.

[34] M. Mravic, B. Peault, A.W. James, Current trends in bone tissue engineering, Biomed Res Int, 2014 (2014) 865270.

[35] K. Nakahama, Cellular communications in bone homeostasis and repair, Cellular and molecular life sciences : CMLS, 67 (2010) 4001-4009.

[36] Z. Bar-Shavit, The osteoclast: a multinucleated, hematopoietic-origin, bone-resorbing osteoimmune cell, Journal of cellular biochemistry, 102 (2007) 1130-1139.

[37] S.C. Miller, L. de Saint-Georges, B.M. Bowman, W.S. Jee, Bone lining cells: structure and function, Scanning microscopy, 3 (1989) 953-960; discussion 960-951.

[38] N. Baldini, E. Cenni, G. Ciapetti, D. Granchi, L. Savarino, 3 - Bone repair and regeneration, in: J.A. Planell, S.M. Best, D. Lacroix, A. Merolli (Eds.) Bone Repair Biomaterials, Woodhead Publishing, 2009, pp. 69-105.

[39] T. Albrektsson, C. Johansson, Osteoinduction, osteoconduction and osseointegration, European spine journal : official publication of the European Spine Society, the European Spinal Deformity Society, and the European Section of the Cervical Spine Research Society, 10 Suppl 2 (2001) S96-101.

[40] M.T. Calejo, T. Ilmarinen, H. Skottman, M. Kellomäki, Breath figures in tissue engineering and drug delivery: State-of-the-art and future perspectives, Acta biomaterialia, 66 (2018) 44-66.

[41] M.I. Santos, R.L. Reis, Vascularization in bone tissue engineering: physiology, current strategies, major hurdles and future challenges, Macromol Biosci, 10 (2010) 12-27.

[42] M. Navarro, A. Michiardi, O. Castaño, J.A. Planell, Biomaterials in orthopaedics, Journal of the Royal Society Interface, 5 (2008) 1137-1158.

[43] L.L. Hench, J.M. Polak, Third-generation biomedical materials, Science (New York, N.Y.), 295 (2002) 1014-1017.

[44] B.M. Holzapfel, J.C. Reichert, J.-T. Schantz, U. Gbureck, L. Rackwitz, U. Nöth, F. Jakob, M. Rudert, J. Groll, D.W. Hutmacher, How smart do biomaterials need to be? A translational science and clinical point of view, Advanced Drug Delivery Reviews, 65 (2013) 581-603.

[45] M. Geetha, A.K. Singh, R. Asokamani, A.K. Gogia, Ti based biomaterials, the ultimate choice for orthopaedic implants – A review, Progress in Materials Science, 54 (2009) 397-425.

[46] V. Mathieu, R. Vayron, G. Richard, G. Lambert, S. Naili, J.-P. Meningaud, G. Haiat, Biomechanical determinants of the stability of dental implants: Influence of the bone-implant interface properties, Journal of Biomechanics, 47 (2014) 3-13.

[47] J.A. Lyndon, B.J. Boyd, N. Birbilis, Metallic implant drug/device combinations for controlled drug release in orthopaedic applications, Journal of Controlled Release, 179 (2014) 63-75.

[48] Y.-J. Park, Y.-H. Song, J.-H. An, H.-J. Song, K.J. Anusavice, Cytocompatibility of pure metals and experimental binary titanium alloys for implant materials, Journal of Dentistry, 41 (2013) 1251-1258.

[49] F.A. Shah, M. Trobos, P. Thomsen, A. Palmquist, Commercially pure titanium (cp-Ti) versus titanium alloy (Ti6Al4V) materials as bone anchored implants — Is one truly better than the other?, Materials Science and Engineering: C, 62 (2016) 960-966.

[50] M.R. Katunar, A. Gomez Sanchez, J. Ballarre, M. Baca, C. Vottola, J.C. Orellano, H. Schell, G. Duffo, S. Cere, Can anodised zirconium implants stimulate bone formation? Preliminary study in rat model, Progress in biomaterials, 3 (2014) 24.

[51] R.M. Hoerth, M.R. Katunar, A. Gomez Sanchez, J.C. Orellano, S.M. Cere, W. Wagermaier, J. Ballarre, A comparative study of zirconium and titanium implants in rat: osseointegration and bone material quality, Journal of materials science. Materials in medicine, 25 (2014) 411-422.

[52] Z. Qu, X. Rausch-Fan, M. Wieland, M. Matejka, A. Schedle, The initial attachment and subsequent behavior regulation of osteoblasts by dental implant surface modification, Journal of Biomedical Materials Research Part A, 82A (2007) 658-668.

[53] A.D. Pye, D.E.A. Lockhart, M.P. Dawson, C.A. Murray, A.J. Smith, A review of dental implants and infection, Journal of Hospital Infection, 72 (2009) 104-110.

[54] C.Y. Guo, J.P. Matinlinna, A.T.H. Tang, Effects of Surface Charges on Dental Implants: Past, Present, and Future, International Journal of Biomaterials, 2012 (2012) 5.

[55] T. Albrektsson, P.I. Branemark, H.A. Hansson, J. Lindstrom, Osseointegrated titanium implants. Requirements for ensuring a long-lasting, direct bone-to-implant anchorage in man, Acta orthopaedica Scandinavica, 52 (1981) 155-170.

[56] F. Rupp, L. Liang, J. Geis-Gerstorfer, L. Scheideler, F. Hüttig, Surface characteristics of dental implants: A review, Dental Materials, 34 (2018) 40-57.

[57] R. Junker, A. Dimakis, M. Thoneick, J.A. Jansen, Effects of implant surface coatings and composition on bone integration: a systematic review, Clinical oral implants research, 20 Suppl 4 (2009) 185-206.

[58] A. Wennerberg, T. Albrektsson, Effects of titanium surface topography on bone integration: a systematic review, Clinical oral implants research, 20 (2009) 172-184.

[59] C.M. Abraham, A brief historical perspective on dental implants, their surface coatings and treatments, The open dentistry journal, 8 (2014) 50-55.

[60] D.M. Dohan Ehrenfest, P.G. Coelho, B.S. Kang, Y.T. Sul, T. Albrektsson, Classification of osseointegrated implant surfaces: materials, chemistry and topography, Trends in biotechnology, 28 (2010) 198-206.

[61] L. Le Guehennec, A. Soueidan, P. Layrolle, Y. Amouriq, Surface treatments of titanium dental implants for rapid osseointegration, Dental materials : official publication of the Academy of Dental Materials, 23 (2007) 844-854.

[62] G. Zhao, Z. Schwartz, M. Wieland, F. Rupp, J. Geis-Gerstorfer, D.L. Cochran, B.D. Boyan, High surface energy enhances cell response to titanium substrate microstructure, Journal of biomedical materials research. Part A, 74 (2005) 49-58.

[63] B.R. Chrcanovic, T. Albrektsson, A. Wennerberg, Reasons for failures of oral implants, Journal of oral rehabilitation, 41 (2014) 443-476.

[64] R. Smeets, B. Stadlinger, F. Schwarz, B. Beck-Broichsitter, O. Jung, C. Precht, F. Kloss, Gr, #xf6, A. be, M. Heiland, T. Ebker, Impact of Dental Implant Surface Modifications on Osseointegration, BioMed Research International, 2016 (2016) 16.

[65] I. Gotman, Characteristics of Metals Used in Implants, Journal of Endourology, 11 (1997) 383-389.

[66] R.I.M. Asri, W.S.W. Harun, M. Samykano, N.A.C. Lah, S.A.C. Ghani, F. Tarlochan, M.R. Raza, Corrosion and surface modification on biocompatible metals: A review, Materials Science and Engineering: C, 77 (2017) 1261-1274.

[67] J. Gallo, M. Holinka, C. Moucha, Antibacterial Surface Treatment for Orthopaedic Implants, International Journal of Molecular Sciences, 15 (2014) 13849.

[68] B. Zhang, D. Myers, G. Wallace, M. Brandt, P. Choong, Bioactive Coatings for Orthopaedic Implants—Recent Trends in Development of Implant Coatings, International Journal of Molecular Sciences, 15 (2014) 11878.

[69] E. Matykina, F. Monfort, A. Berkani, P. Skeldon, G.E. Thompson, J. Gough, Characterization of spark-anodized titanium for biomedical applications, Journal of the Electrochemical Society, 154 (2007) C279-C285.

[70] A. Aladjem, Anodic oxidation of titanium and its alloys, Journal of Materials Science, 8 (1973) 688-704.

[71] A. Valota, D.J. LeClere, P. Skeldon, M. Curioni, T. Hashimoto, S. Berger, J. Kunze, P. Schmuki, G.E. Thompson, Influence of water content on nanotubular anodic titania formed in fluoride/glycerol electrolytes, Electrochimica Acta, 54 (2009) 4321-4327.

[72] C. Pérez-Jorge, A. Conde, A. Arenas Maria, R. Pérez-Tanoira, E. Matykina, J. de Damborenea Juan, E. Gómez-Barrena, J. Esteban, *In vitro* assessment of *Staphylococcus epidermidis* and *Staphylococcus aureus* adhesion on TiO_2 nanotubes on Ti–6Al–4V alloy, Journal of Biomedical Materials Research Part A, 100A (2012) 1696-1705.

[73] M. Mohedano, X. Lu, E. Matykina, C. Blawert, R. Arrabal, M.L. Zheludkevich, Plasma Electrolytic Oxidation (PEO) of Metals and Alloys A2 - Wandelt, Klaus, in: Encyclopedia of Interfacial Chemistry, Elsevier, Oxford, 2018, pp. 423-438.

[74] A.L. Yerokhin, X. Nie, A. Leyland, A. Matthews, S.J. Dowey, Plasma electrolysis for surface engineering, Surface and Coatings Technology, 122 (1999) 73-93.

[75] A.L. Yerokhin, X. Nie, A. Leyland, A. Matthews, Characterisation of oxide films produced by plasma electrolytic oxidation of a Ti–6Al–4V alloy, Surface and Coatings Technology, 130 (2000) 195-206.

[76] A. Gao, R. Hang, L. Bai, B. Tang, P.K. Chu, Electrochemical surface engineering of titanium-based alloys for biomedical application, Electrochimica Acta, 271 (2018) 699-718.

[77] O.A. Galvis, D. Quintero, J.G. Castaño, H. Liu, G.E. Thompson, P. Skeldon, F. Echeverría, Formation of grooved and porous coatings on titanium by plasma electrolytic oxidation in H_2SO_4/H_3PO_4 electrolytes and effects of coating morphology on adhesive bonding, Surface and Coatings Technology, 269 (2015) 238-249.

[78] E. Matykina, R. Arrabal, M. Mohedano, A. Pardo, M.C. Merino, E. Rivero, Stability of plasma electrolytic oxidation coating on titanium in artificial saliva, Journal of materials science. Materials in medicine, 24 (2013) 37-51.

[79] M. Mohedano, R. Guzman, R. Arrabal, J.L. Lopez Lacomba, E. Matykina, Bioactive plasma electrolytic oxidation coatings--the role of the composition, microstructure, and electrochemical stability, Journal of biomedical materials research.Part B, Applied biomaterials, 101 (2013) 1524-1537.

[80] L.H. Li, Y.M. Kong, H.W. Kim, Y.W. Kim, H.E. Kim, S.J. Heo, J.Y. Koak, Improved biological performance of Ti implants due to surface modification by micro-arc oxidation, Biomaterials, 25 (2004) 2867-2875.

[81] M. Mohedano, E. Matykina, R. Arrabal, A. Pardo, M.C. Merino, Metal release from ceramic coatings for dental implants, Dental Materials, 30 (2014) e28-e40.

[82] Y. Wang, L. Wang, H. Zheng, C. Du, ChengyunNing, Z. Shi, C. Xu, Effect of frequency on the structure and cell response of Ca- and P-containing MAO films, Applied Surface Science, 256 (2010) 2018-2024.

[83] P. Whiteside, E. Matykina, J.E. Gough, P. Skeldon, G.E. Thompson, *In vitro* evaluation of cell proliferation and collagen synthesis on titanium following plasma electrolytic oxidation, Journal of Biomedical Materials Research Part A, 94A (2010) 38-46.

[84] X. Rao, C.L. Chu, Q. Sun, Y.Y. Zheng, Fabrication and apatite inducing ability of different porous titania structures by PEO treatment, Materials Science and Engineering: C, 66 (2016) 297-305.

[85] Y.-T. Sul, C.B. Johansson, Y. Jeong, A. Wennerberg, T. Albrektsson, Resonance frequency and removal torque analysis of implants with turned and anodized surface oxides, Clinical oral implants research, 13 (2002) 252-259.

[86] M. Degidi, D. Nardi, A. Piattelli, 10-year follow-up of immediately loaded implants with TiUnite porous anodized surface, Clinical implant dentistry and related research, 14 (2012) 828-838.

[87] A. Rocci, M. Martignoni, J. Gottlow, Immediate loading of Branemark System TiUnite and machined-surface implants in the posterior mandible: a randomized open-ended clinical trial, Clinical implant dentistry and related research, 5 Suppl 1 (2003) 57-63.

[88] M. Karl, T. Albrektsson, Clinical Performance of Dental Implants with a Moderately Rough (TiUnite) Surface: A Meta-Analysis of Prospective Clinical Studies, The International journal of oral & maxillofacial implants, 32 (2017) 717-734.

[89] A. Krząkała, A. Kazek-Kęsik, W. Simka, Application of plasma electrolytic oxidation to bioactive surface formation on titanium and its alloys, RSC Advances, 3 (2013) 19725-19743.

[90] Y.-T. Sul, C.B. Johansson, K. Röser, T. Albrektsson, Qualitative and quantitative observations of bone tissue reactions to anodised implants, Biomaterials, 23 (2002) 1809-1817.

[91] Y.-T. Sul, J. Jönsson, G.-S. Yoon, C. Johansson, Resonance frequency measurements *in vivo* and related surface properties of magnesium-incorporated, micropatterned and magnesium-incorporated TiUnite®, Osseotite®, SLA® and TiOblast® implants, Clinical oral implants research, 20 (2009) 1146-1155.

[92] Y.-T. Sul, B.-S. Kang, C. Johansson, H.-S. Um, C.-J. Park, T. Albrektsson, The roles of surface chemistry and topography in the strength and rate of osseointegration of titanium implants in bone, Journal of Biomedical Materials Research Part A, 89A (2009) 942-950.

[93] Y.T. Sul, C. Johansson, T. Albrektsson, Which surface properties enhance bone response to implants? Comparison of oxidized magnesium, tiUnite, and osseotite implant surfaces, International Journal of Prosthodontics, 19 (2006) 319-328.

[94] Y.T. Sul, Y. Jeong, C. Johansson, T. Albrektsson, Oxidized, bioactive implants are rapidly and strongly integrated in bone. Part 1 - Experimental implants, Clinical oral implants research, 17 (2006) 521-526.

[95] R. Wang, X. He, Y. Gao, X. Zhang, X. Yao, B. Tang, Antimicrobial property, cytocompatibility and corrosion resistance of Zn-doped ZrO_2/TiO_2 coatings on Ti6Al4V implants, Materials science & engineering. C, Materials for biological applications, 75 (2017) 7-15.

[96] M. Chen, L. Yang, L. Zhang, Y. Han, Z. Lu, G. Qin, E. Zhang, Effect of nano/micro-Ag compound particles on the bio-corrosion, antibacterial properties and cell biocompatibility of Ti-Ag alloys, Materials science & engineering. C, Materials for biological applications, 75 (2017) 906-917.

[97] H. Hu, W. Zhang, Y. Qiao, X. Jiang, X. Liu, C. Ding, Antibacterial activity and increased bone marrow stem cell functions of Zn-incorporated TiO_2 coatings on titanium, Acta biomaterialia, 8 (2012) 904-915.

[98] D. Zhao, Y. Lu, Z. Wang, X. Zeng, S. Liu, T. Wang, Antifouling properties of micro arc oxidation coatings containing Cu_2O/ZnO nanoparticles on Ti6Al4V, International Journal of Refractory Metals and Hard Materials, 54 (2016) 417-421.

[99] R. Balcon, R. Beyar, S. Chierchia, I. De Scheerder, P.G. Hugenholtz, F. Kiemeneij, B. Meier, J. Meyer, J.P. Monassier, W. Wijns, Recommendations on stent manufacture, implantation and utilization. Study Group of the Working Group on Coronary Circulation, European heart journal, 18 (1997) 1536-1547.

[100] C. Godavitarne, A. Robertson, J. Peters, B. Rogers, Biodegradable materials, Orthopaedics and Trauma, 31 (2017) 316-320.

[101] M. Peron, J. Torgersen, F. Berto, Mg and Its Alloys for Biomedical Applications: Exploring Corrosion and Its Interplay with Mechanical Failure, Metals, 7 (2017) 252.

[102] R. Biber, J. Pauser, M. Brem, H.J. Bail, Bioabsorbable metal screws in traumatology: A promising innovation, Trauma Case Reports, 8 (2017) 11-15.

[103] B.J. Luthringer, F. Feyerabend, R. Willumeit-Romer, Magnesium-based implants: a mini-review, Magnesium research, 27 (2014) 142-154.

[104] M.P. Staiger, A.M. Pietak, J. Huadmai, G. Dias, Magnesium and its alloys as orthopedic biomaterials: A review, Biomaterials, 27 (2006) 1728-1734.

[105] R. Erbel, C. Di Mario, J. Bartunek, J. Bonnier, B. de Bruyne, F.R. Eberli, P. Erne, M. Haude, B. Heublein, M. Horrigan, C. Ilsley, D. Böse, J. Koolen, T.F. Lüscher, N. Weissman, R. Waksman, Temporary scaffolding of coronary arteries with bioabsorbable magnesium stents: a prospective, non-randomised multicentre trial, The Lancet, 369 (2007) 1869-1875.

[106] P.H. Grewe, D. Thomas, A. Machraoui, J. Barmeyer, K.M. Muller, Coronary morphologic findings after stent implantation, The American journal of cardiology, 85 (2000) 554-558.

[107] R.-X. Yin, D.-Z. Yang, J.-Z. Wu, Nanoparticle Drug- and Gene-eluting Stents for the Prevention and Treatment of Coronary Restenosis, Theranostics, 4 (2014) 175-200.

[108] M.K. Lam, H. Sen, K. Tandjung, K.G. van Houwelingen, A.G. de Vries, P.W. Danse, C.E. Schotborgh, M. Scholte, M.M. Lowik, G.C. Linssen, M.J. Ijzerman, J. van der Palen, C.J. Doggen, C. von Birgelen, Comparison of 3 biodegradable polymer and durable polymer-based drug-eluting stents in all-comers (BIO-RESORT): rationale and study design of the randomized TWENTE III multicenter trial, American heart journal, 167 (2014) 445-451.

[109] T.S.N. Sankara Narayanan, I.S. Park, M.H. Lee, Strategies to improve the corrosion resistance of microarc oxidation (MAO) coated magnesium alloys for degradable implants: Prospects and challenges, Progress in Materials Science, 60 (2014) 1-71.

[110] Z. Li, X. Gu, S. Lou, Y. Zheng, The development of binary Mg-Ca alloys for use as biodegradable materials within bone, Biomaterials, 29 (2008) 1329-1344.

[111] K. Gusieva, C.H.J. Davies, J.R. Scully, N. Birbilis, Corrosion of magnesium alloys: the role of alloying, International Materials Reviews, 60 (2015) 169-194.

[112] Y. Ding, C. Wen, P. Hodgson, Y. Li, Effects of alloying elements on the corrosion behavior and biocompatibility of biodegradable magnesium alloys: a review, Journal of Materials Chemistry B, 2 (2014) 1912-1933.

[113] F. Feyerabend, J. Fischer, J. Holtz, F. Witte, R. Willumeit, H. Drücker, C. Vogt, N. Hort, Evaluation of short-term effects of rare earth and other elements used in magnesium alloys on primary cells and cell lines, Acta biomaterialia, 6 (2010) 1834-1842.

[114] S.V. Verstraeten, L. Aimo, P.I. Oteiza, Aluminium and lead: molecular mechanisms of brain toxicity, Archives of toxicology, 82 (2008) 789-802.

[115] P. Yin, N.F. Li, T. Lei, L. Liu, C. Ouyang, Effects of Ca on microstructure, mechanical and corrosion properties and biocompatibility of Mg-Zn-Ca alloys, Journal of materials science. Materials in medicine, 24 (2013) 1365-1373.

[116] Y.H. Bouchi, B.D. Gogas, Biocorrodible metals for coronary revascularization: Lessons from PROGRESS-AMS, BIOSOLVE-I, and BIOSOLVE-II, Global Cardiology Science & Practice, 2015 (2015) 63.

[117] S. You, Y. Huang, K.U. Kainer, N. Hort, Recent research and developments on wrought magnesium alloys, Journal of Magnesium and Alloys, 5 (2017) 239-253.

[118] N.I. Zainal Abidin, A.D. Atrens, D. Martin, A. Atrens, Corrosion of high purity Mg, Mg2Zn0.2Mn, ZE41 and AZ91 in Hank's solution at 37°C, Corrosion Science, 53 (2011) 3542-3556.

[119] M. Mohedano, B.J.C. Luthringer, B. Mingo, F. Feyerabend, R. Arrabal, P.J. Sanchez-Egido, C. Blawert, R. Willumeit-Römer, M.L. Zheludkevich, E. Matykina, Bioactive plasma electrolytic oxidation coatings on Mg-Ca alloy to control degradation behaviour, Surface and Coatings Technology, 315 (2017) 454-467.

[120] P. Lu, L. Cao, Y. Liu, X. Xu, X. Wu, Evaluation of magnesium ions release, biocorrosion, and hemocompatibility of MAO/PLLA-modified magnesium alloy WE42, Journal of biomedical materials research. Part B, Applied biomaterials, 96 (2011) 101-109.

[121] M. Guo, L. Cao, P. Lu, Y. Liu, X. Xu, Anticorrosion and cytocompatibility behavior of MAO/PLLA modified magnesium alloy WE42, Journal of materials science. Materials in medicine, 22 (2011) 1735-1740.

[122] P. Liu, X. Pan, W. Yang, K. Cai, Y. Chen, Improved anticorrosion of magnesium alloy via layer-by-layer self-assembly technique combined with micro-arc oxidation, Materials Letters, 75 (2012) 118-121.

[123] J.H. Gao, X.Y. Shi, B. Yang, S.S. Hou, E.C. Meng, F.X. Guan, S.K. Guan, Fabrication and characterization of bioactive composite coatings on Mg-Zn-Ca alloy by MAO/sol-gel, Journal of materials science. Materials in medicine, 22 (2011) 1681-1687.

[124] P. Lu, Y. Liu, M. Guo, H. Fang, X. Xu, Corrosion and drug release properties of EN-plating/PLGA composite coating on MAO film, Materials Science and Engineering: C, 31 (2011) 1285-1289.

[125] X. Xu, P. Lu, M. Guo, M. Fang, Cross-linked gelatin/nanoparticles composite coating on micro-arc oxidation film for corrosion and drug release, Applied Surface Science, 256 (2010) 2367-2371.

[126] A. Muñoz-Bonilla, M. Fernández-García, J. Rodríguez-Hernández, Towards hierarchically ordered functional porous polymeric surfaces prepared by the breath figures approach, Progress in Polymer Science, 39 (2014) 510-554.

[127] A. Zhang, H. Bai, L. Li, Breath Figure: A Nature-Inspired Preparation Method for Ordered Porous Films, Chemical Reviews, 115 (2015) 9801-9868.

[128] G. Widawski, M. Rawiso, B. François, Self-organized honeycomb morphology of star-polymer polystyrene films, Nature, 369 (1994) 387.

[129] S. Velayudhan, P.R. Kumar, P.D. Nair, A Novel, Single Step, Highly Sensitive In-Vitro Cell-Based Metabolic Assay Using Honeycomb Microporous Polymer Membranes, Journal of biomedical nanotechnology, 11 (2015) 590-599.

[130] V.G. Fernández-Luna, D. Mallinson, P. Alexiou, I. Khadra, A.B. Mullen, M. Pelecanou, M. Sagnou, D.A. Lamprou, Isatin thiosemicarbazones promote honeycomb structure formation in spin-coated polymer films: concentration effect and release studies, RSC Advances, 7 (2017) 12945-12952.

[131] A.S. de León, J. Rodríguez-Hernández, A.L. Cortajarena, Honeycomb patterned surfaces functionalized with polypeptide sequences for recognition and selective bacterial adhesion, Biomaterials, 34 (2013) 1453-1460.

[132] E. Martínez-Campos, T. Elzein, A. Bejjani, M.J. García-Granda, A. Santos-Coquillat, V. Ramos, A. Muñoz-Bonilla, J. Rodríguez-Hernández, Toward Cell Selective Surfaces: Cell Adhesion and Proliferation on Breath Figures with Antifouling Surface Chemistry, ACS Applied Materials & Interfaces, 8 (2016) 6344-6353.

[133] A. Albanese, M.E. Licata, B. Polizzi, G. Campisi, Platelet-rich plasma (PRP) in dental and oral surgery: from the wound healing to bone regeneration, Immunity & Ageing : I & A, 10 (2013) 23-23.

[134] K. Ito, Y. Yamada, T. Naiki, M. Ueda, Simultaneous implant placement and bone regeneration around dental implants using tissue-engineered bone with fibrin glue, mesenchymal stem cells and platelet-rich plasma, Clinical oral implants research, 17 (2006) 579-586.

[135] D. Ingrassia, M. Sladkova, M. Palmer, W. Xia, H. Engqvist, G.M. de Peppo, Stem cell-mediated functionalization of titanium implants, Journal of materials science. Materials in medicine, 28 (2017) 133.

[136] M. Yamato, T. Okano, Cell sheet engineering, Materials Today, 7 (2004) 42-47.

[137] Y. Haraguchi, T. Shimizu, M. Yamato, T. Okano, Scaffold-free tissue engineering using cell sheet technology, RSC Advances, 2 (2012) 2184-2190.

[138] J. Yang, M. Yamato, C. Kohno, A. Nishimoto, H. Sekine, F. Fukai, T. Okano, Cell sheet engineering: recreating tissues without biodegradable scaffolds, Biomaterials, 26 (2005) 6415-6422.

[139] N. Matsuda, T. Shimizu, M. Yamato, T. Okano, Tissue Engineering Based on Cell Sheet Technology, Advanced Materials, 19 (2007) 3089-3099.

[140] M. Yamato, M. Utsumi, A. Kushida, C. Konno, A. Kikuchi, T. Okano, Thermo-responsive culture dishes allow the intact harvest of multilayered keratinocyte sheets without dispase by reducing temperature, Tissue engineering, 7 (2001) 473-480.

[141] A. Kushida, M. Yamato, C. Konno, A. Kikuchi, Y. Sakurai, T. Okano, Temperature-responsive culture dishes allow nonenzymatic harvest of differentiated Madin-Darby canine kidney (MDCK) cell sheets, Journal of Biomedical Materials Research, 51 (2000) 216-223.

[142] K. Nishida, M. Yamato, Y. Hayashida, K. Watanabe, K. Yamamoto, E. Adachi, S. Nagai, A. Kikuchi, N. Maeda, H. Watanabe, T. Okano, Y. Tano, Corneal reconstruction with tissue-engineered cell sheets composed of autologous oral mucosal epithelium, The New England journal of medicine, 351 (2004) 1187-1196.

[143] Y. Shiroyanagi, M. Yamato, Y. Yamazaki, H. Toma, T. Okano, Transplantable urothelial cell sheets harvested noninvasively from temperature-responsive culture surfaces by reducing temperature, Tissue engineering, 9 (2003) 1005-1012.

[144] Y. Shiroyanagi, M. Yamato, Y. Yamazaki, H. Toma, T. Okano, Urothelium regeneration using viable cultured urothelial cell sheets grafted on demucosalized gastric flaps, BJU international, 93 (2004) 1069-1075.

[145] T. Akizuki, S. Oda, M. Komaki, H. Tsuchioka, N. Kawakatsu, A. Kikuchi, M. Yamato, T. Okano, I. Ishikawa, Application of periodontal ligament cell sheet for periodontal regeneration: a pilot study in beagle dogs, Journal of periodontal research, 40 (2005) 245-251.

[146] N.G. Patel, G. Zhang, Responsive systems for cell sheet detachment, Organogenesis, 9 (2013) 93-100.

[147] R.P. Pirraco, H. Obokata, T. Iwata, A.P. Marques, S. Tsuneda, M. Yamato, R.L. Reis, T. Okano, Development of osteogenic cell sheets for bone tissue engineering applications, Tissue engineering. Part A, 17 (2011) 1507-1515.

[148] R.P. Pirraco, T. Iwata, T. Yoshida, A.P. Marques, M. Yamato, R.L. Reis, T. Okano, Endothelial cells enhance the in vivo bone-forming ability of osteogenic cell sheets, Laboratory investigation; a journal of technical methods and pathology, 94 (2014) 663-673.

[149] N. Kaneshiro, M. Sato, M. Ishihara, G. Mitani, H. Sakai, J. Mochida, Bioengineered chondrocyte sheets may be potentially useful for the treatment of partial thickness defects of articular cartilage, Biochemical and Biophysical Research Communications, 349 (2006) 723-731.

[150] M. Sato, M. Yamato, K. Hamahashi, T. Okano, J. Mochida, Articular Cartilage Regeneration Using Cell Sheet Technology, The Anatomical Record, 297 (2014) 36-43.

[151] S. Hashimoto, Development of thermo-responslve cell cultureware, UpCell®, for regenerative medicine, Kobunshi, 66 (2017) 499-500.

[152] N. Kanai, M. Yamato, T. Ohki, M. Yamamoto, T. Okano, Fabricated autologous epidermal cell sheets for the prevention of esophageal stricture after circumferential ESD in a porcine model, Gastrointestinal Endoscopy, 76 (2012) 873-881.

[153] T. Ohki, M. Yamato, M. Ota, R. Takagi, D. Murakami, M. Kondo, R. Sasaki, H. Namiki, T. Okano, M. Yamamoto, Prevention of esophageal stricture after endoscopic submucosal dissection using tissue-engineered cell sheets, Gastroenterology, 143 (2012) 582-588.e582.

[154] K. Nagase, M. Yamato, H. Kanazawa, T. Okano, Poly(N-isopropylacrylamide)-based thermoresponsive surfaces provide new types of biomedical applications, Biomaterials, 153 (2018) 27-48.

[155] M. Kanzaki, M. Yamato, J. Yang, H. Sekine, C. Kohno, R. Takagi, H. Hatakeyama, T. Isaka, T. Okano, T. Onuki, Dynamic sealing of lung air leaks by the transplantation of tissue engineered cell sheets, Biomaterials, 28 (2007) 4294-4302.

[156] K. Yamamoto, M. Yamato, T. Morino, H. Sugiyama, R. Takagi, Y. Yaguchi, T. Okano, H. Kojima, Middle ear mucosal regeneration by tissue-engineered cell sheet transplantation, NPJ Regenerative medicine, 2 (2017) 6.

[157] H. Shimizu, K. Ohashi, R. Utoh, K. Ise, M. Gotoh, M. Yamato, T. Okano, Bioengineering of a functional sheet of islet cells for the treatment of diabetes mellitus, Biomaterials, 30 (2009) 5943-5949.

[158] K. Ohashi, T. Yokoyama, M. Yamato, H. Kuge, H. Kanehiro, M. Tsutsumi, T. Amanuma, H. Iwata, J. Yang, T. Okano, Y. Nakajima, Engineering functional two- and three-dimensional liver systems *in vivo* using hepatic tissue sheets, Nature medicine, 13 (2007) 880-885.

[159] G. Kuramoto, S. Takagi, K. Ishitani, T. Shimizu, T. Okano, H. Matsui, Preventive effect of oral mucosal epithelial cell sheets on intrauterine adhesions, Human reproduction (Oxford, England), 30 (2015) 406-416.

[160] Y. Kato, T. Iwata, S. Morikawa, M. Yamato, T. Okano, Y. Uchigata, Allogeneic Transplantation of an Adipose-Derived Stem Cell Sheet Combined With Artificial Skin Accelerates Wound Healing in a Rat Wound Model of Type 2 Diabetes and Obesity, Diabetes, 64 (2015) 2723-2734.

[161] I. Aranaz, E. Martinez-Campos, M.E. Nash, M.G. Tardajos, H. Reinecke, C. Elvira, V. Ramos, J.L. Lopez-Lacomba, A. Gallardo, Pseudo-double network hydrogels with unique properties as supports for cell manipulation, Journal of Materials Chemistry B, 2 (2014) 3839-3848.

[162] A. Gallardo, E. Martínez-Campos, C. García, A.L. Cortajarena, J. Rodríguez-Hernández, Hydrogels with Modulated Ionic Load for Mammalian Cell Harvesting with Reduced Bacterial Adhesion, Biomacromolecules, 18 (2017) 1521-1531.

[163] A. Gallardo, N. Lujan, H. Reinecke, C. García, A.D. Campo, J. Rodriguez-Hernandez, Chemical and Topographical Modification of Polycarbonate Surfaces through Diffusion/Photocuring Processes of Hydrogel Precursors Based on Vinylpyrrolidone, Langmuir, 33 (2017) 1614-1622.

[164] M. Teodorescu, M. Bercea, Poly(vinylpyrrolidone) – A Versatile Polymer for Biomedical and Beyond Medical Applications, Polymer-Plastics Technology and Engineering, 54 (2015) 923-943.

[165] F. Haaf, A. Sanner, F. Straub, Polymers of N-Vinylpyrrolidone: Synthesis, Characterization and Uses, Polymer Journal, 17 (1985) 143.

[166] C. Elvira, F. Yi, M.C. Azevedo, L. Rebouta, A.M. Cunha, J. San Roman, R.L. Reis, Plasma- and chemical-induced graft polymerization on the surface of starch-based biomaterials aimed at improving cell adhesion and proliferation, Journal of materials science. Materials in medicine, 14 (2003) 187-194.

[167] H. Vihola, A. Laukkanen, L. Valtola, H. Tenhu, J. Hirvonen, Cytotoxicity of thermosensitive polymers poly(N-isopropylacrylamide), poly(N-vinylcaprolactam) and amphiphilically modified poly(N-vinylcaprolactam), Biomaterials, 26 (2005) 3055-3064.

[168] N.A. Cortez-Lemus, A. Licea-Claverie, Poly(N-vinylcaprolactam), a comprehensive review on a thermoresponsive polymer becoming popular, Progress in Polymer Science, 53 (2016) 1-51.

[169] Y.M. Lim, J.P. Jeun, J.H. Lee, Y.M. Lee, Y.C. Nho, Cell Sheet Detachment from Poly(N-vinylcaprolactam-co-N-isopropylacrylamide) Grafted onto Tissue Culture Polystyrene Dishes, J. Ind. Eng. Chem., 13 (2007) 21-26.

[170] B. Lee, A. Jiao, S. Yu, J.B. You, D.-H. Kim, S.G. Im, Initiated chemical vapor deposition of thermoresponsive poly(N-vinylcaprolactam) thin films for cell sheet engineering, Acta biomaterialia, 9 (2013) 7691-7698.

[171] H.-I.C.Y. Wang, Cell Responses to Surface and Architecture of Tissue Engineering Scaffolds, Regenerative Medicine and Tissue Engineering IntechOpen, 2011.

[172] B. Vagaska, L. Bacakova, E. Filova, K. Balik, Osteogenic cells on bio-inspired materials for bone tissue engineering, Physiological research, 59 (2010) 309-322.

[173] H. Jeon, C.G. Simon, Jr., G. Kim, A mini-review: Cell response to microscale, nanoscale, and hierarchical patterning of surface structure, Journal of biomedical materials research. Part B, Applied biomaterials, 102 (2014) 1580-1594.

[174] L. De Bartolo, M. Rende, S. Morelli, G. Giusi, S. Salerno, A. Piscioneri, A. Gordano, A. Di Vito, M. Canonaco, E. Drioli, Influence of membrane surface properties on the growth of neuronal cells isolated from hippocampus, Journal of Membrane Science, 325 (2008) 139-149.

[175] T.W. Chung, D.Z. Liu, S.Y. Wang, S.S. Wang, Enhancement of the growth of human endothelial cells by surface roughness at nanometer scale, Biomaterials, 24 (2003) 4655-4661.

[176] G. Abagnale, M. Steger, V.H. Nguyen, N. Hersch, A. Sechi, S. Joussen, B. Denecke, R. Merkel, B. Hoffmann, A. Dreser, U. Schnakenberg, A. Gillner, W. Wagner, Surface topography enhances differentiation of mesenchymal stem cells towards osteogenic and adipogenic lineages, Biomaterials, 61 (2015) 316-326.

[177] P. Thevenot, W. Hu, L. Tang, Surface chemistry influence implant biocompatibility, Current topics in medicinal chemistry, 8 (2008) 270-280.

[178] P. Collin-Osdoby, P. Osdoby, RANKL-mediated osteoclast formation from murine RAW 264.7 cells, Methods in molecular biology (Clifton, N.J.), 816 (2012) 187-202.

[179] D.M. Jafarlou, E. Zalnezhad, A.S. Hamouda, G. Faraji, N.A.B. Mardi, M.A. Hassan Mohamed, Evaluation of the Mechanical Properties of AA 6063 Processed by Severe Plastic Deformation, Metallurgical and Materials Transactions A, 46 (2015) 2172-2184.

[180] H. Li, W. He, S. Pang, P.K. Liaw, T. Zhang, *In vitro* responses of bone-forming MC3T3-E1 pre-osteoblasts to biodegradable Mg-based bulk metallic glasses, Materials Science and Engineering: C, 68 (2016) 632-641.

[181] J. Fei, X. Wen, X. Lin, Saijilafu, W. Wang, O. Ren, X. Chen, L. Tan, K. Yang, H. Yang, L. Yang, Biocompatibility and neurotoxicity of magnesium alloys potentially used for neural repairs, Materials Science and Engineering: C, 78 (2017) 1155-1163.

[182] Y.-K. Kim, Y.-S. Jang, Y.-H. Lee, H.-K. Yi, T.-S. Bae, M.-H. Lee, Effect of Ca-P compound formed by hydrothermal treatment on biodegradation and biocompatibility of Mg-3Al-1Zn-1.5Ca alloy; *in vitro* and *in vivo* evaluation, Scientific Reports, 7 (2017) 712.

[183] A.M. Peterson, C. Pilz-Allen, T. Kolesnikova, H. Möhwald, D. Shchukin, Growth factor release from polyelectrolyte-coated titanium for implant applications, ACS applied materials & interfaces, 6 (2013) 1866-1871.

[184] M. Stigter, J. Bezemer, K. De Groot, P. Layrolle, Incorporation of different antibiotics into carbonated hydroxyapatite coatings on titanium implants, release and antibiotic efficacy, Journal of Controlled Release, 99 (2004) 127-137.

[185] Z. Yu, M. Yu, Z. Zhang, G. Hong, Q. Xiong, Bovine serum albumin nanoparticles as controlled release carrier for local drug delivery to the inner ear, Nanoscale research letters, 9 (2014) 1-7.

[186] L.-H. Li, Y.-M. Kong, H.-W. Kim, Y.-W. Kim, H.-E. Kim, S.-J. Heo, J.-Y. Koak, Improved biological performance of Ti implants due to surface modification by micro-arc oxidation, Biomaterials, 25 (2004) 2867-2875.

[187] R. Jugdaohsingh, Silicon and bone health, The journal of nutrition, health & aging, 11 (2007) 99-110.

[188] H. Zreiqat, C.R. Howlett, A. Zannettino, P. Evans, G. Schulze-Tanzil, C. Knabe, M. Shakibaei, Mechanisms of magnesium-stimulated adhesion of osteoblastic cells to commonly used orthopaedic implants, J Biomed Mater Res, 62 (2002) 175-184.

[189] Y. Yamasaki, Y. Yoshida, M. Okazaki, A. Shimazu, T. Uchida, T. Kubo, Y. Akagawa, Y. Hamada, J. Takahashi, N. Matsuura, Synthesis of functionally graded $MgCO_3$ apatite accelerating osteoblast adhesion, J Biomed Mater Res, 62 (2002) 99-105.

[190] S.V. Kellesarian, M. Yunker, R. Ramakrishnaiah, H. Malmstrom, T.V. Kellesarian, V. Ros Malignaggi, F. Javed, Does incorporating zinc in titanium implant surfaces influence osseointegration? A systematic review, The Journal of Prosthetic Dentistry, 117 (2017) 41-47.

[191] T. Notomi, M. Kuno, A. Hiyama, K. Ohura, M. Noda, T.M. Skerry, Zinc-Induced Effects on Osteoclastogenesis Involves Activation of Hyperpolarization-Activated Cyclic Nucleotide Modulated Channels via Changes in Membrane Potential, Journal of bone and mineral research : the official journal of the American Society for Bone and Mineral Research, 30 (2015) 1618-1626.

[192] K. Venkateswarlu, N. Rameshbabu, D. Sreekanth, A.C. Bose, V. Muthupandi, S. Subramanian, Fabrication and characterization of micro-arc oxidized fluoride containing titania films on Cp Ti, Ceramics International, 39 (2013) 801-812.

[193] M. Nagasawa, L.F. Cooper, Y. Ogino, D. Mendonca, R. Liang, S. Yang, G. Mendonca, K. Uoshima, Topography Influences Adherent Cell Regulation of Osteoclastogenesis, Journal of Dental Research, 95 (2016) 319-326.

[194] C. Pontier, M. Viana, E. Champion, D. Bernache-Assollant, D. Chulia, About the use of stoichiometric hydroxyapatite in compression - incidence of manufacturing process on compressibility, European journal of pharmaceutics and biopharmaceutics : official journal of Arbeitsgemeinschaft fur Pharmazeutische Verfahrenstechnik e.V, 51 (2001) 249-257.

[195] C. Pérez-Jorge, A. Conde, M.A. Arenas, R. Pérez-Tanoira, E. Matykina, J.J. de Damborenea, E. Gómez-Barrena, J. Esteban, *In vitro* assessment of *Staphylococcus epidermidis* and *Staphylococcus aureus* adhesion on TiO_2 nanotubes on Ti–6Al–4V alloy, Journal of Biomedical Materials Research Part A, 100A (2012) 1696-1705.

[196] T.L. Burgess, Y.-x. Qian, S. Kaufman, B.D. Ring, G. Van, C. Capparelli, M. Kelley, H. Hsu, W.J. Boyle, C.R. Dunstan, S. Hu, D.L. Lacey, The Ligand for Osteoprotegerin (OPGL) Directly Activates Mature Osteoclasts, The Journal of Cell Biology, 145 (1999) 527-538.

[197] B. Clarke, Normal Bone Anatomy and Physiology, Clinical Journal of the American Society of Nephrology : CJASN, 3 (2008) S131-S139.

[198] A. Gomez-Sanchez, M. Katunar, W. Schreiner, G. Duffo, S. Cere, D.J. Schiffrin, Structure and dielectric properties of electrochemically grown ZrO_2 films, Acta chimica Slovenica, 61 (2014) 316-327.

[199] L.L. Hench, I.D. Xynos, J.M. Polak, Bioactive glasses for *in situ* tissue regeneration, Journal of biomaterials science. Polymer edition, 15 (2004) 543-562.

[200] A. Krzakala, A. Kazek-Kesik, W. Simka, Application of plasma electrolytic oxidation to bioactive surface formation on titanium and its alloys, RSC Advances, 3 (2013) 19725-19743.

[201] I.d.S.V. Marques, V.A.R. Barão, N.C. da Cruz, J.C.-C. Yuan, M.F. Mesquita, A.P. Ricomini-Filho, C. Sukotjo, M.T. Mathew, Electrochemical behavior of bioactive coatings on cp-Ti surface for dental application, Corrosion science, 100 (2015) 133-146.

[202] H. Hu, X. Liu, C. Ding, Preparation and cytocompatibility of Si-incorporated nanostructured TiO_2 coating, Surface and Coatings Technology, 204 (2010) 3265-3271.

[203] Q. Wang, H. Hu, Y. Qiao, Z. Zhang, J. Sun, Enhanced Performance of Osteoblasts by Silicon Incorporated Porous TiO_2 Coating, Journal of Materials Science & Technology, 28 (2012) 109-117.

[204] R. Zhou, D. Wei, S. Cheng, B. Li, Y. Wang, D. Jia, Y. Zhou, H. Guo, The structure and in vitro apatite formation ability of porous titanium covered bioactive microarc oxidized TiO_2-based coatings containing Si, Na and Ca, Ceramics International, 40 (2014) 501-509.

[205] A. Kazek-Kęsik, M. Krok-Borkowicz, E. Pamuła, W. Simka, Electrochemical and biological characterization of coatings formed on Ti–15Mo alloy by plasma electrolytic oxidation, Materials Science and Engineering: C, 43 (2014) 172-181.

[206] H. Li, Y. Sun, J. Zhang, Effect of ZrO_2 particle on the performance of micro-arc oxidation coatings on Ti6Al4V, Applied Surface Science, 342 (2015) 183-190.

[207] X. Liu, H.C. Man, Laser fabrication of Ag-HA nanocomposites on Ti6Al4V implant for enhancing bioactivity and antibacterial capability, Materials Science and Engineering: C, 70 (2017) 1-8.

[208] S.V. Dorozhkin, Bioceramics of calcium orthophosphates, Biomaterials, 31 (2010) 1465-1485.

[209] M.Z. Ibrahim, A.A.D. Sarhan, F. Yusuf, M. Hamdi, Biomedical materials and techniques to improve the tribological, mechanical and biomedical properties of orthopedic implants – A review article, Journal of Alloys and Compounds, 714 (2017) 636-667.

[210] Y. Li, C. Wong, J. Xiong, P. Hodgson, C. Wen, Cytotoxicity of titanium and titanium alloying elements, J Dent Res, 89 (2010) 493-497.

[211] H.S. Hafez, E.M. Selim, F.H. Kamel Eid, W.A. Tawfik, E.A. Al-Ashkar, Y.A. Mostafa, Cytotoxicity, genotoxicity, and metal release in patients with fixed orthodontic appliances: a longitudinal *in-vivo* study, American journal of orthodontics and dentofacial orthopedics: official publication of the American Association of Orthodontists, its constituent societies, and the American Board of Orthodontics, 140 (2011) 298-308.

[212] G.J. Thompson, D.A. Puleo, Ti-6Al-4V ion solution inhibition of osteogenic cell phenotype as a function of differentiation timecourse in vitro, Biomaterials, 17 (1996) 1949-1954.

[213] J.J. Jacobs, A.K. Skipor, J. Black, R. Urban, J.O. Galante, Release and excretion of metal in patients who have a total hip-replacement component made of titanium-base alloy, The Journal of bone and joint surgery. American volume, 73 (1991) 1475-1486.

[214] H. Sudo, H.A. Kodama, Y. Amagai, S. Yamamoto, S. Kasai, In vitro differentiation and calcification in a new clonal osteogenic cell line derived from newborn mouse calvaria, The Journal of cell biology, 96 (1983) 191-198.

[215] E.E. Golub, K. Boesze-Battaglia, The role of alkaline phosphatase in mineralization, Current Opinion in Orthopaedics, 18 (2007) 444-448.

[216] J. He, W. Zhou, X. Zhou, X. Zhong, X. Zhang, P. Wan, B. Zhu, W. Chen, The anatase phase of nanotopography titania plays an important role on osteoblast cell morphology and proliferation, Journal of Materials Science: Materials in Medicine, 19 (2008) 3465-3472.

[217] D. Geblinger, C. Zink, N.D. Spencer, L. Addadi, B. Geiger, Effects of surface microtopography on the assembly of the osteoclast resorption apparatus, Journal of The Royal Society Interface, 9 (2012) 1599-1608.

[218] K. Wang, C. Zhou, Y. Hong, X. Zhang, A review of protein adsorption on bioceramics, Interface Focus, 2 (2012) 259-277.

[219] L. Burgos-Asperilla, M.C. García-Alonso, M.L. Escudero, C. Alonso, Study of the interaction of inorganic and organic compounds of cell culture medium with a Ti surface, Acta biomaterialia, 6 (2010) 652-661.

[220] A. Abarrategi, J. Garcia-Cantalejo, C. Moreno-Vicente, A. Civantos, V. Ramos, J.V. Casado, S. Perez-Rial, R. Martinez-Corria, J.L. Lopez-Lacomba, Gene expression profile on chitosan/rhBMP-2 films: A novel osteoinductive coating for implantable materials, Acta biomaterialia, 5 (2009) 2633-2646.

[221] A. Abarrategi, C. Moreno-Vicente, V. Ramos, I. Aranaz, J.V. Sanz Casado, J.L. Lopez-Lacomba, Improvement of porous beta-TCP scaffolds with rhBMP-2 chitosan carrier film for bone tissue application, Tissue engineering. Part A, 14 (2008) 1305-1319.

[222] J.L. López-Lacomba, J.M. García-Cantalejo, J.V. Sanz Casado, A. Abarrategi, V. Correas Magaña, V. Ramos, Use of rhBMP-2 Activated Chitosan Films To Improve Osseointegration, Biomacromolecules, 7 (2006) 792-798.

[223] O. Geuli, N. Metoki, T. Zada, M. Reches, N. Eliaz, D. Mandler, Synthesis, coating, and drug-release of hydroxyapatite nanoparticles loaded with antibiotics, Journal of Materials Chemistry B, 5 (2017) 7819-7830.

[224] S.H. Uhm, D.H. Song, J.S. Kwon, S.Y. Im, J.G. Han, K.N. Kim, Time-dependent growth of TiO_2 nanotubes from a magnetron sputtered Ti thin film, Thin Solid Films, 547 (2013) 181-187.

[225] H. Sharifi, M. Aliofkhazraei, G.B. Darband, A.S. Rouhaghdam, Tribological properties of PEO nanocomposite coatings on titanium formed in electrolyte containing ketoconazole, Tribology International, 102 (2016) 463-471.

[226] C.J. Ivanoff, G. Widmark, C. Johansson, A. Wennerberg, Histologic evaluation of bone response to oxidized and turned titanium micro-implants in human jawbone, The International journal of oral & maxillofacial implants, 18 (2003) 341-348.

[227] J.A. Shibli, S. Grassi, L.C. De Figueiredo, M. Feres, G. Iezzi, A. Piattelli, Human peri-implant bone response to turned and oxidized titanium implants inserted and retrieved after 2 months, Implant Dentistry, 16 (2007) 252-259.

[228] Y.H. Kim, J.Y. Koak, I.T. Chang, A. Wennerberg, S.J. Heo, A histomorphometric analysis of the effects of various surface treatment methods on osseointegration, International Journal of Oral and Maxillofacial Implants, 18 (2003) 349-356.

[229] I.-J. Hwang, H.-C. Choe, Effects of Zn and Si ions on the corrosion behaviors of PEO-treated Ti-6Al-4V alloy, Applied Surface Science, (2017).

[230] J.-M. Yu, H.-C. Choe, Morphology changes and bone formation on PEO-treated Ti-6Al-4V alloy in electrolyte containing Ca, P, Sr, and Si ions, Applied Surface Science, (2017).

[231] K. Rokosz, T. Hryniewicz, W. Kacalak, K. Tandecka, S. Raaen, S. Gaiaschi, P. Chapon, W. Malorny, D. Matýsek, Ł. Dudek, K. Pietrzak, Characterization of porous phosphate coatings enriched with calcium, magnesium, zinc and copper created on CP titanium grade 2 by plasma electrolytic oxidation, Metals, 8 (2018).

[232] J.-M. Yu, H.-C. Choe, Mg-containing hydroxyapatite coatings on Ti-6Al-4V alloy for dental materials, Applied Surface Science, 432 (2018) 294-299.

[233] D. Aronov, R. Rosen, E.Z. Ron, G. Rosenman, Tunable hydroxyapatite wettability: Effect on adhesion of biological molecules, Process Biochemistry, 41 (2006) 2367-2372.

[234] M. Shemesh, L. Addadi, B. Geiger, Surface microtopography modulates sealing zone development in osteoclasts cultured on bone, Journal of The Royal Society Interface, 14 (2017).

[235] K.H. Park, B. Park, D.S. Yoon, S.-H. Kwon, D.M. Shin, J.W. Lee, H.G. Lee, J.-H. Shim, J.H. Park, J.M. Lee, Zinc inhibits osteoclast differentiation by suppression of Ca^{2+}-Calcineurin-NFATc1 signaling pathway, Cell Communication and Signaling, 11 (2013) 74.

[236] J. Costa-Rodrigues, S. Reis, M.H. Fernandes, Osteoclastogenic modulation by silicon: Cellular and molecular mechanisms, Bone, 48 (2011) S132.

[237] L. Yang, S. Perez-Amodio, F.Y.F. Barrère-de Groot, V. Everts, C.A. van Blitterswijk, P. Habibovic, The effects of inorganic additives to calcium phosphate on in vitro behavior of osteoblasts and osteoclasts, Biomaterials, 31 (2010) 2976-2989.

[238] Y.D. Kwon, D.W. Lee, S.O. Hong, Magnesium vs. machined surfaced titanium - osteoblast and osteoclast differentiation, The journal of advanced prosthodontics, 6 (2014) 157-164.

[239] S. Vahabzadeh, M. Roy, S. Bose, Effects of Silicon on Osteoclast Cell Mediated Degradation, In Vivo Osteogenesis and Vasculogenesis of Brushite Cement, Journal of materials chemistry. B, Materials for biology and medicine, 3 (2015) 8973-8982.

[240] C.M. Botelho, R.A. Brooks, G. Spence, I. McFarlane, M.A. Lopes, S.M. Best, J.D. Santos, N. Rushton, W. Bonfield, Differentiation of mononuclear precursors into osteoclasts on the surface of Si-substituted hydroxyapatite, Journal of biomedical materials research. Part A, 78 (2006) 709-720.

[241] Y. Ramaswamy, C. Wu, H. Zhou, H. Zreiqat, Biological response of human bone cells to zinc-modified Ca–Si-based ceramics, Acta biomaterialia, 4 (2008) 1487-1497.

[242] B.G. Zhang, D.E. Myers, G.G. Wallace, M. Brandt, P.F. Choong, Bioactive coatings for orthopaedic implants-recent trends in development of implant coatings, International journal of molecular sciences, 15 (2014) 11878-11921.

[243] J. Yu, L. Xu, K. Li, N. Xie, Y. Xi, Y. Wang, X. Zheng, X. Chen, M. Wang, X. Ye, Zinc-modified Calcium Silicate Coatings Promote Osteogenic Differentiation through TGF-β/Smad Pathway and Osseointegration in Osteopenic Rabbits, Scientific Reports, 7 (2017) 3440.

[244] A.W. Glover, A.J.A. Santini, J.S. Davidson, J.A. Pope, Mid- to long-term survivorship of oxidised zirconium total knee replacements performed in patients under 50 years of age, The Knee, 25 (2018) 617-622.

[245] T. Hanawa, Y. Tsutsumi, Calcium phosphate formation on titanium and zirconium and its application to medical devices, Bioceramics Development and Applications, 1 (2011).

[246] J.R. Gamboa, S. Mohandes, P.L. Tran, M.J. Slepian, J.-Y. Yoon, Linear fibroblast alignment on sinusoidal wave micropatterns, Colloids and Surfaces B: Biointerfaces, 104 (2013) 318-325.

[247] M. Hulander, A. Lundgren, L. Faxalv, T.L. Lindahl, A. Palmquist, M. Berglin, H. Elwing, Gradients in surface nanotopography used to study platelet adhesion and activation, Colloids and surfaces. B, Biointerfaces, 110 (2013) 261-269.

[248] V. Vogel, M. Sheetz, Local force and geometry sensing regulate cell functions, Nature reviews. Molecular cell biology, 7 (2006) 265-275.

[249] C.L. Gilchrist, D.S. Ruch, D. Little, F. Guilak, Micro-scale and meso-scale architectural cues cooperate and compete to direct aligned tissue formation, Biomaterials, 35 (2014) 10015-10024.

[250] R.A. Gittens, T. McLachlan, R. Olivares-Navarrete, Y. Cai, S. Berner, R. Tannenbaum, Z. Schwartz, K.H. Sandhage, B.D. Boyan, The effects of combined micron-/submicron-scale surface roughness and nanoscale features on cell proliferation and differentiation, Biomaterials, 32 (2011) 3395-3403.

[251] K.-S. Lee, H.-J. Kim, Q.-L. Li, X.-Z. Chi, C. Ueta, T. Komori, J.M. Wozney, E.-G. Kim, J.-Y. Choi, H.-M. Ryoo, S.-C. Bae, Runx2 Is a Common Target of Transforming Growth Factor β1 and Bone Morphogenetic Protein 2, and Cooperation between Runx2 and Smad5 Induces Osteoblast-Specific Gene Expression in the Pluripotent Mesenchymal Precursor Cell Line C2C12, Molecular and Cellular Biology, 20 (2000) 8783-8792.

[252] D.P.L. Lin, R. Carnagarin, A. Dharmarajan, C.R. Dass, Transdifferentiation of myoblasts into osteoblasts - possible use for bone therapy, The Journal of pharmacy and pharmacology, 69 (2017) 1661-1671.

[253] M. Ahmad, D. Gawronski, J. Blum, J. Goldberg, G. Gronowicz, Differential response of human osteoblast-like cells to commercially pure (cp) titanium grades 1 and 4, J Biomed Mater Res, 46 (1999) 121-131.

[254] A. Civantos, E. Martínez-Campos, V. Ramos, C. Elvira, A. Gallardo, A. Abarrategi, Titanium Coatings and Surface Modifications: Toward Clinically Useful Bioactive Implants, ACS Biomaterials Science & Engineering, 3 (2017) 1245-1261.

[255] A. Rutkovskiy, K.-O. Stensløkken, I.J. Vaage, Osteoblast Differentiation at a Glance, Medical Science Monitor Basic Research, 22 (2016) 95-106.

[256] Y. Wang, J. Lou, L. Zeng, J. Xiang, S. Zhang, J. Wang, F. Xiong, C. Li, Y. Zhao, R. Zhang, Osteogenic potential of a novel microarc oxidized coating formed on Ti6Al4V alloys, Applied Surface Science, 412 (2017) 29-36.

[257] R.E. Marquis, Antimicrobial actions of fluoride for oral bacteria, Canadian journal of microbiology, 41 (1995) 955-964.

[258] I.A.J. van Hengel, M. Riool, L.E. Fratila-Apachitei, J. Witte-Bouma, E. Farrell, A.A. Zadpoor, S.A.J. Zaat, I. Apachitei, Selective laser melting porous metallic implants with immobilized silver nanoparticles kill and prevent biofilm formation by methicillin-resistant *Staphylococcus aureus*, Biomaterials, 140 (2017) 1-15.

[259] W.K. Jung, H.C. Koo, K.W. Kim, S. Shin, S.H. Kim, Y.H. Park, Antibacterial Activity and Mechanism of Action of the Silver Ion in *Staphylococcus aureus* and *Escherichia coli*, Applied and Environmental Microbiology, 74 (2008) 2171-2178.

[260] P. Tian, X. Liu, Surface modification of biodegradable magnesium and its alloys for biomedical applications, Regenerative Biomaterials, 2 (2015) 135-151.

[261] F. Monfort, A. Berkani, E. Matykina, P. Skeldon, G.E. Thompson, H. Habazaki, K. Shimizu, Development of anodic coatings on aluminium under sparking conditions in silicate electrolyte, Corrosion Science, 49 (2007) 672-693.

[262] M. Szczepanski, M. Kamianowska, G. Kamianowski, Effects of fluorides on apoptosis and activation of human umbilical vein endothelial cells, Oral diseases, 18 (2012) 280-284.

[263] T.R. Arnett, Extracellular pH Regulates Bone Cell Function, The Journal of Nutrition, 138 (2008) 415S-418S.

[264] T. Nordstrom, O.D. Rotstein, R. Romanek, S. Asotra, J.N. Heersche, M.F. Manolson, G.F. Brisseau, S. Grinstein, Regulation of cytoplasmic pH in osteoclasts. Contribution of proton pumps and a proton-selective conductance, The Journal of biological chemistry, 270 (1995) 2203-2212.

[265] G.L. Jones, A. Motta, M.J. Marshall, A.J. El Haj, S.H. Cartmell, Osteoblast: Osteoclast co-cultures on silk fibroin, chitosan and PLLA films, Biomaterials, 30 (2009) 5376-5384.

[266] P.W. Serruys, M.J. Kutryk, A.T. Ong, Coronary-artery stents, New England Journal of Medicine, 354 (2006) 483-495.

[267] L. Xu, A. Yamamoto, *In vitro* degradation of biodegradable polymer-coated magnesium under cell culture condition, Applied Surface Science, 258 (2012) 6353-6358.

[268] L. Xu, A. Yamamoto, Characteristics and cytocompatibility of biodegradable polymer film on magnesium by spin coating, Colloids and Surfaces B: Biointerfaces, 93 (2012) 67-74.

[269] Y. Chen, Y. Song, S. Zhang, J. Li, C. Zhao, X. Zhang, Interaction between a high purity magnesium surface and PCL and PLA coatings during dynamic degradation, Biomedical Materials, 6 (2011) 025005.

[270] R.-C. Zeng, L.-y. Cui, K. Jiang, R. Liu, B.-D. Zhao, Y.-F. Zheng, *In Vitro* Corrosion and Cytocompatibility of a Microarc Oxidation Coating and Poly(l-lactic acid) Composite Coating on Mg–1Li–1Ca Alloy for Orthopedic Implants, ACS Applied Materials & Interfaces, 8 (2016) 10014-10028.

[271] I. Yilgor, E. Yilgor, C. Kosak Soz, Superhydrophobic Polymer Surfaces: Preparation, Properties, and Applications, 2016.

[272] A.F. Khan, M. Saleem, A. Afzal, A. Ali, A. Khan, A.R. Khan, Bioactive behavior of silicon substituted calcium phosphate based bioceramics for bone regeneration, Materials Science and Engineering: C, 35 (2014) 245-252.

[273] G.W. Brindley, R. Hayami, Kinetics and mechanism of formation of forsterite (Mg_2SiO4) by solid state reaction of MgO and SiO_2, The Philosophical Magazine: A Journal of Theoretical Experimental and Applied Physics, 12 (1965) 505-514.

[274] J. Liu, Y. Lu, X. Jing, Y. Yuan, M. Zhang, Characterization of plasma electrolytic oxidation coatings formed on Mg–Li alloy in an alkaline silicate electrolyte containing silica sol, Materials and Corrosion, 60 (2009) 865-870.

[275] M. Carboneras, M.C. García-Alonso, M.L. Escudero, Biodegradation kinetics of modified magnesium-based materials in cell culture medium, Corrosion Science, 53 (2011) 1433-1439.

[276] C.J. Tredwin, A.M. Young, E.A. Abou Neel, G. Georgiou, J.C. Knowles, Hydroxyapatite, fluor-hydroxyapatite and fluorapatite produced via the sol-gel method: dissolution behaviour and biological properties after crystallisation, Journal of materials science. Materials in medicine, 25 (2014) 47-53.

[277] Y. Shen, W. Liu, C. Wen, H. Pan, T. Wang, B.W. Darvell, W.W. Lu, W. Huang, Bone regeneration: importance of local pH-strontium-doped borosilicate scaffold, Journal of Materials Chemistry, 22 (2012) 8662-8670.

[278] H. Li, J. Chang, Bioactive silicate materials stimulate angiogenesis in fibroblast and endothelial cell co-culture system through paracrine effect, Acta Biomater, 9 (2013) 6981-6991.

[279] E.J. Kim, S.Y. Bu, M.K. Sung, M.K. Choi, Effects of silicon on osteoblast activity and bone mineralization of MC3T3-E1 cells, Biological trace element research, 152 (2013) 105-112.

[280] X. Ge, Y. Leng, C. Bao, L. Xu Sherry, R. Wang, F. Ren, Antibacterial coatings of fluoridated hydroxyapatite for percutaneous implants, Journal of Biomedical Materials Research Part A, 95A (2010) 588-599.

[281] D.E. Clapham, Calcium Signaling, Cell, 131 (2007) 1047-1058.

[282] J. Loeper, J. Goy-Loeper, L. Rozensztajn, M. Fragny, The antiatheromatous action of silicon, Atherosclerosis, 33 (1979) 397-408.

[283] X. Wu, S. Wang, Regulating MC3T3-E1 cells on deformable poly(epsilon-caprolactone) honeycomb films prepared using a surfactant-free breath figure method in a water-miscible solvent, ACS Appl Mater Interfaces, 4 (2012) 4966-4975.

[284] N.M.M. Pires, B.L. van der Hoeven, M.R. de Vries, L.M. Havekes, B.J. van Vlijmen, W.E. Hennink, P.H.A. Quax, J.W. Jukema, Local perivascular delivery of anti-restenotic agents from a drug-eluting poly(ε-caprolactone) stent cuff, Biomaterials, 26 (2005) 5386-5394.

[285] X. Yu, T. Takayama, S.A. Goel, X. Shi, Y. Zhou, K.C. Kent, W.L. Murphy, L.-W. Guo, A rapamycin-releasing perivascular polymeric sheath produces highly effective inhibition of intimal hyperplasia, Journal of Controlled Release, 191 (2014) 47-53.

[286] W. Xu, K. Yagoshi, Y. Koga, M. Sasaki, T. Niidome, Optimized polymer coating for magnesium alloy-based bioresorbable scaffolds for long-lasting drug release and corrosion resistance, Colloids and Surfaces B: Biointerfaces, 163 (2018) 100-106.

[287] B.-S. Kim, S.-S. Yang, C.S. Kim, Incorporation of BMP-2 nanoparticles on the surface of a 3D-printed hydroxyapatite scaffold using an ε-polycaprolactone polymer emulsion coating method for bone tissue engineering, Colloids and Surfaces B: Biointerfaces, 170 (2018) 421-429.

[288] G. Gratzl, C. Paulik, S. Hild, J.P. Guggenbichler, M. Lackner, Antimicrobial activity of poly(acrylic acid) block copolymers, Materials Science and Engineering: C, 38 (2014) 94-100.

[289] P.P. Leung, A.E. Yousef, T.H. Shellhammer, Antimicrobial properties of nisin-coated polymeric films as influenced by film type and coating conditions, Journal of Food Safety, 23 (2007) 1-12.

[290] J.M. Shin, J.W. Gwak, P. Kamarajan, J.C. Fenno, A.H. Rickard, Y.L. Kapila, Biomedical applications of nisin, Journal of applied microbiology, 120 (2016) 1449-1465.

[291] M. Millette, C. Le Tien, W. Smoragiewicz, M. Lacroix, Inhibition of *Staphylococcus aureus* on beef by nisin-containing modified alginate films and beads, Food Control, 18 (2007) 878-884.

[292] T. Krivorotova, A. Cirkovas, S. Maciulyte, R. Staneviciene, S. Budriene, E. Serviene, J. Sereikaite, Nisin-loaded pectin nanoparticles for food preservation, Food Hydrocolloids, 54 (2016) 49-56.

[293] M.H. Stenzel, C. Barner-Kowollik, T.P. Davis, Formation of honeycomb-structured, porous films via breath figures with different polymer architectures, Journal of Polymer Science Part A: Polymer Chemistry, 44 (2006) 2363-2375.

[294] M. Hernández-Guerrero, M.H. Stenzel, Honeycomb structured polymer films via breath figures, Polymer Chemistry, 3 (2012) 563-577.

[295] H. Bai, C. Du, A. Zhang, L. Li, Breath Figure Arrays: Unconventional Fabrications, Functionalizations, and Applications, Angewandte Chemie International Edition, 52 (2013) 12240-12255.

[296] M. Álvarez-Paino, A. Muñoz-Bonilla, F. López-Fabal, J.L. Gómez-Garcés, J.P.A. Heuts, M. Fernández-García, Effect of glycounits on the antimicrobial properties and toxicity behavior of polymers based on quaternized DMAEMA, Biomacromolecules, 16 (2015) 295-303.

[297] Y. Xue, H. Xiao, Y. Zhang, Antimicrobial polymeric materials with quaternary ammonium and phosphonium salts, Int J Mol Sci, 16 (2015) 3626-3655.

[298] T.R. Stratton, J.L. Rickus, J.P. Youngblood, *In Vitro* Biocompatibility Studies of Antibacterial Quaternary Polymers, Biomacromolecules, 10 (2009) 2550-2555.

[299] P. Dutta, J. Dey, A. Shome, P.K. Das, Nanostructure formation in aqueous solution of amphiphilic copolymers of 2-(N,N-dimethylaminoethyl)methacrylate and alkylacrylate: Characterization, antimicrobial activity, DNA binding, and cytotoxicity studies, International journal of pharmaceutics, 414 (2011) 298-311.

[300] P. Kumar, J.N. Kizhakkedathu, S.K. Straus, Antimicrobial Peptides: Diversity, Mechanism of Action and Strategies to Improve the Activity and Biocompatibility *In Vivo*, Biomolecules, 8 (2018) 4.

[301] A. Prince, P. Sandhu, P. Ror, E. Dash, S. Sharma, M. Arakha, S. Jha, Y. Akhter, M. Saleem, Lipid-II Independent Antimicrobial Mechanism of Nisin Depends On Its Crowding And Degree Of Oligomerization, Scientific Reports, 6 (2016) 37908.

[302] A. Guiotto, M. Pozzobon, M. Canevari, R. Manganelli, M. Scarin, F.M. Veronese, PEGylation of the antimicrobial peptide nisin A: problems and perspectives, Farmaco (Societa chimica italiana: 1989), 58 (2003) 45-50.

[303] S.J. Wang, P. Greer, R. Auerbach, Isolation and propagation of yolk-sac-derived endothelial cells from a hypervascular transgenic mouse expressing a gain-of-function fps/fes proto-oncogene, In vitro cellular & developmental biology. Animal, 32 (1996) 292-299.

[304] C. Guégan, J. Garderes, G. Le Pennec, F. Gaillard, F. Fay, I. Linossier, J.M. Herry, M.N.B. Fontaine, K.V. Réhel, Alteration of bacterial adhesion induced by the substrate stiffness, Colloids and Surfaces B: Biointerfaces, 114 (2014) 193-200.

[305] F. Meeussen, E. Nies, H. Berghmans, S. Verbrugghe, E. Goethals, F. Du Prez, Phase behaviour of poly(N-vinyl caprolactam) in water, Polymer, 41 (2000) 8597-8602.

[306] G.B. Schneider, A. English, M. Abraham, R. Zaharias, C. Stanford, J. Keller, The effect of hydrogel charge density on cell attachment, Biomaterials, 25 (2004) 3023-3028.

[307] B. Yang, C. Wang, Y. Zhang, L. Ye, Y. Qian, Y. Shu, J. Wang, J. Li, F. Yao, A thermoresponsive poly(N-vinylcaprolactam-co-sulfobetaine methacrylate) zwitterionic hydrogel exhibiting switchable anti-biofouling and cytocompatibility, Polymer Chemistry, 6 (2015) 3431-3442.

[308] J. Tan, R.A. Gemeinhart, M. Ma, W. Mark Saltzman, Improved cell adhesion and proliferation on synthetic phosphonic acid-containing hydrogels, Biomaterials, 26 (2005) 3663-3671.

[309] M. Ohgaki, T. Kizuki, M. Katsura, K. Yamashita, Manipulation of selective cell adhesion and growth by surface charges of electrically polarized hydroxyapatite, J Biomed Mater Res, 57 (2001) 366-373.

[310] D. Liu, T. Wang, X. Liu, Z. Tong, Cell proliferation and cell sheet detachment from the positively and negatively charged nanocomposite hydrogels, Biopolymers, 101 (2014) 58-65.

[311] J.B. Schlenoff, Zwitteration: Coating Surfaces with Zwitterionic Functionality to Reduce Nonspecific Adsorption, Langmuir, 30 (2014) 9625-9636.

[312] M. Tanahashi, T. Matsuda, Surface functional group dependence on apatite formation on self-assembled monolayers in a simulated body fluid, Journal of Biomedical Materials Research, 34 (1998) 305-315.

[313] S.M. Mihaila, R.L. Reis, A.P. Marques, M.E. Gomes, Hydrogels in Bone Tissue Engineering: A Multi-Parametric Approach, in: Gels Handbook, World Scientific, 2016, pp. 165-197.

[314] M.G. Gulcihan Gulseren, Hakan Ceylan, Ayse B. Tekinay, Mustafa O. Guler, Nanomaterials for Bone Tissue Regeneration and Orthopedic Implants, in: Therapeutic Nanomaterials, Wiley, 2016.

[315] M. Guvendiren, J.A. Burdick, The control of stem cell morphology and differentiation by hydrogel surface wrinkles, Biomaterials, 31 (2010) 6511-6518.

[316] Z. Zhao, J. Gu, Y. Zhao, Y. Guan, X.X. Zhu, Y. Zhang, Hydrogel Thin Film with Swelling-Induced Wrinkling Patterns for High-Throughput Generation of Multicellular Spheroids, Biomacromolecules, 15 (2014) 3306-3312.

[317] J. Lim, I. Jun, Y.B. Lee, E.M. Kim, D. Shin, H. Jeon, H. Park, H. Shin, Fabrication of cell sheets with anisotropically aligned myotubes using thermally expandable micropatterned hydrogels, Macromolecular Research, 24 (2016) 562-572.

[318] R. Guzman, S. Nardecchia, M.C. Gutierrez, M.L. Ferrer, V. Ramos, F. del Monte, A. Abarrategi, J.L. Lopez-Lacomba, Chitosan scaffolds containing calcium phosphate salts and rhBMP-2: *in vitro* and *in vivo* testing for bone tissue regeneration, PloS one, 9 (2014) e87149.